Synthesis and Characterization of Two Pyrene Labeled Gemini Surfactants and their Interactions with Oppositely Charged Molecules

by

Abdullah Ba Salem

A thesis

presented to the University of Waterloo

in fulfillment for the degree of

Doctor of Philosophy

in

Chemistry

Waterloo, Ontario, Canada, 2022

Examining Committee Membership

The following served on the Examining Committee for this thesis. The decision of the Examining Committee is by majority vote.

External Examiner	**Dr. Marc Ilies** Professor Pharmaceutical Sciences, Temple University
Supervisor	**Dr. Jean Duhamel** Professor Chemistry, University of Waterloo
Internal Member	**Dr. Mario Gauthier** Professor Chemistry, University of Waterloo
Internal Member	**Dr. Juewen Liu** Professor Chemistry, University of Waterloo
Internal-external Member	**Dr. Shawn Wittig** Professor Pharmacy, University of Waterloo

Author’s Declaration

This thesis consists of material all of which I authored or co-authored: see Statement of Contributions included in the thesis. This is a true copy of the thesis, including any required final revisions, as accepted by my examiners. I understand that my thesis may be made electronically available to the public.

Statement of Contributions

I completed all work and writing presented in this thesis with consultation with my supervisor Prof. Jean Duhamel. This thesis consists in part of three manuscripts written for publication.

Chapter 2: Ba-Salem, A. O.; Duhamel, J. Determination of the Aggregation Number of Pyrene-Labeled Gemini Surfactant Micelles by Pyrene Fluorescence Quenching Measurements. *Langmuir*, **2021**, *37*, 19, 6069-6079. DOI: 10.1021/acs.langmuir.1c00847

Chapter 3: Ba-Salem, A. O.; Duhamel, J. Synthesis and Characterization of a Pyrene-Labeled Gemini Surfactant Sensitive to the Polarity of its Environment. *Langmuir*, **2021**, *37*, 47, 13824-13837. DOI: 10.1021/acs.langmuir.1c01759

Chapter 4: Ba-Salem, A. O.; Gong, R.; Duhamel, J. Characterization of the Interactions between a Cationic Pyrene-Labeled Gemini Surfactant and the Anionic Surfactant Sodium Dodecyl Sulfate. *Langmuir* Submitted. I would like to acknowledge Dr. Elyse Roach from the Advanced Analysis Center at the University of Guelph for performing all the TEM experiments.

Chapter 5: I would like to acknowledge Dr. Elyse Roach from the Advanced Analysis Center at the University of Guelph for performing all the TEM experiments.

Abstract

Cationic gemini surfactants (GS) have attracted the attention of the scientific community as potential carriers of genetic cargo for gene transfection applications. These GS/polynucleotides complexes have been extensively studied in the literature, although most of the focus has been geared toward the characterization of the polynucleotide component of these complexes. This thesis utilizes steady-state (SSF) and time-resolved (TRF) fluorescence in conjunction with the model free analysis (MFA) to study and characterize two gemini surfactants, which were covalently labeled with the fluorescent dye pyrene. Pyrene was selected as the fluorophore for its ability to form an excimer upon encounter between an excited and a ground-state pyrene. First, two cationic gemini surfactants denoted as Py-3-12 and PyO-3-12 were prepared and their successful synthesis was confirmed by ^{1}H NMR. The surfactants were constituted of two dimethylammonium bromide headgroups linked by a propyl spacer, where one headgroup bore a dodecyl chain and the other headgroup bore either a 1-pyrenehexyl or a 1-pyrenemethoxyhexyl group for Py-3-12 and PyO-3-12, respectively. The properties of Py-3-12 and PyO-3-12 were investigated by determining their critical micelle concentration (CMC) and average aggregation number (N_{agg}). The fluorescence from the pyrene excimer was employed for the first time to determine N_{agg} for the micelles generated by these pyrene-labeled gemini surfactants (PyLGS). Since PyO-3-12 was shown to be more sensitive of the polarity of its local environment, it was deemed a better fluorescent probe than Py-3-12. After the behavior of the PyLGS had been characterized in solution, their interactions with other molecules were studied.

The improved properties of PyO-3-12 led to the study of its complexation with the anionic surfactant sodium dodecyl sulfate (SDS). Three series of PyO-3-12 solutions were prepared, where [PyO-3-12] was kept constant at 1, 4, and 16 μM, which is below the CMC of

0.33 mM of PyO-3-12, while the SDS concentration was varied from 0 to 200 mM. The SSF and MFA results showed that complexation of PyO-3-12 with SDS was complete at the equicharge point. As more SDS molecules were added to these systems, these complexes remained stable resulting in small changes in the trends obtained from the analysis of the SSF spectra and the MFA of the TRF decays. The PyO-3-12/SDS complexes were found to break down into smaller complexes as the [SDS] increased from 2 to the 8 mM CMC of SDS as a result of the incorporation of more SDS molecules into the PyO-3-12/SDS complexes. The smaller PyO-3-12/SDS complexes that existed at the CMC of SDS retained their composition for [SDS] between the CMC and 50 mM, as SDS micelles began to form. Increasing [SDS] above 50 mM led to the complete decomposition of the PyO-3-12/SDS complexes and resulted in SDS micelles hosting a single PyO-3-12 surfactant. These findings showed that the use of fluorescence techniques like SSF and the combination of TRF with the MFA provides a powerful tool to probe the interactions between PyLGS and oppositely charged surfactants at PyLGS concentrations, that were as low as 1 μM, much lower than their CMC and thus low enough to enable the study of their interactions between unassociated surfactants. Other techniques such as light scattering would require far higher concentrations of surfactants to study these aggregates.

The complexation of Py-3-12 and PyO-3-12 with calf thymus DNA (CT-DNA) was investigated in the fourth research chapter of this thesis. The concentrations of Py-3-12 and PyO-3-12 were kept constant below their respective CMC, while the CT-DNA concentration was varied and the (–/+) ratio, representing the ratio of the [CT-DNA] expressed in base pair concentration over [PyLGS], was used to describe changes in the [CT-DNA]. Both surfactants formed stable complexes with CT-DNA over a range of (–/+) ratios around unity, as indicated by the constant parameters retrieved from the analysis of the SSF spectra and the MFA of the TRF decays. PyO-3-12 also provided some insight about the polarity of the local environment

inside the PyO-3-12/CT-DNA complexes, which was found to be less hydrophobic than the interior of the PyO-3-12 micelles. The stability of the PyO-3-12/CT-DNA complexes prepared with a (–/+) ratio of 1.5 was further investigated as SDS, used to represent the negatively charged amphiphilic molecules found in cell membranes, was added to the solution. At low [SDS], addition of SDS molecules led to their association with the PyO-3-12/CT-DNA complexes in a process leading to the dissociation of the PyO-3-12/CT-DNA into *ter*-complexes made of individual CT-DNA molecules coated with a layer of positively charged PyO-3-12 further wrapped in a layer of SDS. Above an [SDS] of 0.5 mM, the DNA molecules were released from the *ter*-complexes leading to the formation of PyO-3-12/SDS complexes, which had been studied earlier. The complete release of CT-DNA from the PyO-3-12/CT-DNA complexes further supports the well-accepted notion that gemini surfactants are good candidates as carriers of genetic material.

In summary, this thesis has developed the use of PyLGS to characterize the interactions between unassociated gemini surfactants and oppositely charged molecules like SDS and CT-DNA. Taking advantage of the outstanding sensitivity of fluorescence, these studies can be conducted at surfactant concentrations, that are 1 to 2 orders of magnitude lower than their CMC, while the photophysical properties of the pyrenyl label affords insights into the structure and conformation adopted by the complexes generated with the PyLGS.

Acknowledgements

I would like to express my sincere appreciation and gratitude to my supervisor Prof. Jean Duhamel for his invaluable support, ideas, guidance, and mentorship throughout my long PhD journey. His patience, devotion, and commitment have been imperative to my development as a scientist. He was truly helpful over my thesis-writing process, and I am extremely grateful to him for that.

I would like to also thank my committee members: Prof. Mario Gauthier, Prof. Juewen Liu, and Prof. Shawn Wettig for their helpful support, guidance and discussions to finish this thesis.

A special thank you for the current and previous Duhamel and Gauthier's lab members for their valuable inputs, memories, and creating such an amazing working environment.

I would like to thank my parents for their support and love during my long journey to get to my PhD. My appreciations to my wife Aisha and my children Omar, Ahmed, and Sara for being on my side throughout the years and being my rock when things were tough.

Finally, I would like to thank the Hadramout Foundation – Human Development (HFHD) for the scholarship and the Natural Sciences and Engineering Research Council of Canada (NSERC) for funding.

Dedication

To my parents……. Omar & Fawziayh

To my beloved wife…….Aisha

To my amazing children…. Omar, Ahmed & Sara

Table of Contents

List of Figures

List of Tables

List of Abbreviations

^{1}H NMR	proton nuclear magnetic resonance
AFM	atomic force microscopy
BSA	bovine serum albumin
CAC	critical aggregation concentration
CHO	Chinese hamster ovarian cells
CMC	critical micellization concentration
CL-DNA	cationic liposomes/DNA complexes
cryo-TEM	cryogenic-transmission electron microscope
CTAB	cetyltrimethylammonium bromide
CT-DNA	calf thymus DNA
DAC	dodecylammonium chloride
DCM	dichloromethane
DDAO	dodecyldimethylamine oxide
DLS	dynamic light scattering
DMSO	dimethyl sulfoxide
DNA	deoxyribonucleic acid
DNT	2,6-dinitrotoluene
DOPC	dipalmitoylphosphatidylcholine
DOPE	1,2-dioleoyl-sn-glycero-3-phosphoethanolamine
DoTAB	dodecyltrimethylammonium bromide
DPH	1,6-diphenyl-1,3,5-hexatriene
DS	degree of substitution
FM	fluorescence microscopy
FRET	Förster resonance energy transfer
GdmCl	guanidinium chloride
GS	gemini surfactant
HLB	hydrophilic-lipophilic balance

HPLC	high pressure liquid chromatography
IRF	instrument response function
ITC	isothermal titration calorimetry
LLS	laser light scattering
LSCT	lower critical solution temperature
MFA	model free analysis
MVLBG2	multivalent cationic lipid with a di-oleyl tail
NaCMC	sodium carboxymethylcellulose
PEF	pyrene excimer formation
PEG	Poly(ethylene glycol)
PNIPAM	poly(N-isopropylacrylamide)
PSP	polymer saturation point
Py	pyrene
PyLGS	pyrene labeled gemini surfactant
SANS	small angle neutron scattering
SAXS	small angle X-ray scattering
SDS	sodium dodecyl sulfate
SDS-PAGE	SDS-polyacrylamide gel electrophoresis
SLS	static light scattering
SPC	single photon counting
SSF	steady-state fluorescence
RNA	ribonucleic acid
TPC	time-per-channel
TRF	time-resolved-fluorescence
TTAC	tetradecyltrimethylammonium chloride
TTPB	tetradecyltriphenylphosphonium bromide
XRD	X-ray diffraction

List of Symbols

$[Mic]$	micelle concentration
$[Py]_{loc}$	local pyrene concentration
$[Q]_b$	concentration of quenchers bound to micelles
$[Q]_o$	initial quencher concentration
$[Q]_w$	concentration of quenchers in water
$[S]$	surfactant concentration
$<k>$	average rate constant of excimer formation
$<n>$	average number of quenchers per micelle
$<n>_d$	average number of quenchers per micelle leading to dynamic quenching
$<n>_s$	average number of quenchers per micelle leading to static quenching
$<\tau_{E0}>/<\tau_E>$	ratio of average excimer lifetime without quencher to the average excimer lifetime with quencher
D^*	poorly stacked pyrene dimers
$E0^*$	well-stacked pyrene dimers
f_{agg}	molar fraction of aggregated pyrenes
f_D	molar fraction of poorly stacked pyrene dimers
f_{diff}	molar fraction of pyrenes forming excimer by diffusion
f_{E0}	molar fraction of well-stacked pyrene dimers
f_{free}	molar fraction of free pyrenes that do not form excimer
I_1	fluorescence intensity at the first peak in the SSF spectrum of the pyrene monomer
I_1/I_3	ratio of the fluorescence intensity of the first peak over that of the third peak in the SSF spectrum of the pyrene monomer
I_3	fluorescence intensity of the third peak in the SSF spectrum of the pyrene monomer

I_E	fluorescence intensity of the pyrene excimer
I_{E0}/I_E	ratio of fluorescence intensity of the pyrene excimer without quencher over that with quencher
I_M	fluorescence intensity of the pyrene monomer
I_E/I_M	ratio of the fluorescence intensity of the pyrene excimer over that of the pyrene monomer
K	binding constant
k_{diff}	rate constant of excimer formation through diffusive encounters between an excited and ground-state pyrene
k_q	rate constant for dynamic quenching
k_{qM}	rate constant for pyrene monomer quenching
λ_{em}	wavelength of emission
λ_{ex}	wavelength of excitation
N_{agg}	aggregation number of a surfactant micelle
P	packing parameter
Py_{agg}*	aggregated pyrenes
Py_{diif}*	pyrenes that form an excimer through diffusive encounters
Py_{free}*	pyrenes that are isolated in solution and cannot form excimer
R_G	radius of gyration
τ_D	lifetime of the improperly stacked excimer
τ_E	lifetime of the excimer with quencher
τ_{E0}	lifetime of the properly stacked excimer
τ_M	lifetime of the monomer
τ_{M0}	lifetime of the monomer without quencher

Chapter 1 Literature Review

1.1. **Gemini Surfactants**

Over the past three decades, various experimental techniques have been employed to study and characterize both anionic[1-5] and cationic[6-12] gemini surfactants. Gemini surfactants are composed of two ionic head groups, two hydrophobic tails that are generally alkyl, and either a rigid[1,13] or flexible[14,15] spacer connecting the two head groups. Figure 1.1 shows a general schematic diagram of gemini surfactants. Although these molecules have been reported in the literature since the 1960's,[16] the term gemini surfactants was only coined in the early 1990's by Menger and Littau.[17] In contrast to their monovalent counterparts, gemini surfactants are more effective in reducing surface tension, have superior wetting ability, and often have one- to two-orders-of-magnitude lower critical micelle concentrations (CMC).[1,14,18] As is the case for most surfactants, gemini surfactants assemble in a variety of morphologies in solution, including vesicles, wormlike rods, and spherical micelles.[15-20] Gemini surfactants have been used in a plethora of industries due to their exceptional and unique properties. Gemini surfactants are used for gene transfection,[21-24] enhanced oil recovery,[25,26] phase transfer catalysis,[27] and drug delivery,[28-30] but also as antibacterial agents,[13,31] corrosion inhibitors,[32,33] and in cosmetic products.[34]

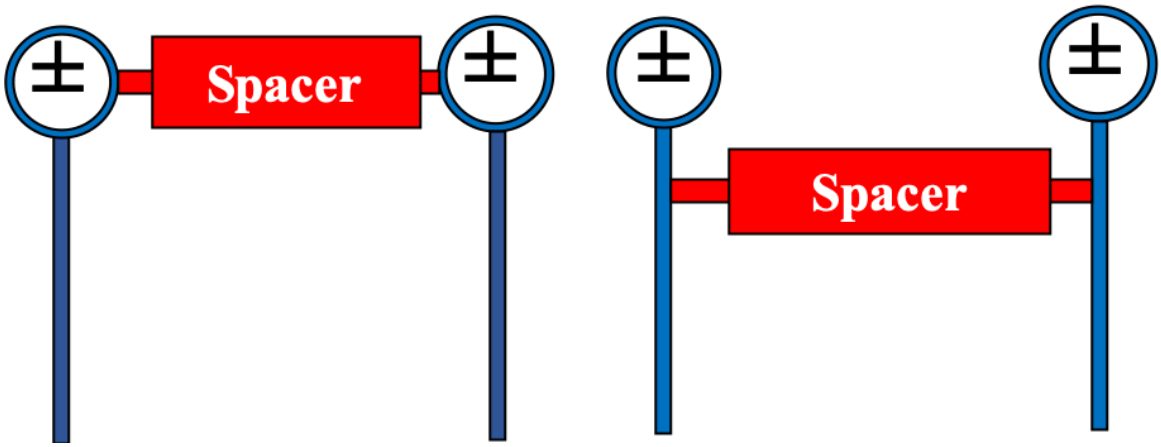

Figure 1.1 General schematic diagram of gemini surfactants.

In this thesis, the use of pyrene-labeled cationic gemini surfactants and their interactions with DNA was investigated, with the goal of further supporting their potential as non-viral vectors for gene transfection. *N,N-bis*[(Dimethylalkyl)-α,ω-alkanediammonium dibromide is an example of a cationic gemini surfactant. It represents the most studied class of gemini surfactants, and it is commonly referred to as *m-s-m*.[22] It is composed of two dimethyl ammonium bromide head groups, two alkyl tails, and a spacer, with the alkyl tails and spacer being composed of *m* and *s* carbon atoms, respectively.

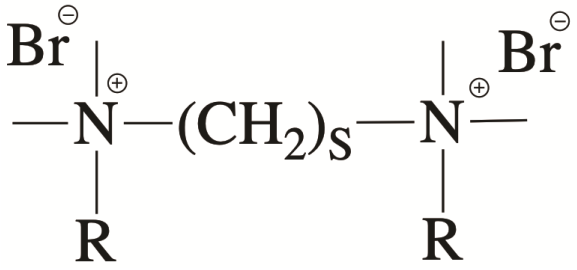

Figure 1.2 Chemical structure of N,N-bis[(dimethylalkyl)-α,ω-alkanediammonium dibromide] referred to as m-s-m, where R = C_mH_{2m+1}.

1.1.1 Physical Properties of Gemini Surfactants

As mentioned before, gemini surfactants are amphiphilic synthetic molecules composed of two single surfactants. Their unique structure contributes to their distinct physicochemical properties, such as their low CMC and the diverse structures of their aggregates. The steric restriction imposed by the spacer between the head groups contributes to these peculiar surfactant characteristics, which may be adjusted by modifying the spacer length, and chemical structure.[35] Modifications can be applied not only to the spacer, but also to the surfactant alkyl tails whose length and type can be altered to extend their range of applications, such as by adjusting their biocompatibility and biodegradability for gene and/or drug delivery, increasing their wetting properties, enhancing the emulsification of oil in water, or increasing their surface

tension.[19] Figure 1.3 provides a schematic representation of all the different micellar shapes that a surfactant could take in an aqueous solution.

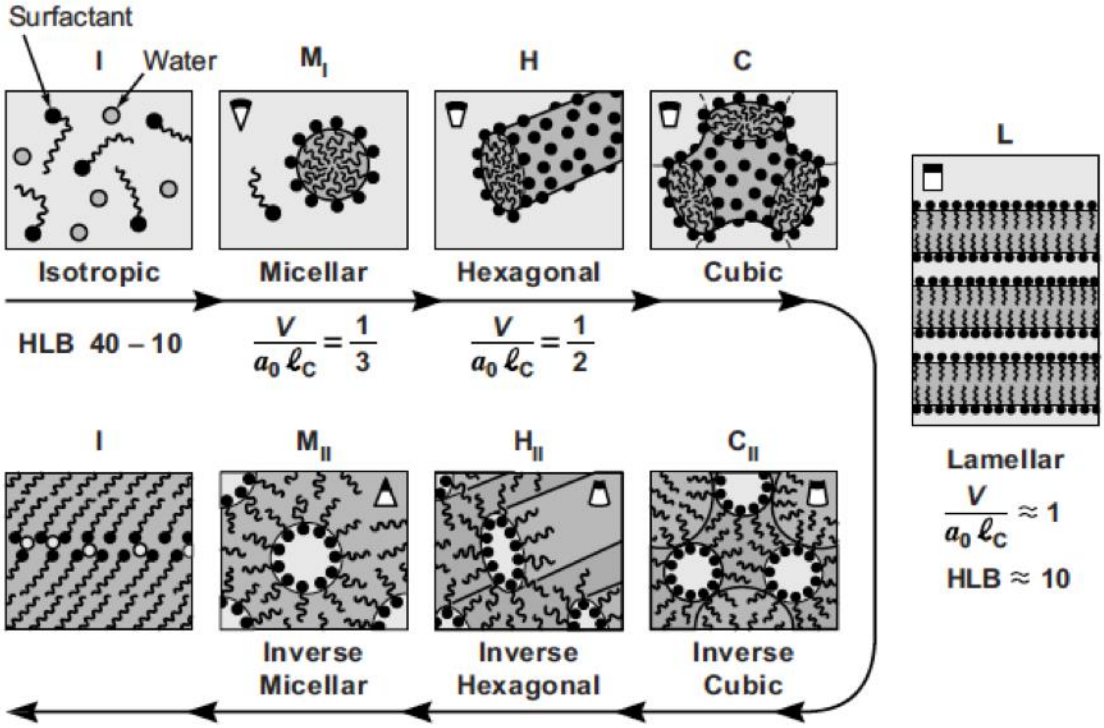

Figure 1.3 The different types of structures and "mesophases" formed by surfactants in aqueous solutions. Reproduced with permission from Elsevier, Amsterdam.[36]

1.1.1.1 Spacer modifications

Gemini surfactants possess a wider range of properties compared to regular surfactants. This is due to the different distributions of distances between the head groups in the micelles generated by these two families of surfactants.[34] While this distribution for traditional surfactants goes through a peak at a thermodynamic equilibrium distance d_T of 0.7–0.9 nm, the distribution obtained for gemini surfactants is bimodal, with a first peak at a thermodynamic equilibrium distance d_T and a second, smaller peak at a distance d_S equal to the spacer size.[37] Consequently, d_S is affected by the lengths and angles of the bonds between the spacer atoms. The bimodal distribution of head group distances and the chemical bonds between the head groups have a significant effect on the packing of the surfactant tails in the micellar interior,

on the local curvature of the micellar surface around a surfactant and, therefore, on the micellar shape and properties in solution. In this context, cryogenic transmission electronic microscopy (cryo-TEM) has been used to examine the effect of the spacer length on the micellar structures generated by 12-*s*-12 gemini surfactants with spacer lengths *s* ranging from 4 to 12 carbon atoms.[38] At a concentration of 2 wt%, 12-2-12 produced rod-like micelles, whereas 12-3-12 formed spheroidal micelles at a concentration of 7 wt%. Dodecyltrimethylammonium bromide, the single tail analog of both 12-2-12 and 12-3-12, generated solely spherical micelles regardless of concentration or ionic strength. At concentrations between 5 and 7 wt%, the solutions of 12-4-12, 12-8-12, and 12-12-12 displayed tightly packed spherical micelles, whereas the surfactants 12-16-12 and 12-20-12 formed vesicles.[34] These observations highlight the influence of the spacer length *s* and its influence on the structure of the produced surfactant aggregates.

The packing parameter *P* is very useful for predicting the shape of micellar aggregates and it is defined by Equation 1.1,

$$P = \frac{v}{l\, a_o} \tag{1.1}$$

where *v* and *l* are the volume and length of the hydrophobic chains, respectively, and a_o is the surface area generated by the head group.[39] In contrast, the nature and length of the spacer represents one more factor, that needs to be accounted for with gemini surfactants to determine *P*. Unfortunately, the influence of the spacer on *P* is difficult to describe. Due to the modularity afforded by gemini surfactants in terms of the chemical composition of their alkyl tails and spacers, numerous micellar structures can be obtained, and they must be examined one by one.[40]

Table 1.1 Packing parameter P ranges and their predicted micellar shapes in aqueous solutions[41]

Packing Parameter *P*	General Surfactant Structure	Aggregate Structure
< 0.33	Single chain and relatively large headgroup	Spherical micelles
0.33 – 0.50	Relatively small headgroup, or ionic surfactant in the presence of excess electrolyte	Cylindrical micelles
0.50 – 1.00	Double chains (flexible) with a large headgroup	Vesicles and flexible bilayer
1.00	Double chains with a small headgroup or immobile chains	Planar bilayer structure
> 1.00	Double chains with a small headgroup, bulky hydrophobic groups	Inverted micelles

Beside its effect on the type of aggregates generated by gemini surfactants, the effect of the spacer length on the association between gemini surfactants and DNA has also been investigated. To this end, another series was prepared where the gemini surfactants had two hexadecyl tails and two pyridinium head groups separated by a spacer made of *s* = 3, 4, 8, and 12 methylene groups. The chemical structure of these gemini surfactants, referred to as P16-3, 4, 8, and 12, is shown in Figure 1.4.[42] These surfactants were utilized as non-viral delivery vehicles for plasmid DNA into human rhabdomyosarcoma cell lines (RD-4). The helper lipid 1,2-dioleyl-sn-glycero-3-phosphoethanolamine (DOPE) was used to aid the transfection efficiency and its effect was assessed as well. The three surfactants P16-4, P16-8, and P16-12 were selected for transfection studies. While all surfactants compacted the plasmid DNA, P16-4 was the most efficient at compacting and transfecting DNA. This was due to the specific spacer length of the surfactant, which could match the distance between two phosphate groups

to allow the pyridinium headgroups to act as counter ions. Subsequently, the hydrophobic forces between the alkyl tails helped condense the DNA and allowed it to self-assemble into nanoparticles. A longer spacer creates interactions between pyridinium headgroups and phosphates, that are further apart along the DNA strand, which result in looser aggregates. The decrease in the compaction of the nanoparticles formed with P16-8 and P16-12 reduced their capacity to transfect cell membranes. This conclusion explains why P16-8 and P16-12 showed no transfection activity. Furthermore, the presence of DOPE in the formulation of the nanoparticles was not found to affect transfection.[42]

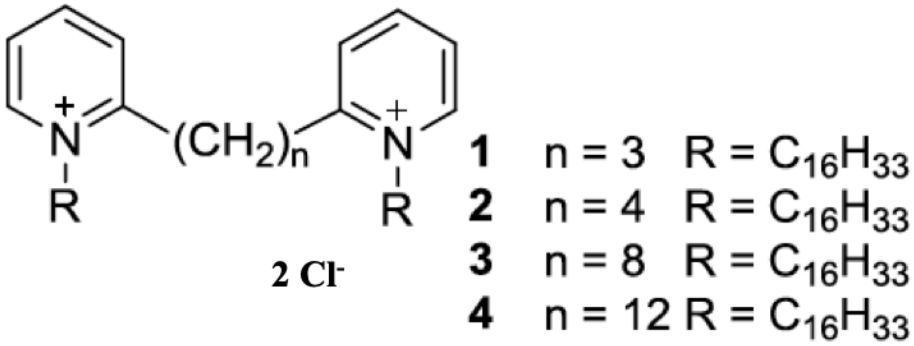

Figure 1.4 Chemical structure of the bispyridinium gemini surfactants with varying alkyl linker lengths.[42]

1.1.1.2 Modification of hydrophobic tails

Another way to manipulate the properties of gemini surfactants is by altering the nature and length of the hydrophobic tails. Similar to monomeric surfactants, the CMC of gemini surfactants decreases with increasing length of the hydrophobic tails.[19,40] As for the linker length, the effect of the hydrophobic tails on the properties of *N*,*N*-bis[(dimethyl alkyl)-α,ω-alkanediammonium dibromide], also called *m*-*s*-*m* surfactants and whose structure was shown in Figure 1.2, has been carefully characterized. Gemini surfactants with symmetric, asymmetric, and branched tails were studied in two reports to assess the effect of the alkyl length on the properties of the surfactants and their transfection efficiency.[43-45] Elongating the tails, while keeping the spacer length unchanged, reduced the packing parameter *P*, resulting

in undesirable morphological changes in the self-assembly. *In vitro* experiments showed that phytanyl substituted surfactants had a higher transfection efficiency than their symmetrical counterparts (16-3-16).[45] The improved transfection efficiency was attributed to the greater degree of micellization (α) of the phytanyl substituted surfactants, their capacity to form vesicles without DNA, and their ability to morph into inverted hexagonal structures when DNA was added to the system. Using SAXS and optical microscopy, the Safinyia laboratory demonstrated that the co-lipid DOPE induced the formation of inverted hexagonal morphologies for the DNA duplexes, which improved the transfection of the DNA cargo through endocytosis.[46,47] Increased α values are related to a larger dissociation of counter-ions from the micelles, which promotes micelle-DNA associations, resulting in stronger polyplexes and therefore increased transfection efficiency.[48]

Asymmetric gemini surfactants, where one alkyl tail was modified with a pyrenyl group to yield the Py-*s*-*m* surfactants, have been synthesized with alkyl spacers having different lengths, with a special focus on propyl (*s* = 3) and hexyl (*s* = 6) spacers.[10] The large pyrene group added to these surfactants had a significant effect on their micellization. The Py-*s*-*m* surfactants had substantially smaller CMCs compared to their symmetrical *m*-*s*-*m* equivalents, and they tended to produce both pre-micellar and micellar aggregates, with Py-6-12 being more likely to form pre-micellar aggregates. The pyrenyl pendants of the Py-*s*-*m* surfactants allowed the use of fluorescence to probe the lipoplex/polyplex generated from the associations between DNA and these gemini surfactants.[10] The research described in this thesis builds on these earlier studies on Py-*s*-*m* surfactants to further characterize the properties of Py-*s*-*m* surfactants using more advanced fluorescence methodologies.

In another example, the tails of gemini surfactants with pyridinium headgroups were altered by replacing the hexadecyl tail of the P16-*s* surfactants, whose structure was shown in Figure 1.4, by tridecafluorooctyl chains to yield the surfactants FGP*s* with *s*= 3, 4, 8, and 12.[49]

The addition of fluorine atoms to the alkyl chains of the gemini surfactants increased the hydrophobicity of the tails, which in turn lowered the CMC of these fluorinated surfactants compared to their hydrocarbon counterparts.[50] In terms of transfection efficiency, FGP4 did not perform as well as P16-4, which was the most efficient of the gemini surfactants. Within experimental error, FGP8 performed as well as P16-4. The compaction of DNA with FGP8 was found by AFM to yield smaller and more uniform objects than P16-4, a feature, that was attributed to the introduction of the more hydrophobic fluorine atoms into the tails of the FGP*s* gemini surfactants. Overall, the previous studies showed that lipoplexes prepared with gemini surfactants with longer ($m \geq 14$), more branched (phytanyl), or more hydrophobic (i.e. fluorinated) alkyl tails demonstrated enhanced in vitro transfection compared to complexes prepared with gemini surfactants having shorter and less hydrophobic tails.

1.1.1.3 Headgroup modifications

The density and structure of the headgroups have been shown to have an effect on the effectiveness of gene delivery.[24,51] Gemini surfactants have also been prepared with headgroups that include specific features such as biodegradability and biocompatibility by using carbohydrate-based headgroups. Reduced carbohydrates such as glucose and mannose serving as water-soluble headgroups were connected to an alkyl spacer via tertiary amines or amides to which various alkyl tails were attached.[52] The inclusion of glucose or mannose in the headgroup made the gemini surfactants more biocompatible and prolonged the vector's half-life, while interacting with Chinese hamster ovarian (CHO) cells.[53] These carbohydrate-based headgroups result in varying degrees of hydration, that lead to the creation of different aggregate types. Altering the surface area of the headgroup allows the formation of different morphological assemblies.[54]

Amino acids can be introduced into the structure of gemini surfactants to improve their immunogenicity. The efficacy of six members of a novel class of serine-derived gemini

surfactants was described in a recent study. The surfactants, whose chemical structure is presented in Figure 1.5, were found to safely facilitate the transfection of genetic material.[55] The ammonium headgroups of these serine-based gemini surfactants were linked with a pentamethylene spacer via an amine, amide, or ester bond to yield the (*m*Ser)$_2$N5, (*m*Ser)$_2$CON5, and (*m*Ser)$_2$COO5 surfactants with *m* = 12, 14, 16, and 18, respectively. The effects of the different bond types connecting the spacer to the headgroups and alkyl tail length on gene transfection were evaluated. Both the hydrophobic tail and the bond type had an influence on the lipoplexes formed between DNA and the serine-based gemini surfactants with or without a 2:1 DOPE:cholesterol co-lipid system. Although all (*m*Ser)$_2$N5 surfactants promoted transfection, no pattern was uncovered between alkyl tail length and transfection efficiency. The (16Ser)$_2$N5 sample was the least effective contrary to previously published data on gemini surfactants with bis-quaternary ammonium headgroups and a C16 tail, which had demonstrated the greatest transfection performance.[56] Additionally, the use of serine in these surfactants introduced more complexity to their chemical structure and might have a substantial effect on their physicochemical properties, thereby impacting transfection. The complexes formed with DNA and the serine-based gemini surfactants varied in size from 163 nm to 3 μm, with the inclusion of the co-lipid facilitating the formation of larger complexes at various charge ratios. Introduction of negatively charged DNA to the positively charged aggregates of gemini surfactants led to a decrease in zeta potential and the total charge of the complexes remained positive. The 2:1 DOPE:cholesterol co-lipid formulation applied in this investigation improved the transfection performance of the (*m*Ser)$_2$N5 surfactants. These complexes took advantage of their ability to escape lysosomal breakdown thanks to the presence of DOPE and the low cytotoxicity of cholesterol, which is less prone to interact with serum proteins. Yet the various effects imparted by the helper lipids on the transfection efficiency of the complexes suggested that different aggregate types were generated depending

on the alkyl tail length of the serine-based gemini surfactants. Furthermore, the negative charges of the complexes formed with a mixture of serine-based gemini surfactants and helper lipids made them much less susceptible to react with serum proteins, as was also found for other complexes prepared between DNA and lipids.[57]

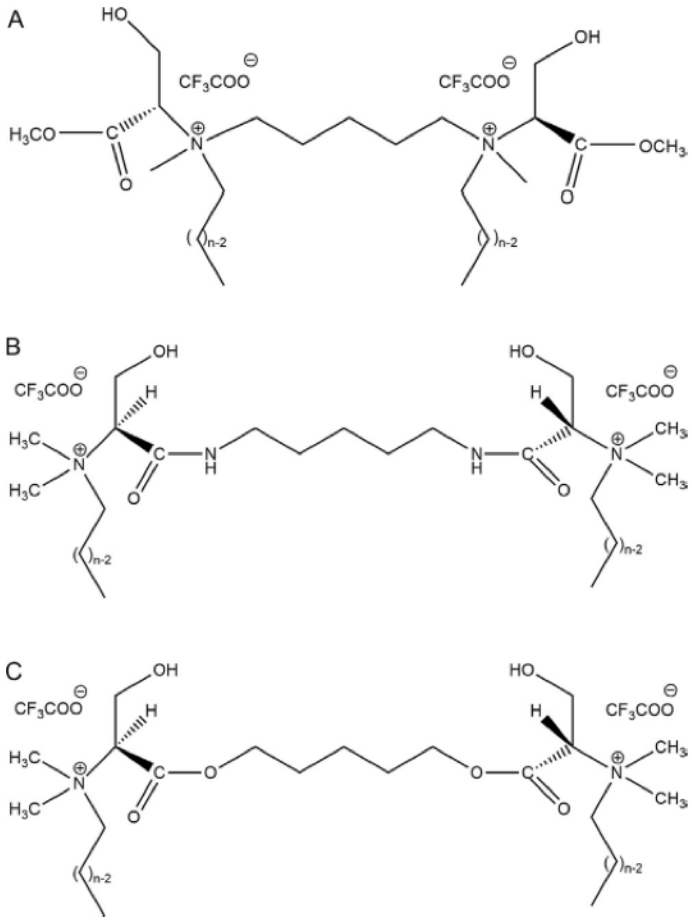

Figure 1.5 Structures of the serine-substituted gemini surfactants A) $(mSer)_2N_5$, B) $(12Ser)_2CON_5$, and C) $(12Ser)_2CON_5$ where the pentamethylene spacer was linked to the ammonium headgroups via an amine, amide, and ester bond, respectively.[55]

1.2. **Interactions between Surfactants and Other Molecules**

For centuries, the use of surfactants has been associated with human development, from the early use of soaps to the more advanced and innovative applications developed nowadays for these molecules.[41,58] Further applications of these amphiphilic molecules were found by

exploring their interactions with other, typically oppositely charged, molecules such as surfactants,[59-62] biomolecules,[63-66] and polymers.[67-71] Such mixtures often result in synergetic effects and new properties, which are far better than those of the constituting components. Several industries have benefitted from the improved properties of the complexes generated between surfactants and other molecules, as they are used for enhanced oil recovery, drug delivery, food processing, and agriculture to name but a few applications.[25,72-74] Mixing an ionic surfactant with a non-ionic surfactant represents one example, where the properties of the mixture are improved compared to those of its constituting parts, since the cloud point of the nonionic surfactant is increased or completely eliminated due to the production of a mixed micellar system.[41]

1.2.1 Mixed Surfactants Systems

Significant contributions have been made in previous years to characterize the solution characteristics of mixed surfactant systems. The widespread use of such systems in a broad range of research and industrial applications necessitates a thorough understanding of their performance and the mechanisms involved in controlling their properties such as colloidal stability and aggregate size. The stability of mixed micellar systems has been evaluated using a variety of different theories, most of which are based on thermodynamic principles.[61]

An example of the synergetic effects resulting from the interactions between different surfactants was identified by Somasundaran et al. for the non-ionic surfactant dodecyloxyheptaethoxyethyl alcohol ($C_{12}EO_8$), which does not adsorb on solid surfaces on its own. Yet, synergic adsorption of $C_{12}EO_8$ was observed with the anionic surfactant sodium *p*-octylbenzenesulfonate (C_8PhS), facilitating the adsorption of $C_{12}EO_8$ on an oppositely charged alumina surface.[75] In these settings, the creation of micelles involving both surfactants is driven by interactions between the alkyl tails of the surfactants. Notably, a pH-dependent co-adsorption was also noticed for mixtures of C_8PhS and $C_{12}EO_8$. C_8PhS promoted and inhibited

the adsorption of $C_{12}EO_8$ at pH 5 and 10, respectively, suggesting a synergic adsorption through the association of hydrocarbon chains at reduced pH.

Two types of mixed micelles were found to coexist with mixtures of pentadecyl ethoxylated nonylphenol (NP-15), a neutral surfactant, and the cationic surfactant *n*-tetradecyltrimethylammomium chloride (TTAC) in solution.[76] Huang et al. determined three concentration regimes defining the phase diagram shown in Figure 1.6 for the formation of mixed micelles. In Regime A, where the concentration of both surfactants is low, the surfactants are unassociated and exist as monomers. In regime B, NP-15, which is more surface active, generates NP-15-rich micelles, where the cationic surfactant TTAC is incorporated as its concentration increases, therefore altering the makeup of the micelles. Regime C corresponds to the concentration region where two distinct types of micelles coexist, one being NP-15-rich with a few TTAC units and the other being TTAC-rich with a few NP-15 units.[76] An application for the modelling of the interactions between different surfactants and solid surfaces is to predict whether synergistic or antagonistic effects will be observed for the adsorption of the mixed surfactants.

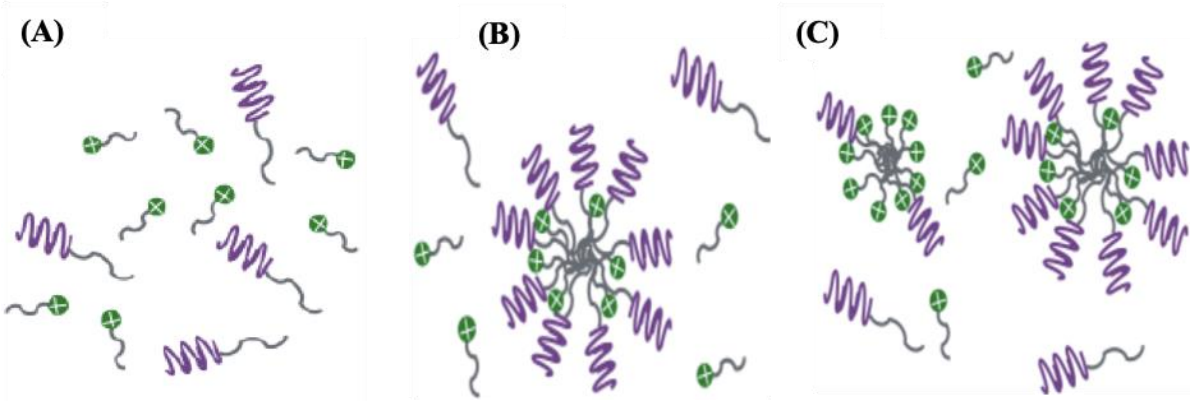

Figure 1.6 Schematic diagram representing the surfactant concentration regimes where A) TTAC and NP-15 coexist as unassociated unimers, B) NP-15 surfactants form micelles hosting a few TTAC surfactants, and C) TTAC forms micelles with a few NP-15 surfactants, which coexist with NP-15 micelles mixed with a few TTAC surfactants.[76]

1.2.2 Surfactant/Polymer Interactions

As with surfactant mixtures, surfactant-polymer blends can improve the properties of a formulation compared to the properties that would be achieved if each constituting element was used separately. As a result, many surfactant-based products, such as those used in the medicinal, cosmetic, and detergent industries, contain also water-soluble polymers.[20,77] In such cases, the driving force leading to the associations between the surfactants and polymers constituting the blends must be thoroughly characterized, since these studies provide a better understanding as to why these systems behave the way they do and may aid in developing blends with even better properties.[77]

As was discussed earlier, surfactants self-assemble above the CMC into aggregates, that can take a variety of morphologies (see Figure 1.3). The introduction of polymers to a surfactant solution can result in the formation of surfactant aggregates at a concentration that is much lower than the CMC as a result of surfactant-polymer interactions, a process referred to as polymer-induced micellization. The associations between polymers and surfactants occur within a concentration range marked by two boundaries. The critical aggregation concentration (CAC) represents the polymer and surfactant concentration at which the polymer/surfactant complexes begin to form, while the polymer saturation point (PSP) represents the concentration at which point the polymer chains become overloaded with bound surfactant molecules.[58] The interactions between polymers and surfactants fall generally into two main categories. The first category describes the associations between ionic polymers and oppositely charged surfactants, while the second category represents the interactions between nonionic polymers and any type of surfactant.[78] In the case of ionic polymers, electrostatic forces dominate the formation of complexes between ionic polymers and oppositely charged surfactants at low surfactant concentration. When all the ions on a charged polymer have been neutralized, hydrophobic interactions drive the binding of more surfactants onto the polymer

already coated with surfactants at increasing surfactant concentrations. In contrast, hydrophobic interactions drive the interactions between nonionic polymers and ionic surfactants. For instance, the interactions between nonionic poly(ethylene glycol) (PEG) and the anionic surfactant sodium dodecyl sulfate (SDS) have been extensively researched and strong binding of SDS to PEG has been observed.[79] These interactions are governed by the equilibrium describing the polymer-induced micellization at low SDS concentrations and ion-dipole interactions at high SDS concentrations.[80,81] Interestingly, the surfactant dodecyl trimethylammonium bromide (DoTAB), which has the same dodecyl tail as SDS but has a positively charged hydrophilic headgroup, can only bind to hydrophobically modified water-soluble polymers in water,[82] but does not bind significantly to PEG. Over the years, the binding of surfactants to charged polymers and the associated mechanisms have been found to depend on the surfactant type and the molecular weight, chemical makeup, hydrophobic content, or degree of ionization of the charged polymers. In the absence of electrostatic forces, interactions between nonionic polymers and surfactants are comparatively weaker. Nonionic surfactants often have CMC values, that are orders of magnitude lower than those of ionic surfactants, as their CMC is highly impacted by electrostatic repulsion, which hinders the association of ionic surfactants into micelles.[83] Thus, nonionic surfactants produce micellar aggregates and interact poorly with nonionic polymers, in comparison to the much stronger interactions observed between ionic polymers and oppositely charged surfactants as well as nonionic polymers and charged surfactants. Furthermore, the temperature, the solvent conditions, the presence of electrolytes, and the chemical nature of polymers and surfactants all have a substantial effect on their associations.

Nagarajan proposed a thermodynamic approach for predicting how surfactants bind to polymers in water.[84] His model considers a polymer constituted of polar and apolar segments. The interface between the polar and apolar segments constitutes the preferred region for

surfactant adsorption onto the polymer. The model predicted that an increase in the content of apolar segments in the polymer would lead to an increase in the amount of polymer-bound surfactant, as had been reported in the literature. The predictive power of the model developed by Nagarajan led to further theoretical and experimental studies aiming to develop a better understanding of the driving forces leading to the formation of surfactant-polymer complexes.[85-88] For instance, Nagarajan[89] and the Ruckenstein groups[90] refined this earlier model by considering that the shielding effect induced by the polymer located at the micelle/water interface could be accounted for by considering either the area per surfactant a_{Pol} of the micellar core shielded by the polymer or the change in interfacial tension between the surfactant aggregate and water due to the presence of the polymer, respectively. The predictions made by both models showed good agreement with experimental results indicating the value of such theoretical models to predict the associations that could occur between different polymers and surfactants.[85,86]

As the surfactant concentration is increased past the CAC, binding of surfactants to a polymer will continue until the surfactant concentration nears the polymer saturation point (PSP), where the polymer chains become overloaded with surfactant molecules. As the surfactant concentration is further increased past the PSP, free surfactant micelles form and a decrease in surface tension is observed until a constant value is reached. Figure 1.7 shows the surface tension behavior at the CMC, CAC, and PSP. In Figure 1.7, the polymer concentration is kept constant and the surfactant concentration is varied. Figure 1.7 illustrates that PSP > CMC > CAC, and the CAC and PSP take values that are comparable to the CMC of a surfactant in a majority of polymer/surfactant systems with minimal interactions between polymer chains and surfactant molecules.

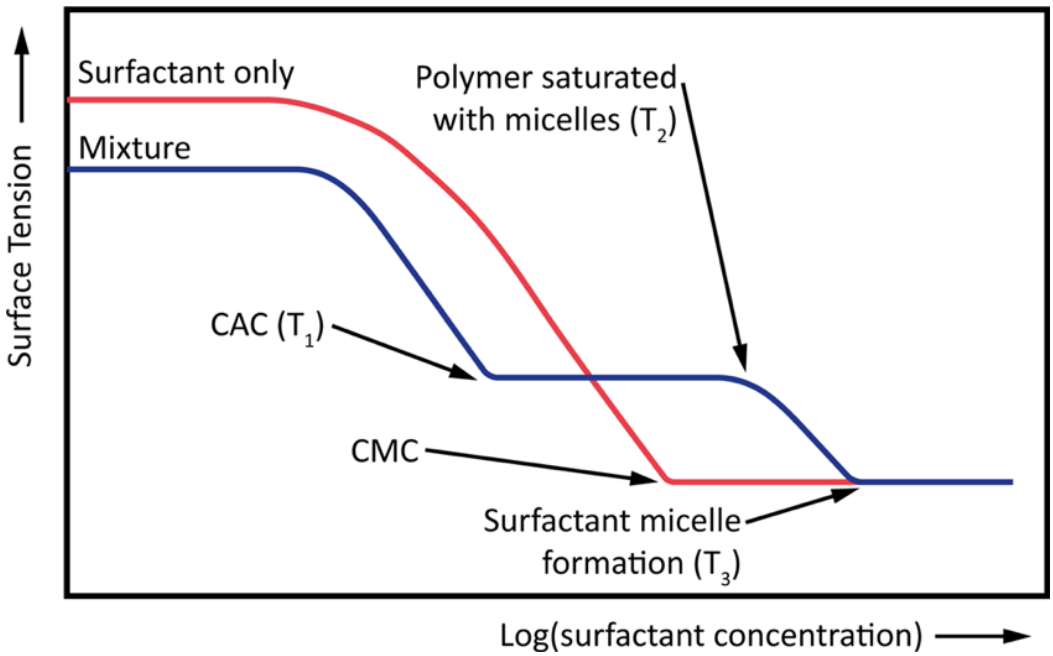

Figure 1.7 Surface tension plots for pure surfactant (red trace) and surfactant-polymer (blue trace) mixtures, where T_1 represents the critical aggregation concentration, T_2 represents the polymer saturation point, and T_3 represent the point surfactant-only micelles starts to form.[91]

Unsurprisingly, interactions between surfactants and polymers bearing like charges are often weak, since electrostatic repulsions tend to dominate over non-electrostatic forces, particularly for polymers with a fairly homogeneous charge distribution along the backbone. However, if the charges are clustered in certain locations throughout the polymer backbone, hydrophobic encounters may still occur in the neutral segments of the chain.[41]

Poly(N-isopropylacrylamide) (PNIPAM) is by far the most extensively studied thermo-responsive polymer. The 32 ^{o}C lower critical solution temperature (LCST) of PNIPAM in water implies that PNIPAM transitions from a water-soluble to a water-insoluble polymer, when the solution temperature is increased from below to above its LCST.[92] Consequently, its associations with surfactants have received considerable attention. The influence of surfactants on the morphological rearrangement of PNIPAM in water has been widely investigated through a variety of methods, that include laser light scattering (LLS), conductimetric studies, small angle X-ray scattering (SAXS), fluorescence spectroscopy, and NMR.[93-95] Loh et al.

studied the association of PNIPAM with the anionic surfactant SDS and three cationic surfactants, namely dodecyltrimethylammonium bromide (DTAB), hexadecyltrimethylammonium bromide (CTAB), and dodecylammonium chloride (DAC).[96] Using isothermal titration calorimetry (ITC) to study polymer-surfactant associations, they discovered that temperature had a significant effect on the interaction of PNIPAM with charged surfactants. A rise in temperature led to an enhancement in polymer-surfactant interactions due to a decrease in PNIPAM hydration, which was particularly pronounced around the LCST. Several surfactants exhibited varying degrees of binding to PNIPAM, with the binding strength increasing according to the sequence SDS > CTAB > DAC > DTAB. This series demonstrates that anionic surfactants bind more strongly to nonionic PNIPAM and that the hydrophobic nature of the surfactant has a significant influence on this association. The ITC study also found that the number of bound surfactant molecules and the total energy of interaction remained constant for all surfactants over the 17 – 29 ^{o}C range of temperature studied.[96]

Additionally, the morphology of SDS aggregates bound to PNIPAM was investigated by Chee et al. using time-resolved fluorescence anisotropy.[97] SDS was found to associate and generate micellar aggregates along the PNIPAM chain at SDS concentrations above the CAC. At temperatures below the LCST, electrostatic repulsions between the ionic headgroups of SDS molecules complexed with PNIPAM resulted in a conformational change for the PNIPAM chains from an elastic, solvent filled coil for the PNIPAM chains without SDS to a surfactant-swollen structure for the PNIPAM chains complexed with SDS. At the LCST, SDS adsorbed onto and broke down aggregates of collapsed PNIPAM chains to generate isolated spherical PNIPAM globules that were stabilized in water by the complexed SDS molecules. Adding more SDS led to a conformational change of the PNIPAM chains from a globule to a swollen coil.[98] Stabilization of individual PNIPAM chains at temperatures above the LCST is assumed

to occur through the formation of a layer of SDS adsorbed at the surface of a collapsed PNIPAM chain, in a process that prevents phase separation. Many more examples of polymer-surfactant systems can be found in the literature and their description is beyond the scope of this thesis.

1.2.3 Surfactant/Biomolecules Interactions

The complexation of surfactants with biomolecules such as proteins, polysaccharides, and DNA is of considerable importance in biotechnology but also industries involved in a variety of fields such as food, personal care, drug development, or the environment.[21,99-102] In the biomedical field, for example, protein–surfactant complexes are employed to create hydrogels.[103,104] Hydrogels serve as the foundation for fibrous proteins, e.g. fibroin, that are employed for tissue regeneration and delivery of therapeutics.[105,106] Another application for surfactant-biomolecule complexes is the use of cationic surfactants with genetic materials such as DNA and RNA for gene delivery.[10,21,22] In this section, a brief review of some studies reported in the literature of such surfactant-biomolecule complexes is conducted.

1.2.3.1 Surfactant/Proteins Systems

Protein–surfactant associations are driven by three basic interactions resulting from electrostatic, hydrophobic, and Van der Waals forces.[107] Such molecular associations have an effect on a protein native conformation, encouraging or inhibiting denaturation, complexation, and loss of enzymatic ability, among other aspects.[108] Protein–surfactant complexes generated with globular proteins such as bovine serum albumin (BSA),[62,65] β-lactoglobulin,[109-111] and β-glucosidase[112,113] are extensively investigated. By comparison, relatively limited research on fibrous protein–surfactant complexes have been reported.

The binding of surfactants to proteins proceeds according to a well-defined sequence of events. At first, the surfactants target charged domains along the protein backbone in a process driven by electrostatic attraction with the oppositely charged headgroups of the

surfactant, resulting in the formation of a hairy-worm structure.[41] With the hydrocarbon tails of the bound surfactants protruding outward in the aqueous phase and free to associate, hydrophobic domains are generated along the protein backbone that act as seed sites for further surfactant accretion eventually resulting in protein-associated micellar aggregates. Due to charge neutralization, the first electrostatic interaction between surfactants and proteins also results in the collapse of the protein native conformation, as illustrated in Figure 1.8, a reduction in solubility, leading finally to the protein precipitating out of solution. Strong surfactant binding requires that both the ionic headgroup and hydrocarbon chain of the surfactant be engaged in the binding. Larger surfactant-protein ratios might result in a flip of the protein charge and backbone expansion may take place.[41]

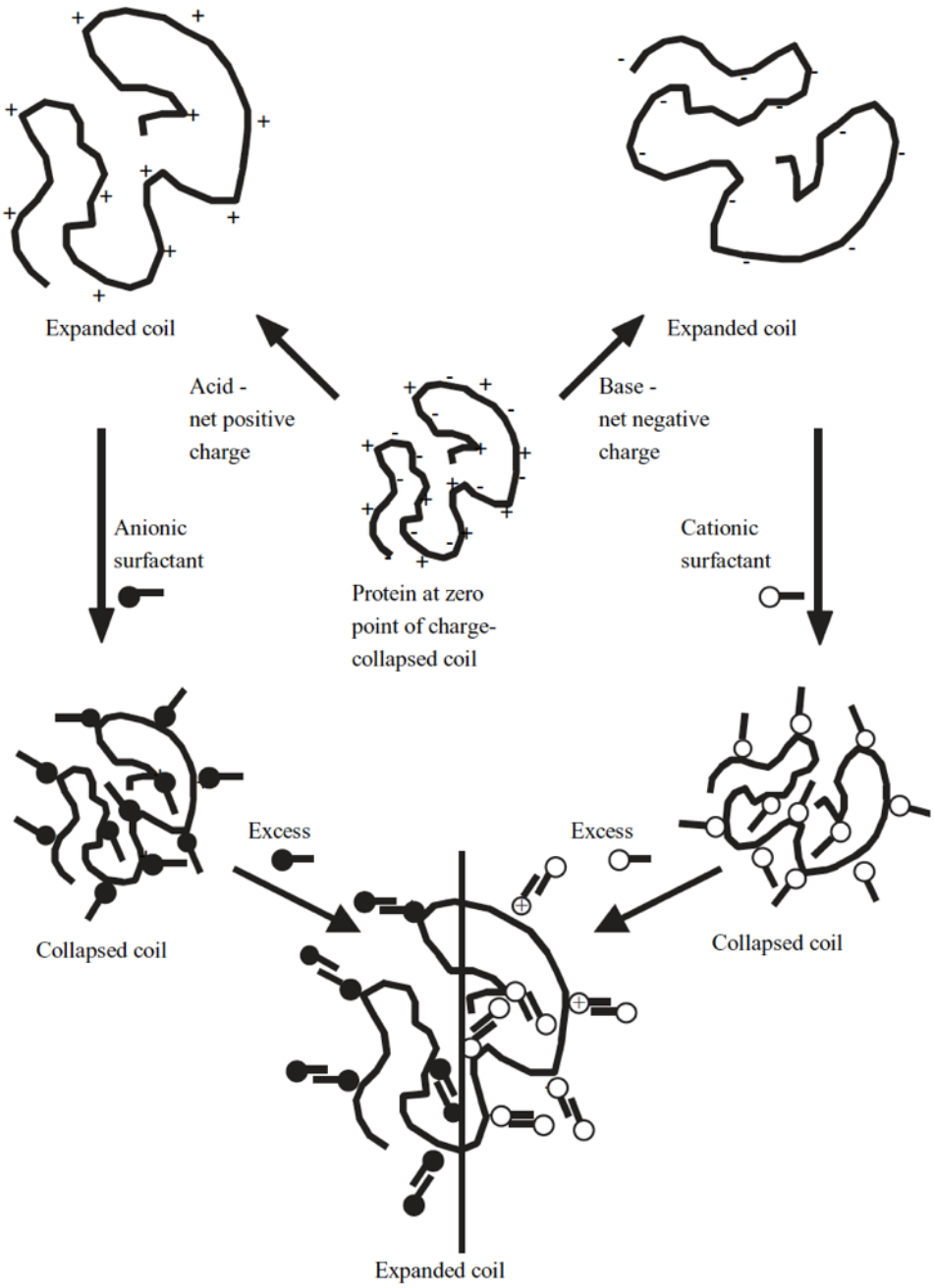

Figure1.8 Schematic illustration of collapsed and expanded proteins in response to the adsorption of an oppositely charged surfactant. Reproduced with permission from John Wiley & Sons, Inc.[41]

Numerous studies have been carried out to characterize the structure of proteins associated with SDS micelles. The interest behind this research is to better understand what happens to a protein as it is subjected to SDS–polyacrylamide gel electrophoresis (SDS–

PAGE), which is the method that is most applied to confirm the size and purity of proteins by separating protein–SDS aggregates according to their size in a polyacrylamide gel.[114] The separation depends on the hydrodynamic volume of the surfactant-protein complex and therefore on its structure. In a SDS-PAGE experiment, the protein:SDS weight ratio is maintained fixed at a value between 1 and 1.4 and the protein molecular weight scales as the protein Stokes radius resulting in a linear relationship between the logarithm of the molecular weight and the protein displacement in the gel.[115] A similar relationship can be observed upon denaturing a protein with 6 M guanidinium chloride (GdmCl),[115] albeit the interactions with SDS and GdmCl are different resulting in different morphologies of the aggregates. According to Reynolds and Tanford's pioneering studies,[116,117] the protein–SDS complexes often form "rod-like" elongated ellipsoids. The size of the protein, which determines the extent of its displacement in the polyacrylamide gel matrix, is related to its molecular weight and it is enhanced by a 15 Å thickness representing the length of the SDS hydrocarbon tail. The linear relationship between the molecular weight of a protein and its displacement during an SDS-PAGE experiment provides a morphological framework to relate protein size to gel displacement without the need to explain the complicated structure of the resulting SDS-protein complexes in further details. These complexes are believed to yield one of two possible conformations. The extended protein backbone can be wrapped around the micelles, as in the protein-decorated model, or SDS micelles may be generated on separate regions of the extended protein, as in the pearls on a string model.[118]

Viscometric,[119] DLS,[120] NMR,[121] and fluorescence[122] studies all corroborate the decorated micelle model, which is comparable to the complexes produced between surfactants and polymeric materials.[123] Additionally, the decorated micelle model gained substantial structural evidence from SANS measurements,[124,125] which found that three distinct micelles coexisted on the backbone of the 452 residue-long N-5′-phosphoribosyl anthranilate isomerase

at SDS concentrations below the saturation of binding equivalent to 1 SDS molecule for every 2 residues. At even lower concentrations corresponding to 1 SDS molecule for every 4 residues, two micelles merged into one resulting in a two-micelle cluster. Nevertheless, SANS experiments indicated that the interactions between BSA and lithium dodecyl sulfate yielded globular micelles randomly decorating the protein chain,[126] which could be described as the "pearls on a necklace" model. SAXS has also been applied to characterize the BSA–SDS interactions according to the "pearls on a necklace" model.[127] Ferguson plots of aggregate mobility in SDS-PAGE experiments conducted with varying acrylamide concentrations gave additional support for this model.[128] These studies illustrate the importance of studying protein/surfactant complexes as their existence enables the widespread use of SDS-PAGE to characterize the molecular weight and purity of proteins.

1.2.3.2 Surfactant/Polysaccharide Systems

Extensive research has been carried out over the past few decades on the associations between surfactants and polysaccharides and their complexes have found a broad array of applications. These investigations have led to the conclusion that both cooperative and non-cooperative interactions are taking place between polysaccharides and surfactants and the binding dynamics of surfactants onto polysaccharides have been investigated.[129-132]

Carboxymethylcellulose (CMC) is a major cellulose ether derivative that may be synthesized by the reaction of cellulose with chloroacetic acid under alkaline conditions. At pH greater than 4, CMC is a polyanion whose sodium salt is referred to as sodium carboxymethyl cellulose (NaCMC).[129] The associations of NaCMC with a variety of cationic surfactants have been characterized and they were found to occur in a manner comparable to that observed for synthetic polyanions. For instance, surfactant-polymer interactions occur at surfactant concentrations slightly lower than the CAC, indicating that noncooperative binding takes place. However, the binding, which is noncooperative before the CAC, grows

increasingly cooperative after the CAC.[133] The number of regions on NaCMC, where cationic surfactants can bind, diminishes as the surfactant concentration is raised before reaching the PSP. Consequently, hydrophobic, rather than electrostatic, interactions dominate the binding process at high surfactant concentration, and these interactions can lead to phase separation followed by the appearance of a condensed phase.[134] Upon binding of surfactants onto NaCMC, the NaCMC backbone collapses somewhat at low surfactant concentrations, reflecting a reduced solubility that leads to the formation of aggregates that are highly polydisperse. When the surfactant concentration is further increased, the condensed complexes become increasingly hydrophobic and NaCMC precipitates out of solution. In contrast to elastic synthetic polymeric materials, NaCMC is a semi-flexible polymer with a stiff chain, which may impede the backbone collapse and give rise to various aggregate morphologies.[135]

The associations of NaCMC with the cationic surfactants DoTAB and CTAB have been investigated by dynamic and static light scattering, viscometry, XRD, and potentiometry.[134,135] These studies showed that at low polyelectrolyte concentration, NaCMC and surfactant molecules produced spherical, stiff, and monodisperse complexes, whereas at high polyelectrolyte concentration, they generated bulkier, polydisperse, and softer complexes. Interestingly, increasing the length of the surfactant hydrophobic chains by 4 methyl units significantly altered the complex size, as the NaCMC/CTAB complexes were much bigger than the NaCMC/DoTAB complexes. Mata et al. reached similar conclusions when they examined the size of complexes generated by NaCMC with DoTAB, tetradecyltrimethylammonium bromide (TTAB), and CTAB.[136] Additionally, they observed that an increase in the headgroup size of the surfactant by using TTAB, tetradecylpyridinium bromide (TPyB), and tetradecyltriphenylphosphonium bromide (TTPB) resulted in a sharper increase in the size of the surfactants-NaCMC complexes with increasing surfactant concentration. The association of NaCMC and CTAB was also found to be primarily

influenced by the degree of substitution (DS) of NaCMC but not its molecular weight.[137] The influence of solution environmental factors such as ionic strength and temperature on the formation of complexes of NaCMC/surfactants has also been investigated.[129,138] Since the ionic strength of the solution affects the CMC of DoTAB, different trends are obtained depending on whether the onset DoTAB concentration C_1, where binding of DoTAB to NaCMC happens, is below or above the CMC. If C_1 is smaller than the CMC, DoTAB forms complexes with NaCMC at C_1 until the NaCMC chains are saturated at *C*" and no binding occurs with increasing DoTAB concentration, with DoTAB micelles forming at the CMC. If C_1 is larger than the CMC, DoTAB micelles form at the CMC before binding to NaCMC at C_1 until the NaCMC chains are saturated at *C*" and DoTAB micelles form. Many other examples of polysaccharides/surfactants systems and their applications have been investigated in the literature, such as chitosan/surfactants,[130,139,140] starch/surfactants,[131,132,141,142] and galactomannans/surfactants[143,144] systems.

1.2.4 Surfactant/DNA Systems

DNA–surfactant aggregates have garnered popularity as promising and effective materials for a variety of uses that include optoelectronics to biomedical applications in recent years. The breadth of applications found for DNA-surfactant complexes arise from the exceptional versatility of their self-assembly, covering packing spatial arrangements ranging from highly ordered lamellar, hexagonal, and cubic configurations to disordered isotropic states. These systems are composed of DNA strands from which non-covalently associated surfactants extend as side chains. Although most surfactant-DNA aggregates are often prepared in aqueous solution,[10,22] they are also produced without solvents as lyotropic[46,47] and thermotropic[145,146] liquid crystals or films.[147,148] Apart from gene transfection, surfactant-DNA complexes have been used in a variety of other applications, including as drug carriers and scaffolds for FRET measurements, as spacers to prevent concentration-induced fluorescence

quenching of dyes, and even as elements of optoelectronic devices such as organic light emitting diodes and photovoltaic cells.[149]

Earlier research showed that the addition of CTAB to an aqueous solution of a large DNA molecule leads to a transition of the DNA conformation from an extended coil to a packed globule.[150] The complexation of surfactant molecules with DNA strands occurs predominantly through electrostatic interactions, as long as complexation takes place below the surfactant CMC. Adding salt to DNA-cationic surfactant complexes in solution raises their CAC as favorable electrostatic interactions between DNA and the cationic surfactant are weakened by the increased ionic strength.[150] Additionally, ^{23}Na NMR experiments have demonstrated that cationic surfactants substitute sodium as the counterions for the DNA molecules and that DNA similarly replaces the counterions of the surfactants.[151] DNA-surfactant associations are cooperative, as indicated by the sigmoidal adsorption isotherms. Binding of cationic surfactants to DNA proceeds in a manner comparable to that outlined in Section 1.2.2 for the complexation between oppositely charged surfactants and polymers. Electrostatic forces drive the associations between single surfactant molecules and DNA, in a process that exposes the surfactant hydrophobic tails to water, which promotes their associations into aggregates, that are stabilized by the hydrophobic contacts. Once enough surfactant has been added to the solution, DNA-surfactant micellar aggregates form via hydrophobic interactions between the surfactant hydrophobic tails. These micellar aggregates then act as multivalent ions, which condense the DNA into a compact globule.[152] Surfactants with a longer hydrocarbon tail prompt DNA condensation at a significantly lower surfactant concentration than those with a shorter hydrocarbon tail, for instance, 8.0 μM for CTAB with a 16-carbons tail vs. 80 μM for DTAB with a 12-carbons tail.[153] Additionally, force-extension (*F-x*) relationships established with laser tweezers indicated that short tailed surfactants such as octyltrimethylammonium bromide (OTAB) do not induce DNA

condensation upon binding, possibly due to their ability to locate themselves in the DNA grooves where they would undergo some hydrophobic interactions.[154] By comparison, surfactants with a longer alkyl tail such as DTAB promote DNA condensation via intermolecular associations involving the nonpolar tails that are most probably oriented away from the DNA backbone.[154]

A number of new positively charged surfactants with easy to cleave hydrophilic isothiouronium headgroups were also prepared and their interactions were examined with a plasmid DNA, which resulted in the formation of DNA-rich particles. The complexes led to the formation of small spherical particles with diameters of 20 to 40 nm and larger particles with sizes of 100 to 200 nm, that were aggregates of the smaller particles.[155] Further research led to the design of a surfactant with a cleavable isothiouronium headgroup able to condense plasmid DNA into nanoparticles that would not aggregate (see Figure 1.9), thanks to the stabilization resulting from the oxidative transformation of the surfactant into a gemini lipid.[156] A variety of cationic surfactants with tail lengths ranging from 12 to 16 carbons and having two different headgroups, namely ornithine and spermine, were also prepared using a flexible synthetic polymer approach. The generation and stabilization of the complexes with the plasmid DNA, and also the particle size, zeta potential, structure, and transfection performance, were examined. Condensation of DNA led to the formation of particles with a small size of 35 (±5) nm, which was compatible with nuclear pore-crossing, an important feature to deliver genetic material to a cell.[156]

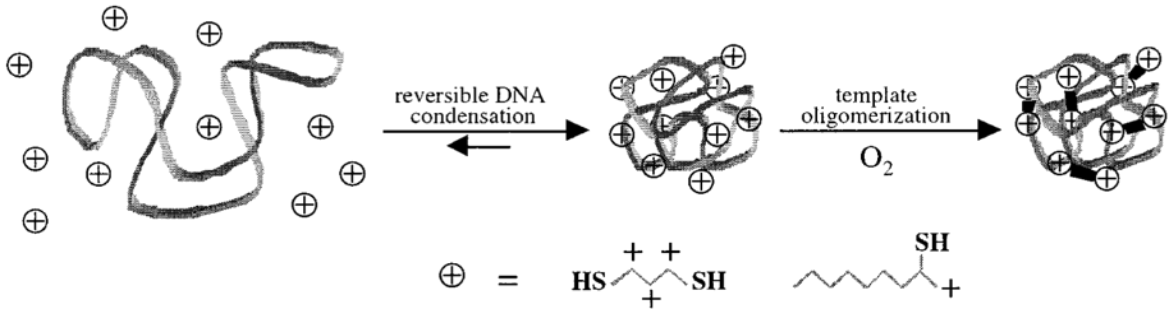

Figure 1.9 Condensation of plasmid DNA by surfactants with a cleavable isothiouronium headgroup. The multivalent headgroups prevent the dissociation of the surfactant from the particles, which remain frozen after the oxidative transformation. Reproduced with permission from ACS Publications.[156]

The DNA-surfactants complexes that have been studied in the literature are not limited to cationic surfactants. The interactions of nonionic[157] and zwitterionic[158] surfactants with DNA have also been described. Negatively charged surfactants were found to have no substantial impact on the morphological behavior of DNA unless the concentration of DNA was substantially high or if no interaction occurred between the internal surface of the DNA backbone and the surfactant molecules. Nonetheless, nonionic surfactants seem to have a distinct effect on the structure of a DNA molecule. It was discovered using fluorescence microscopy that DNA strands display a distinct coil to globule transformation at very high Triton X-100 concentration.[157] The appearance of DNA globules was not observed at low Triton X-100 concentrations, even at concentrations just above the CMC. DNA compression occurred exclusively in Triton X-100 solutions containing 50 to 90 wt% Triton X-100.[157] The conformational transformations of linear DNA were studied in the presence of dodecyldimethylamine oxide (DDAO), an amphiphile which exists in both a neutral or cationic protonated state depending on the solution pH.[158] Cationic mixed vesicles composed of DDAO and DOPE were generally more effective at compressing DNA than DDAO micelles. Addition of DNA to low pH vesicular DDAO/DOPE mixture induced vesicle

breakdown and the creation of multilamellar complexes. Under high pH conditions, DNA did not associate with the neutral vesicles, but caused complexation and flocculation.[158]

The effects described thus far illustrate the variety of aggregate types generated by surfactants on their own and upon complexation with other molecules. Consequently, the characterization of these complex self-assembled entities requires the use of multiple experimental techniques. The main techniques applied to characterize the structures generated by the self-association of surfactants are described in the next section.

1.3. Characterization of Surfactants and their Interactions with other Molecules

1.3.1 CMC Determination

Micellar aggregates are ordered structures made of surfactants, which are amphiphile molecules, that can be neutral or charged. The size of micelles ranges from a few to hundreds of nanometers. Micelles result from the self-assembly of surfactants in water through hydrophobic interactions between their alkyl tails, that leads to the formation of a hydrophobic core stabilized by the hydrophilic headgroups. These headgroups are oriented toward the aqueous phase in a manner that reduces the interactions between the hydrophobic tails of the surfactants and water.[41,58,159] Micelles are viewed as efficient vehicles to carry nonpolar molecules in a variety of pharmacological, therapeutic, and medicinal applications.[160-162] The critical micelle concentration (CMC) is the surfactant concentration necessary to spontaneously form micelles. It is the primary parameter that characterizes micelle formation and stability.[41,58] Techniques capable of determining the CMC of surfactants include surface tension,[163-165] light scattering,[166] conductometry,[166,167] isothermal titration calorimetry (ITC),[168,169] turbidity measurements,[170] and fluorescence.[171-174] Figure 1.10 illustrates the

typical plots where the parameters, obtained from different techniques, are plotted as a function of surfactant concentration to determine the CMC.

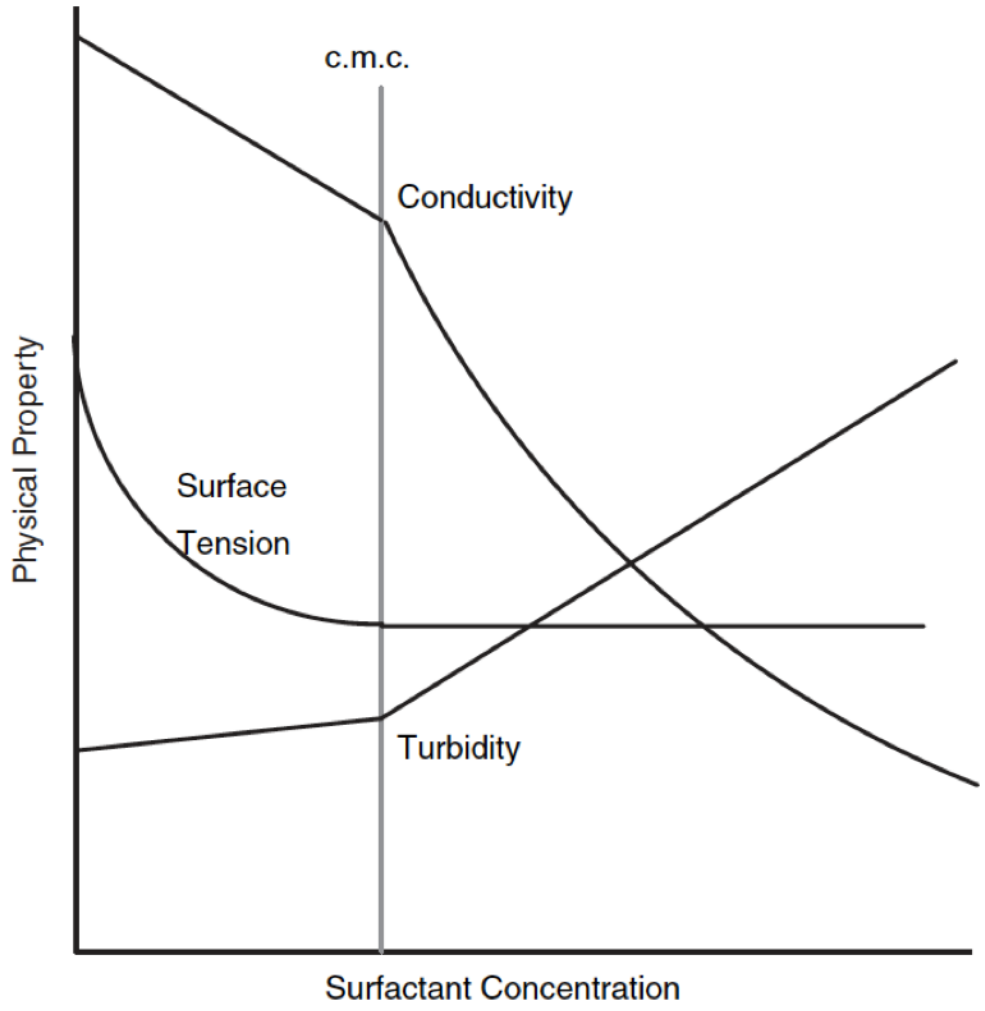

Figure 1.10 General plot of different physical properties represented as a function of surfactant concentration and the way they are used to determine the CMC. Reproduced with permission from John Wiley & Sons, Inc.[41]

Considering the significance of the CMC to characterize surfactants, it is noticeable that numerous CMC values published in the literature and obtained with different techniques show significant differences, even for common surfactants. Table 1.2 provides a list of published CMC values for the cationic surfactant CTAB.

Table 1.2 CMC values determined for CTAB by different techniques as reported in the literature.[175]

Technique	Parameter	Dye	CMC Value, mM
Fluorescence	Change in band ratios (I_1/I_3 ratio)	Pyrene	0.90
Fluorescence	Spectral shift of I_{max}	Coumarin 153	0.86
Fluorescence	Anisotropy	1,6-Diphenyl-1,3,5-hexatriene (DPH)	0.65
Surface tension	Surface tension	N/A	0.96
Conductimetry	Conductivity	N/A	0.98

The discrepancies shown in Table 1.2 might be the result of inherent shortcomings associated with different techniques, the existence of unidentified contaminants in commercially available surfactants arising from the different synthetic routes used in their preparation, as well as the type of methodology applied to the data analysis. Furthermore, given the absence of systematic benchmarks for dye-free or dye-dependent techniques, it cannot be ruled out that the dyes used to probe the properties of surfactants might influence the CMC determination, even at the very low probe concentrations needed for fluorescence detection. Another factor that can impact the CMC value is the ionic strength.[58] Due to these different artefacts affecting the CMC determination, many techniques and procedures have been developed in recent years to determine the CMC of surfactants beside the classical techniques mentioned above. In this thesis, we utilized the fluorescence emitted by a pyrenyl group covalently attached to the surfactants to determine their CMC using the model free analysis (MFA) of the fluorescence decays acquired with the pyrene-labeled surfactants.

A recent report by Scholz et al., where the CMC for the anionic surfactant SDS was determined for samples purchased from two different commercial sources using five different

techniques, represents a good example of the effect that surfactant impurities have on their CMC determination.[175] The SDS samples obtained from two commercial vendors had a purity of 95 and 99 % based on the total alkyl sulfate composition. The CMC was determined by surface tension, conductivity, and the fluorescence of three probes, namely pyrene, 1,6-diphenyl-1,3,5-hexatriene (DHP), and Nile red. According to Figure 1.11, the CMC values reported for the 95 %-pure SDS samples were always less than half the CMC determined for the 99 %-pure SDS sample. This study highlighted the importance of surfactant purity for CMC measurements regardless to the technique used.

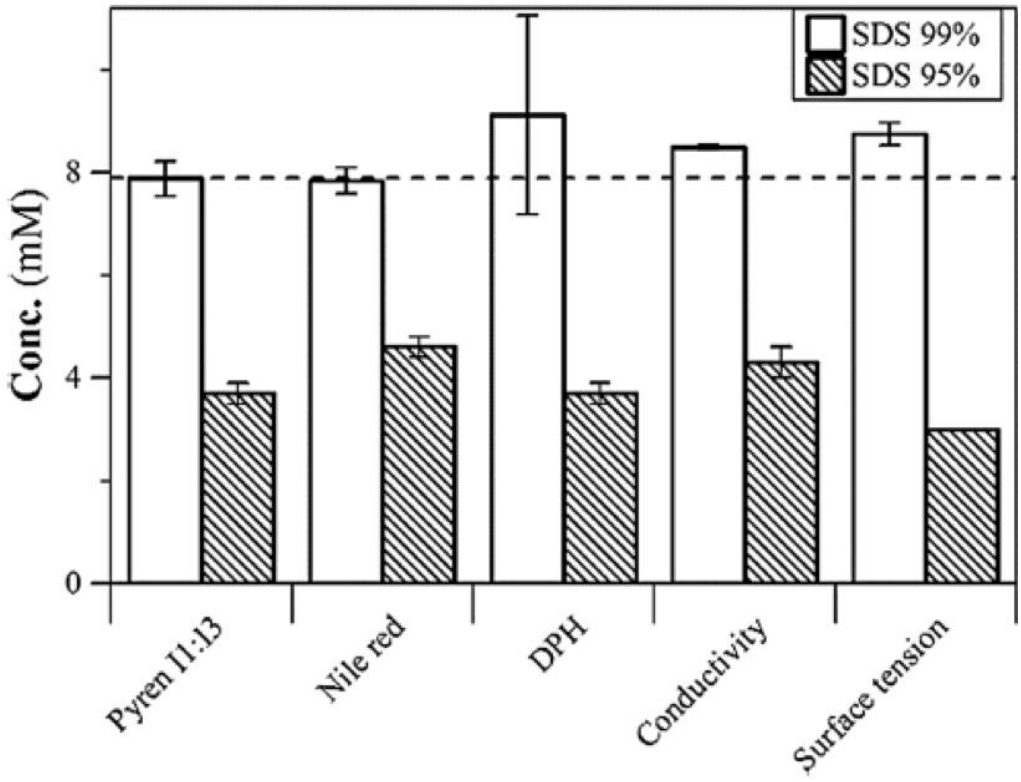

Figure 1.11 CMC values determined with five techniques for two different SDS samples with purity equal to 95 and 99 % as reported by Scholz et al.[175]

1.3.2 Aggregation Number Determination

The second most important parameter that must be determined to better characterize a surfactant is the aggregation number (N_{agg}), which represents the average number of surfactant molecules per micelle. N_{agg} is influenced by several variables such as the packing parameter

shown in Equation 1.1, which depends on the surfactant structure, temperature,[36,177,178] type and quantity of electrolytes present in the aqueous solution,[179,180] and additives.[58,181] The N_{agg} value helps describe the micellar size and configuration, which is useful in assessing the stability of and potential applications for the surfactant micelles. Experimental methods capable of determining N_{agg} are thus of significant importance. Several procedures have been reported in the literature to determine N_{agg} for surfactants based on thermodynamic principles and NMR, but these methods were found to be only effective for small N_{agg} values.[182]

1.3.2.1 Aggregation Number Determination by Light Scattering

Static light scattering (SLS) has been applied to determine N_{agg} based on the Debye equation shown in Equation 1.2 for some surfactants in the literature.[183]

$$\frac{K([Surf]-CMC)}{I(q,[Surf])}=\frac{1}{MP(q)}+2B([Surf]-CMC) \tag{1.2}$$

The Debye equation relates the reduced scattering intensity (I(q, [Surf])) to the CMC and concentration of the surfactant, the second virial coefficient (B), the weight average micelle molecular weight (M), and the form factor ($P(q)$). In turn, the form factor is defined in Equation 1.3,

$$\frac{1}{P(q)}=1+\frac{q^2 R_G^2}{3}+... \tag{1.3}$$

where R_G is the radius of gyration of the micelle and q is the scattering vector given in Equation 1.4.

$$q=\frac{4\pi n}{\lambda}\sin\left(\frac{\theta}{2}\right) \tag{1.4}$$

In Equation 1.4, n is the refraction index of the pure solvent, λ is the wavelength of the incident laser source and θ is the detection angle. The final parameter in the Debye equation is K, which is a constant, which is calculated with Equation 1.5.

$$K = \frac{4\pi^2 n^2 (dn/dc)^2}{N_A \lambda^4} \quad (1.5)$$

In Equation 1.5, dn/dc is the refractive index increment of the surfactant in the solvent and N_A is the Avogadro number. Now that all the parameters are defined, N_{agg} can be calculated by dividing the molecular weight M of a surfactant micelle determined with Equation 1.2 by the molecular weight of the surfactant molecule (M_o) as shown in Equation 1.6.

$$N_{agg} = M/M_o \quad (1.6)$$

The main drawback of the methodology based on static light scattering to determine N_{agg} is the need to extrapolate the data to low surfactant concentrations, that approach the CMC. Considering that the micelle size depends on the surfactant concentration for a majority of surfactants, extrapolation to low surfactant concentration will alter the size of the micelle.[182] In theory, SANS could be used to determine N_{agg}, which would also provide some insights on the shape of the micelles as well. In practice, the limited availability of SANS instruments and the high cost of the experiments, that often involve the use of expensive deuterated solvents or samples, make the use of SANS impractical.

1.3.2.2 Aggregation Number Determination by Fluorescence Quenching

The most popular and robust methodology to find N_{agg} is based on the use of fluorescence quenching experiments.[182] The use of fluorescence quenching avoids most of the issues raised earlier for scattering techniques.[182,184]

Upon excitation of a dye *D* in the presence of a quencher *Q*, the excited dye can either fluoresce with its natural lifetime (τ_o) or encounter a quencher and undergo quenching with a quenching rate constant (k_q) as described in Scheme 1.1.

$$h\nu + D + Q \longrightarrow D^* + Q \xrightarrow{k_q} D + Q$$
$$\downarrow 1/\tau_o$$

Scheme 1.1. Kinetic scheme for the quenching of a dye (*D*) by a quencher (*Q*).

Fluorescence quenching can occur in a static or dynamic manner. Static quenching reflects the possibility that the dye and quencher form a complex in the ground-state that leads to the instantaneous quenching of the dye after it was excited. Dynamic quenching results from the slow diffusive encounters between the excited dye and quencher. Dynamic quenching can be probed by time-resolved (TRF) and steady-state (SSF) fluorescence experiments, whereas static quenching occurs too quickly to be detected through TRF but can be characterized from SSF experiments. Both processes must be accounted for to describe how the SSF intensity varies as a function of quencher concentration. This is accomplished by considering Equation 1.7.

$$\frac{I_o}{I} = (1 + K_S[Q]) \times (1 + K_D[Q]) \tag{1.7}$$

In Equation 1.7, I and I_o are the fluorescence intensities of the dye with or without quencher, [*Q*] is the quencher concentration, K_S represents the equilibrium constant for the complexation of the dye with the quencher, and K_D is the dynamic quenching constant, which is also referred to as the Stern-Volmer constant, and is equal to the product $k_q \times \tau_o$. Equation 1.7 describes the quenching of a dye by a quencher in a homogenous solution. To apply the

principle of fluorescence quenching to a micellar solution where both dye and quencher are bound to the micelles, a few assumptions have to be made. The first assumption is that quenching takes place in a dynamic manner and that no intermicellar exchange of the dye and quencher occurs within the timeframe of the experiment.[184-186] This assumption implies that the dye and quencher occupancy times in a micelle are substantially greater than the fluorescence lifetime of the dye. Another assumption is that quenching occurs on a much shorter time scale than fluorescence (i.e. $k_q >> \tau_o^{-1}$). Finally, dyes and quenchers are assumed to distribute themselves randomly among the micelles according to a Poisson distribution. According to this model, the fluorescence signal arises solely from those micelles occupied with a dye alone, since the presence of one or more quenchers in a micelle would lead to instantaneous quenching. Consequently, the I_o/I ratio reflects the Poisson probability of having no quencher in a micelle given in Equation 1.8 as a function of the average number of quenchers per micelle (<*n*>), which is also equal to the ratio of the quencher concentration over the micelle concentration.[184]

$$\frac{I_o}{I} = \exp(< n >) = \exp\left(\frac{[Q]}{[Micelle]}\right) \tag{1.8}$$

Application of Equation 1.8 to the analysis of the fluorescence spectra acquired with a surfactant solution containing dyes and quenchers yields <*n*>. In turn, Equation 1.9 can then be applied to obtain N_{agg} from <*n*> since all other parameters ([*Q*], [*Surf*], and CMC) are known.

$$< n >= N_{agg} \times \frac{[Q]}{[Surf] - CMC} \tag{1.9}$$

In practice, a plot of <*n*> against quencher concentration obtained at a constant surfactant concentration, that is above the CMC, yields a straight line and N_{agg} can be easily

calculated from the slope. This robust methodology has been used to determine N_{agg} for many surfactants in the literature.

1.3.3 Determination of the Structure of Complexes Prepared with Surfactants

After the CMC and N_{agg} of a surfactant have been determined, there is a strong interest in characterizing the internal structure of the micelles and that of the complexes formed between the surfactant and other molecules. Understanding the structures of these aggregates allows for better utilization of surfactants in different applications like gene transfection, drug delivery, cosmetics, and enhanced oil recovery. Many techniques have been employed to determine the structure of these aggregates and micelles, such as scattering, microscopy, and fluorescence. Dynamic and static light scattering (DLS & SLS),[10,187,188] small angle X-ray and neutron scattering (SAXS & SANS),[44,46,47,189] atomic force microscopy (AFM),[44,190-192] transmission electron microscopy (TEM),[46,189,193] and pyrene excimer fluorescence (PEF)[10,194] are some of the techniques that have been used in the literature to elucidate the structure of micellar aggregates.

1.3.3.1 Light Scattering Techniques

Light scattering is part of the conventional methods applied to the analysis of colloidal and polymer aggregates in solution.[195] Both dynamic and static light scattering have been utilized to determine the size of micellar aggregates. The theory behind static light scattering has been discussed earlier with Equations 1.2 – 1.4. Light scattering techniques have been used to determine the diffusion coefficients of micelles and aggregates in solution.[196] One of the main pitfalls of light scattering is the presence of dust in the sample. Dust in the solution not only reduces the signal-to-noise ratio for the actual object under study, but more importantly distorts the intensity autocorrelation function in a manner that severely limits the validity of light scattering studies.

Wang et al. prepared two pyrene-labeled gemini surfactants and used dynamic light scattering to study the micelles generated by these surfactants.[10] The first surfactant was named Py-3-12. Py-3-12 is constituted of two dimethylammonium bromide headgroups linked by a propyl spacer with one headgroup bearing a 1-pyrenehexyl group and the other a dodecyl chain. The hydrodynamic diameter of the Py-3-12 micelles was found to equal 2.5 (±0.1) nm at 25 °C. The hydrodynamic diameter for the other surfactant Py-6-12, where the two headgroups were linked with a hexyl spacer, was found to equal 3.1 (±0.2) nm at 45 °C. The hydrodynamic diameter for Py-6-12 was measured at 45 °C and not at 25 °C due to its high Krafft temperature. Many other reports can be found in the literature where dynamic and static light scattering have been applied to study surfactants and their aggregates.

1.3.3.2 Small Angle X-ray and Neutron Scattering SAXS & SANS

SAXS and SANS are both based on the same fundamental principle as light scattering, but they use different waves to interact with matter, namely X-rays for SAXS and neutrons for SANS. While light scattering causes variations in the polarizability of the medium, which are taken into account through the refractive index and its change with the concentration of the molecule under study (d*n*/d*c*), X-rays and neutrons cause changes in the electron density and the neutron scattering-length density, respectively.[195] The wavelength of X-ray sources varies usually between 0.07 and 0.2 nm, while the wavelength for neutron sources ranges from 0.1 to 2 nm. This gives SAXS and SANS an advantage over the visible light scattering methods as they can probe matter at a smaller length scale. To eliminate interferences, the observations are made at extremely small angles, often smaller than 2 degrees.[197] Figure 1.12 shows the typical setup of a SAXS or SANS instrument.

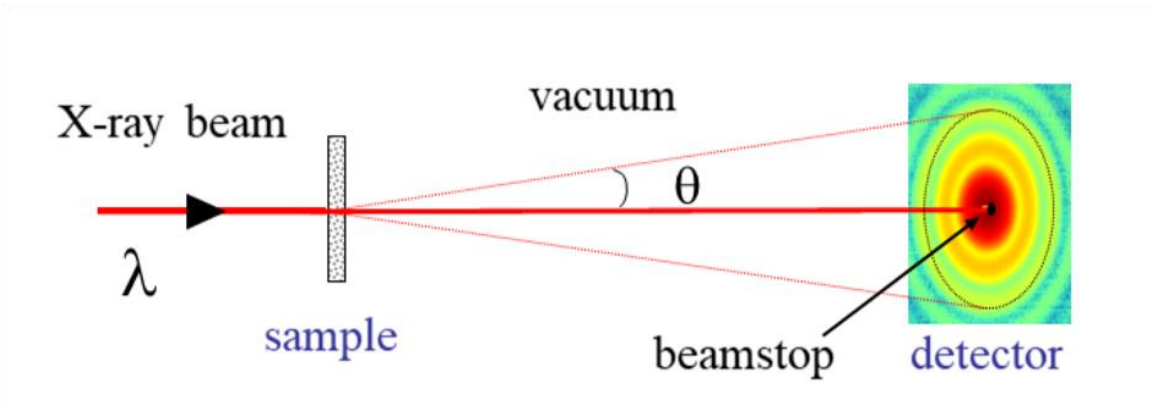

Figure 1.12 Schematic representation of a SAXS or SANS instrument.[198]

Gómez-Graña et al. reported the use of SAXS and SANS to characterize the bilayers formed by CTAB and a gemini surfactant around gold nanoparticles.[199] They found that the bilayer was 32 (±2) Å thick, with residual intertwining of the hydrophobic chains. In these experiments, the presence of extra surfactant molecules produced regular spherical micelles distinct from the bilayer structures, which generated a strong background, complicating the measurement of the thickness of the surfactant by SANS.[199]

Safinya's research group was able to use synchrotron SAXS to identify the different internal structures of complexes generated between DNA and cationic liposomes (CL-DNA complexes) with and without the use of the helper lipid DOPE.[46,47] Figure 1.13 depicts three different phases of CL–DNA complexes that have been identified. The most prevalent morphology is the lamellar state.[46]

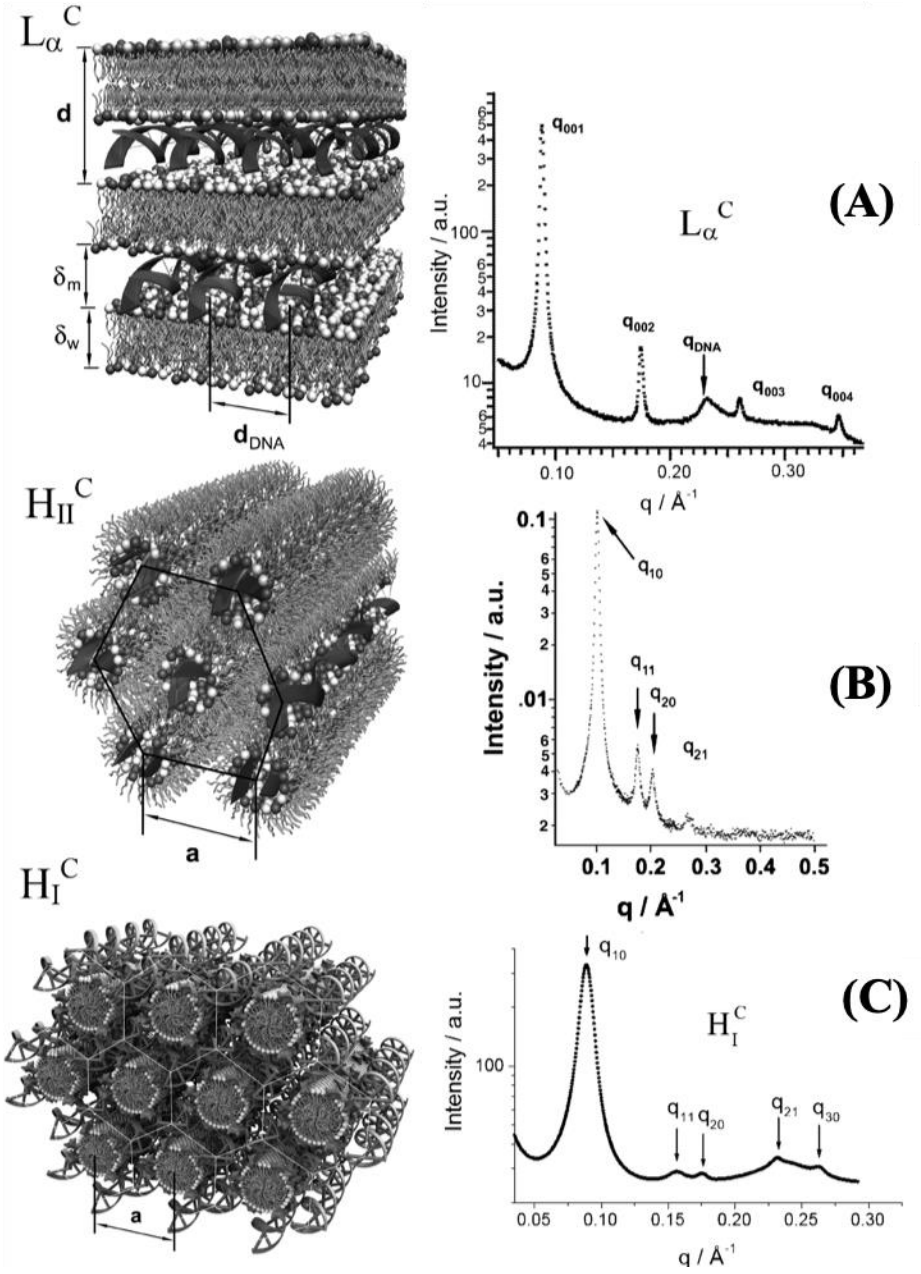

Figure 1.13 The internal nanoscale architecture of the three states found for CL–DNA complexes is shown with their corresponding SAXS patterns. (A) lamellar, (B) inverted hexagonal, and (C) hexagonal.

CL–DNA complexes prepared with the helper lipid DOPE and the 1,2-dioleoyl-3-trimethylammonium propane (DOTAP) lipid exhibit an inverted hexagonal phase at particular lipid/DNA compositions. A third CL-DNA hexagonal phase was discovered a few years later.[47] In these formulations, the conical shape of DOPE promotes a negative lipid membrane

curvature due to its small headgroup, whereas lipids with a big head-group result in a positive curvature of the lipid membrane. The hexagonal phase was attained with the dendritic lipid MVLBG2 bearing 16 positive charges in its head-group, that expanded the headgroup enough to promote a positive curvature, but it was only obtained within a narrow range of lipid compositions with around 25 mol% cationic lipid and 75 mol% of the dipalmitoylphosphatidylcholine (DOPC) lipid.[200] The morphology of the CL–DNA complexes was found to have a significant impact on the transfection efficiency. SAXS and SANS are powerful tools among the techniques available to study aggregates and complexes prepared from surfactants, but the main drawback with them is the limited availability of these instruments. Another one is the high cost of these experiments, which often limits the use of these powerful techniques.

1.3.3.3 Atomic Force Microscopy (AFM)

Atomic force microscopy is a prominent technique for studying the complexes of surfactants with other molecules such as DNA and other surfactants.[190-192] AFM provides images of surfactant aggregates with a sub-nanometer resolution, which is thousands of times more powerful than regular optical microscopy. The data is acquired by using a piezoelectric controlled probe to scan the surface in the contact or tapping mode.[201] Figure 1.14 shows the setup of a typical AFM instrument. In a typical experiment, the surfactant solution is deposited on a mica surface, where surfactant aggregates adsorb through electrostatic interactions. Scanning the surface reveals the structure of the objects that have been deposited on the mica plate. The main drawback of AFM is that the images generated by AFM for surfactant complexes might represent complexes that are distorted due to the adsorption of this soft material on a surface, that might result in the misrepresentation of the objects being investigated. Nevertheless, microscopy provides insightful information about the morphology of the complexes formed.

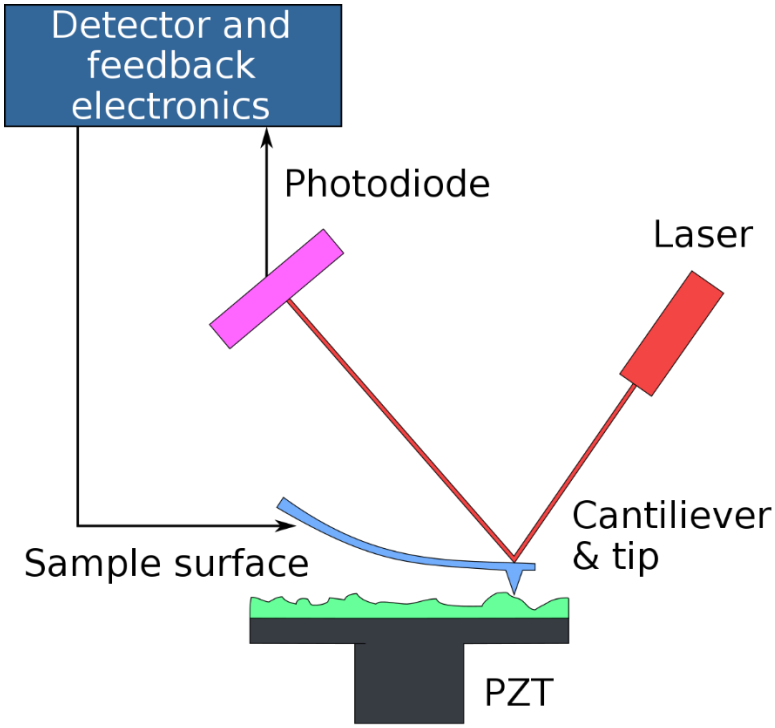

Figure 1.14 Diagram of a typical AFM instrument.

Miyazawa et al. studied the compaction of T4 DNA with the gemini surfactant 12-3-12 (see structure in Figure 1.2) using AFM and fluorescence microscopy (FM).[202] An increase in surfactant concentration from 0 to 10 μM in a solution, where the concentration of DNA was kept constant at 0.1 μM, led to the transition of DNA from a coil to first a semi-folded and second a folded conformation. With gemini surfactant concentrations of 0.2 and 1 μM, a 'rings-on-a-string' architecture comprised of several fused rings was observed. Numerous rings were detected, linked together by extended coil sections running along a single DNA molecule (see Figure 1.15). Electrostatic attraction between gemini surfactants and DNA promoted the condensation of DNA. The significantly smaller headgroup of the 12-3-12 surfactant might have resulted in a larger packing parameter leading to the formation of spherical aggregates, with the DNA being condensed in the surfactant collapsed sections, leading to the 'rings-on-a-string' architecture.

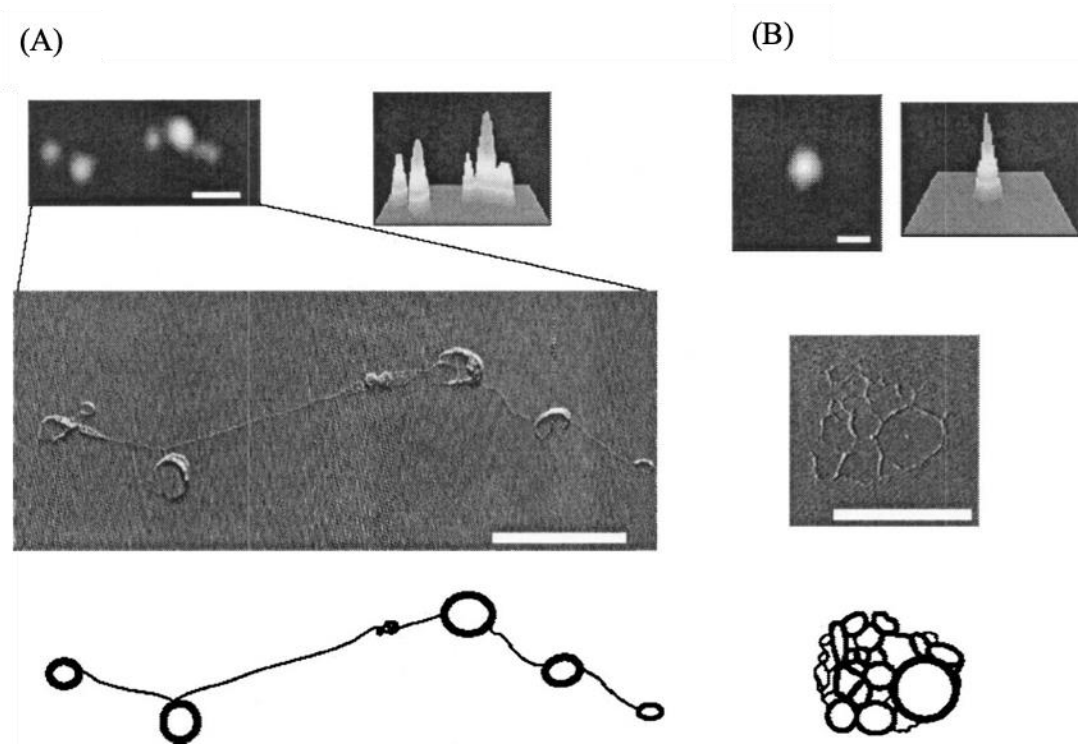

Figure 1.15 Images obtained by FM (top) and AFM (middle) with graphical depictions of partly folded and folded DNA (bottom). The AFM scans show (A) the partly folded rings-on-a-string architecture and (B) the folded network structure made up of several fused rings.[202]

1.3.3.4 Pyrene Excimer Fluorescence PEF

The use of the dye pyrene as a fluorescent probe to study micellar aggregates has been widely reported in the literature,[10,122,171,207-214] specially to find the aggregation number of surfactant micelles as described earlier. The long lifetime, high molar extinction coefficient, and hydrophobicity of pyrene make it an ideal fluorophore to study such hydrophobic aggregates.[203] The ability of pyrene to form an excited dimer (excimer), either when an excited pyrene encounters a ground-state pyrene during its lifetime or upon direct excitation of a pre-formed pyrene aggregate, allows one to probe the dynamics experienced by the pyrene dye inside the hydrophobic microdomains.[212-214] Figure 1.16 shows the kinetic scheme for pyrene excimer formation (PEF) and the associated SSF spectra. Two important ratios can be attained from the analysis of the SSF spectra of pyrene, namely the I_E/I_M and I_1/I_3 ratios. I_E/I_M represents

the ratio of the fluorescence intensity of the excimer over that of the monomer. I_E/I_M is proportional to the product $k_{diff}\times[Py]_{loc}$, where k_{diff} is the bimolecular rate constant for diffusive PEF and $[Py]_{loc}$ is the local concentration of ground-state pyrene experienced by an excited pyrene.[204,213] I_1/I_3 is the ratio of the fluorescence intensity of the first monomer peak divided by that of the third monomer peak. It reflects the polarity of the local environment experienced by an excited pyrene.[171,205,206]

Beside SSF, TRF can also be used to acquire the fluorescence decays of pyrene, which can be analyzed to extract more specific information about the system under study. Over the past 25 years, the Duhamel laboratory has developed new models to probe polymeric systems at the molecular level through the analysis of the multiexponential TRF decays of pyrene. The two main models are the fluorescence blob model (FBM)[207] and the model free analysis (MFA).[208-210] These models are based on principles that were first applied to study a variety of pyrene-labeled polymers in solution,[211-213] but studies have expanded their realm of applications to the study of amphiphilic molecules in solution.[194,214,215]

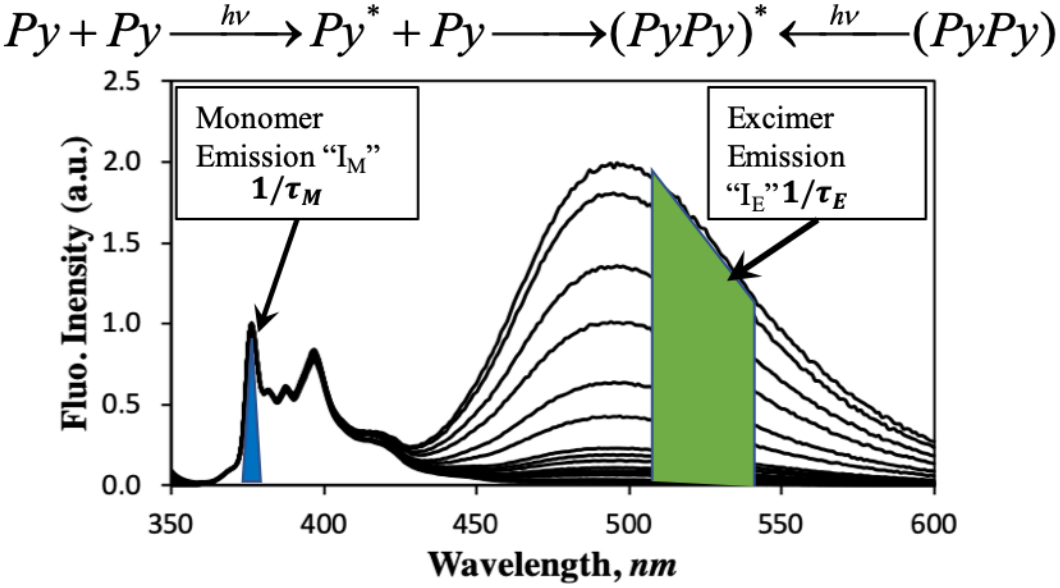

Figure 1.16 Kinetic scheme for pyrene excimer formation and the associated SSF spectra.

Wang et al. were the first to synthesize the two pyrene-labeled gemini surfactants referred to as Py-3-12 and Py-6-12, depending on whether the two dimethyl ammonium bromide headgroups were linked by a propyl or hexyl spacer.[10] They applied the traditional techniques to study and characterize the surfactants, such as isothermal titration calorimetry, dynamic light scattering, zeta potential, atomic force microscopy, and circular dichroism (CD). These classical techniques provided useful information about the surfactants and their behavior in solution, yet the fact that the fluorescent pyrenyl group was covalently attached to the surfactants opened a unique opportunity to apply fluorescence to probe the surfactant as it interacted with other molecules such as other surfactants during micellization or oppositely charged macromolecules such as DNA. In the case of the Py-3-12 and Py-6-12 surfactants, the SSF and TRF decays of their solutions with and without DNA were analyzed to study their interactions as they formed micelles on their own or complexed with DNA.[10]

This early study was extended by Keyes et al., who applied the model free analysis (MFA) developed in the Duhamel laboratory to the TRF decays acquired with Py-3-12.[194] The model free analysis describes the state of the pyrenyl labels, whether they are unassociated or complexed, through the determination of the molar fractions of the different forms of pyrenes (isolated, forming excimer by diffusion, or aggregated), their dynamics through the average rate constant for PEF, and an absolute measure of the I_E/I_M ratio, which is expected to match that obtained by SSF. The MFA yields the molar fraction of pyrenes that cannot form excimer and act as if they were free in solution (f_{free}), are pre-aggregated and form excimer instantaneously (f_{agg}), and form excimer via diffusive encounters (f_{diff}). Identifying the different pyrene species in solution led to the determination of the CMC of Py-3-12 and provided a means to characterize the complexes produced between Py-3-12 and DNA.

In summary, PEF is a powerful analytical tool to study colloidal systems in water, whose application remains rudimentary in the literature. It is one of the very few techniques

that allows investigators to study the behavior of polymers and surfactants at the molecular level in solution. Most other techniques are either not sensitive enough like DLS and SLS to probe the complexes made with surfactants in the micromolar range, too expensive and not readily accessible to many laboratories like SANS and SAXS, or require that samples be deposited on surface like for AFM, which might change the morphology of the complexes compared to their original conformation in solution.

1.4. **Thesis Goals and Outline**

The key objective of this research was to study the interactions between two pyrene-labeled gemini surfactants and DNA by applying the MFA to their TRF decays. The two gemini surfactants used in this thesis were Py-3-12 and PyO-3-12.

Chapter 2 focused on the synthesis and characterization of Py-3-12. A modified synthesis route from the one developed by Wang et al.[10] was introduced to prepare Py-3-12, which gave a higher yield than previously reported. The CMC of the surfactant was determined using two different techniques, namely the common surface tension methodology and that reported by Keyes et al. through the application of the MFA of the fluorescence decays acquired with Py-3-12 solutions.[194] The CMC of Py-3-12 was found to equal 0.15 (±0.02) mM, which agreed relatively well with the published values.[10,194] To complete the characterization of Py-3-12, the aggregation number (N_{agg}) of the Py-3-12 micelles needed to be determined. This turned out to be a challenging task as the classical methodology developed by Turro and Yekta,[184] Infelta,[185] and Tachiya[186] required the use of a long-lived dye like pyrene, that needed to be incorporated into the Py-3-12 micelles. Unfortunately, the large $[Py]_{loc}$ of pyrene inside the Py-3-12 micelles, where each constituting Py-3-12 surfactant bore one pyrenyl label, meant that it would be impossible to detect the signal from a pyrene molecule, that would have been incorporated inside the Py-3-12 micelles to determine their N_{agg}. Instead, the inherent fluorescence of the pyrene excimer generated by the Py-3-12 micelles was employed to

determine N_{agg} for the Py-3-12 micelles. After accounting for both static and dynamic quenching of the pyrene excimer produced in the Py-3-12 micelles, N_{agg} was found to equal 14 (±0.2). This work represented the first example where N_{agg} had been determined for micelles generated from a pyrene-labeled surfactant.

The synthesis and characterization of a specially designed pyrene-labeled surfactant, namely PyO-3-12, is described in Chapter 3. PyO-3-12 had the same chemical structure as Py-3-12 except for the 1-pyrenehexyl pendant in Py-3-12, which had been replaced by a 1-pyrenemethyl hexyl ether pendant for PyO-3-12. The introduction of the oxygen in the position β-to the pyrenyl group endowed PyO-3-12 with the ability to probe the polarity of its local environment through the I_1/I_3 ratio, a spectroscopic feature that was sorely missing for Py-3-12.[209] After having demonstrated that the sensitivity of the I_1/I_3 ratio to the polarity of the solvent was much enhanced for PyO-3-12 compared to Py-3-12, the procedure developed in Chapter 2 to determine the CMC and N_{agg} for pyrene-labeled surfactants was applied to PyO-3-12 and its CMC and N_{agg} were determined to equal 0.38 (±0.05) mM and 23 (±2), respectively.

The aim of Chapter 4 was to assess the superior spectroscopic properties of the positively charged PyO-3-12 surfactant by studying its interactions with an oppositely charged surfactant, namely negatively charged sodium dodecylsulfate (SDS). The interactions between PyO-3-12 and SDS were studied at a constant PyO-3-12 concentration, which was kept below the CMC of PyO-3-12 to avoid any excimer formation due to micelle formation, by varying the concentration of SDS. A large increase in PEF was observed at the equicharge point, confirming the complexation of PyO-3-12 and SDS. The finding, that the I_1/I_3 ratio of the PyO-3-12/SDS complexes was much lower than that of PyO-3-12 in SDS micelles, suggested that the PyO-3-12/SDS complexes could be multilamellar vesicles, where the PyO-3-12 surfactants located in the inner vesicle leaflets would be shielded from water and would probe a more

hydrophobic environment. Significant changes in the I_1/I_3 and I_E/I_M ratios led to the identification of several distinct concentration regimes, corresponding to the formation, progressive disintegration, and complete dissociation of the PyO-3-12/SDS complexes. This study established PyO-3-12 as an important fluorescent probe to study colloids prepared from the complexation of surfactants.

The interactions between DNA and the gemini surfactants Py-3-12 and PyO-3-12 were investigated in Chapter 5. Working at a constant gemini surfactant concentration below the CMC, the DNA concentration was varied from below to above the equicharge point using the (–/+) ratio to represent the ratio of the DNA concentration, expressed in DNA base pairs, over the gemini surfactant concentration. The (–/+) ratio was varied for both surfactants from 0 to 10, implying that at the end of any experiment, the DNA concentration was 10 times larger than that of the gemini surfactant. The structure of the aggregates prepared from the complexation of DNA with the gemini surfactants was inferred from the analysis of the SSF spectra and the MFA of the TRF decays. The study demonstrated that the chemical composition of the complexes, where the gemini surfactants were bound to DNA, did not change for (–/+) ratios that were below or above unity, as $[Py]_{loc}$ remained constant. The addition of SDS to solutions of the complexes prepared by mixing the gemini surfactants with DNA led to the complete release of the DNA molecules through the complexation of the gemini surfactants with SDS.

Finally, the results obtained in this thesis were summarized in Chapter 6, where some possible experiments are suggested as future work. This thesis illustrates how pyrene-labeled surfactants like Py-3-12 and PyO-3-12 can be employed to probe complex colloidal systems under extremely dilute conditions and use the rudimentary information provided by the fluorescence to provide structural and dynamic information about the complexes generated in solution.

Chapter 2 Determination of the Aggregation Number of Pyrene-labeled Gemini Surfactant Micelles by Pyrene Fluorescence Quenching Measurements

Adapted with permission from Ba-Salem, A. O., Duhamel, J.; Determination of the Aggregation Number of Pyrene-Labeled Gemini Surfactant Micelles by Pyrene Fluorescence Quenching Measurements. *Langmuir,* **2021**, *37*, 19, 6069-6079.

2.1. **Abstract**

A cationic gemini surfactant referred to as Py-3-12 and composed of two alkylated diammonium bromide headgroups, a propyl spacer, and a dodecyl and 1-pyrenehexyl hydrophobic tails was synthesized. Its critical micelle concentration (CMC) was determined to equal 0.15 (±0.02) mM by surface tension and time-resolved fluorescence measurements. The state of the pyrene molecules, whether they were incorporated inside the Py-3-12 micelles or unassociated in the aqueous solution, was determined by applying the global model free analysis (MFA) to the fluorescence decays acquired with Py-3-12 aqueous solutions. The unassociated Py-3-12 surfactants emitted as pyrene monomers and showed a long fluorescence lifetime. The excited pyrenyl groups located inside Py-3-12 micelles formed excimer by rapid encounter with a ground-state pyrene with an average rate constant equal to 0.69 (±0.06) ns^{-1}, in a process, which was detected by a short component in the fluorescence decay of the pyrene monomer coupled to a short rise time in the fluorescence decay of the pyrene excimer. After having characterized the photophysical properties of Py-3-12 in aqueous solution, the number (N_{agg}) of surfactants per micelle was determined by conducting quenching experiments with dinitrotoluene (DNT). Although DNT is fairly hydrophobic, it was found to partition itself between the Py-3-12 micelles and the aqueous phase. Fluorescence quenching experiments performed on the pyrene monomer and excimer generated by the Py-3-12 aqueous solutions yielded the concentration ($[Q]_b$) of DNT bound to the Py-3-12 micelles and the average number $\langle n \rangle_d$ of DNT quenching an excimer by diffusive encounters. A combination of steady-state and time-resolved fluorescence quenching experiments on the excimer yielded the number ($\langle n \rangle_s$) of DNT molecules, that were bound to the micelles and quenched the excimer in a static manner. A plot of the sum $\langle n \rangle_d + \langle n \rangle_s$ as a function of $[Q]_b$ yielded an N_{agg} value of 14.0 (±0.2) Py-3-12 units per micelle. This study represents the first example in the literature where N_{agg} is determined for a micelle where each surfactant molecule is labeled with pyrene.

2.2. **Introduction**

Although molecules obtained by connecting two surfactants by a spacer at or near their headgroups have been reported since the late 1960's,[1] they were first introduced as gemini surfactants by Menger and Littau in 1991.[2] The interest in gemini surfactants stems from their unique, and usually superior, properties compared to their monomeric counterparts. Among these properties are their outstandingly lower critical micellar concentration (CMC), which is two-to-three orders of magnitude smaller than for regular surfactants, higher surface activity, and enhanced wetting ability.[3-8] Like many surfactants, gemini surfactants associate in solution into a range of assemblies and morphologies such as vesicles, wormlike rods, or spherical micelles.[9-11] Due to these superior and unique features, gemini surfactants have been employed in a wide range of practical applications, such as gene delivery,[3-5] antimicrobial agents,[7] enhanced oil recovery,[8] food processing, cosmetics and body products, phase transfer catalysis, and drug delivery.[5,12-14]

Gemini surfactants are constituted of two headgroups, two hydrophobic, typically alkyl, tails, and a spacer. One example of a cationic gemini surfactant is *N,N-bis*-(dimethylalkyl)-α,ω-alkanediammonium dibromide, which is constituted of two ammonium bromide headgroups, two alkyl tails, and a spacer, where the alkyl tails and spacer are constituted of *m* and *s* carbon atoms, respectively. This surfactant family is referred to as *m-s-m* and it is the most studied group of cationic gemini surfactants.[4] In particular, their cationic headgroups allow them to bind tightly to the negatively charged phosphate anions along the DNA backbone to generate DNA-surfactant aggregates, also called lipoplexes, which are being considered as non-viral vectors for gene delivery.[3-5] While the interactions between DNA and cationic gemini surfactants can be characterized by a variety of techniques such as atomic force microscopy, calorimetry, and scattering measurements,[15] none of these techniques can actually probe individual surfactant molecules as they interact with themselves or oppositely charged

macromolecules such as DNA. This is most unfortunate as the morphology of lipoplexes, which are aggregates constituted of surfactants and DNA, has been found to have a profound impact on the ability of a lipoplex to go across a lipid bilayer membrane, a strong indication of possible cell transfection.[16-18] Yet, the morphology of lipoplexes, which is usually defined with respect to the arrangement of the DNA macromolecules in the lipoplexes,[16-18] depends also on the arrangement of the surfactants. A tool capable of following the arrangement of surfactants as they interact with themselves or with DNA would thus be most valuable.

Such a tool was introduced in 2007, when Wang et al. replaced one alkyl chain of the 12-3-12 and 12-6-12 diquaternary ammonium gemini surfactants by a pyrene derivative to yield Py-3-12 and Py-6-12 (see chemical structure of Py-3-12 in Figure 2.1).[19] The introduction of the pyrenyl dye into the surfactant enabled the use of fluorescence to study the behavior of the pyrene-labeled gemini surfactants in solution. This approach departed from the major techniques used to study surfactants in solution such as conductimetry, surface tension, or calorimetry, which probe the properties of the surfactant solution. In contrast, the fluorescence of the pyrene-labeled surfactant enabled one to study directly the surfactant itself. Py-3-12 and Py-6-12 were found to form micelles with a CMC, which was significantly lower than the CMC of 12-3-12 and 12-6-12 due to the presence of the hydrophobic pyrenyl group. Both Py-3-12 and Py-6-12 were also found to interact strongly with DNA. While this early study was most informative,[19] it was the later application of the model free analysis (MFA) of the fluorescence decays acquired with aqueous Py-3-12 solutions, that provided a clear depiction of the different states of the pyrene molecules, and thus the Py-3-12 surfactants, in solution.[20] The MFA identified three pyrene species in solution, namely the pyrenyl labels that were isolated and did not form excimer (Py_{free}*), that formed excimer by diffusive encounters (Py_{diff}*) inside a Py-3-12 micelle with a large rate constant $\langle k \rangle$ due to the large local pyrene concentration inside a micelle, and that were aggregated (Py_{agg}*) and formed excimer instantaneously upon

excitation. The MFA of the fluorescence decays retrieved the molar fractions f_{free}, f_{diff}, and f_{agg} of the pyrene species Py_{free}*, Py_{diff}*, and Py_{agg}*, respectively. As the concentration of Py-3-12 increased, f_{diff} increased as more excimer was formed inside the micelles, f_{free} decreased as the overall contribution of unassociated surfactants in water decreased, and f_{agg} took a constant value of 0.13 ± 0.03 across the range of concentrations studied. Most interestingly, the product f_{free}×[Py-3-12] yielded the concentration of unassociated surfactant, which was found to remain constant and equal to 0.22 mM above the CMC of Py-3-12. This value happened to match perfectly the CMC of 0.22 mM, which had been found for this Py-3-12 sample by surface tension and conductivity measurements, thus demonstrating the ability of the MFA to describe quantitatively the state of the pyrene-labeled gemini surfactants in solution.[20]

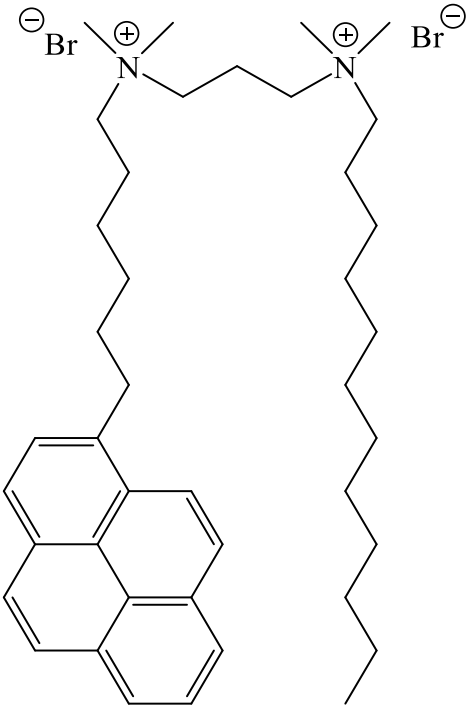

Figure 2.1 Structure of the pyrene-labeled gemini surfactant Py-3-12.

Beside the CMC and the rate constant of pyrene excimer formation (PEF), the last parameter to be determined for a complete characterization of the Py-3-12 surfactants by fluorescence is the number (N_{agg}) of surfactants constituting a Py-3-12 micelle. Yet while the fluorescence of pyrene is routinely applied to determine N_{agg} for surfactant micelles by

following the robust methodology developed for long-lived fluorescent dyes associated with surfactant micelles by Turro and Yekta,[21] Infelta, Graetzel, and Thomas,[22] and Tachiya,[23] this methodology needs to be reconsidered for the Py-3-12 micelles, where each surfactant is labeled with a pyrene unit. In this case, the fluorescence emitted by the pyrenyl groups of the Py-3-12 surfactants would dwarf the emission of a small amount of pyrene probe added to an aqueous solution of Py-3-12 micelles to conduct the quenching experiments, that would yield N_{agg}. Yet while being more challenging, an aqueous solution of Py-3-12 surfactants at a concentration above the CMC offers some clear advantages compared to a non-fluorescent surfactant, as it opens two fluorescence channels, which can be used independently to determine N_{agg}. If a hydrophobic quencher is added to the aqueous Py-3-12 solution, the fluorescence emitted by unassociated Py-3-12 surfactants as long-lived pyrene monomers provides information about the concentration of quencher in the water phase ($[Q]_w$), while the fluorescence of the excimer, formed quasi-instantaneously between the pyrenyl labels located inside a Py-3-12 micelle, can be used to determine the average number ($<n>$) of hydrophobic quenchers bound to the Py-3-12 micelles. In turn, a plot of $<n>$ as a function of the concentration of quenchers bound to the Py-3-12 micelles ($[Q]_b = [Q]_o - [Q]_w$, where $[Q]_o$ is the total quencher concentration), would yield N_{agg} for the Py-3-12 micelles.[21-23]

The implementation of this procedure to determine N_{agg} for the Py-3-12 micelles is described in the present report using 2,6-dinitrotoluene (DNT) to quench the pyrene excimer generated inside the Py-3-12 micelles. DNT was selected as being the second-best pyrene excimer quencher from a list of 12 potential quenchers, where trinitrotoluene had the highest quenching efficiency for the pyrene excimer but was discarded, since it is a well-known explosive.[24] Combined with the MFA, this study provides a powerful experimental means to analyze the fluorescence emitted by Py-3-12 surfactants in a manner that yields all the parameters required for a complete characterization of the Py-3-12 surfactant and its micelles.

This is accomplished by assigning the state of all pyrenyl species, whether they are unassociated in water, or forming excimer either diffusively or through direct excitation of a pyrene aggregate inside a micelle, the dynamics experienced by the surfactants inside a micelle with $<k>$, along with the micellar size from N_{agg}. The complete quantitative characterization of the aqueous solution of Py-3-12 suggests that Py-3-12 behaves like typical ionic surfactants. This study opens the path toward more advanced investigations for the quantitative characterization of the interactions of Py-3-12 with other molecules such as DNA.

2.3. **Experimental**

Chemicals: Pyrene, 2,6-dinitrotoluene (DNT), aluminum chloride, 6-bromohexanoyl chloride, triethylsilane, trifluoroacetic acid, *N*,*N*,*N*′,*N*′-tetramethyl-1,3-propanediamine, and 1-bromododecane were purchased from Sigma-Aldrich and used as received unless stated otherwise. Dimethyl sulfoxide (DMSO), dichloromethane (DCM), acetone, and acetonitrile were HPLC-grade solvents from Sigma-Aldrich. Doubly distilled deionized water was obtained from Millipore Milli-RO 10 Plus and Milli-Q UF Plus (Bedford, MA) and was used to prepare all aqueous solutions.

Synthesis of Py-3-12: The procedure proposed by Wang et al.[19] was applied as shown in Scheme 1. The individual steps involved in the preparation of Py-3-12 are described in the following sections.

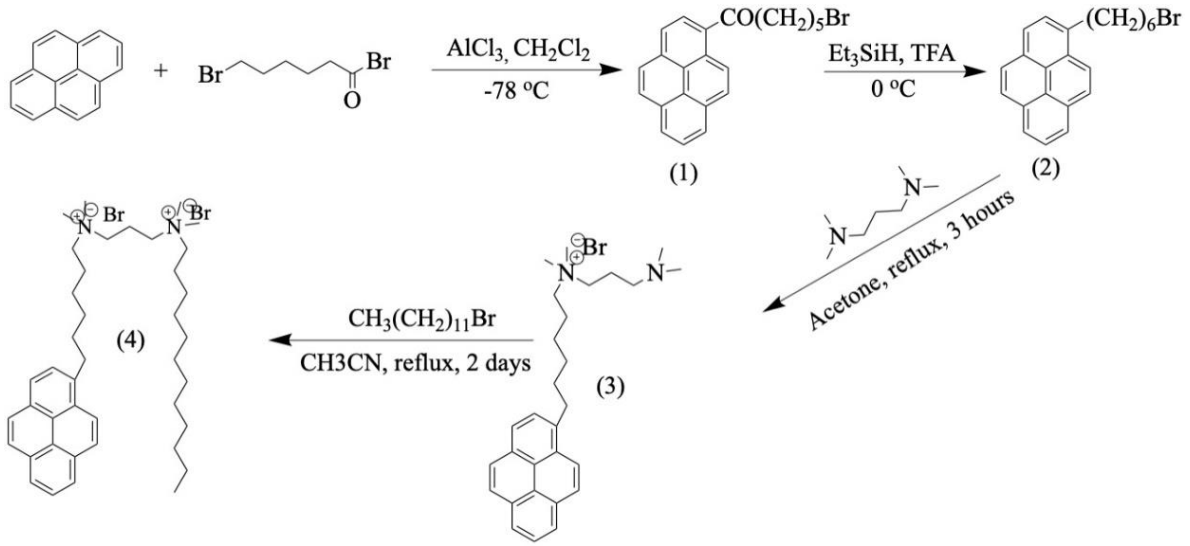

Scheme 2.1. Reaction scheme for the synthesis of Py-3-12.

Synthesis of 5-bromohexane-1-pyrene ketone (1). Pyrene (5.0 g, 24.7 mmol) was dissolved in 50 mL of DCM before $AlCl_3$ (4.0 g, 30 mmol) was added to the solution. The solution was cooled in an acetone bath with dry ice at −78 °C for 10 minutes. 6-Bromohexanoyl chloride (1.85 mL, 12.35 mmol) was added dropwise and the reaction was left to run for 3 hours at −78 °C after which, the reaction was quenched by careful addition of 1 M HCl until bubbles stopped forming. The organic layer was separated before being washed with 30 mL of brine solution. The organic layer was dried with Na_2SO_4 and the solvent was removed under reduced pressure. The resulting oil was purified by flash chromatography using a silica gel column (DCM:hexane 1:9), which yielded a yellow powder product (4.73 g, 49%). The ^{1}H NMR spectrum of (1) is shown as Figure S2.1 in Supporting Information (SI).

Synthesis of 6-(1-pyrenebromohexane) (2): 5-Bromohexane-1-pyrene ketone (1) (4.6 g, 12 mmol) was dissolved in 75 mL of DCM to which 20 mL of trifluoracetic acid was added. The reaction mixture was cooled to 0 °C. Triethylsilane (3.5 mL, 30.1 mmol) was added dropwise to the solution and the reaction was left to run at room temperature under nitrogen atmosphere for 3 days. The reaction was then neutralized by using a saturated solution of sodium bicarbonate, and the oil layer was separated and dried using Na_2SO_4. The solvent was removed

under reduced pressure and flash chromatography with silica gel was used to purify the product (DCM/hexane 1:9) to afford a final product as a white solid (4.03 g, 92%). The ^{1}H NMR spectrum of (2) is shown as Figure S2.2 in SI.

Synthesis of (N-(3-dimethylaminopropyl)-N,N-dimethyl-6-(pyren-6-yl)-hexan-1-ammonium bromide) (3): The synthesis was carried with acetone as a solvent instead of acetonitrile as for Wang et al.[19] for better heat control of the reaction.[25] In a round bottom flask equipped with a condenser, 6-(1-pyrenebromohexane) (2) (4.30 g, 11.8 mmol) was dissolved in 50 mL of anhydrous acetone to which *N*,*N*,*N*′,*N*′-tetramethyl-1,3-propanediamine (3.94 mL, 23.5 mmol) was added. The reaction was left to reflux for 3 hours. Three quarters of the solvent was removed under reduced pressure. The final product formed upon addition of diethyl ether was filtered and dried. The final product was a white powder (5.10 g, 87%). The ^{1}H NMR spectrum of (3) is shown in Figure S2.3 in SI.

Synthesis of N^1-dodecyl,N^1,N^1,N^3,N^3-tetramethyl-N^3-(6-(pyren-6-yl)-hexyl)propane-1,3-diammonium dibromide (4) (*Py-3-12*): (*N*-(3-Dimethylaminopropyl)-*N*,*N*-dimethyl-6-(pyren-6-yl)-hexan-1-ammonium bromide) (3) (0.145 g, 0.29 mmol) was dissolved in 25 mL of anhydrous acetonitrile placed in a round bottom flask. 1-Bromododecane (0.13 g, 0.58 mmol) was added to the mixture. The reaction was refluxed for 2 days. Then the solvent was removed under reduced pressure and a white product was formed. The final product was recrystallized from acetonitrile and chloroform several times (0.20 g, 93%). The ^{1}H NMR spectrum of (4) is shown in Figure S2.4 in SI. The molar absorbance coefficient of (4) at 344 nm in water equaled 29,200 $M^{-1}\cdot s^{-1}$.

Surface Tension: Surface tension measurements were conducted with a DuNuoy ring tensiometer manufactured by Central Scientific Co. Inc. The platinum-iridium ring had a ring radius to wire radius ratio of 53.6. All surface tension measured needed to be corrected using

the Harkins and Jordan method according to the manufacturer guidance. These experiments have been described in more detail in an earlier publication.[26]

Preparation of the Py-3-12 solutions with quencher: Py-3-12 was carefully weighed to prepare aqueous solutions with a known Py-3-12 concentration. For the fluorescence quenching experiments, two Py-3-12 aqueous stock solutions (20 mL) were prepared with Py-3-12 concentrations of 7.9 μM and 2.2 mM, that were below and above the CMC of 0.15 (±0.02) mM for Py-3-12, respectively. The stock solutions were divided into two vials containing 10 mL each. A 0.96 M stock solution of DNT in DMSO was prepared. The required amount of DNT solution in DMSO was added to one of the two vials to generate a 1.63 mM DNT concentration. This amount of DMSO represented 0.29 vol% of the stock solution and was deemed negligible in the fluorescence quenching experiments. The Py-3-12 solution with 1.63 mM DNT was titrated with the Py-3-12 solution without quencher to adjust the quencher concentration, while ensuring that the Py-3-12 concentration would remain constant.

Steady-State Fluorescence: Steady-state fluorescence (SSF) spectra were acquired with a Photon Technology International (PTI) spectrofluorometer equipped with an Ushio UXL-75Xe Xenon lamp and a PTI 814 photomultiplier detection system. All fluorescence spectra were acquired using the right-angle and front-face geometry for Py-3-12 concentrations below and above 0.2 mM, respectively. The samples were excited at 344 nm and their fluorescence intensity was scanned from 350 to 600 nm. The efficiency of pyrene excimer formation (PEF) was quantified with the fluorescence intensity ratio of the excimer over the monomer, namely the I_E/I_M ratio. It was calculated by dividing the fluorescence intensities of the pyrene excimer (I_E) obtained from the integral of the fluorescence signal in the fluorescence spectrum from 500 to 530 nm for the pyrene excimer by that of the monomer (I_M) obtained from the integral of the fluorescence spectrum taken from 372 to 378 nm. Although I_M was obtained by integrating the first peak in the pyrene monomer spectrum, which corresponds to the symmetry

forbidden 0-0 transition, this peak has a much reduced sensitivity to the polarity of the environment, since the pyrenyl label was substituted by a long alkyl chain like the hexyl linker connecting pyrene to the ammonium nitrogen in Py-3-12.[27] Consequently, the reduced sensitivity of the I_M intensity to solvent polarity will not affect the conclusions drawn from the analysis of the fluorescence spectra.

Time-Resolved Fluorescence: Two types of fluorescence decay measurements were conducted. The fluorescence decays of aqueous Py-3-12 solutions without quencher were acquired with a HORIBA FluoroHub equipped with a DeltaDiode at 336 nm. These experiments were aimed at characterizing the rapid pyrene excimer formation (PEF) inside the micelles. The decays were obtained with a time-per-channel of 0.102 ns/ch and the fluorescence signal was collected until the monomer and excimer decays reached 20,000 counts at their decay maximum. These decays were fitted according to the model free analysis (MFA). The fluorescence quenching experiments monitored the longer part of the fluorescence decays of the pyrene monomer and excimer and were performed with an IBH time-resolved fluorometer equipped with a NanoLED 340 diode with an excitation selected at 344 nm with an excitation monochromator and emission at 375 and 510 nm for the pyrene monomer and excimer, respectively. The monomer and excimer decays were acquired with a longer time-per-channel of 2.04 and 1.02 ns/ch, respectively. Since the monomer decay contained a short-lived component corresponding to PEF inside the Py-3-12 micelles, they were acquired up to 150,000 counts at the decay maximum to ensure that the decays would have a minimum of 20,000 counts just past the short component to ensure reliable analysis of the long tail of the decay. The excimer decays were acquired with 20,000 counts at the decay maximum. The instrument response function (IRF) was obtained in the same manner for both instruments by placing an aluminum reflective monolith in the sample holder and acquiring a decay with 20,000 counts at the decay maximum with the emission monochromator set at the same wavelength as the excitation

wavelength. In both instruments, the monomer and excimer fluorescence decays used a 370 and 490 nm cut off filter, respectively, to minimize stray light from reaching the detector. The fit of the fluorescence decays was done by convoluting the function of interest to the IRF, optimizing the parameters used in the different functions according to the Marquardt-Levenberg algorithm,[28] and comparing the convolution products with the experimental decays.

Individual analysis of the fluorescence decays: The monomer ($X = M$) and excimer ($X = E$) fluorescence decays were fitted individually with sums of n exponentials as shown in Equation 2.1.

$$[X^*]_{(t)} = [X^*]_{(t=0)} \sum_{i=1}^{n} a_{Xi} \times \exp(-t / \tau_{Xi}) \qquad (2.1)$$

In Equation 1, the a_{Xi} coefficients are the pre-exponential factors corresponding to the exponential having a decay time τ_{Xi}. Both parameters were optimized according to the Marquardt-Levenberg algorithm.[26]

The excimer decays acquired with a longer time-per-channel were also fitted according to the micelle model described by Equation 2.2 with the program miscat2bg.

$$[E^*]_{(t)} = \left([E0^*]_{(t=0)} e^{-t/\tau_{E0}} + [D^*]_{(t=0)} e^{-t/\tau_D} \right) \times \exp\left[- < n >_d \times (1 - \exp(-k_q t)) \right] \qquad (2.2)$$

Equation 2.2 accounts for the fact that two pyrene excimer species were detected in the excimer fluorescence decays, namely the short- and long-lived excimer species $E0^*$ and D^* emitting with their lifetime τ_{E0} and τ_D, respectively. Equation 2.2 also used the parameters $<n>_d$ and k_q, which are the average number of DNT molecules bound to the Py-3-12 micelles, which quench the pyrene excimer through diffusive encounters, and the rate constant for the quenching of an excimer by a quencher inside a micelle. In this analysis, the parameters $[E0^*]_{(t=0)}$, $[D^*]_{(t=0)}$, $<n>_d$, and k_q were optimized according to the Marquardt-Levenberg algorithm.[26]

Global model free analysis (MFA) of the fluorescence decays: The MFA was introduced 15 years ago[29] and has been reviewed numerous times.[30-32] The MFA represents a global fit of the pyrene monomer and excimer fluorescence decays. The monomer fluorescence decay is fit with a sum of several exponentials, where one of the exponentials has its decay time assigned to that of the natural lifetime (τ_M) of the pyrene monomer. The other decay times are expected to represent PEF and are allowed to float, while retaining the same value in Equations S2.1 and S2.2 provided in the Supporting Information (SI) and used to fit the monomer and excimer decays, respectively. The MFA has been shown to reliably retrieve the average rate constant $<k>$ for PEF and the molar fractions f_{diff}, f_{free}, and f_{agg} of the pyrene species in solution that form excimer by diffusive encounters, cannot form excimer and emit with the natural lifetime (τ_M) of pyrene, and are aggregated and form excimer instantaneously, respectively. The molar fractions are derived from the pre-exponential factors retrieved from the MFA of the fluorescence decays assuming a same molar extinction coefficient for all pyrenyl species involved. These analyses were conducted with the program sumegs34bg, which optimized τ_M.

2.4. **Results and Discussion**

The CMC of Py-3-12 was determined by measuring the surface tension of Py-3-12 aqueous solutions as a function of the surfactant concentration as shown in Figure 2.2. The profile shown in Figure 2.2 is typical of an ionic surfactant, with the surface tension of the solution decreasing with increasing Py-3-12 concentration from 72 mN/m, which corresponds to the surface tension of water, until it reached a plateau value of 49.5 mN/m for Py-3-12 concentrations above 0.15 (± 0.01) mM. The Py-3-12 concentration of 0.15 mM at the breakpoint is the CMC of this surfactant. This CMC value was slightly lower than that of 0.22 mM reported earlier for the same surfactant,[19,20] probably due to small differences in the overall purity of the Py-3-12 samples obtained in this and the earlier studies, since they were the result of two different syntheses. Sample purity was assessed from the chemical composition of the

Py-3-12 sample determined from the analysis of the ^{1}H NMR spectra, which typically results in a ±5 % margin of error depending on the boundaries selected for the integration of the NMR peaks.

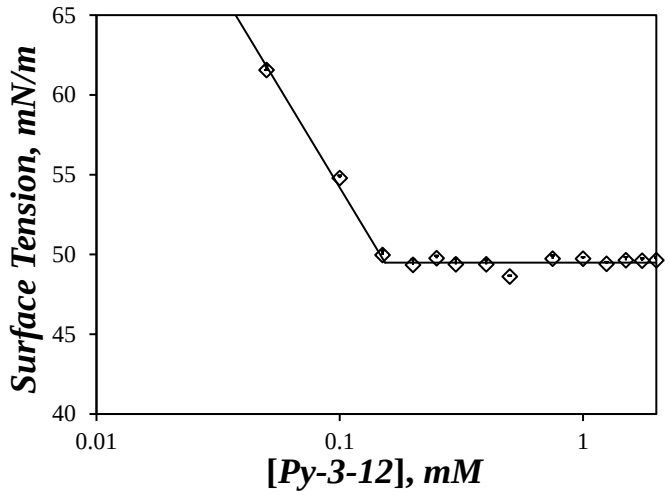

Figure 2.2 Plot of surface tension as a function of Py-3-12 concentration.

The fluorescence spectra of aqueous solutions of the Py-3-12 sample were acquired as a function of concentration and they are shown in Figure 2.3A. The fluorescence spectra present the typical spectral features expected for an excimer-forming pyrene derivative. Sharp fluorescence peaks were observed between 370 and 410 nm representing the fluorescence of the pyrene monomer and the broad structureless emission centered at 480 nm reflected pyrene excimer formation. To account for the large Py-3-12 concentrations, the fluorescence measurements were conducted using the front-face geometry, which resulted in some scattering in the fluorescence spectra at the shorter wavelengths. The most dilute 0.02 mM Py-3-12 solution showed hardly any excimer fluorescence, as the surfactants were too far apart in the solution to encounter diffusively. An increase in the Py-3-12 concentration led to an increase in diffusive encounters between Py-3-12 molecules, which resulted in an increase in PEF in Figure 2.3A.

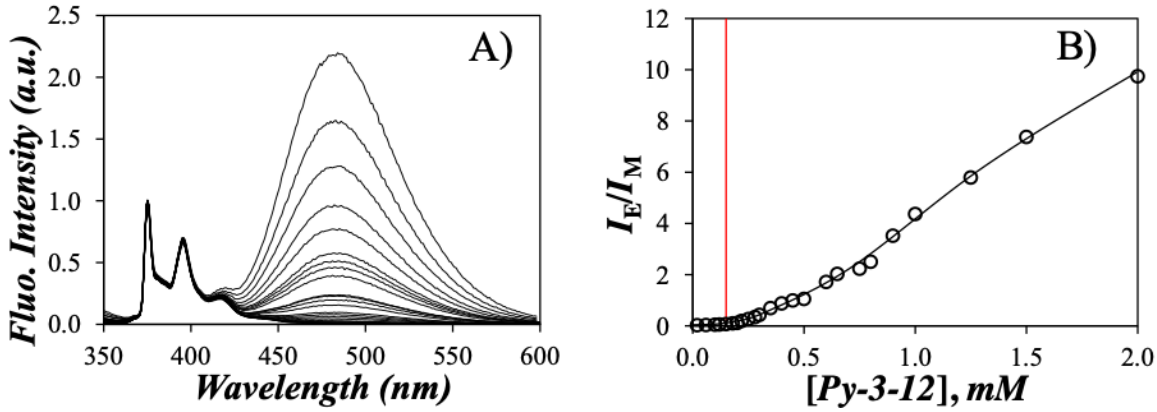

Figure 2.3 A) Fluorescence spectra acquired with Py-3-12 concentrations ranging from 0.02 to 0.8 mM. B) Plot of I_E/I_M as a function of Py-3-12 concentration. The red vertical line denotes the CMC of Py-3-12. The inset shows the I_E/I_M ratio for low [Py-3-12]. λ_{ex} = 344 nm.

The effect that the Py-3-12 concentration has on PEF is best illustrated by plotting the I_E/I_M ratio as a function of Py-3-12 concentration in Figure 2.3B. As the Py-3-12 concentration increased past a break point located around 0.15 mM, which is the CMC of Py-3-12 as determined by surface tension measurements (see Figure 2.2), I_E/I_M began to increase steadily. The increase in I_E/I_M could not be solely attributed to micelle formation as an excited pyrene is well-known to form excimer upon diffusive encounter with a ground-state pyrene, that might be located in a micelle or in the aqueous solution. To assess the path, which actually led to PEF, and thus rationalize the trend shown in Figure 2.3B, the time-resolved fluorescence decays of the pyrene monomer and excimer needed to be acquired and fit globally according to the model free analysis (MFA). The MFA was applied to the fluorescence decays acquired with aqueous solutions of Py-3-12 at concentrations greater than 0.1 mM, so that the excimer would be generated in sufficient amount to acquire the fluorescence decays within a reasonable experimental time. The fits were excellent, resulting in χ^2 that were lower than 1.10 and residuals and autocorrelation of the residuals that were randomly distributed around zero. An example of the quality of the fits can be seen in Figure 2.4A and B for the pyrene monomer

and excimer decays, respectively. The parameters retrieved from the fits were listed in Tables S2.1-S2.3 in SI.

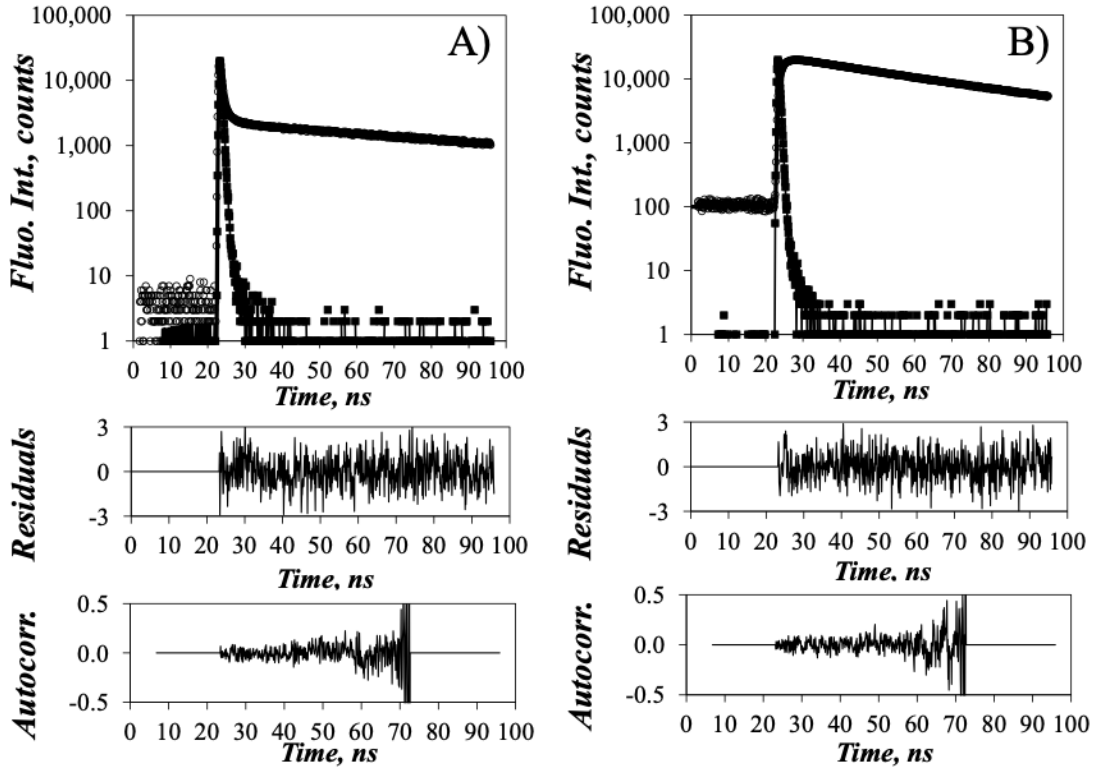

Figure 2.4 Fluorescence decays of the pyrene A) monomer (λ_{em} = 375 nm) and B) excimer (λ_{em} = 510 nm) for a 0.6 mM Py-3-12 aqueous solution. λ_{ex} = 344 nm, χ^2 = 0.984.

The fluorescence decays of the pyrene monomer in Figure 2.4A showed a rapid decay at the early times indicating rapid quenching of the pyrene monomer due to PEF occurring inside the Py-3-12 micellar interior. The large local pyrene concentration ($[Py]_{loc}$) inside the Py-3-12 micelles resulted in efficient PEF. The Py-3-12 molecules, that were not associated and were located in the water phase, emitted with a 95 (±2) ns long decay time for Py-3-12 concentrations between 0.1 and 2.0 mM, that corresponded to the natural lifetime (τ_M) of this pyrenyl derivative found to equal 103 ns for Py-3-12 obtained at a concentration of 7.9×10^{-6} M. The decrease in decay time from 103 to 95 (±2) ns could be attributed to residual PEF occurring by diffusive encounters between unassociated Py-3-12 molecules in water and pyrene quenching by the bromide anions. Based on the Stern-Volmer plot in Figure S2.5

obtained from the quenching of Py-3-12 by NaBr, quenching of Py-3-12 by NaBr takes place with a quenching rate constant of 5.0 (±0.2)×10^7 $M^{-1}\cdot s^{-1}$. Quenching by NaBr would thus lead to a reduction in lifetime from 103 (±2) ns to 100 (±2) ns when the Py-3-12 concentration was increased from 2.5×10^{-6} M to 2.5 mM, respectively. A further decrease in the lifetime of Py-3-12 from 100 (±2) ns to ~95 (±2) ns could be assigned to residual pyrene-pyrene encounters in the aqueous phase. The pyrene excimer yielded a fast rise time in Figure 2.4B, that occurred on the same time scale as the rapid decay observed in the monomer fluorescence decay in Figure 2.4A, before showing the long-lived fluorescence decays of the two pyrene excimer species *E*0* and *D** with lifetimes of 31 (±4) ns and 67 (±3) ns, respectively. The occurrence of two excimer species is generally observed, when PEF takes place in confined geometries, such as in the interior of Py-3-12 micelles, where the mobility of the pyrenyl labels is somewhat restricted.[20,28,29] The molar fractions f_{diff}, f_{free}, and f_{agg} of the different pyrene species were calculated from the parameters retrieved from the MFA of the decays and they are presented in Figure 2.5A. At low Py-3-12 concentration, where little excimer is formed, most Py-3-12 molecules were unassociated and f_{free} approached unity, while f_{diff} and f_{agg}, which reflected excimer formation by diffusive encounters between an excited and a ground-state pyrene and direct excitation of a pyrene aggregate, respectively, were small and close to zero. As the Py-3-12 concentration increased past 0.15 mM, which is the CMC of this surfactant obtained by surface tension measurements (see Figure2.2), f_{free} decreased and f_{diff} increased precipitously. f_{agg} increased more progressively for Py-3-12 concentrations above the CMC. The trends displayed by the molar fractions f_{free}, f_{diff}, and f_{agg} in Figure 2.5A agree with the notion that the free Py-3-12 surfactants associate above the CMC to form micelles, where they would induce PEF either by diffusive encounters between an excited and ground-state pyrene or direct excitation of a pyrene aggregate. The formation of pyrene aggregates inside the Py-3-12

micelles is a consequence of the high $[Py]_{loc}$ experienced by the pyrenyl labels inside the micelles.

The notion that PEF occurred inside Py-3-12 micelles was further reinforced by plotting the rate constant $<k>$ for PEF in Figure 2.5B. $<k>$ is equal to the product $k_{diff} \times [Py]_{loc}$, where k_{diff} is the bimolecular rate constant for PEF between an excited and a ground-state pyrene. When PEF occurs in a homogeneous pyrene solution, $<k>$ increases linearly with pyrene concentration, as has been reported earlier for ethyl 4-(1-pyrene)butyrate.[33] The $<k>$-*vs*-[Py-3-12] profile shown in Figure 2.5B certainly did not show this behavior. At Py-3-12 concentrations lower than the CMC of Py-3-12 determined by surface tension measurements, $<k>$ took a small value of 0.13 (±0.03) ns^{-1}, reflecting PEF occurring by slow diffusive encounters between unassociated Py-3-12 molecules in the water phase. For Py-3-12 concentrations slightly larger than the CMC, $<k>$ showed a significant increase to a value of ~ 0.9 ns^{-1}, before decreasing to a plateau value of 0.69 (±0.05) ns^{-1} for Py-3-12 concentrations between 0.4 and 2.0 mM. The increase in $<k>$ at the CMC reflects the large increase in $[Py]_{loc}$ upon formation of the Py-3-12 micelles. The relatively constant $<k>$ value obtained for Py-3-12 concentrations larger than 0.4 mM indicates that the rate of PEF does not change with Py-3-12 concentration at surfactant concentrations larger than the CMC, as would be expected if PEF occurred mostly inside Py-3-12 micelles, where $[Py]_{loc}$ remains the same regardless of the overall surfactant concentration in the solution.

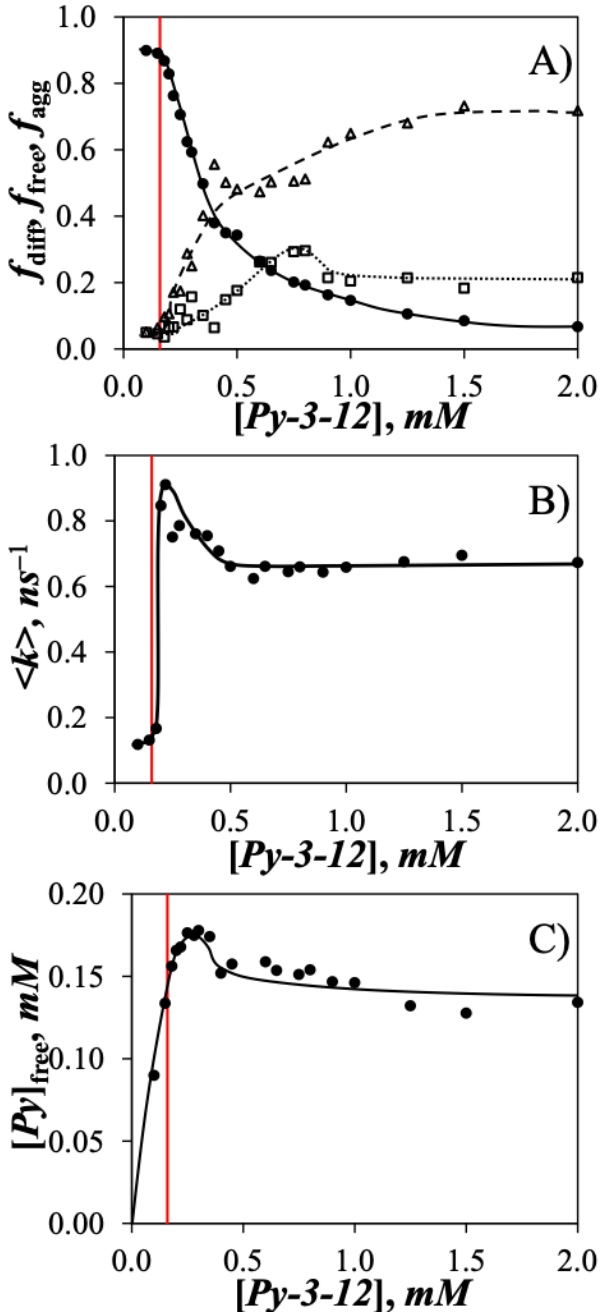

Figure 2.5 Plots of A) the molar fractions *(▲) f_{diff}, (●) f_{free}, and (□) f_{agg}*, B) <k>, and C) $[Py]_{loc}$ as a function of Py-3-12 concentration. The lines are drawn to guide the eye. The vertical red line indicates the CMC of Py-3-12 at 0.15 mM.

Finally, the concentration of unassociated pyrene ($[Py_{free}]$) in the aqueous Py-3-12 solutions could be calculated simply from the product [Py-3-12]×f_{free}. $[Py_{free}]$ is plotted as a function of Py-3-12 concentration in Figure 2.5C. It is found to increase linearly with increasing Py-3-12 concentration at low surfactant concentration before passing through a

maximum $[Py]_{free}$ value of 0.18 mM and then clustering around an average value of 0.15 (±0.01) mM for Py-3-12 concentrations larger than 0.4 mM. This behavior agrees with what would be expected for surfactant molecules before and after the CMC. Above the CMC, the concentration of unassociated Py-3-12 remained constant and equal to 0.15 (±0.01) mM, in agreement with the CMC of 0.15 (±0.02) determined by surface tension measurements.

The trends shown in Figure 2.5 demonstrate that Py-3-12 exhibits the behavior expected for a surfactant having a CMC of 0.15 (±0.02) mM based on the fluorescence and surface tension measurements. The parameters obtained by fluorescence and surface tension measurements were internally consistent with each other and agreed with the results reported earlier.[20] Having demonstrated that this Py-3-12 sample formed micelles above its CMC, fluorescence quenching measurements were conducted with dinitrotoluene (DNT) as a quencher to estimate N_{agg} for the Py-3-12 micelles. DNT was selected based on its known ability to effectively quench the pyrene excimer.[24] The low solubility of DNT in water reported to equal 204 mg/L[34] was expected to help DNT target the Py-3-12 micelles, where it would quench the pyrene excimer fluorescence. The ability of DNT to quench the pyrene monomer in water is illustrated in Figure 2.6A and B, where a strong decrease in fluorescence intensity and fluorescence lifetime was observed upon addition of increasing concentrations of DNT to a dilute aqueous solution of 7.9×10^{-6} M Py-3-12. It is important to note that the quenching of the fluorescence of the pyrene monomer is overestimated in Figure 2.6A due to the absorbance of DNT in water, which reaches 0.45 at the excitation wavelength of Py-3-12. An absorbance of 0.45 is much larger than the 0.05 absorbance recommended to avoid the innerfilter effect.[35] Fortunately, the fluorescence decays are not affected by the inner filter effect and the decay times retrieved from the monoexponential fit of the fluorescence decays could be used to build the Stern-Volmer plot in Figure 2.6C. A perfect straight line was obtained, whose slope of 616 M^{-1} equaled the product $k_q\times\tau_M$, where k_q is the bimolecular quenching rate constant and τ_M is

the natural lifetime of Py-3-12 in water found to equal 103 ns. Consequently, k_q was thus determined to equal 6.0×10^9 $M^{-1}\cdot s^{-1}$.

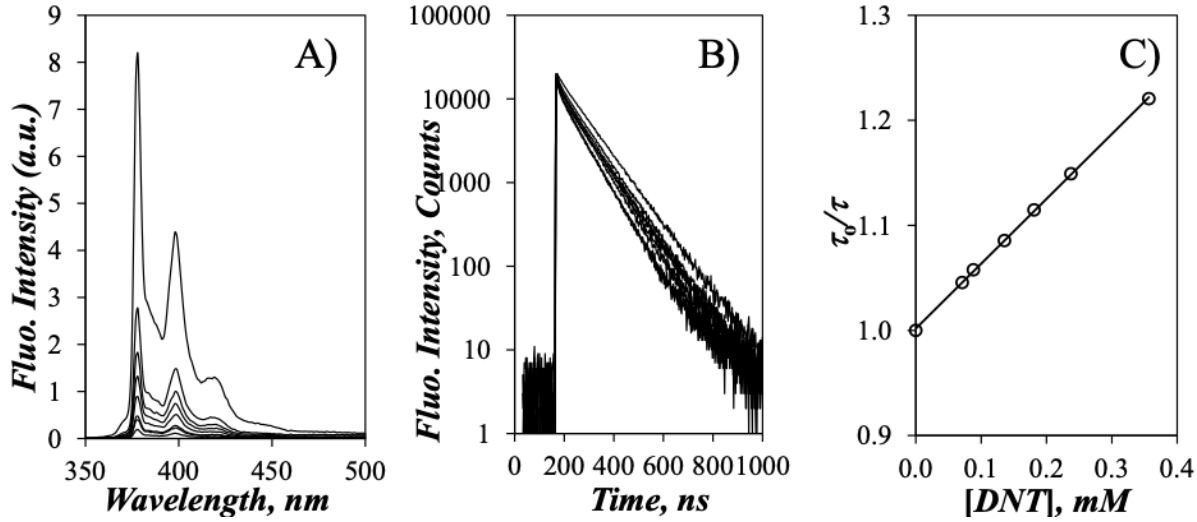

Figure 2.6 A) Fluorescence spectra and B) fluorescence decays of pyrene in a 7.9×10^{-6} M aqueous solution of Py-3-12 upon addition of DNT. From top to bottom: [DNT] = 0, 0.07, 0.09, 0.14, 0.18, 0.24, 0.36 mM. C) Stern-Volmer plot obtained from the decay times retrieved from the monoexponential analysis of the decays in Figure 2.6B.

The fluorescence quenching experiments were then repeated with a much more concentrated Py-3-12 solution of 2.2 mM, which was above the CMC (0.15 mM). In these experiments, the absorbance due to pyrene equaled 64, which dwarfed the maximum absorbance of 0.36 obtained for the largest DNT concentration used in these quenching experiments. Since the Py-3-12 concentration was fixed to 2.2 mM, the fluorescence intensity of the Py-3-12 solutions shown in Figure 2.7A could not be affected by changes in DNT concentration, whose absorbance was so much lower than that of Py-3-12. The fluorescence spectra showed a massive decrease in the fluorescence intensity of the pyrene excimer, indicating that DNT was targeting the Py-3-12 micelles.

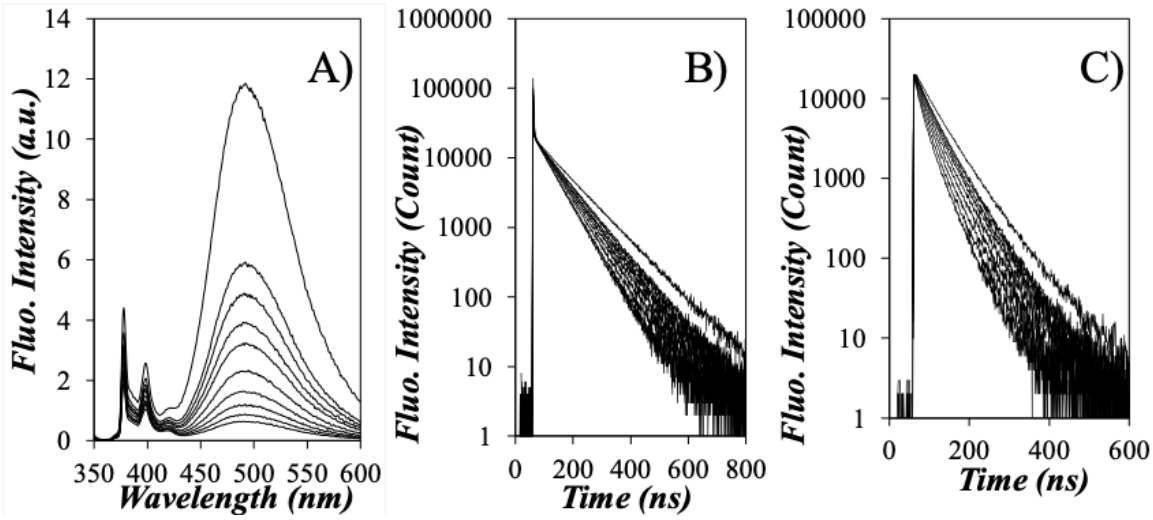

Figure 2.7 A) Steady-state fluorescence spectra and the fluorescence decays of the pyrene B) monomer and C) excimer for an aqueous solution of 2.2 mM Py-3-12 with different DNT concentrations. From top to bottom: [DNT] = 0.0, 0.35, 0.45, 0.55, 0.67, 0.83, 1.02, 1.24, 1.45, and 1.63 mM.

All fluorescence decays of the pyrene monomer in Figure 2.7B acquired with a 2.04 ns/ch time-per-channel (TPC) showed a spike at the early times, similar to that observed in Figure 2.4A for the fluorescence decay of the pyrene monomer acquired with a much shorter time-per-channel of 0.102 ns/ch. This spike, which occurred within ~7 ns or less than 4 channels in Figure 2.7B, reflected the rapid excimer formation from pyrene monomers located inside Py-3-12 micelles. The longer-lived decay, that appeared across the entire temporal window in Figure 2.7B, was due to the unassociated Py-3-12 surfactants in water, whose concentration equaled the CMC. The fact that the long-lived decay in Figure 2.7B became shorter upon increasing the DNT concentration indicated that some DNT molecules were also present in water, where they could quench the pyrene monomer fluorescence of unassociated Py-3-12 molecules. The long-lived part of the decays could be fitted with a biexponential, that yielded a long decay time (τ_L) with over 90% of the pre-exponential weight, which was

attributed to the decay time reflecting the quenching of the unassociated Py-3-12 surfactants by DNT in water.

Since τ_L responded to the DNT concentration in water ($[Q]_w$), $[Q]_w$ could be determined with Equation 2.3, which is derived from the equation obtained for the Stern-Volmer plot describing the quenching of unassociated Py-3-12 by DNT in Figure 2.6C. Due to the equilibrium described in Equation 2.4 between the DNT molecules, that were free in water or bound to the Py-3-12 micelles, Equation 2.5 predicts that a plot of $[Q]_b$ (= $[Q]_o - [Q]_w$, where $[Q]_o$ is the total DNT concentration in solution) as a function of $[Q]_w$ should yield a straight line passing through the origin, with a slope given by Equation 2.6, where K is the equilibrium constant and $[S]$ is the Py-3-12 concentration equal to 2.2 mM in these experiments. The concentrations $[Q]_w$ obtained from Equation 2.3 needed to be offset by a small amount $[Q]_{wo}$, which corresponded to the DNT concentration required to reduce the natural lifetime (τ_M) of 103 ns for a 7.9×10^{-6} M Py-3-12 aqueous solution to the τ_{L0} value of 99.6 ns, which was obtained for a 2.2×10^{-3} M Py-3-12 concentration. As mentioned earlier, the shorter lifetime obtained for the pyrene monomer at a Py-3-12 concentration of 2.2 mM could be due to residual PEF taking place between unassociated Py-3-12 molecules in water and quenching from the bromide anions. The plot of $[Q]_b$ as a function of $[Q]_w$ in Figure 2.8A was obtained with a $[Q]_{wo}$ value of 55 (±4)$\times10^{-6}$ M and yielded a straight line with a slope equal to 0.48 (±0.01). The procedure described above enabled the determination of the concentration ($[Q]_b$) of DNT molecules, that had partitioned themselves into the Py-3-12 micelles, and this information was then applied toward the determination of N_{agg}.

$$[Q]_w = \left(\frac{\tau_M}{\tau_L} - 1\right) \times \frac{1}{k_q \tau_M} - [Q]_{wo} \tag{2.3}$$

$$Q_w + \text{Mic} \underset{}{\overset{K}{\rightleftharpoons}} Q_b \tag{2.4}$$

$$K = \frac{[Q]_b}{[Q]_w \times [Mic]} \tag{2.5}$$

$$slope = K \times ([S] - \mathrm{CMC})/N_{agg} \tag{2.6}$$

The fluorescence spectra and excimer fluorescence decays of Py-3-12 were then analyzed to determine the number of DNT molecules bound per Py-3-12 micelle. The excimer fluorescence decays presented in Figure 2.7C showed no rise time, as excimer formation occurred on such a fast time scale inside the Py-3-12 micelles, that it could not be detected when the decays were acquired with a time-per-channel of 1.02 ns/ch, which was much larger than that of 0.102 ns/ch used for the excimer decay shown in Figure 2.4B. The excimer fluorescence decays in Figure 2.7C were fit according to Equation 2.2 to yield $<n>_d$, the average number of DNT molecules per micelles, that quenched the pyrene excimer by diffusive encounters. $<n>_d$ was plotted as a function of $[Q]_b$ in Figure 2.8B. At low DNT concentration, $<n>_d$ increased linearly with increasing $[Q]_b$, as would be expected from the well-known Equation 2.7.[21] The faster increase in $<n>_d$ with increasing $[Q]_b$ observed at higher DNT concentration in Figure 2.8B was probably a consequence of differences in quenching between the two pyrene excimer species *E*0* and *D** identified in this study.

$$< n > = \frac{N_{agg}}{[S] - CMC} \times [Q]_b \tag{2.7}$$

The analysis of the fluorescence decays with Equation 2.2 yielded the molar fractions f_{E0} and f_D of the short-lived *E*0* and longer-lived *D** excimer, respectively, which were plotted in Figure 2.8C as a function of $[Q]_b$. The continuous decrease in f_D with increasing DNT concentration indicates that the longer-lived *D** species, which is likelier to be protected from

quenching by oxygen dissolved in water and must be located closer to the center of the micelles, are specifically targeted by DNT. The efficient quenching of D^* results in a large k_q of 4.0 (±0.3)×10^7 ns^{-1} and a decrease in the D^* population as depicted by the decrease in f_D. As D^* is being depleted upon further increasing the quencher concentration, the $E0^*$ species, whose short lifetime τ_{E0} suggests that it must be exposed to water and located closer to the micellar interface, is being quenched with a lower k_q of 2.2 (±0.1)×10^7 ns^{-1} and f_{E0} approaches unity in Figure 2.8C. The break in the trend of $<n>_d$ for $[Q]_b$ ~ 0.3 M marks the point, where most of the excimer species D^* were quenched. The quenching appears to be more dynamic for the $E0^*$ species resulting in more DNT molecules contributing to dynamic quenching and less static quenching as will be seen hereafter.

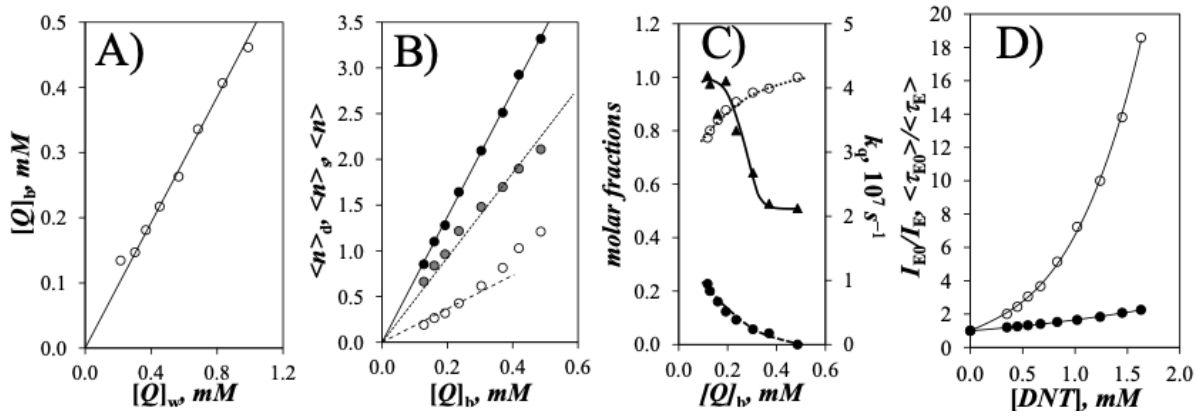

Figure 2.8 Plots of A) $[Q]_b$ as a function of $[Q]_w$, B) (O) $<n>_d$, (O) $<n>_s$, and (●) <n> (= $<n>_d$ + $<n>_s$), C) (O) f_{E0}, (●) f_D, and (▲) k_q as a function of $[Q]_b$, and D) (O) I_{E0}/I_E and (●) τ_{E0}/τ_E as a function of the overall DNT concentration.

While important, the dynamic quenching of the Py-3-12 micelles probed by the parameters $<n>_d$ and k_q in Figure 2.8 represented a small contribution to the overall quenching of the pyrene excimer. As it turned out, quenching of the excimer was much more pronounced in the fluorescence spectra, where the excimer fluorescence intensity (I_E) decreased by close to 20-fold, when the DNT concentration was increased from 0.0 to 1.6 mM, but the number

average lifetime of the excimer ($<\tau_E>$), obtained from the pre-exponential factors and decay times retrieved from the biexponential fits of the excimer decays, decreased by only 2.3-fold over the same concentration range. These considerations are illustrated more clearly in Figure 2.8D, which shows the ratios $<\tau_{E0}>/<\tau_E>$ and I_{E0}/I_E as a function of DNT concentration. The fact, that the I_{E0}/I_E ratio was much larger than the $<\tau_{E0}>/<\tau_E>$ ratio at all DNT concentrations, demonstrated that quenching of the excimer was mostly static in nature, a quenching mechanism, that is not captured by the analysis of the excimer fluorescence decays with Equation 2.2. Static quenching of the pyrene excimer by DNT could occur either through complexation of a DNT molecule with either a single pyrene monomer, that would be quenched instantaneously before having had time to form an excimer, or a pyrene aggregate, that would also prevent excimer formation. Whatever the process, static quenching resulted in the instantaneous disappearance of a substantial number of pyrene excimer due to DNT molecules, that were bound to the Py-3-12 micelles but were not accounted for by $<n>_d$.

Viewing the Py-3-12 micelles as spheres of action, where static quenching took place, the number $<n>_s$ of DNT molecules contributing to static quenching could be determined with Equation 2.8.[33]

$$< n >_s = Ln\left(\frac{I_{E0} / I_E}{< \tau_{E0} > / < \tau_E >}\right) \tag{2.8}$$

A plot of $<n>_s$ as a function of $[Q]_b$ is provided in Figure 2.8B. $<n>_s$ was about twice larger than $<n>_d$ reflecting the strong static nature of the quenching of the pyrene excimer by DNT. At $[Q]_b$ greater than ~0.3 mM, the $<n>_s$-*vs*-$[Q]_b$ showed a downward bend suggesting a slowing of static quenching, which matched the increase in dynamic quenching observed with $<n>_d$. These results are internally consistent and suggest that the long-lived *D** excimer species is more readily quenched through static quenching compared to the shorter-lived *E*0* excimer

species. As D^* becomes mostly quenched at $[Q]_b$ greater than 0.3 mM, the quenching shows a more dynamic character for the $E0^*$ species. Both effects seem to cancel each other, since summing $\langle n \rangle_d$ and $\langle n \rangle_s$ yielded $\langle n \rangle$, the total number of quenchers bound per Py-3-12 micelle, which increased linearly with increasing $[Q]_b$ in Figure 2.8B. The slope of the $\langle n \rangle$-*vs*-$[Q]_b$ straight line equaled 6.8 (±0.1), which resulted in an N_{agg} value of 14.0 (±0.2), a reasonable N_{agg} value for gemini surfactant micelles.[36-39]

The N_{agg} value could also be employed to determine the equilibrium constant (K) describing the binding of DNT to the Py-3-12 micelles by using Equation 2.5. Since the slope of the straight line obtained in Figure 2.8A equaled 0.48 (±0.01), K was found to equal 2.9 (±0.1)×10^3 M. This fairly low K value combined with the rather low concentration of Py-3-12 micelles equal to 0.15 mM [= ([Py-3-12]-CMC)/N_{agg}] explains why a majority of the DNT molecules partitioned into the aqueous phase. It is noteworthy that it would have been impossible to detect that the quencher was not fully bound to the Py-3-12 micelles, if the surfactant had not been fluorescently labeled, as is the case for Py-3-12. The partitioning of DNT in the water phase was clearly identified in Figure 2.7B, which showed how the long lifetime of unassociated Py-3-12 molecules in water was progressively reduced by continuous addition of DNT to the solution.

N_{agg} could also be used to estimate the radius of the hydrophobic core of the Py-3-12 micelles from the volume of the two hydrophobic tails and the linker of a Py-3-12 molecule, knowing that a pyrenyl, methylene, and methyl group occupy 0.259,[40] 0.028,[41] and 0.049 nm^3[3,39] respectively. Considering that one Py-3-12 molecule is constituted of 1 pyrenyl, 20 methylene, and 1 methyl groups, its hydrophobic parts generate a volume equal to 0.87 nm^3, so that the hydrophobic interior of a Py-3-12 micelles can be viewed as a sphere with a 2.8 nm diameter. This hydrophobic volume is similar to that generated by an SDS micelles, whose 62 dodecyl chains with a unit volume of 0.35 nm^3 would generate a micelle having a hydrophobic interior

equivalent to a sphere with a 3.4 nm diameter. Consequently, the results obtained thus far with Py-3-12 all indicate that this pyrene-labeled surfactant behaves in a similar manner as typical surfactants, the main difference being that its pyrenyl label makes it possible to apply fluorescence to probe its behavior in solution.

2.5. **Conclusions**

This study has illustrated the obvious advantages of dealing with pyrene-labeled surfactants. Such surfactants offer two observation channels with the fluorescence decays of the pyrene monomer and excimer and two different time scales for their study. Considering the fluorescence decay of the pyrene monomer as the first observation channel, the long-lived component in the monomer fluorescence decay describes unassociated Py-3-12 surfactants in water, thus providing an experimental means for probing the aqueous phase. The short component in the pyrene monomer decays describes the rapid diffusive encounters in the hydrophobic interior of the Py-3-12 micelles. The accuracy of the parameters retrieved from the analysis of the short component in the monomer decay is substantially improved by applying the global MFA to the pyrene monomer and excimer decays, thus involving the second observation channel. Whereas the long-lived component of the pyrene monomer fluorescence decays provides information about unassociated Py-3-12 molecules in water, the long-lived component of the excimer reflects the interior of the Py-3-12 micelles. Together, these two observation channels and different time scales afford a complete overview of an aqueous solution of pyrene-labeled surfactants, that are either unassociated or forming micelles in water. These concepts were applied to the characterization of Py-3-12 in water in the present study.

Taking advantage of the two fluorescence channels afforded by Py-3-12, the global MFA of the pyrene monomer and excimer fluorescence decays yielded the CMC of Py-3-12 in water, whose value of 0.15 (±0.01) mM matched that of 0.15 (±0.02) mM obtained by surface

tension, in agreement with earlier studies.[19,20] It is thus now possible to describe the behavior of aqueous micellar solutions by probing the surfactant molecules at the molecular level to determine their different states directly from the molar fractions f_{diff}, f_{agg} and f_{free}, their dynamics with $<k>$, their CMC, and the size of their assemblies through N_{agg}, as long as the surfactant of interest is being labeled with a pyrenyl derivative.

Chapter 3 Synthesis and Characterization of a Pyrene-Labeled Gemini Surfactant Sensitive to the Polarity of its Environment

3.1. **Abstract**

The synthesis of the cationic gemini surfactant PyO-3-12 was designed to include two dimethyl ammonium groups, one dodecyl tail, and 1-pyrenemethyl hexyl ether tail into the structure of the surfactant. The pyrenyl label ensured that the fluorescence of pyrene could be employed to probe the behavior of PyO-3-12 at the molecular level. The introduction of the oxygen atom in the β–position to pyrene was found to be critical for restoring the sensitivity of the pyrenyl label to the polarity of its environment. The properties of PyO-3-12 were characterized in water by surface tension and fluorescence measurements. The fluorescence methodology that was applied to study the properties of PyO-3-12 was the same as that introduced earlier to characterize the gemini surfactant Py-3-12, which was analogous to PyO-3-12 but without an oxygen atom in the alkyl linker connecting the pyrenyl label to the ammonium cation. This methodology involved the global model free analysis (MFA) of the pyrene monomer and excimer fluorescence decays to provide quantitative information about the state (unassociated-*vs*-aggregated) of PyO-3-12. The MFA was combined with a fluorescence quenching study with 2,6-dinitrotoluene to determine the size of the PyO-3-12 micelles. PyO-3-12 was found to behave like a typical gemini surfactant, exhibiting a critical micelle concentration (CMC) of 0.38 (±0.05) mM and an aggregation number (N_{agg}) equal to 23 (±2). Besides restoring the ability of PyO-3-12 to probe the polarity of its environment, the oxygen atom in the β–position next to pyrene brought some pyrenyl labels closer to the interface between the micellar interior and the aqueous phase, in a process that increased the effective volume of the hydrophobic part of PyO-3-12. This led to an increase in the packing parameter of PyO-3-12 and, consequently, an increase in N_{agg} to 23 (±2) compared to the N_{agg} value of 14 (±0.2) obtained for Py-3-12. The methodology described in this study to prepare and characterize pyrene-labeled surfactants at the molecular level is general and can be applied to study any pyrene-labeled surfactant and its interactions with oppositely charged macromolecules.

3.2. **Introduction**

Two surfactant molecules linked at or near their headgroup are called gemini surfactants.[1] Although studies of such molecules have been reported as far back as the late 1960s,[2] their systematic characterization began only in the 1990s, after realizing how unique their properties were compared to those of their monomeric counterparts.[1] Their structure leads to a diverse range of solution properties and aggregate morphologies, which take the form of spherical micelles, wormlike rods, and vesicles[3-5] depending on the type and size of the connecting spacer.[6-9] Gemini surfactants have garnered significant research interest in recent years due to their possible use in gene delivery,[10-12] improved oil recovery,[13] the development of highly porous materials,[14] drug loading and release, and soil remediation.[15-17]

N,*N*-*bis*(Dimethylalkyl)-α,ω-alkanediammonium dibromide is an example of a family of cationic gemini surfactants, which has been most studied in the scientific literature.[8,11] It is composed of two ammonium bromide headgroups, two alkyl tails, and a spacer, where the alkyl tails and spacer are composed of *m* and *s* carbon atoms, respectively. These gemini surfactants are classified as *m*-*s*-*m*.[11] In particular, their cationic headgroups allow them to form stable complexes with the negatively charged phosphate anions along a DNA helix. These aggregates, referred to as DNA-surfactant aggregates or lipoplexes, are being studied as non-viral carriers for gene transfection.[10-12] Although various techniques such as atomic force microscopy, calorimetry, and light scattering[12] have been employed to analyze the interactions between DNA and cationic gemini surfactants, none of these techniques probes individual surfactant molecules directly as they interact with one another in a micelle or with oppositely charged molecules such as DNA. The current inability to probe the behavior of gemini surfactants at the molecular level is limiting the design of gemini surfactants with improved properties for specific applications. For instance, the morphology of lipoplexes has been shown to significantly affect their ability to cross a lipid bilayer membrane, an indicator for the

feasibility of cell transfection.[18-20] However, while the arrangement of DNA helices in lipoplexes, be it lamellar or hexagonal, has been intensively characterized,[19,20] the distribution and alignment of the gemini surfactants inside lipoplexes with respect to the DNA helices need to be better understood. A robust methodology designed to monitor at the molecular level the interactions of these surfactants with DNA and themselves would be a tremendous asset to implement further improvements in the design of lipoplexes for gene delivery.

One such methodology was introduced in 2007 by Wang et al., whereby one of the alkyl tails on the cationic surfactants 12-3-12 and 12-6-12 was replaced with a pyrenyl label to yield Py-3-12 and Py-6-12.[21] The chemical structure of Py-3-12 is shown in Figure 3.1A. With this modification, fluorescence could be applied to investigate the activity of pyrene-labeled gemini surfactants in solution. This methodology differed from the conventional methods for studying surfactants in solution, such as conductimetry, surface tension, or calorimetry, which all probe various properties of the surfactant solution, but not the surfactant itself. In contrast, the fluorescence of the pyrene-labeled surfactant allowed for the direct examination of the surfactant at the molecular level by taking advantage of the ability of an excited pyrene to form an excimer upon encounter with a ground-state pyrene. Due to the hydrophobic pyrenyl group, Py-3-12 and Py-6-12 formed micelles with a CMC marginally lower than that of 12-3-12 and 12-6-12. Py-3-12 and Py-6-12 were both observed to strongly interact with DNA.[21] While the study by Wang et al. paved the way for applying fluorescence to probe the self-association of gemini surfactants, it was the subsequent application of the model free analysis (MFA) of the fluorescence decays acquired with aqueous Py-3-12 solutions, which identified the various states of the pyrene molecules in solution, and hence the states of the Py-3-12 surfactant, whether unassociated or micellized.[22] The MFA yielded also the CMC of Py-3-12, which matched that found by conductimetry and surface tension,[22] and a recent extension of this

methodology, which was discussed in Chapter 2, yielded the aggregation number (N_{agg}) of the Py-3-12 micelles.[23]

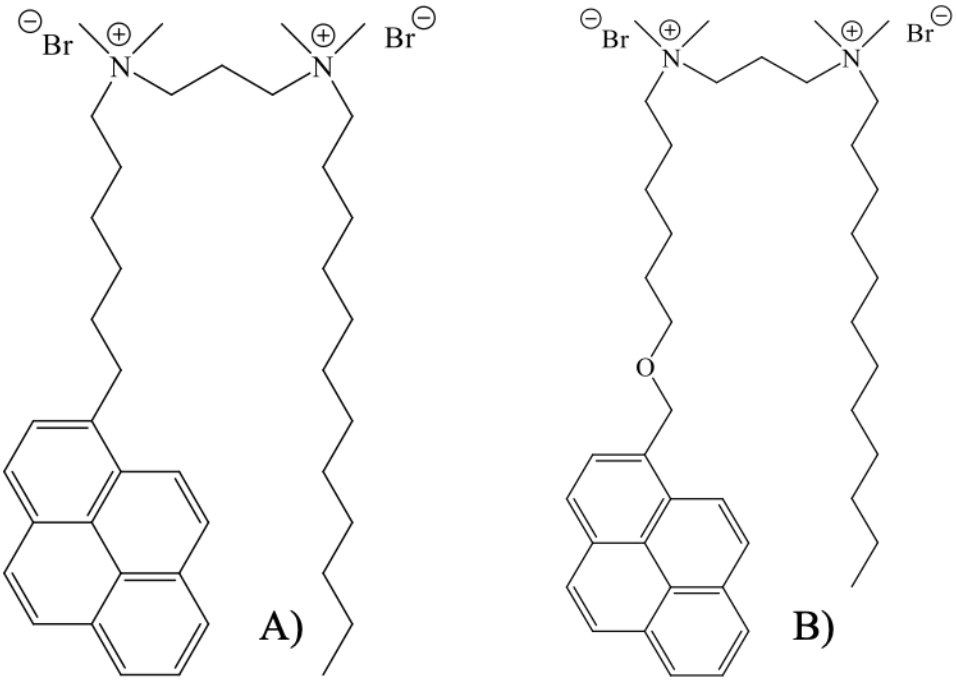

Figure 3.1 Chemical structure of (A) Py-3-12 and (B) PyO-3-12.

The studies conducted so far with Py-3-12 and Py-6-12 took full advantage of the increase in pyrene excimer formation (PEF) occurring when an excited and a ground-state pyrene encounter upon aggregation of the surfactants during micellization or lipoplex formation.[21-23] However, the second most important photophysical property of pyrene, which is to probe the polarity of its local environment,[24,25] has not been much used. The polarity of the local environment probed by an excited pyrene can be characterized from its I_1/I_3 ratio, which represents the ratio of the fluorescence intensity of the first peak (I_1) over that of the third peak (I_3) in the steady-state fluorescence spectrum of the pyrene monomer. The transition corresponding to the first fluorescence band (I_1), which is also the 0-0 transition of pyrene, is very weak in apolar solvents, to the point that it is described as symmetry forbidden in numerous publications, but is significantly stronger in more polar solvents, which explains the sensitivity of the I_1/I_3 ratio to solvent polarity, taking a value of 0.58 in hexane or 1.87 in

water.[25] Unfortunately, Py-3-12, like most pyrene derivatives modified with a long alkyl chain, loses the ability to probe the polarity of its local environment.[26] As the polarity of the environment probed by Py-3-12 undergoes major changes, when Py-3-12 transitions from its unassociated to aggregated form, a gemini surfactant, that would respond to both aggregation but also changes in solvent polarity, would be most advantageous to study surfactant aggregation during micellization or lipoplex formation. As it turns out, a recent study indicated the introduction of an oxygen in the β–position to pyrene restores the ability of pyrene to probe the polarity of its local environment.[26] It implied that replacing the 1-pyrenyl label of Py-3-12 by a 1-pyrenemethoxy group would yield PyO-3-12, whose structure is shown in Figure 3.1B, and where the fluorescence of the 1-pyrenemethoxy group would respond to both aggregation and the polarity of its environment. This strategy was implemented in this chapter, which describes the synthesis and characterization of the new gemini surfactant PyO-3-12.

3.3. **Experimental**

Materials: 1-Pyrenemethanol, 1,6-dibromohexane, hexadecyltrimethylammonium bromide, sodium hydroxide, magnesium sulfate, *N*,*N*,*N*',*N*'-tetramethylpropane-1,3-diamine, 1-bromododecane, and 2,6-dinitrotoluene (DNT) were purchased from Sigma-Aldrich and used as received unless stated otherwise. Dimethyl sulfoxide (DMSO), dichloromethane (DCM), petroleum ether, acetone, and acetonitrile were HPLC-grade solvents from Sigma-Aldrich. Doubly distilled deionized water from Millipore Milli-RO 10 Plus and Milli-Q UF Plus (Bedford, MA) was used to prepare all aqueous solutions.

PyO-3-12 was synthesized according to Scheme 3.1 and the steps leading to its preparation are described in detail in the following sections.

Synthesis of 1-(((6-bromohexyl)oxy)methyl)pyrene (**1**). The synthesis followed a reported protocol.[27] In a round bottom flask, sodium hydroxide (0.26 g, 6.45 mmol) was dissolved in 30 mL of water, to which 1-pyrenemethanol (0.60 g, 2.58 mmol) was added. The suspension was

stirred for 5 minutes before adding 1,6-dibromohexane followed by hexadecyl-trimethyl-ammonium bromide (CTAB, 0.024 g, 0.065 mmol), and the mixture was left to react at 70 ºC overnight. After washing the reaction mixture three times with DCM (3 × 25 mL), the organic layers were combined and washed with brine and dried using magnesium sulfate $MgSO_4$. DCM was removed under reduced pressure. The crude product was purified using column chromatography (petroleum ether / DCM = 1:1) to afford (**1**) (0.61 g, 60%) as a white solid. The ^{1}H NMR spectrum of (**1**) is shown as Figure S3.1 in Appendix A: Supporting Information (SI).

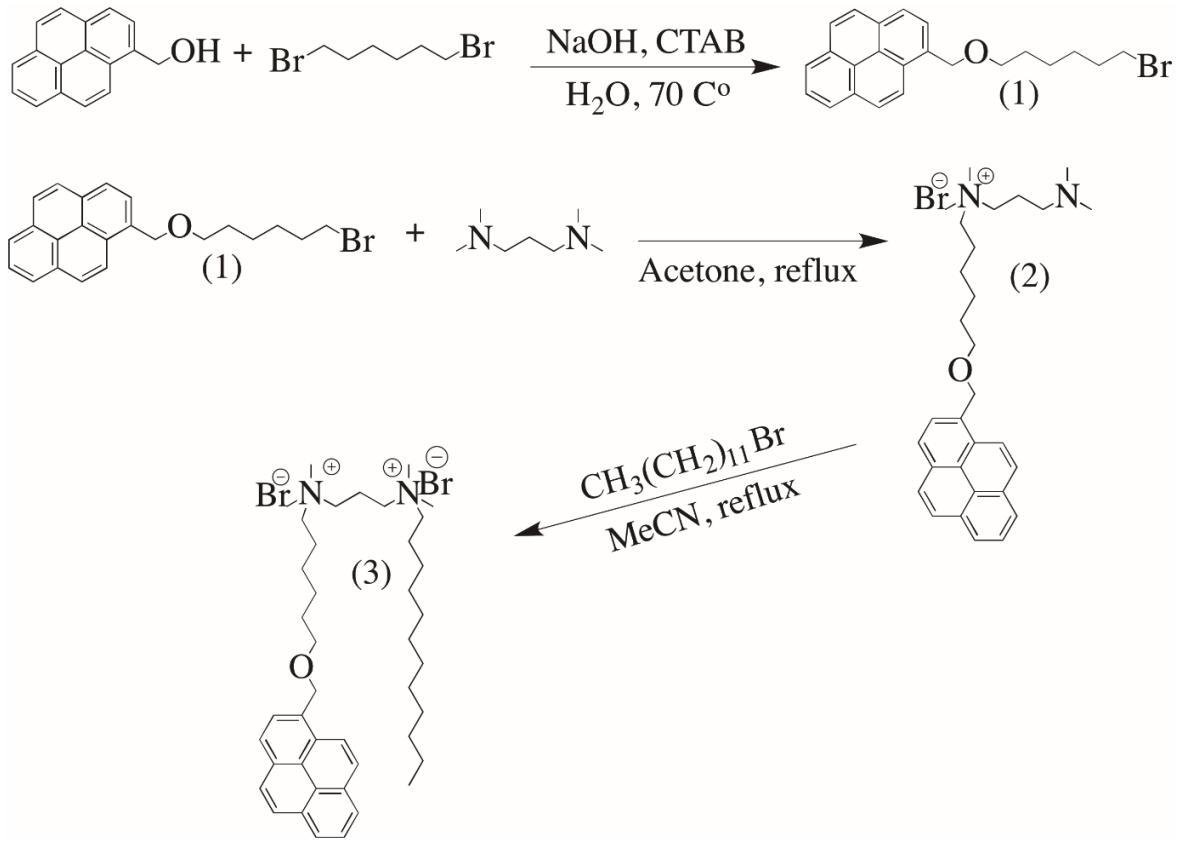

Scheme 3.1. Reaction scheme for the synthesis of PyO-3-12.

Synthesis of N-(3-(dimethylamino)propyl)-N,N-dimethyl-6-(pyren-1-ylmethoxy)hexan-1-ammonium bromide (**2**). 1-(((6-Bromohexyl)oxy)methyl)pyrene (0.17 g, 0.43 mmol) was dissolved in 0.5 mL of acetone with *N*,*N*,*N*',*N*'-tetramethylpropane-1,3-diamine (0.11 g, 0.86 mmol). The reaction mixture was left to reflux for 3 hours.[28] After the reaction had cooled to

room temperature, a white precipitate formed and acetone was removed under reduced pressure to yield (**2**), which was recrystallized from acetonitrile/diethyl ether with a yield of 93% (0.21 g). The ^{1}H NMR spectrum of (**2**) is shown as Figure S3.2 in SI.

*Synthesis of mono(N^1-dodecyl-N^1,N^1,N^3,N^3-tetramethyl-N^3-(6-(pyren-2-ylmethoxy)hexyl) propane-1,3-diammonium) monobromide (PyO-3-12) (**3**)*. *N*-(3-(dimethylamino)propyl)-*N*,*N*-dimethyl-6-(pyren-1-ylmethoxy)hexan-1-ammonium bromide (0.30 g, 0.57 mmol) was dissolved in 5 mL of acetonitrile to which 1-bromododecane (0.32 g, 1.28 mmol) was added. The mixture was left under reflux for 48 hours, after which the solvent was removed under reduced pressure to yield the final product PyO-3-12 as a white powder, which was repeatedly washed with diethyl ether until a clean ^{1}H NMR spectrum could be obtained. The ^{1}H NMR spectrum of (**3**) is shown in Figure S3 in SI.

Surface tension: Surface tension measurements were conducted with a DuNuoy ring tensiometer manufactured by Central Scientific Co. Inc. The platinum-iridium ring had a ring radius to wire radius ratio of 53.6. All measured surface tensions needed to be corrected by a factor determined from a chart supplied by the manufacturer. These experiments have been described in more detail in an earlier publication.[29]

Preparation of the PyO-3-12 solutions with quencher: Two aqueous stock solutions of PyO-3-12 with a concentration of 9.5 μM and 2.3 mM, that were below and above the CMC of 0.38 (±0.05) mM, were prepared by dissolving a pre-weighed mass of PyO-3-12 into 20 mL of doubly distilled deionized water. Each stock solution was divided into two vials containing 10 mL of each stock solution. A 0.96 M stock solution of DNT in DMSO was prepared. The required amount of DNT solution in DMSO was added to one of the two vials of the 9.5 μM and 2.3 mM PyO-3-12 stock solutions to generate a DNT solution with a concentration of 0.52 or 1.89 mM, which was, respectively, below and above the solubility limit of 1.12 mM for DNT in water.[30] Since the concentration of the 2.3 mM PyO-3-12 solution was above the CMC,

the PyO-3-12 micelles were expected to host the excess DNT, whose concentration of 1.89 mM was above its solubility limit, thus helping to target the PyO-3-12 micelles. The amount of DMSO used to prepare the PyO-3-12 stock solutions with DNT in water represented less than 0.31 vol% of the PyO-3-12 solution and was deemed negligible in the fluorescence quenching experiments. The 9.5 μM and 2.3 mM PyO-3-12 stock solutions with 0.52 and 1.89 mM DNT, respectively, were titrated with the corresponding PyO-3-12 solution without DNT to adjust the quencher concentration, while ensuring that the PyO-3-12 concentration would remain constant.

Steady-state fluorescence: Steady-state fluorescence spectra were collected on a Horiba QM-400 spectrofluorometer fitted with an Ushio UXL-75Xe xenon arc flash lamp. All solutions were characterized using right-angle geometry, except for the solutions for the N_{agg} and CMC measurements due to the inner-filter effect observed at high PyO-3-12 concentrations. Excitation of the solutions was carried out at 344 nm and their fluorescence emission was measured between 350 and 600 nm. The emission of pyrene was monitored using 1 nm excitation and emission slit widths. The PEF efficiency was determined by the ratio of the fluorescence intensity of the excimer to that of the monomer, referred to as the I_E/I_M ratio. The I_E/I_M ratio was determined by dividing the integral of the SSF spectrum between 500 and 530 nm by the integral of the SSF spectrum between 372 and 378 nm to obtain the fluorescence intensities of the pyrene excimer (I_E) and monomer (I_M), respectively. The I_1/I_3 ratio was determined by dividing the peak maximum of the fluorescence intensity at 376 nm (± 1 nm depending on the solvent) for I_1 by the peak maximum of the fluorescence intensity at 387 nm (± 3 nm depending on the solvent) for I_3. The I_1/I_3 ratio reflected the polarity of the local environment being probed by pyrene.

Time-resolved fluorescence: Two types of fluorescence decay measurements were conducted. A HORIBA FluoroHub equipped with a DeltaDiode at 336 nm was used to acquire the

fluorescence decays of the aqueous PyO-3-12 solutions without quencher. The fast time response of the fluorometer enabled the characterization of the rapid pyrene excimer formation (PEF) inside the micelles. A minimum of 20,000 counts was accumulated at the maximum of the monomer and excimer decays, which were acquired with a time-per-channel of 0.102 ns/ch. These decays were fitted according to the model free analysis (MFA). The fluorescence quenching experiments were conducted with an IBH time-resolved fluorometer equipped with a NanoLED 340 diode to excite the solutions at 344 nm with an excitation monochromator, while the emission of the monomer at 375 nm and the excimer at 510 nm were selected with an emission monochromator. These experiments targeted the longer part of the fluorescence decays of the pyrene monomer and excimer, which were acquired with a longer time-per-channel of 2.04 and 1.02 ns/ch, respectively. The monomer and excimer decays were acquired with 20,000 counts at the decay maximum. The instrument response function (IRF) was obtained in the same manner for both instruments by reflecting the signal of the excitation light against an aluminum monolith and collecting it by setting the wavelength of the emission monochromator to the same wavelength as the excitation wavelength. The IRF was acquired with 20,000 counts at the decay maximum. Cut off filters at 370 and 490 nm were used in both instruments during the acquisition of, respectively, the monomer and excimer fluorescence decays in order to minimize stray light from reaching the detector. The fit of the fluorescence decays was conducted by optimizing the parameters used in the different functions of interest with the Marquardt-Levenberg algorithm.[31] These functions were then convoluted with the IRF and their convolution product was compared with the experimental decays. A fluorescence decay fit was deemed satisfactory if the χ^2 was smaller than 1.3 and the residuals and autocorrelation of the residuals were randomly distributed around zero.

Individual analysis of the fluorescence decays: Equation 3.1 represents a sum of *n* exponentials, that was used to fit the monomer ($X = M$) and excimer ($X = E$) fluorescence decays individually.

$$[X^*]_{(t)} = [X^*]_{(t=0)} \sum_{i=1}^{n} a_{Xi} \times \exp(-t / \tau_{Xi}) \qquad (3.1)$$

The pre-exponential factors (a_{Xi}) and decay times (τ_{Xi}) used in Equation 1 were optimized according to the Marquardt-Levenberg algorithm.[29]

The excimer decays acquired with a longer time-per-channel were also fitted according to the micelle model described by Equation 3.2 with the program miscat2bg.[32,33]

$$[E^*]_{(t)} = \left([E0^*]_{(t=0)} e^{-t/\tau_{E0}} + [D^*]_{(t=0)} e^{-t/\tau_D} \right) \times \exp\left[- < n >_d \times (1 - \exp(-k_q t)) \right] \qquad (3.2)$$

Equation 3.2 uses the concentration of the short- and long-lived excimer species *E*0* and *D**, whose respective lifetimes τ_{E0} and τ_D were determined from the analysis of the excimer fluorescence decays. Fitting the excimer decays with Equation 3.2 yielded the parameters $<n>_d$ and k_q, which are the average number of DNT molecules bound to the PyO-3-12 micelles, which quench the pyrene excimer through diffusive encounters, and the rate constant for the quenching of an excimer by a quencher inside a micelle, respectively. The Marquardt-Levenberg algorithm was applied to optimize the parameters $[E0^*]_{(t=0)}$, $[D^*]_{(t=0)}$, $<n>_d$, and k_q in this analysis.[29] The excimer decays acquired with a time-per-channel of 1.02 ns/ch showed a very small (2 %) long-lived contribution (see entry without DNT in Table S3.7), which could have been some pyrene monomer leaking into the excimer decay. Since this long-lived component was not accounted for by Equation 3.2, the excimer decays were fitted with Equation 3.2 over the first 360 channels to cut out this weak long-lived contribution from the decay analysis.

Global model free analysis (MFA) of the fluorescence decays: The global MFA of the pyrene monomer and excimer fluorescence decays was introduced 15 years ago[34] and has been reviewed numerous times.[35,36] The MFA uses a sum of several exponentials to fit the monomer

decays. The decay time of one of the exponentials is fixed to that of the lifetime (τ_M) of the pyrene monomer to account for those pyrenyl labels, that do not form excimer. The other exponentials are expected to represent PEF and their decay times, although floating, take the same value in the excimer decay. The MFA of the fluorescence decays yields the average rate constant $<k>$ for PEF and the molar fractions f_{diff}, f_{free}, and f_{agg} of the pyrene species in solution referred to as Py_{diif}*, that form excimer by diffusive encounters, Py_{free}*, that are isolated, cannot form excimer, and emit with the lifetime τ_M, and Py_{agg}*, that are aggregated and form excimer instantaneously. The pre-exponential factors retrieved from the MFA of the fluorescence decays were combined to determine the molar fractions f_{diff}, f_{free}, and f_{agg} of the pyrenyl species Py_{diif}*, Py_{free}*, and Py_{agg}*, respectively, according to a methodology that is described in detail in the SI. The MFA of the fluorescence decays was conducted with Equations S3.1 and S3.2 given in Supporting Information (SI), whose parameters listed in Tables S3.2-S3.8 were also optimized with the Marquardt-Levenberg algorithm,[31] using the program sumegs12bg.

3.4. **Results and Discussion**

Since the fluorescence intensity is a relative quantity, any measurement based on the analysis of a fluorescence intensity, be it a Stern-Volmer plot, the efficiency of fluorescence resonance energy transfer, or fluorescence anisotropy, requires some sort of internal or external normalization.[37] In this context, dyes with emission bands in their fluorescence spectrum, whose fluorescence intensity ratio can be quantitatively related to the properties of the local environment experienced by the dye, are highly valuable, since the normalization is carried out internally with a single fluorescence spectrum. What makes pyrene stand out among all other dyes is that its fluorescence spectrum yields two fluorescence intensity ratios, namely the I_E/I_M and I_1/I_3 ratios, that provide different information about the local environment of pyrene. The fluorescence intensity ratio I_E/I_M of the pyrene excimer over the monomer is proportional to the product $k_{diff}\times[Py]_{loc}$, where k_{diff} is the rate constant for pyrene excimer formation (PEF) by

diffusive encounters between an excited and a ground-state pyrene and $[Py]_{loc}$ is the local concentration of ground-state pyrenes experienced by an excited pyrene. Consequently, the parameters k_{diff} and $[Py]_{loc}$ provide information about the internal dynamics and the local density, respectively, of an environment probed by a pyrene molecule. Similarly, the I_1/I_3 ratio provides information about the polarity of the environment experienced locally by an excited pyrene.[24,25]

While a low or high I_E/I_M ratio obtained earlier with the gemini surfactant Py-3-12 was quite useful to assess whether Py-3-12 was unassociated in water or aggregated in a micelle,[23] the I_1/I_3 ratio of Py-3-12 was not much sensitive to the polarity of its environment. The sensitivity of the I_1/I_3 ratio to solvent polarity is due to the fact that the fluorescence band used to calculate I_1 is very weak for pyrene in apolar solvents, but is significantly stronger in solvents of increasing polarity.[24,25] However, attaching a long alkyl chain to pyrene, such as the hexyl linker connecting the pyrenyl and ammonium groups of Py-3-12 in Figure 3.1A, breaks the symmetry and strongly attenuates the sensitivity of the I_1/I_3 ratio to solvent polarity.[24-26] Since replacing the carbon in an alkyl chain *beta*-to a given pyrene derivative with an oxygen restores this sensitivity,[26] PyO-3-12, whose chemical structure was shown in Figure 3.1B, was synthesized according to Scheme 3.1. Its fluorescence spectrum was acquired in different solvents. They are presented in Figure 3.2A and compared in Figure 3.2B to those obtained for Py-3-12 in the same solvents. Comparison of Figures 3.2A and B makes abundantly clear, that the fluorescence spectra of PyO-3-12 and Py-3-12 do and do not respond to solvent changes, as the fluorescence spectra shown in Figures 3.2A and B show substantial and insignificant changes with the solvent used to prepare the solutions of PyO-3-12 and Py-3-12, respectively. The fluorescence spectra of PyO-3-12 and Py-3-12 shown in Figure 3.2A and B, respectively, focused on the front part of the spectra to highlight differences in the I_1/I_3 ratios. The entire

fluorescence spectra of PyO-3-12 and Py-3-12, where residual excimer formation was observed in some of the organic solvents, can be viewed in Figure S3.4A and B in SI, respectively.

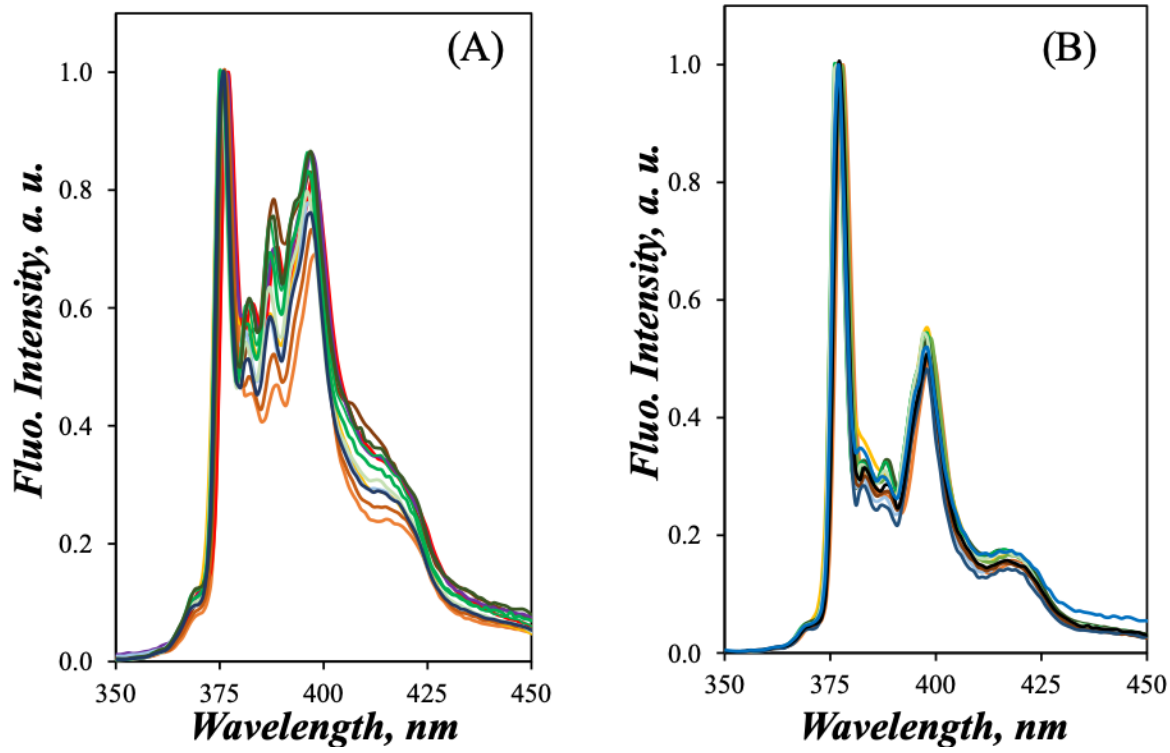

Figure 3.2 Steady-state fluorescence spectra of (A) PyO-3-12 and (B) Py-3-12 in 14 solvents: ( ) 1,4-dioxane, ( ) toluene, ( ) ethyl acetate, ( ) tetrahydrofuran, ( ) dichloromethane, ( ) 1-hexanol, ( ) 2-propanol, ( ) acetone, ( ) ethanol, ( ) methanol, ( ) acetonitrile, ( ) N,N-dimethylformamide, ( ) dimethylsulfoxide, ( ) water). [Py] = 2.5×10^{-6} M; spectra were normalized to 1.0 at the first peak at ~ 377 nm corresponding to the 0-0 transition.

These changes in fluorescence spectra can be better visualized by determining the I_1/I_3 ratio of PyO-3-12 and Py-3-12. Figure 3.3 shows the I_1/I_3 ratio of molecular pyrene obtained from reference #25 plotted as a function of the I_1/I_3 ratio of PyO-3-12 and Py-3-12. The I_1/I_3 ratio of PyO-3-12 are scattered around the 1:1 diagonal marked as a solid line in Figure 3 and show a strong correlation with the I_1/I_3 ratio of pyrene, which is itself strongly correlated with solvent polarity,[24,25] confirming that the I_1/I_3 ratio of PyO-3-12 must also be strongly correlated

to solvent polarity. In contrast, the I_1/I_3 ratios of Py-3-12 are much further away from the 1:1 diagonal indicating a much weaker correlation to solvent polarity, as suggested by the lack of change in the fluorescence spectra shown in Figure 3.2B for Py-3-12. Indeed, I_1/I_3 ranged from 1.3 in apolar dioxane to 2.1 in polar DMSO corresponding to a 68% increase, whereas I_1/I_3 increased from 3.1 in 2-propanol to 4.0 in acetone corresponding to a substantially lower 29 % increase. Figures 3.2 and 3.3 demonstrate the superiority of PyO-3-12 as a fluorescent probe to investigate the polarity of the local environment probed by an excited pyrene, which confirms the importance of adding a heteroatom in the β–position to pyrene. The I_1/I_3 ratios of PyO-3-12 and Py-3-12 in different solvents have been listed in Table S3.1 in SI.

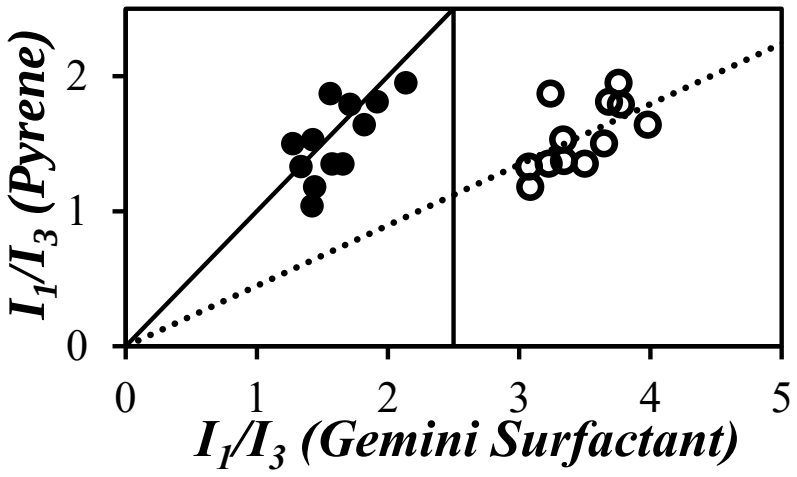

Figure 3.3 Comparison of the I_1/I_3 ratio of molecular pyrene reported by Dong and Winnik[25] as a function of the I_1/I_3 ratio of (●) PyO-3-12 and (ʘ) Py-3-12.

The difference between the ability of PyO-3-12 and Py-3-12 at probing the polarity of their local environment was further illustrated in Figure 3.4 where the fluorescence spectra of 2.5×10^{-6} M PyO-3-12 and Py-3-12 was compared in water and in an aqueous solution of 200 mM sodium dodecyl sulfate (SDS). Since the CMC of SDS in water equals 8 mM,[38,39] a concentration of 200 mM SDS ensured the formation of numerous negatively charged SDS micelles, that would promote the association of the positively charged pyrene-labeled gemini surfactants, which would allow the study of their fluorescence in the apolar interior of the SDS

micelles. The fluorescence spectra were normalized by dividing the fluorescence intensity at each wavelength by the integral of the spectra. This representation led to the conclusion that the probability of emitting a photon at 376 nm, where the fluorescence decays of the pyrene monomer were acquired, was similar whether PyO-3-12 was in water or in a less polar environment such as the interior of SDS micelles. Comparison of the fluorescence spectra also indicated that the I_1/I_3 ratios of PyO-3-12 in water and 200 mM SDS are clearly different, yielding values of 1.73 and 1.45, respectively, corresponding to a 19% decrease. The lower I_1/I_3 ratio of 1.73 for PyO-3-12 than that of 1.87 reported for molecular pyrene in water[25] was attributed to the dodecyl alkyl tail of PyO-3-12, which generates a more hydrophobic environment for the pyrenyl moiety. The I_1/I_3 ratio of 1.45 for PyO-3-12 in 200 mM SDS micelles was larger than that of 1.03 (±0.04) for molecular pyrene in SDS micelles,[24,40] suggesting that the pyrenyl moiety of PyO-3-12 might reside closer to the interface between the SDS micellar core and water, and thus experience a more polar environment, than molecular pyrene. In contrast, the fluorescence spectra of Py-3-12 in water and in 200 mM SDS were almost superimposable in Figure 3.4B, yielding I_1/I_3 ratios equal to 3.37 and 3.15, respectively, corresponding to a 7% decrease. The more than twice lower decrease in I_1/I_3 going from water to 200 mM SDS observed for Py-3-12 compared to PyO-3-12 agreed with the poorer sensitivity of Py-3-12 to the polarity of its environment already illustrated in Figure 3.3.

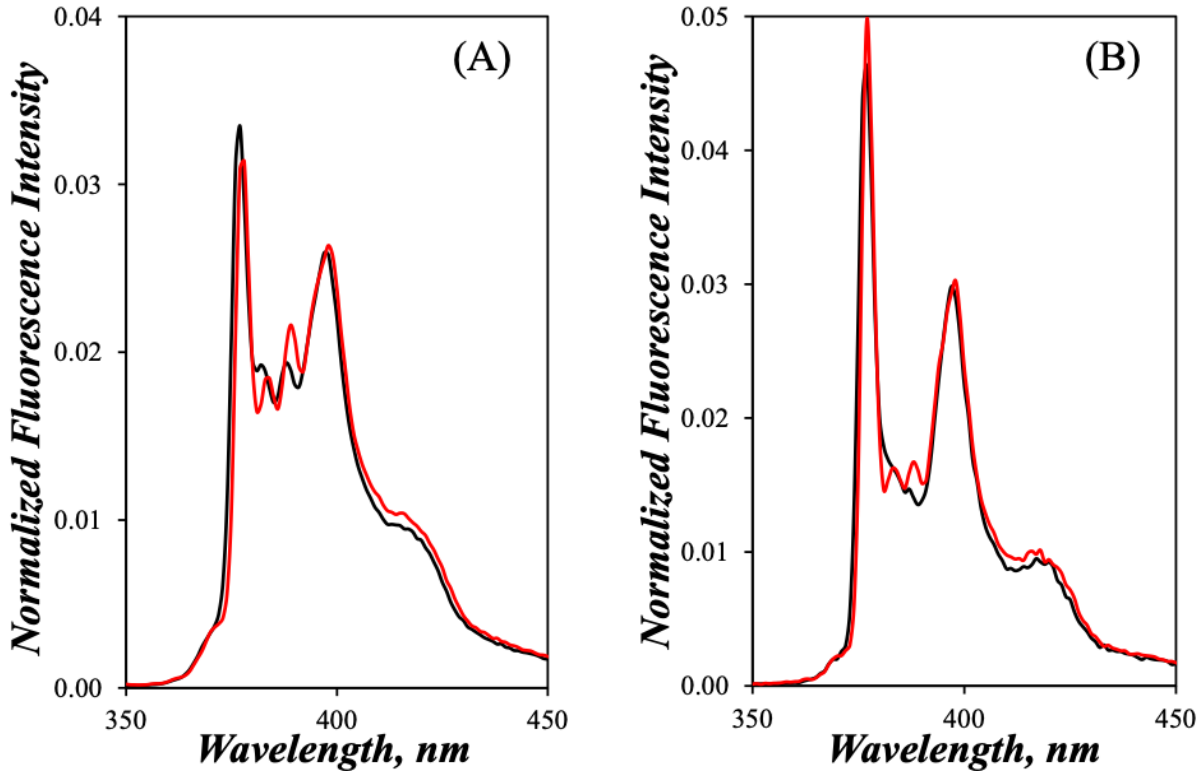

Figure 3.4 Fluorescence spectra of A) PyO-3-12 and B) Py-3-12 in (———) water and (———) 200 mM SDS aqueous solution. Spectra were normalized by their integral. λ_{ex} = 346 nm.

After having demonstrated the sensitivity of PyO-3-12 to solvent polarity, its properties as a possible gemini surfactant were investigated starting with its critical micelle concentration (CMC) by applying the procedure, that was described earlier for Py-3-12.[23] First, the surface tension of aqueous solutions of PyO-3-12 was measured and plotted as a function PyO-3-12 concentration in Figure 3.5. The surface tension-*vs*-[PyO-3-12] profile shown in Figure 3.5 is that expected for an ionic surfactant in aqueous solution, as the surface tension dropped from 72 mN/m in water to a plateau of 45.6 (±0.5) mN/m for PyO-3-12 concentrations above 0.43 (± 0.04) mM. The concentration of 0.43 mM represents the CMC of PyO-3-12. The CMC of PyO-3-12 is higher than the CMC of 0.15 mM found for Py-3-12.[23] The oxygen atom in the alkyl chain linking pyrene to the ammonium cation seems to make PyO-3-12 more hydrophilic, so that a higher PyO-3-12 concentration was required to induce micellization.

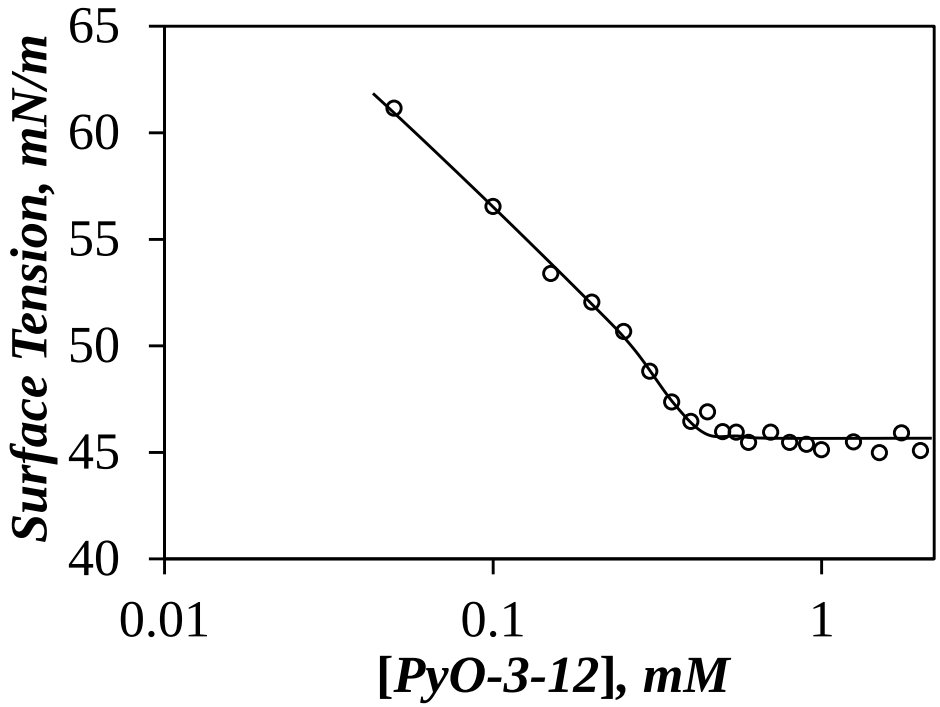

Figure 3.5 Plot of surface tension as a function of PyO-3-12 concentration.

Figure 3.6A represents the fluorescence spectra of aqueous solutions of the PyO-3-12 sample as a function of its concentration. The fluorescence spectra have the spectral features expected from an excimer-forming pyrene derivative. The fluorescence of the pyrene monomer yields sharp bands between 370 and 410 nm, while the broad structureless emission centered at 480 nm is typical of the pyrene excimer. The fluorescence experiments were carried out using the front-face geometry to account for the high PyO-3-12 concentrations, which led to residual scattering in the fluorescence spectra at shorter wavelengths. The most dilute 0.05 mM PyO-3-12 solution exhibited no excimer fluorescence, owing to the surfactant molecules being too distant in the solution to interact diffusively. An increase in the concentration of PyO-3-12 below the CMC resulted in an increase in diffusive encounters between PyO-3-12 molecules, leading to an increase in PEF in Figure 3.6A. Above the CMC, PEF increased more readily as the addition of PyO-3-12 resulted in the formation of micelles, where the high $[Py]_{loc}$ resulted in much more efficient PEF.

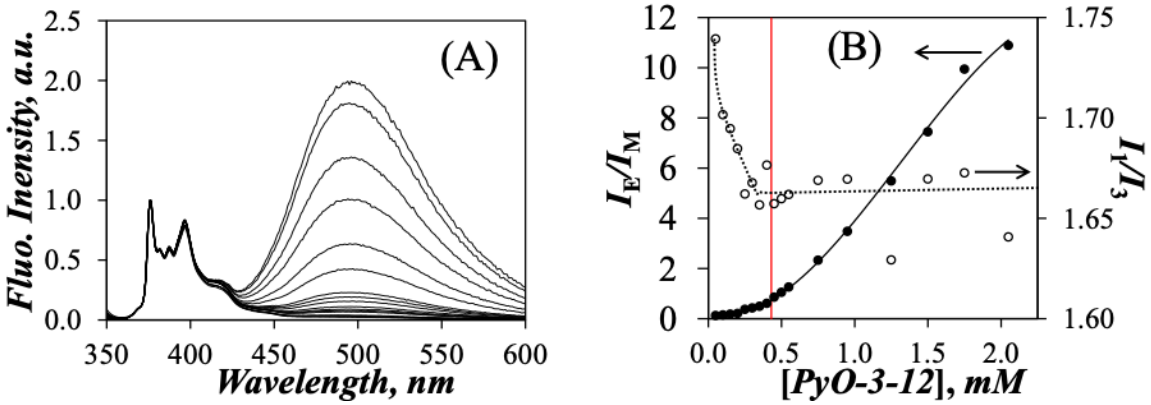

Figure 3.6 A) Fluorescence spectra acquired with PyO-3-12 concentrations ranging from 0.05 to 2.05 mM. B) Plot of (●) I_E/I_M and (ʘ) I_1/I_3 as a function of PyO-3-12 concentration. The red vertical line denotes the CMC of PyO-3-12 determined by surface tension.

The effect of the PyO-3-12 concentration on PEF was better represented in Figure 3.6B, where the I_E/I_M ratio was plotted as a function of PyO-3-12 concentration. As the concentration of PyO-3-12 rose above 0.43 mM, which corresponds to the CMC of PyO-3-12 determined by surface tension measurements in Figure 3.5, I_E/I_M began to increase more rapidly as PEF occurred efficiently inside the PyO-3-12 micelles, that were generated above the CMC. However, the smooth increase in I_E/I_M with increasing concentration observed around a PyO-3-12 concentration of 0.43 (±0.04) mM made it difficult to use the I_E/I_M-*vs*-[PyO-3-12] trend to find the CMC. The I_1/I_3 ratio was also plotted as a function of PyO-3-12 concentration in Figure 3.6B. Contrary to the I_E/I_M ratio, I_1/I_3 showed a clear break point in Figure 3.6B despite the fact, that it only ranged from 1.74 at 0.05 mM PyO-3-12 to 1.67 (±0.01) for PyO-3-12 concentrations greater than 0.28 (±0.08) mM, a 4 % decrease. While an I_1/I_3 ratio of 1.74 would be typical of a 1-pyrenemethoxy derivative in an aqueous environment, an I_1/I_3 ratio of 1.67 is not indicative of the hydrophobic environment expected from the interior of PyO-3-12 micelles. As it turns out, this high I_1/I_3 ratio for PyO-3-12 concentrations above its CMC is the result of an artefact. As the time-resolved fluorescence study will illustrate, PEF in the PyO-3-12 micelles is very efficient, which reduces the lifetime, and thus the quantum yield, of the

pyrene monomer in the micelles by more than 20-fold compared to unassociated PyO-3-12 surfactants in water. As a result, most of the fluorescence signal of the pyrene monomer comes from PyO-3-12 in water, resulting in the high I_1/I_3 ratio observed at PyO-3-12 concentrations larger than the CMC. Despite this weaker response to the polarity of its environment in water, the break point in Figure 3.5B corresponding to a PyO-3-12 concentration of 0.28 (±0.08) mM was taken as the CMC of PyO-3-12 as determined from its I_1/I_3 ratio. The lower CMC value of 0.28 mM in Figure 3.6B compared to 0.43 mM determined from surface tension measurements is certainly a consequence of the strong fluorescence of PyO-3-12 in water, which attenuates the magnitude of the change in the I_1/I_3 ratio upon PyO-3-12 micellization resulting in the narrower range of I_1/I_3 values between 1.74 and 1.67 in Figure 3.6B, making the CMC determination more difficult. Nevertheless, the CMC of 0.28 mM is reasonable when considering the range of CMC values, that are typically obtained by different techniques for a same surfactant.[41]

As had been established earlier with Py-3-12, the state of the PyO-3-12 surfactants, whether unassociated in water or aggregated inside a micelle at PyO-3-12 concentrations below or above the CMC, respectively, could be easily confirmed by conducting the model free analysis (MFA) of the pyrene monomer and excimer fluorescence decays acquired at different PyO-3-12 concentrations. Aqueous solutions with PyO-3-12 concentrations greater than 0.05 mM were prepared to ensure that adequate excimer was produced to acquire the fluorescence decays within a suitable experimental time. Good fits were obtained, resulting in χ^2, that were lower than 1.18 and residuals and autocorrelation of the residuals, that were randomly distributed around zero. Figures 3.7A and B illustrate the quality of the fits for the pyrene monomer and excimer decays, respectively. The parameters retrieved from the fits were listed in Tables S3.2-S3.4 in SI.

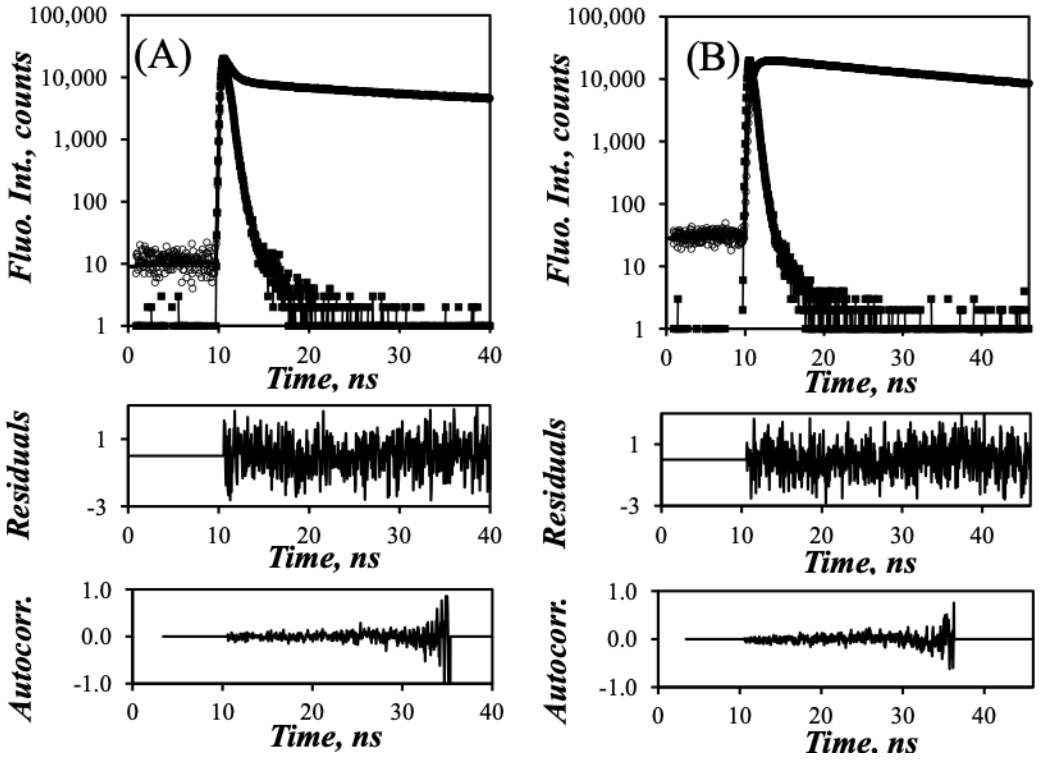

Figure 3.7 Fluorescence decays of the pyrene A) monomer (λ_{em} = 375 nm) and B) excimer (λ_{em} = 510 nm) for a 1.95 mM PyO-3-12 aqueous solution. λ_{ex} = 344 nm, χ^2 = 1.13.

After excitation, PyO-3-12 showed a rapid decrease in fluorescence in Figure 3.7A due to efficient PEF induced by the many ground-state pyrenes located in the micellar core. The longer part of the decay corresponded to long-lived PyO-3-12 molecules, that were unassociated in water. The fluorescence decays of the pyrene monomer were acquired with a long time-per-channel of 2.04 ns/ch to monitor the long lifetime of PyO-3-12 as a function of PyO-3-12 concentration. The long decay time was attributed to the pyrene monomer lifetime (τ_M) of PyO-3-12, which showed a small but linear decrease with increasing PyO-3-12 concentration according to Equation 3.3. The decrease in τ_M found in Equation 3.3 was attributed to some PEF occurring by diffusive encounters between unassociated PyO-3-12 molecules in water as the PyO-3-12 concentration was increased and residual quenching by the increasing bromide counterions (see Figure S3.4), as had been found earlier for Py-3-12.[23]

$$\tau_M = 144.6 - 10.64 \times [\text{PyO-3-12}] \quad (3.3)$$

The monomer and excimer decays of the PyO-3-12 aqueous solutions were collected with a short time-per-channel of 0.051 ns/ch to capture the fast PEF occurring inside the PyO-3-12 micelles and the MFA of the decays was conducted by fixing τ_M to its value determined with Equation 3.3 at each PyO-3-12 concentration. The fluorescence decay of the pyrene excimer in Figure 6B exhibited a fast rise time on the same time scale as the fast decay component observed in the monomer fluorescence decay in Figure 3.7A, followed by the long-lived fluorescence decays of the two pyrene excimer species *D** and *E*0* with lifetimes τ_D and τ_{EO} equal to 10 (±2) and 37 (±3) ns, respectively. Two excimer species are often observed, when PEF occurs in confined geometries, like that generated in the interior of PyO-3-12 micelles, where the conformational freedom of the pyrenyl labels is constrained.[22,29,32] The pyrene species *D** and *E*0* are attributed to pre-formed pyrene dimers, that are poorly and well stacked, respectively. The 10 ns lifetime found for the *D** species is shorter than 30 – 70 ns, which is the lifetime range typically expected for a pyrene excimer. The shorter lifetime suggested that some pyrenyl groups might be located closer to the micellar surface, where they would form the excimer *D**, that would be quenched effectively by the bromide counterions. This conclusion agrees with the larger than expected I_1/I_3 ratio of 1.45 found for PyO-3-12 associated with SDS micelles in Figure 3.4A, which suggested that the pyrenyl moiety of PyO-3-12 is located at the interface between the SDS hydrophobic interior and water.

The molar fractions f_{free}, f_{diff}, and f_{agg} of the various pyrene species were determined using the parameters from the MFA of the decays and are shown in Figure 3.8A according to the procedure outlined in SI. At low PyO-3-12 concentrations, where little excimer is produced, the majority of PyO-3-12 molecules were unassociated with f_{free} approaching 0.61 (±0.03), while f_{diff} and f_{agg} were small at ~ 0.14 (±0.01) and ~ 0.26 (±0.04), respectively, indicating residual PEF occurring in water probably due to a small fraction of PyO-3-12 pre-aggregates.

As the PyO-3-12 concentration rose above the CMC of 0.43 mM determined by surface tension measurements in Figure 3.4, f_{free} decreased and f_{diff} and f_{agg} increased rapidly with increasing PyO-3-12 concentration. This behavior is the one expected of a surfactant undergoing micellization at the CMC. Contrary to the Py-3-12 micelles, where PEF occurred principally by diffusive encounters of the pyrenyl groups and little aggregation was observed with the ratio $f_{agg}/(f_{diff}+f_{agg})$ equal to 0.29 (±0.08) for Py-3-12 concentrations above the CMC, the same ratio was twice larger and equaled 0.60 (±0.05) for PyO-3-12 concentrations above the CMC of 0.43 mM. This substantial enhancement in pyrene aggregation inside PyO-3-12 micelles was attributed to the ether linkage in the pyrene linker, which must help promote the location of the pyrenyl labels at the micelle/water interface, resulting in increased concentration and leading to enhanced pyrene aggregation. It might be these pyrene aggregates, that emitted with a shorter lifetime τ_D of ~10 ns due to their greater solvent exposure.

The average rate constant $<k>$ for PEF was plotted as a function of PyO-3-12 concentration in Figure 3.8B. Whereas the I_E/I_M ratio discussed in Figure 3.5B is proportional to the product $k_{diff}\times[Py]_{loc}$, $<k>$ is actually equal to this product. In Figure 3.8B, $<k>$ was found to increase with increasing PyO-3-12 concentration, showing a first break point around the CMC of PyO-3-12 at 0.43 mM, before plateauing at a value of 0.18 (±0.01)$\times10^9$ s^{-1} for PyO-3-12 concentrations larger than 1.5 mM. In homogeneous solutions of pyrene or of a pyrene derivative, $<k>$ increases linearly with increasing pyrene concentration, as reported previously for ethyl 4-(1-pyrene)butyrate.[42] The change in regime around the CMC from $<k>$ increasing with increasing PyO-3-12 concentration to $<k>$ being constant with PyO-3-12 concentration in Figure 3.7B reflects a change in the $[Py]_{loc}$ experienced by an excited pyrene. At low PyO-3-12 concentration, the solution is homogeneous and $[Py]_{loc}$ equals the overall PyO-3-12 concentration. But as PEF transitions from diffusive encounters between pyrenyl labels homogeneously distributed in aqueous solution to pyrenyl labels concentrated in the interior of

PyO-3-12 micelles, $[Py]_{loc}$ plateaus and so does $\langle k \rangle$ in Figure 3.8B at high PyO-3-12 concentration. For PyO-3-12 concentrations larger than 1.5 mM, $[Py]_{loc}$ simply represents the concentration of pyrenyl labels inside the PyO-3-12 micelles, which does not change with PyO-3-12 concentration. This observation is also another evidence, that PyO-3-12 forms micelles, with a micellar interior generating a constant $[Py]_{loc}$.

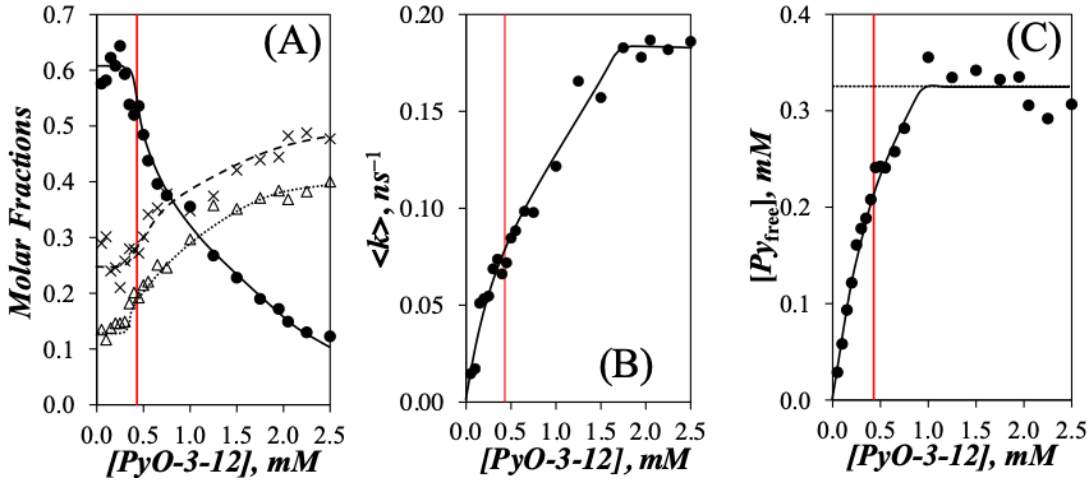

Figure 3.8 Plots of A) the molar fractions (▲) f_{diff}, (●) f_{free}, and (×) f_{agg}, B) $\langle k \rangle$, and C) $[Py]_{free}$ as a function of PyO-3-12 concentration. The lines are drawn to guide the eye. The vertical red line indicates the CMC of 0.43 mM for PyO-3-12 determined by surface tension.

Finally, the concentration of unassociated pyrene ($[Py_{free}]$) in aqueous PyO-3-12 solutions was calculated from the product $f_{free} \times$[PyO-3-12]. In Figure 3.8C, $[Py_{free}]$ is plotted as a function of PyO-3-12 concentration. At low surfactant concentrations, $[Py_{free}]$ increases linearly with increasing PyO-3-12 concentration until plateauing at a $[Py_{free}]$ value of 0.33 (±0.02) mM for PyO-3-12 concentrations larger than 1.0 mM. The constancy of $[Py]_{free}$ in solution at high PyO-3-12 concentration is the behavior expected from a surfactant above its CMC, which in the case of PyO-3-12 would equal the value of $[Py]_{free}$ in the plateau region. The CMC of 0.33 (±0.02) mM obtained from fluorescence measurements was in relatively good agreement with the CMC value of 0.43 (±0.04) mM obtained from surface tension measurements, suggesting a CMC of 0.38 (±0.05) taken as the average of both values.

After establishing that PyO-3-12 behaved as a surfactant and formed micelles above its CMC, fluorescence quenching experiments were conducted with 2,6-dinitrotoluene (DNT) to determine the aggregation number (N_{agg}) of the PyO-3-12 micelles. It must be pointed out at this juncture that the N_{agg} experiments required the preparation of a new batch of PyO-3-12. While most properties observed for PyO-3-12 were similar for both batches of PyO-3-12, the long decay time of the PyO-3-12 monomer did not decrease as quickly as predicted with Equation 3 in water, so that τ_M was measured at the different PyO-3-12 concentrations used in the second part of this study instead of using Equation 3.3.

N_{agg} for PyO-3-12 was determined according to the same methodology, that was recently applied to determine N_{agg} for Py-3-12 in Chapter 2.[23] The methodology is based on Equation 3.4,[38] where $<n>$ is the average number of quenchers per micelle, $[Q]_b$ is the concentration of quencher bound to the PyO-3-12 micelles, and $[S]$ is the PyO-3-12 concentration. In these experiments, DNT was selected as a quencher, since it was found to be an efficient quencher of the pyrene excimer.[43] Furthermore, the low solubility of 204 mg/L or 1.1 mM for DNT in water was expected to promote the incorporation of DNT from the aqueous phase into the hydrophobic interior of the PyO-3-12 micelles, where it would be able to quench the pyrene excimer fluorescence.[30] Nevertheless, the DNT molecules partitioned themselves between the aqueous phase and the PyO-3-12 micelles. This required that the concentration of DNT in water ($[Q]_w$) be measured in order to determine $[Q]_b$ (= $[Q]_o - [Q]_w$, where $[Q]_o$ is the total quencher concentration) and find N_{agg} with Equation 3.4. $[Q]_w$ was determined by taking advantage of the long lifetime of unassociated PyO-3-12 in water, whose reduction due to the quenching by DNT in water was directly related to the bimolecular quenching rate constant (k_{qM}) of the pyrene monomer in water and the concentration of DNT in water according to the Stern-Volmer relationship given in Equation 3.5.

$$< n >= N_{agg} \times \frac{[Q]_b}{[S] - CMC} \tag{3.4}$$

$$\frac{\tau_{M0}}{\tau_M} = 1 + k_{qM} \tau_{M0} [Q]_w \tag{3.5}$$

In Equation 3.5, τ_{M0} and τ_M are the lifetime of PyO-3-12 in water without and with DNT, respectively. To determine k_{qM}, the steady-state and time-resolved fluorescence measurements were conducted on a dilute aqueous solution of 9.5×10^{-6} M PyO-3-12, where PyO-3-12 did not form micelles.

The fluorescence spectra of the 9.5×10^{-6} M PyO-3-12 solution without excimer fluorescence are shown in Figure 3.9A, which illustrates the efficient quenching of the PyO-3-12 fluorescence with increasing DNT concentration. Nevertheless, the decrease in fluorescence in Figure 3.9A was overestimated due to the inherent absorption of DNT, that reached 0.43 at the highest DNT concentration in water. This absorbance was 10-times larger than the 0.05 absorbance required to avoid the inner filter effect, which artificially decreases the fluorescence intensity.[35] Fortunately, the fluorescence decays of the 9.5×10^{-6} M PyO-3-12 aqueous solution shown in Figure 3.9B were not affected by the inner filter effect. They were fitted with a biexponential function, where the second decay time was recovered with over 90% of the pre-exponential weight and was attributed to the lifetime (τ_M) of PyO-3-12 monomer in water. As more DNT was added to the solution, PyO-3-12 exhibited a shorter decay reflecting its quenching by DNT. A Stern-Volmer plot is shown in Figure 3.9C, where the ratio τ_{M0}/τ_M is represented as a function of DNT concentration. A linear trend was obtained in agreement with Equation 3.5 with a slope equal to 853 M^{-1}. Since the slope equals the product $k_{qM}\times\tau_{M0}$, the bimolecular quenching rate constant k_{qM} was found to equal 5.8×10^9 $M^{-1}s^{-1}$, using the τ_{M0} value determined experimentally to equal 147 ns. The k_{qM} value obtained for PyO-3-12 was

very close to that of 6.0×10^9 $M^{-1}\cdot s^{-1}$, which had been determined for Py-3-12.[23] This result indicated that DNT quenched both surfactants in a similar manner at a surfactant concentration lower than the CMC.

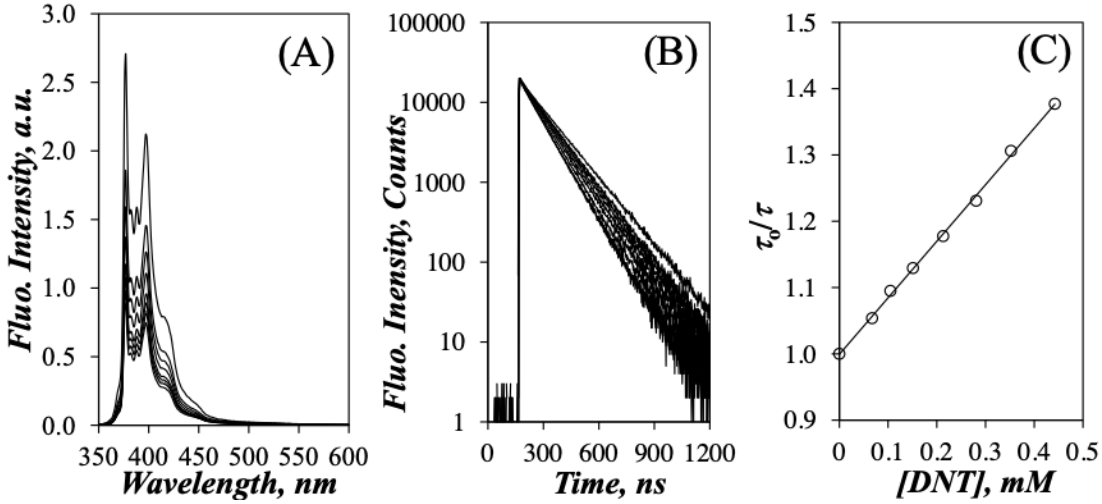

Figure 3.9 A) Fluorescence spectra and B) fluorescence decays of the pyrene monomer of a 9.5×10^{-6} M PyO-3-12 aqueous solution upon addition of DNT. From top to bottom: [DNT] = 0, 0.07, 0.10, 0.15, 0.21, 0.28, 0.35, and 0.44 mM. C) Stern-Volmer plot obtained from the decay times retrieved from the biexponential analysis of the decays in Figure 3.8B.

The fluorescence quenching experiments were then performed with a concentration of PyO-3-12 of 2.3 mM, which was significantly higher than the CMC of 0.38 mM. At this PyO-3-12 concentration, the pyrenyl labels had an absorbance of 65, far above the maximum absorbance of 1.8, corresponding to the highest DNT concentration used in these quenching studies. Consequently, the change in DNT concentration was not expected to affect the fluorescence emitted by the PyO-3-12 solution. The fluorescence spectra of the 2.3 mM PyO-3-12 solution revealed that, when the DNT concentration increased from 0 to 1.88 mM, the fluorescence of the pyrene monomer and excimer decreased by 3.5 and 20 folds, respectively, confirming that DNT was targeting the PyO-3-12 micelles.

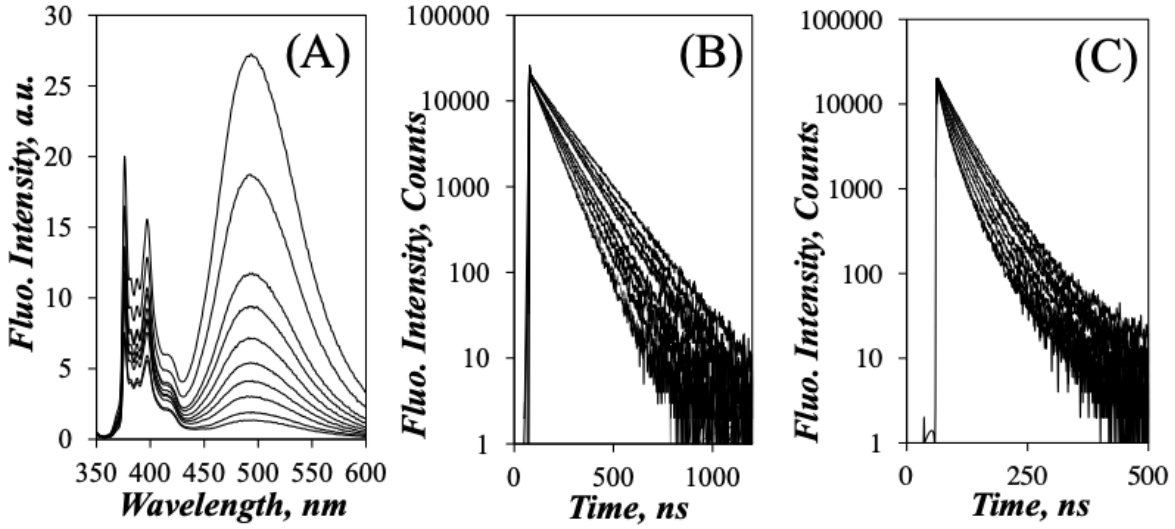

Figure 3.10 A) Steady-state fluorescence spectra and fluorescence decays of the pyrene B) monomer and C) excimer for an aqueous solution of 2.3 mM PyO-3-12 with different DNT concentrations. From top to bottom: [DNT] = 0.0, 0.18, 0.41, 0.55, 0.70, 0.87, 1.07, 1.29, 1.58, and 1.88 mM.

The monomer decays shown in Figure 3.10B were acquired with a 2.04 ns/ch time-per-channel (TPC). The spike at the early time reflects rapid PEF inside the PyO-3-12 micelles. It was observed to take place over ~4 ns in Figure 3.7A for the fluorescence decays of the pyrene monomer acquired with a much shorter time-per-channel of 0.051 ns/ch, representing two channels in Figure 3.10B. In comparison, the contribution of this spike appeared smaller in the case of PyO-3-12 than for Py-3-12.[23] This observation was a consequence of the higher CMC of PyO-3-12, with the contribution of unassociated PyO-3-12 surfactants being more important at a surfactant concentration of 2.3 mM for PyO-3-12 than 2.2 mM for Py-3-12, which had a lower CMC of 0.15 mM.

The unassociated PyO-3-12 surfactants in the aqueous phase were represented by the long component in the monomer fluorescence decays shown in Figure 3.10B. The shortening of the long-lived contribution to the monomer decays upon increasing the DNT concentration was a clear indication, that the unassociated PyO-3-12 molecules in water were quenched by

DNT molecules dissolved in water. This implied that the decay time (τ_M) corresponding to the long-lived PyO-3-12 species in Figure 3.10B could be employed to determine the concentration of DNT in water using Equation 3.5, since k_{qM} and τ_{M0} were known. The long-lived component of the decays could be fitted with a biexponential function, where the contribution of the longest decay time shown in Table S3.6 in SI represented more than 90% of the pre-exponential weight and was attributed to τ_M. Equation 3.5 was re-arranged into Equation 3.6 to yield $[Q]_w$, where $[Q]_{wo}$ represents the DNT concentration equal to 57 (±3)×10^{-6} M, that would be needed to reduce the lifetime of pyrene from 147 ns for a 9.5×10^{-6} M PyO-3-12 aqueous solution to 140 ns for a 2.3×10^{-3} M PyO-3-12 concentration.

The equilibrium representing the partitioning of DNT between the aqueous phase and the PyO-3-12 micelles is described in Equation 3.7 and yields Equation 3.8, which predicts that plotting $[Q]_b$ (= $[Q]_o - [Q]_w$, where $[Q]_o$ is the total DNT concentration in solution) as a function of $[Q]_w$ should yield a straight line passing through the origin. Figure 3.11A shows that a plot of $[Q]_b$-*vs*-$[Q]_w$ yielded a straight line with a *slope* of 0.38 (±0.01), similar in magnitude to that of 0.48 (±0.01), which had been found earlier for Py-3-12.[23] The *slope* is also equal to the product $K\times[Mic]$, where K is the equilibrium constant and $[Mic]$ is the PyO-3-12 micelle concentration given by ($[S]$-CMC])/N_{agg}. As shown in Equation 3.9, knowing N_{agg} would yield K, since the other parameters including the *slope* (=0.34), [PyO-3-12] (= 2.3 mM), and CMC (=0.38 mM) would all be known.

$$[Q]_w = \left(\frac{\tau_{M0}}{\tau_M} - 1\right) \times \frac{1}{k_{qM}\tau_{M0}} - [Q]_{wo} \tag{3.6}$$

$$Q_w + \text{Mic} \underset{}{\overset{K}{\rightleftharpoons}} Q_b \tag{3.7}$$

$$K = \frac{[Q]_b}{[Q]_w \times [Mic]} \tag{3.8}$$

$$slope = K \times ([S] - \mathrm{CMC})/N_{agg} \tag{3.9}$$

As discussed in Chapter 2,[23] the average number ($<n>$) of bound DNT molecules per PyO-3-12 micelle, required to find N_{agg} according to Equation 3.4, equaled the sum $<n>_d$ + $<n>_s$, where $<n>_d$ and $<n>_s$ represent the average number of bound DNT molecules that would quench the pyrene excimer in a dynamic and static manner, respectively. $<n>_d$ and $<n>_s$ were determined from the analysis of the fluorescence spectra and excimer fluorescence decays of PyO-3-12. The decays of the excimer for PyO-3-12 shown in Figure 3.10C did not exhibit a rise time due to rapid PEF, because the excimer fluorescence decays were acquired with a time-per-channel of 1.02 ns/ch, 20 times larger than that of 0.051 ns/ch used for the excimer decays shown in Figure 3.7B. The fluorescence decays of the excimer in Figure 3.10C were fitted using Equation 3.2 to obtain $<n>_d$. In Figure 3.11B, $<n>_d$ was plotted as a function of $[Q]_b$, which had been determined at all DNT concentrations in Figure 3.11A. $<n>_d$ increased linearly with increasing $[Q]_b$ at low concentration, as predicted by the well-established Equation 3.4,[38] but showed a downward trend at higher concentration, where a higher loading of DNT might be distorting the PyO-3-12 micelles.

Analysis of the excimer fluorescence decays with Equation 3.2 yielded the molar fractions f_D and f_{E0} of the short- (D*) and longer-lived (E0*) excimer species, respectively, which were plotted as a function of $[Q]_b$ in Figure 3.11C. Within experimental error, the molar fractions f_D and f_{E0} remained constant with DNT concentration, taking an average value of 0.12 (±0.05) and 0.88 (±0.05), respectively. Dynamic quenching of the pyrene excimer by DNT occurred with a rate constant k_q, that remained constant and equal to 1.6 (±0.1) $\times 10^7$ s^{-1} over most of the range of DNT concentrations in Figure 3.11C, before increasing to 20 μs^{-1} for the

largest DNT concentration. The increase in k_q at high DNT concentration might have been a result of the distortion of the PyO-3-12 micelles at this high loading regime.

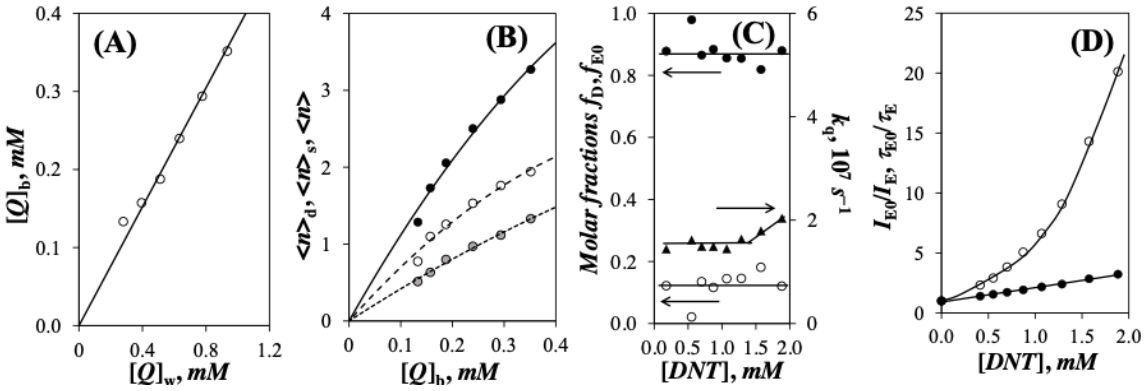

Figure 3.11 Plots of A) $[Q]_b$ as a function of $[Q]_w$, B) (O) $\langle n \rangle_d$, (●) $\langle n \rangle_s$, and (●) $\langle n \rangle$ (= $\langle n \rangle_d + \langle n \rangle_s$), C) (O) f_{E0}, (●) f_D, and (▲) k_q as a function of $[Q]_b$, and D) (O) I_{E0}/I_E and (●) τ_{E0}/τ_E as a function of the overall DNT concentration.

It might seem surprising at first glance, that the PyO-3-12 micelles could be distorted at such a low loading of DNT molecules, since $\langle n \rangle_d$ remained smaller than 2 in Figure 3.11B over the entire DNT concentration range. Due to the finite size of surfactant micelles, it is often difficult to add too many quenchers inside a micelle, above all for small micelles, but an average number of 2 quenchers per micelle is usually considered reasonable. The issue is that $\langle n \rangle_d$ represents the DNT molecules, that quench the pyrene excimer by diffusive encounters. As was observed for Py-3-12, DNT molecules form ground-state complexes with a substantial number of pyrene dimers, which leads to static quenching, which is not probed by the excimer fluorescence decays, which only reflect dynamic quenching. The existence of static quenching is demonstrated in Figure 3.11D, where the ratio of the excimer fluorescence intensities without and with DNT (I_{E0}/I_E) and the ratio of the number average lifetime of the excimer decays acquired without and with quencher ($\langle \tau_{E0} \rangle / \langle \tau_E \rangle$) were compared by plotting them against $[Q]_b$. The ratio $\langle \tau_{E0} \rangle / \langle \tau_E \rangle$ only increased 3.2 folds, when the total DNT concentration was increased from 0.0 to 1.88 mM, whereas the ratio I_{E0}/I_E increased 20 folds. The much stronger

quenching of the pyrene excimer observed in the fluorescence spectra compared to the fluorescence decays was a clear indication, that quenching of the excimer by DNT occurred in a static manner. Static quenching of the pyrene excimer could occur according to several pathways, by complexation of DNT with unassociated pyrenes inside the PyO-3-12 micelles, by complexation of DNT with pre-aggregated pyrene molecules, or by a combination of both pathways. Whichever the mechanism, static quenching resulted in the instantaneous elimination of a significant number of pyrenes forming excimer due to DNT molecules bound to the PyO-3-12 micelles but not taken into account by $<n>_d$. By viewing the PyO-3-12 micelles as spheres of action, where static quenching of the pyrene excimer occurred, Equation 3.10 was derived to calculate the number $<n>_s$ of DNT molecules, that would quench the pyrene excimer inside the PyO-3-12 micelles in a static manner.[35]

$$< n >_s = Ln\left(\frac{I_{E0} / I_E}{< \tau_{E0} > / < \tau_E >} \right) \qquad (3.10)$$

$<n>_s$ was plotted as a function of $[Q]_b$ in Figure 3.11B and it showed the same downward curvature, that had been observed for $<n>_d$. Although $<n>_s$ was smaller than 2 over the entire DNT concentration range, the sum $<n>$ ($=<n>_d + <n>_s$) plotted in Figure 3.11B was mostly larger than 2, reflecting a fairly large loading of DNT molecules in the PyO-3-12 micelles, which suggested, that the PyO-3-12 micelles might be distorted at higher DNT concentrations. Fitting the $<n>$-*vs*-$[Q]_b$ plot in Figure 3.11B with a second order polynomial yielded a good fit, whose tangent at the origin found to equal 11.9 (±0.7) was taken to represent the quantity N_{agg}/([*S*] – CMC) in Equation 3.4. Since [*S*] (= 2.3 mM) and CMC (= 0.38 mM) were known, N_{agg} was found to equal 23 (±2) units. An N_{agg} value of 23 is reasonable, when compared to other gemini surfactants.[44-47] The N_{agg} value for the PyO-3-12 micelles was larger than that of 14.0 (±0.2) found for the Py-3-12 micelles.[23] This larger N_{agg} value was attributed

to the oxygen atom of the 1-pyrenemethoxy label in PyO-3-12, which pulled the pyrene-labeled tail of PyO-3-12 toward the micellar surface as was found for the PyO-3-12 associated with SDS micelles in Figure 3.4A, thus increasing the volume of the hydrophobic part of PyO-3-12, which increased the packing parameter of PyO-3-12, and thus N_{agg}.[48]

The determination of N_{agg} opened the path to the calculation of the equilibrium constant *K* for the binding of DNT to the PyO-3-12 micelles with Equation 3.9. Since the slope of the straight line in Figure 3.11A equaled 0.34 (±0.01), *K* was determined to be 4.5 (±0.1)×10^3 M. The *K* value for PyO-3-12 was similar in magnitude to that of 2.9 (±0.1)×10^3 M found earlier for Py-3-12.[23] The fairly low *K* values found for both surfactants rationalize the large fraction of DNT molecules found in the aqueous phase (see Figure 3.11A), which was identified thanks to the ability of PyO-3-12 to probe the aqueous phase. Like Py-3-12, PyO-3-12 offers two channels of observation, one inside the PyO-3-12 micelles through the excimer fluorescence and another through the long-lived emission of the pyrene monomer obtained from the unassociated PyO-3-12 surfactants. But unlike Py-3-12, PyO-3-12 can also probe the polarity of its environment. While this effect was not as pronounced as expected to determine the CMC of PyO-3-12 in Figure 3.6B due to the presence of strongly emitting unassociated PyO-3-12 surfactants, it is bound to become most useful, when PyO-3-12 is employed to probe the interactions of other amphiphilic molecules with polynucleotides.

3.5. **Conclusion**

Pyrene-labeled surfactants like Py-3-12[21-23] are ideal fluorescent probes to study the interactions of amphiphilic molecules with oppositely charged macromolecules such as oligo- and polynucleotides. However, the lack of sensitivity of Py-3-12 to the polarity of its immediate environment limits its applicability for the study of complexes generated between surfactants and polynucleotides encountered in lipoplexes. To resolve the lack of sensitivity to the polarity of the environment, PyO-3-12 was prepared by replacing a methylene group by an oxygen

atom at the β–position in the alkyl chain connecting the pyrenyl group to the ammonium cation. Its ability to probe the polarity of its environment was demonstrated in Figures 3.2 and 3.3 and the behavior of PyO-3-12 was characterized in water. PyO-3-12 was found to behave like a typical gemini surfactant, exhibiting an N_{agg} value of 23 (±2) and a CMC equal to 0.38 (±0.05) mM by taking the average of 0.33 (±0.02) and 0.43 (±0.04) mM obtained by fluorescence and surface tension measurements, respectively. These values were reasonable when compared to published reports.[40-43] The increase in micellar size observed for PyO-3-12 compared to Py-3-12 with an N_{agg} of 14 (±0.2) was attributed to the oxygen in the alkyl chain connecting the pyrenyl group to the ammonium cation, which would induce the pyrenyl groups to locate close to the micellar surface. This process increased the volume of the hydrophobic part of PyO-3-12, which increased its packing parameter, resulting in an increase in N_{agg}.

This study was enabled by taking advantage of the unique spectral features of the dye pyrene. The excimer fluorescence in the fluorescence spectra and the short-lived pyrene species identified in the monomer and excimer fluorescence decays stemmed solely from the PyO-3-12 micelles and they were analyzed to characterize the state of the pyrenyl labels inside the micelles. In contrast, the long-lived pyrene species observed in the monomer fluorescence decays provided an observation channel into the aqueous phase. Combining the information obtained from both the micellar and aqueous phases resulted in a complete description of the PyO-3-12 surfactant in water. The methodology described in this study is general for pyrene-labeled surfactants and can now be applied to characterize more complex systems involving the interactions of amphiphilic molecules and oligo- or polynucleotides, that can be probed with Py-3-12 or PyO-3-12.

Chapter 4 Characterization of the Interactions between a Cationic Pyrene-Labeled Gemini Surfactant and the Anionic Surfactant Sodium Dodecyl Sulfate

4.1. **Abstract**

The gemini surfactant PyO-3-12, made of two dimethylammonium bromides joined by a propyl linker and bearing a dodecyl pendant on one side and a 1-pyrenemethoxyhexyl group on the other side, was employed to probe the interactions between positively charged PyO-3-12 and negatively charged sodium dodecyl sulfate (SDS). PyO-3-12 was selected for its ability to respond to the polarity of its local environment through the fluorescence intensity ratio I_1/I_3 of the first-to-third fluorescence peaks of the pyrene monomer and the local pyrene concentration $[Py]_{loc}$ through the I_E/I_M ratio of the pyrene excimer-to-pyrene monomer fluorescence intensity. Furthermore, analysis of the fluorescence decays of aqueous solutions of PyO-3-12 and SDS yielded a measure of the internal dynamics, local concentration, and state (associated-*versus*-unassociated) of PyO-3-12 in solution. By following these parameters for aqueous solutions prepared with a constant PyO-3-12 concentration of either 1, 4, or 16 μM and SDS concentrations ranging from 0 to 200 mM, six SDS concentration regimes were identified to describe the interactions between PyO-3-12 and SDS in pure water. Sharp transitions of the parameters describing the fluorescence of pyrene marked the boundaries between the different regimes. Perhaps the most important transition was the one defining the formation of the PyO-3-12/SDS aggregates, which was completed at the equicharge point, implying that they were constituted of 1 meq of PyO-3-12 and 2 meq of SDS. The low I_1/I_3 ratio obtained for the PyO-3-12/SDS aggregates suggested that they were multilamellar aggregates, that would shield the pyrenyl labels from polar water. The formation of these multilamellar aggregates was confirmed by transmission electron microscopy (TEM), which demonstrated the existence of multilamellar vesicles, whose presence increased with decreasing PyO-3-12 concentration. This study suggests that the combination of PEF and TEM provides an interesting experimental means to probe the assemblies generated from oppositely charged surfactants at surfactant concentrations, that are much lower than their CMC.

4.2. **Introduction**

The asymmetric gemini surfactant PyO-3-12, whose chemical structure is shown in Figure 1, was introduced in a recent publication as a fluorescent molecular marker with superior photophysical properties, that should allow the study of complex colloidal systems.[1] Some important molecular features in the design of PyO-3-12 included an oxygen atom in the position *beta* to the pyrenyl moiety, whose presence was required for pyrene to sense the polarity of its local environment,[1,2] and a dodecyl chain to help solvate the pyrenyl moieties, as they clustered inside the interior of a PyO-3-12 micelle to allow pyrene excimer formation (PEF) through diffusive encounters between an excited and a ground-state pyrene. PyO-3-12 exhibited the same behavior as any gemini surfactant, forming micelles above its 0.38 mM critical micelle concentration (CMC) with an aggregation number (N_{agg}) equal to 23.[1] What distinguishes PyO-3-12 from other fluorescent markers is that the combined analysis of its fluorescence spectra and decays provides an impressively broad range of information about the colloidal systems it interacts with. Indeed, its fluorescence yields quantitative information about the polarity of its local environment, its state as an unassociated or aggregated surfactant, and its local concentration given by the local pyrene concentration $[Py]_{loc}$.[1] Combined with the exquisite sensitivity afforded by fluorescence, these spectroscopic features suggested that PyO-3-12 should be an excellent fluorescent probe to study complex colloids.

As a first example of the investigative capabilities afforded by PyO-3-12, its behavior was monitored in the present report as it interacted with oppositely charged sodium dodecyl sulfate (SDS). Mixtures of oppositely charged surfactants are referred to as catanionic surfactant mixtures (CSM). CSM were established in 1989 as a simple means to generate multilamellar vesicles from cheaper surfactants compared to vesicles prepared from much more expensive lipids.[3] Since then, CSM have been the subject of sustained research, that has focused mostly on the study of singly charged surfactants,[4-14] although a few examples of

surfactant systems involving doubly charged gemini surfactants like PyO-3-12 have also been reported.[15-19] CSM have shown promises in the preparation of model membranes,[20] for drug delivery,[21] and as microreactors.[22] By and large, the vast majority of CSM are prepared by mixing concentrated solutions of oppositely charged surfactants to obtain a given surfactant composition before diluting the CSM to the desired total surfactant concentration. The high sensitivity of surface tension or conductimetry at low surfactant concentration is typically applied to measure the critical aggregation concentration (CAC) of the CSM, while the nature of the objects generated by the CSM, either vesicles, rods, or micelles, is determined through scattering and microscopy experiments at higher surfactant concentrations in the 0.1 – 5 wt% range.[3-19] This range of higher surfactant concentrations is usually above the CMC of the oppositely charged surfactants used to generate the aggregates, which prevents the study of the aggregates formed between unassociated surfactants. Yet the study of the interactions between unassociated oppositely charged surfactants could uncover some fundamental principles controlling the formation of the colloids generated from their association.

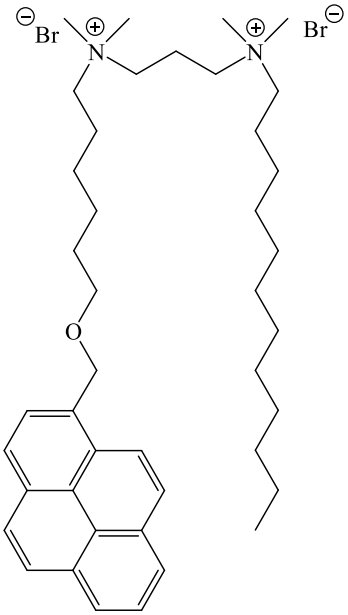

Figure 4.1 Chemical structure of PyO-3-12.

In contrast, the present study takes advantage of the outstanding sensitivity of fluorescence to probe the objects formed through the association of PyO-3-12 and SDS at total surfactant concentrations ranging from 8×10^{-5} to 5.8 wt%. In these fluorescence experiments, the PyO-3-12 concentration was maintained constant and equal to 1, 4, and 16 μM, which was, respectively, 380, 95, and 24 times lower than the CMC of 0.38 mM found for PyO-3-12,[1] while the SDS concentration was varied from 0.1 μM to 200 mM, where the lowest SDS concentration was 80,000 times lower than the CMC of 8 mM reported for SDS.[23,24] These concentration ranges allowed the study of surfactant aggregates generated in CSM prepared from stock solutions of fully unassociated PyO-3-12 and SDS. Since some of the surfactant concentrations used in these experiments were 2 – 3 orders of magnitude lower than the concentrations used for the scattering experiments typically employed to characterize the structure of colloids generated from CSM, structural information about the PyO-3-12/SDS aggregates needed to be extracted from the analysis of the fluorescence data obtained with PyO-3-12. Multilamellar PyO-3-12/SDS aggregates began to form at SDS concentrations lower than the equimolar point. The propensity of these multilamellar aggregates to form multilamellar vesicles increased with decreasing PyO-3-12 concentration. These aggregates formed with a 1:2 PyO-3-12:SDS molar ratio and their chemical composition did not change with PyO-3-12:SDS molar ratio suggesting that unassociated surfactants with opposite charges form neutral aggregates regardless of the concentration of the surfactants. These conclusions were reached through the analysis of various fluorescence parameters obtained with PyO-3-12 and the existence of multilamellar PyO-3-12/SDS aggregates and vesicles was confirmed by transmission electron microscopy (TEM). This study illustrates the remarkable photophysical capabilities of pyrene-labeled surfactants such as PyO-3-12 and how they can be employed in conjunction with TEM to probe complex colloidal systems at the molecular level.

4.3. **Experimental**

Chemicals: Sodium dodecyl sulfate (SDS), sodium chloride (NaCl), and pyrene were purchased from Sigma-Aldrich. SDS and NaCl were used as received, while pyrene was crystalized in ethanol. To this end, activated charcoal was added to the hot pyrene solution in ethanol before any crystals formed, the charcoal was filtered, and the hot pyrene solution in ethanol was left to cool to room temperature. Doubly distilled deionized water from Millipore Milli-RO 10 Plus and Milli-Q UF Plus (Bedford, MA) was used to prepare all aqueous solutions. The synthesis of PyO-3-12 has been described in detail in an earlier report.[22]

Preparation of PyO-3-12 and SDS solutions: To prepare solutions with different SDS concentrations while keeping the PyO-3-12 concentration constant, two solutions needed to be prepared. The first solution was made with double the desired PyO-3-12 concentration. The other solution was made with double the desired SDS concentration. Then equal amounts of both solutions were mixed together to obtain a solution of the PyO-3-12/SDS mixture with the desired concentration of PyO-3-12 and SDS. These solutions were left for at least one hour to reach equilibrium. Finally, these solutions were studied with different fluorescence techniques. One noteworthy observation was that application of heat or sonication, when preparing the PyO-3-12 solutions, led to an increase in excimer formation reflecting aggregation of the pyrenyl labels, that might be due to degradation of PyO-3-12. Consequently, all PyO-3-12 aqueous solutions were prepared without application of heat or sonication.

Steady-state fluorescence (SSF): SSF spectra were acquired with a Photon Technology International (PTI) spectrofluorometer equipped with an Ushio UXL-75Xe Xenon lamp and a PTI 814 photomultiplier detection system. The fluorescence spectra of all the solutions were acquired with the right-angle geometry. The samples were excited at 344 nm and their fluorescence intensity was scanned from 350 to 600 nm. The efficiency of pyrene excimer formation (PEF) was quantified from the fluorescence intensity ratio I_E/I_M, where I_E and I_M are

the fluorescence intensity of the pyrene excimer and monomer, respectively. I_M and I_E were calculated by taking the integral under the fluorescence spectrum from 372 to 378 nm and from 500 to 530 nm, respectively. The I_1/I_3 fluorescence intensity ratio was calculated by dividing the fluorescence intensity peak maxima at about 375 nm for I_1 and 386 nm for I_3. The I_1/I_3 ratio is indicative of the polarity of the local environment probed by pyrene.

Time-resolved fluorescence: The fluorescence decays of aqueous solutions of PyO-3-12 and SDS mixtures were acquired with a HORIBA FluoroHub equipped with a DeltaDiode at 336 nm. On the emission side, 370 and 470 nm cutoff filters were used to minimize scattering from the solutions being detected during the decay acquisition of the pyrene monomer and excimer, respectively. The fluorescence decays were obtained with a time-per-channel of 0.102 ns/ch to zoom in on the fast decay component representing PEF and the fluorescence signal was collected until the monomer and excimer decays reached 20,000 counts at their decay maximum. These decays were fitted according to the model free analysis (MFA). The instrument response function (IRF) was obtained in the same manner for both instruments by placing an aluminum reflective monolith in the sample holder and acquiring a decay with 20,000 counts at the decay maximum with the emission monochromator set at the same wavelength as the 344 nm excitation wavelength. The MFA was conducted by fitting the pyrene monomer and excimer fluorescence decays globally after convoluting the function of interest to the IRF. Optimization of the parameters employed in the different functions used to fit the fluorescence decays was carried out according to the Marquardt-Levenberg algorithm[25] by comparing the convolution products with the experimental decays.

The fluorescence decays of the pyrene monomer ($X = M$) and excimer ($X = E$) were fitted individually with sums of n exponentials, as seen in Equation 4.1.

$$[X^*]_{(t)} = [X^*]_{(t=0)} \sum_{i=1}^{n} a_{Xi} \times \exp(-t / \tau_{Xi}) \tag{4.1}$$

The a_{Xi} coefficients in Equation 1 are the pre-exponential factors corresponding to the exponential decay time τ_{Xi}.

Global model free analysis (MFA) of the fluorescence decays: The MFA was established 15 years ago[26] and has been reviewed many times since then.[27-29] The MFA involves the global fit of the fluorescence decays of the pyrene monomer and excimer. The monomer fluorescence decays are fitted with a sum of exponentials, where the decay time of one of the exponentials is fixed to the lifetime of the pyrene monomer (τ_M). The MFA has been shown to reliably retrieve the average rate constant $<k>$ for PEF and the molar fractions f_{diff}, f_{free}, and f_{agg} of the pyrene species in solution, that form excimer by diffusive encounters, cannot form excimer and emit with the natural lifetime (τ_M) of pyrene, and are aggregated and form excimer instantaneously, respectively. These parameters provide information about the dynamics and state of the pyrenyl moieties in solution. The procedure used to fit the fluorescence decays according to the MFA can be found in the Appendix A: Supporting Information (SI). The parameters were optimized according to the Marquardt-Levenberg algorithm.[27]

Transmission Electron Microscopy: Samples were adhered to Formvar coated copper grids and allowed to dry for 2 minutes. Excess liquid was blotted away before being stained with 1% (w/v) uranyl acetate. Grids were then observed using an FEI Tecnai G2 F20 transmission electron microscope operated at 200 kV and equipped with a bottom mount Gatan 4k CCD camera under standard operating conditions.

4.4. **Results**

The interactions between SDS and PyO-3-12 were monitored at PyO-3-12 concentrations of 1, 4, and 16 μM, which were, respectively, 380, 95, and 24 times lower than the 0.38 mM CMC of PyO-3-12.[1] This condition ensured that if PEF was observed, it could only arise from interactions between PyO-3-12 and SDS, since PyO-3-12 micelles, where PEF would otherwise occur between nearby PyO-3-12 molecules, could not form at these low PyO-3-12

concentrations. Compared to the fluorescence spectra resulting from the interactions between pyrene and SDS in Figure S1 in Supporting Information (SI), the interactions between PyO-3-12 and SDS appeared to be much more complex, as shown from the changes observed in the fluorescence spectra of 4 μM PyO-3-12 when the SDS concentration increased from 0 to 200 mM in Figure 4.2.

In pure water, 4 μM PyO-3-12 generates no excimer in Figure 2A and shows the typical spectral features of the pyrene monomer with sharp fluorescence peaks between 370 and 410 nm. As SDS is added to the PyO-3-12 solution, PEF occurs at the expense of the pyrene monomer, whose fluorescence intensity decreases. Since PyO-3-12 cannot form micelles, PEF results from the formation of PyO-3-12/SDS aggregates beginning at SDS concentrations as low as 0.1 μM, that brings PyO-3-12 molecules together thus promoting PEF. The pyrene monomer and excimer fluorescence continue to, respectively, decrease and increase with increasing SDS concentration in Figure 4.2A until a concentration of 7 μM is reached around the equicharge point of 8 μM between PyO-3-12 and SDS. The fluorescence spectra of PyO-3-12 remained unchanged for SDS concentrations ranging from 7 μM to 2 mM in Figure 4.2B, showing a prominent excimer fluorescence with little pyrene monomer fluorescence. In Figure 4.2B, PEF is most efficient over this SDS concentration range spanning close to 3 orders of magnitude. As the SDS concentration approaches the CMC of 8 mM, both monomer and excimer fluorescence intensities increase slightly between 2 and 10 mM SDS in Figure 4.2C. The formation of more SDS micelles above the CMC as more SDS is added to the solution results in a significant increase in the fluorescence intensity of the pyrene monomer shown in Figure 4.2D, while the fluorescence intensity of the pyrene excimer remains constant up to an SDS concentration of 50 mM. The excimer fluorescence intensity decreases when the SDS concentration reaches 60 mM, before reaching 0 for SDS concentrations of 100 and 200 mM. This behavior reflects the isolation of PyO-3-12 surfactants in the many SDS micelles

generated above the CMC of SDS, resulting in the progressive increase in pyrene monomer fluorescence in Figure 4.2D. The spectral features described in Figure 4.2 are summarized in Figures 4.3A and B, where the monomer (I_M) and excimer (I_E) fluorescence intensities and the I_E/I_M and I_1/I_3 ratios are plotted as a function of SDS concentration.

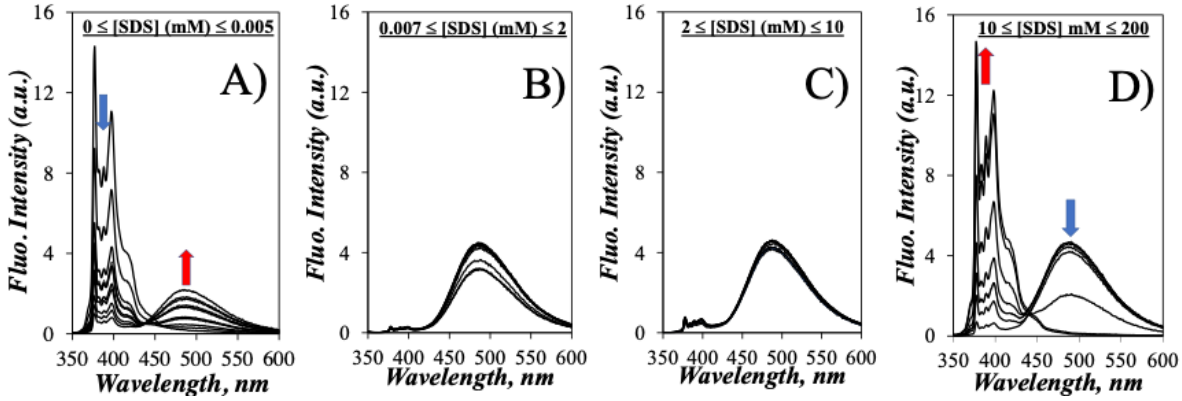

Figure 4.2 Fluorescence spectra of PyO-3-12 in water with SDS concentrations between A) 0 and 0.005 mM, B) 0.007 and 2 mM, C) 2 and 10 mM, and D) 10 and 200 mM. [PyO-3-12] = 4 μM; λ_{ex} = 344 nm.

The fluorescence intensities I_E and I_M are shown in Figure 4.3A. For increasing SDS concentration below the equicharge point at 8 μM, I_M and I_E continuously decrease and increase, respectively. For SDS concentrations above the equicharge point and below 2 mM, both I_M and I_E remain constant with SDS concentration. Around the CMC of SDS at 8 mM, both I_M and I_E show a small increase, but whereas I_M shows a continuous increase with increasing SDS concentration above the CMC, I_E remains constant for SDS concentrations larger than the CMC, suggesting that PyO-3-12/SDS aggregates retain the same composition, as SDS micelles form. It is only when the SDS concentration reaches 60 mM that I_E begins to decrease to 0 for SDS concentration equal to or larger than 100 mM. At this point, all PyO-3-12/SDS aggregates, that contained enough PyO-3-12 to form excimer, have dissociated and the PyO-3-12 molecules are isolated in SDS micelles, where they emit as pyrene monomer.

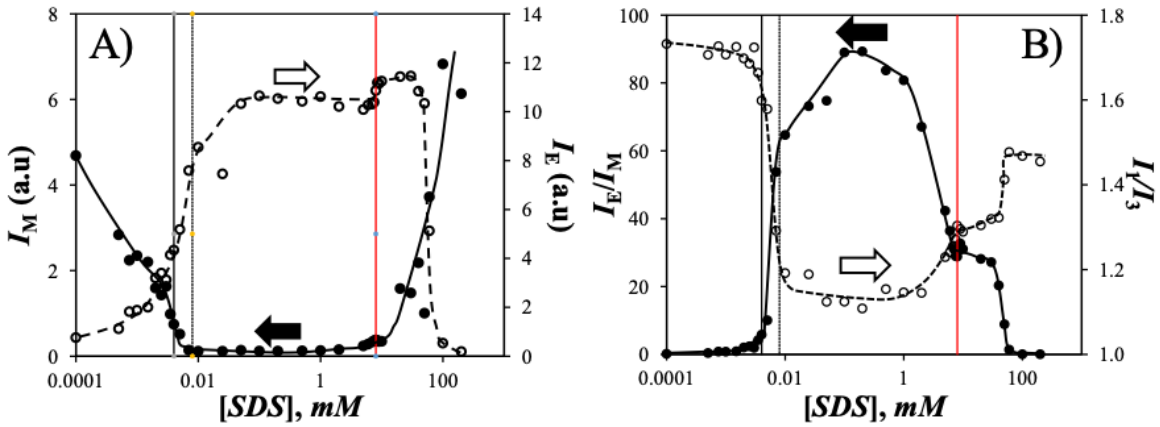

Figure 4.3 Plot of A) (●) I_M and (○) I_E and B) the ratios (●) I_1/I_3 and (○) I_E/I_M as a function of SDS concentration. [PyO-3-12] = 4 μM.

Figure 4.3B shows I_E/I_M and I_1/I_3 as a function of SDS concentration. The I_E/I_M ratio reflected the observations made about I_M and I_E in Figure 4.3A. I_E/I_M took a value close to 0 for SDS concentrations between 0 and the equimolar point (4 μM), increasing significantly for SDS concentrations between the equimolar and equicharge (8 μM) point, retaining a very high value for SDS concentrations between 7 μM and 2 mM, before decreasing significantly between 2 and the 8 mM CMC of SDS, remaining constant between 8 and 50 mM, and decreasing to 0 for SDS concentrations larger than 60 mM. The sudden increase in I_E/I_M between the equimolar and equicharge points in Figure 4.3B suggests that electrostatic forces are driving the interactions between SDS and PyO-3-12 to form aggregates. However, the sudden increase in I_E/I_M close to the equicharge point should not hide the fact that I_M decreases and I_E increases gradually for SDS concentrations between 0.1 μM and 8 μM in Figure 4.3A, reflecting the progressive formation of PyO-3-12/SDS aggregates over a range of SDS concentrations covering close to two orders of magnitude. Although the I_E/I_M ratio shows some fluctuations for SDS concentrations between 7 μM and 2 mM, these variations are believed to be due to small changes in I_M, which result in larger changes in I_E/I_M due to the small I_M values obtained in this concentration range (see I_M in Figure 3A). If the accretion of SDS molecules

to the PyO-3-12/SDS aggregates formed at the equicharge point was taking place as the SDS concentration increased from 7 μM to 2 mM, this process would dilute PyO-3-12 more than 100 folds in the PyO-3-12/SDS aggregates and would be accompanied by a significant decrease in I_E/I_M. Instead, the relatively constant and large I_E/I_M ratio obtained for SDS concentrations between 7 μM and 2 mM suggests that the PyO-3-12/SDS aggregates retain a same chemical composition as that obtained at the equicharge point regardless of the SDS concentration in this concentration range. It is only after the SDS concentration reaches 2 mM that an increase in SDS concentration significantly reduces the I_E/I_M ratio, suggesting that SDS molecules interact with the PyO-3-12/SDS aggregates, in a process that would reduce the local pyrene concentration ($[Py]_{loc}$) inside a surfactant aggregate and thus the I_E/I_M ratio. Interestingly, the decrease in I_E/I_M observed for SDS concentrations larger than 2 mM stops as soon as the SDS concentration reaches the CMC. Above the CMC, SDS molecules associate into SDS micelles and the PyO-3-12/SDS aggregates retain a similar chemical composition up to an SDS concentration of 50 mM, at which point I_E in Figure 4.3A begins to decrease with increasing SDS concentration. The I_E/I_M ratio approaches 0 at large SDS concentrations, indicating that PyO-3-12 molecules are isolated inside SDS micelles.

The significant changes in I_E/I_M observed with SDS concentration in Figure 4.3B were mirrored by similarly significant changes in the I_1/I_3 ratio in Figure 4.3B, demonstrating that the large changes in I_E/I_M were associated with changes in the polarity of the medium experienced by the pyrenyl moiety of PyO-3-12. Figure 4.3B shows that the I_1/I_3 ratio decreases from 1.69 (±0.05) to 1.15 (±0.03) for SDS concentrations between 0 and 5 μM and between 10 μM and 2 mM, respectively. The decrease in I_1/I_3 reflects a decrease in the polarity of the environment experienced by the pyrenyl moiety, thus confirming the association of PyO-3-12 and SDS surfactants to form PyO-3-12/SDS aggregates, where the pyrenyl moieties probe a less polar environment compared to water. I_1/I_3 increases from 1.15 (±0.03) to 1.30 (±0.02) as

the SDS concentration increases from 2 to 8 mM, confirming further interactions between the PyO-3-12/SDS aggregates and SDS in this concentration range. The I_1/I_3 ratio remains constant at 1.30 (±0.02) for SDS concentrations between 8 and 40 mM, suggesting that the chemical composition of the PyO-3-12/SDS aggregates is not changed in this range of SDS concentrations, where SDS molecules seem to form micelles independently of the PyO-3-12/SDS aggregates. I_1/I_3 increases suddenly between 40 and 60 mM SDS, above which it remains constant and equal to 1.47 (±0.01). This value is that expected for isolated PyO-3-12 molecules inside SDS micelles as was reported in an earlier study.[1] The good agreement between the SDS concentrations, where significant changes in I_E/I_M and I_1/I_3 occur, confirms that these transitions are the result of interactions between PyO-3-12 and SDS molecules.

The fact that I_1/I_3 took a value of 1.15 for the PyO-3-12/SDS aggregates at SDS concentrations between 10 μM and 2 mM and 1.47 at SDS concentrations above 60 mM, where PyO-3-12 is isolated in SDS micelles, merits discussion. Due to its design, PyO-3-12 senses the polarity of its environment as effectively as pyrene,[1,2] whose I_1/I_3 ratio has been reported to equal 1.03 (±0.04) in SDS micelles.[24,30] The I_1/I_3 ratio of 1.47 found for PyO-3-12 in SDS micelles was attributed to the tendency of the oxygen beta to pyrene to locate itself at the water-micelle interface, where the pyrenyl group would probe a more polar environment.[1] The significantly lower I_1/I_3 ratio obtained for the PyO-3-12/SDS aggregates compared to the I_1/I_3 ratio of PyO-3-12 in SDS micelles suggests that the pyrenyl moieties of PyO-3-12 in the surfactant aggregates are less exposed to water than in the SDS micelles. The large I_E/I_M ratio, indicating a high $[Py]_{loc}$, and the low I_1/I_3 ratio, indicating that the pyrenyl moieties are shielded from water, suggest that the association of PyO-3-12 with SDS results in the formation of large PyO-3-12/SDS aggregates, where the pyrenyl labels located in the interior of the surfactant aggregates are shielded from water and yield low I_1/I_3 ratios. Since CSMs often result in the formation of large multilamellar vesicles,[3-19] these large PyO-3-12/SDS aggregates might be

multilamellar vesicles, where the PyO-3-12 molecules located in the inner leaflets experience a less polar environment. This proposal was confirmed by the images presented in Figure 4.4, which were acquired by transmission electron microscopy (TEM). Although changes in surfactant concentration and temperature can occur during the acquisition of TEM images, which can lead to changes in the morphology of surfactant aggregates, TEM images are widely used in the literature to support the nature of surfactant aggregates.[9,10,16-18,31] The TEM images shown in Figure 4.4 illustrate the propensity of CSMs of PyO-3-12 and SDS to form multilamellar aggregates that progressively morph into vesicles as the PyO-3-12 concentration decreases from 25, to 4, and finally 1 μM. In the case of the solutions with 4 μM PyO-3-12, Figures 4.4C and D indicate the coexistence of vesicles (see green arrow in Figure 4.4C and Figure 4.4D) and multilamellar aggregates. Consequently, the I_1/I_3 ratio seems to provide information about the nature of the PyO-3-12/SDS aggregates. In a multilamellar aggregate, interactions between PyO-3-12 and water would occur at the top and bottom outermost layers from the stacked lamellae constituting a surfactant aggregate, whereas the inner leaflets would be less exposed resulting in an overall lower I_1/I_3 ratio. In the case of multilamellar vesicles, interactions between PyO-3-12 and water would only occur in the outermost bilayer of the vesicle, so that the PyO-3-12 molecules located in the inner bilayers would result in an even lower I_1/I_3 ratio than that obtained for the multilamellar aggregates. The increase in I_1/I_3 observed for SDS concentrations between 2 and 8 mM in Figure 4.3B could signal a decrease in the size of the PyO-3-12/SDS aggregates upon their association with SDS molecules. The breakup of the large PyO-3-12/SDS aggregates shown in Figure 4 obtained at the equicharge point into smaller ones upon interactions with SDS molecules would be an entropically favored process that would result in more PyO-3-12 surfactants being closer to water and experiencing a more polar environment resulting in a higher I_1/I_3 ratio.

Surfactant concentration at the equicharge point	Overall features	Specific features
[PyO-3-12] = 25 µM [SDS] = 50 µM	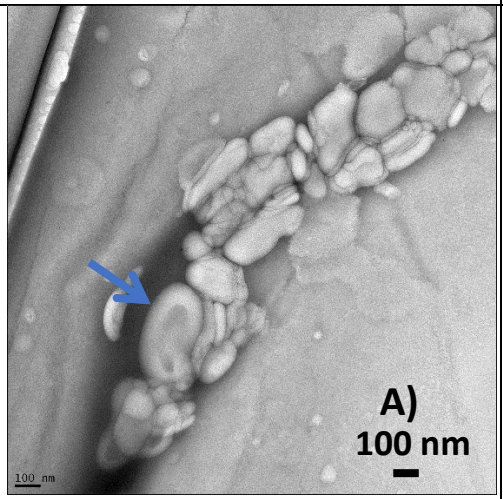	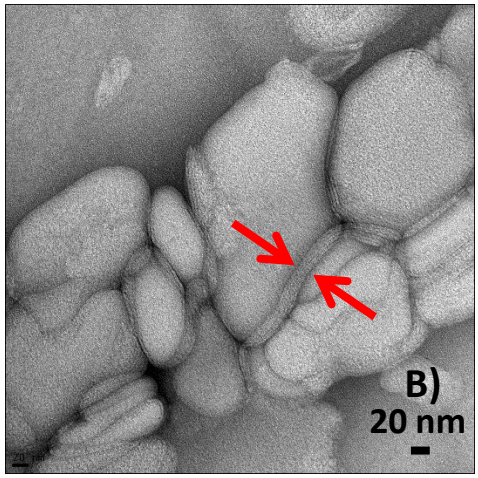
[PyO-3-12] = 4 µM [SDS] = 8 µM	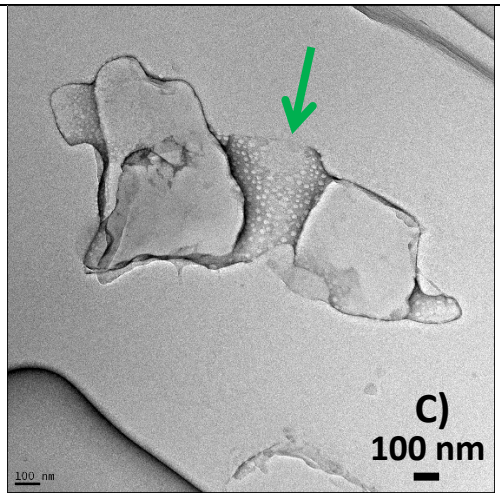	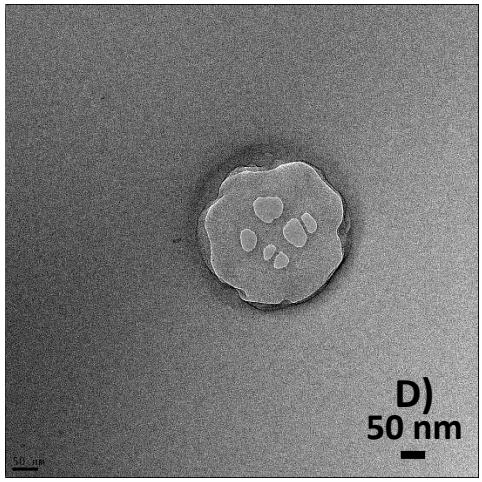
[PyO-3-12] = 1 µM [SDS] = 2 µM	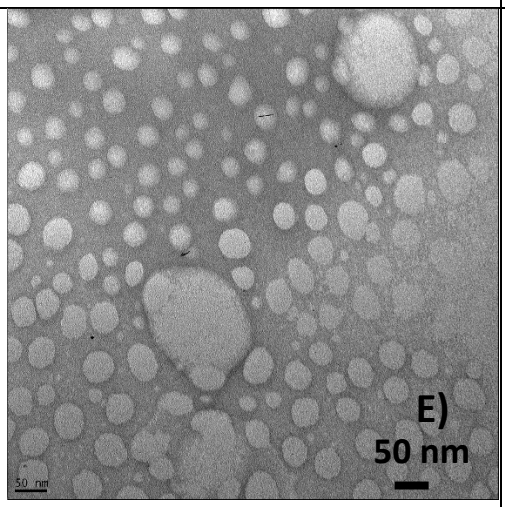	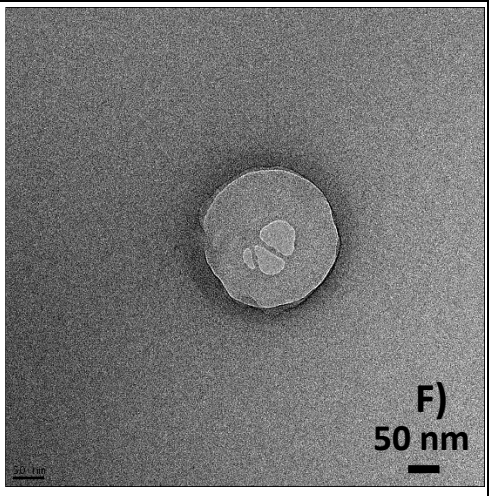

Figure 4.4 TEM images of the PyO-3-12/SDS aggregates taken at the equicharge point. The blue, red, and green arrows in Figures 4.4A, B, and C indicate a half-formed vesicle, a stack of five lamellae each 4 nm thick, and several multilamellar vesicles, respectively.

To assess the state (unassociated or aggregated) and the dynamics experienced by the PyO-3-12 surfactants, the pyrene monomer and excimer fluorescence decays of the PyO-3-12/SDS mixtures were acquired and fitted according to the model free analysis (MFA). All the parameters retrieved from the MFA of the decays were listed in Tables S4.1-S4.6 in SI. The MFA yields the molar fractions of pyrene species in solution f_{free}, f_{diff}, and f_{agg}, where f_{free} represents those unassociated pyrenes, that emit as if they were free in solution, f_{diff} represents those pyrenes that form excimer via diffusive encounters, and f_{agg} represents the pre-aggregated pyrenes, that form excimer instantaneously upon direct excitation. The MFA also yields $<k>$, which is the average rate constant of pyrene excimer formation (PEF), the average lifetime $<\tau>$ of the excited pyrenes forming excimer by diffusion, and the excimer lifetimes τ_{E0} and τ_D, which represent the pyrenes forming well and poorly stacked excimer.

The MFA parameters were combined into Equation S4.11 given in SI to yield the absolute I_E/I_M(MFA) ratio and it was plotted as a function of SDS concentration in Figure 4.5A for comparison with the relative I_E/I_M ratio shown in Figure 4.3B obtained from the analysis of the fluorescence spectra. The excellent agreement between the relative I_E/I_M and absolute I_E/I_M(MFA) ratios confirmed the validity of the MFA and the trends obtained with the parameters retrieved through the MFA of the fluorescence decays are discussed hereafter.

The molar fractions f_{free}, f_{diff}, and f_{agg} were plotted as a function of SDS concentration in Figure 4.5B. Since the MFA was applied to fit the monomer and excimer fluorescence decays globally, the solution must generate some excimer to apply the MFA. This explains why no MFA parameters are reported at the very low (< 2 μM) and very high (> 50 mM) SDS concentrations, since under these conditions, the PyO-3-12 surfactants were mostly

unassociated either in water or in SDS micelles, respectively, and little excimer was formed (see Figure 4.5A).

The profiles obtained with the molar fractions in Figure 4.5B and $<k>$ in Figure 4.5C confirm that the association of PyO-3-12 and SDS proceeds according to the same six SDS concentration regimes, that were identified in Figure 4.3. The addition of SDS to an aqueous solution of 4 μM PyO-3-12 leads to the formation of PyO-3-12/SDS aggregates, resulting in an increase in f_{diff} and f_{agg} and a decrease in f_{free} with increasing SDS concentration. Interestingly, the formation of surfactant aggregates stops at the equicharge point ([SDS] = 8 μM), above which f_{diff} and f_{agg} remain constant and f_{free} equals 0. This result suggests that the aggregates are constituted of a 1:2 mixture of PyO-3-12:SDS surfactants. These PyO-3-12/SDS aggregates appear to be sufficiently stable to be impervious to further addition of SDS since f_{diff}, f_{agg}, and f_{free} remain constant for SDS concentrations between 7 μM and 2 mM and equal to 0.83 (±0.01), 0.17 (±0.01), and 0.00 (±0.00), respectively. Based on these values, PEF occurs mostly by diffusive encounters in the PyO-3-12/SDS aggregates, although residual aggregation occurs between the pyrenyl groups. Although wavy, $<k>$ takes a large but constant value equal to 0.19 (±0.01) ns^{-1}. As the SDS concentration reaches 2 mM, SDS molecules begin to interact with the equicharged PyO-3-12/SDS aggregates, resulting in the dilution of the pyrenyl labels, where the pyrenyl moieties are less aggregated (f_{agg} decreases) and form excimer more slowly ($<k>$ decreases) due to the dilution of PyO-3-12 in the surfactant aggregates. The accretion of SDS molecules to the equicharged PyO-3-12/SDS aggregates stops at an SDS concentration of 8 mM, corresponding to the CMC of SDS. At this point, further addition of SDS results in the formation of SDS micelles, so that the PyO-3-12/SDS aggregates retain the same composition that they had at the CMC. When the SDS concentration reaches 50 mM, enough SDS micelles have been created to induce the dissociation of the PyO-3-12/SDS aggregates leading to the

incorporation of individual PyO-3-12 surfactants inside SDS micelles. As a result, all the parameters reflecting PEF decrease such as f_{diff} and <k>.

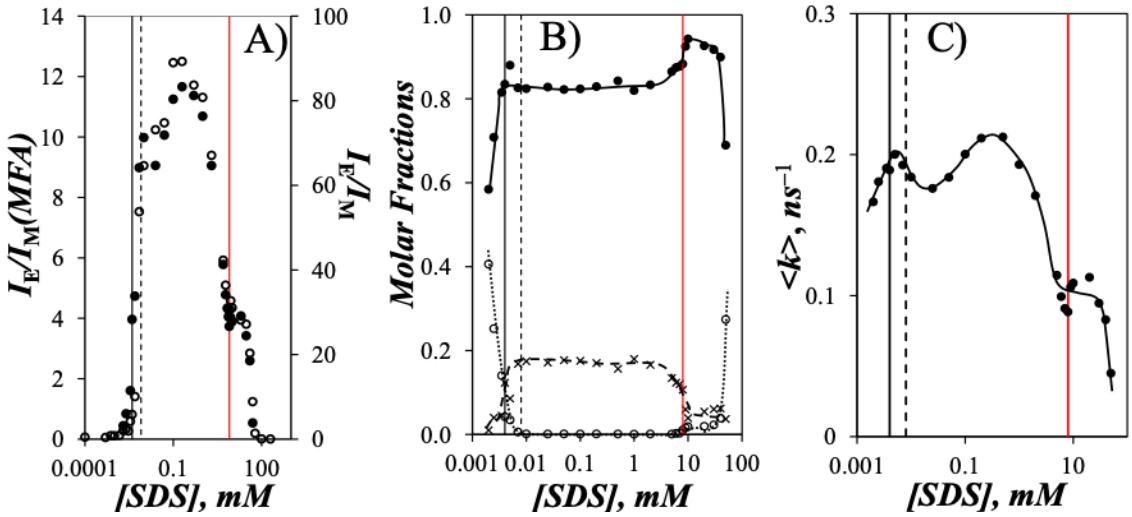

Figure 4.5 Plots of A) the I_E/I_M ratio obtained from (●) the MFA analysis of the fluorescence decays and (○) the analysis of the fluorescence spectra, B) the molar fractions (●) f_{diff}, (×) f_{agg}, and (○) f_{free}, and C) the average rate constant (<k>) of PEF as a function of SDS concentration. The solid and dashed vertical black lines represent the equimolar (4.0 μM) and equicharge (8.0 μM) SDS concentration. The red vertical line represents the CMC of SDS (8 mM). [PyO-3-12] = 4 μM.

Since the PyO-3-12 charges appear to play an important role in the formation of the PyO-3-12/SDS aggregates, the experiments were repeated with a 4-fold larger PyO-3-12 concentration equal to 16 μM. The fluorescence spectra of the solutions were acquired and the fluorescence intensities of the pyrene monomer (I_M) and excimer (I_E) were calculated and plotted as a function of SDS concentration in Figure 4.6A. As was observed with 4 μM PyO-3-12 in Figure 4.3A, a gradual decrease in I_M and increase in I_E was found for SDS concentration increasing from 1 μM to the equicharge point of 32 μM. These gradual changes in I_E and I_M reflected the progressive formation of PyO-3-12/SDS aggregates over a range of SDS concentration that spanned close to two orders of magnitude.

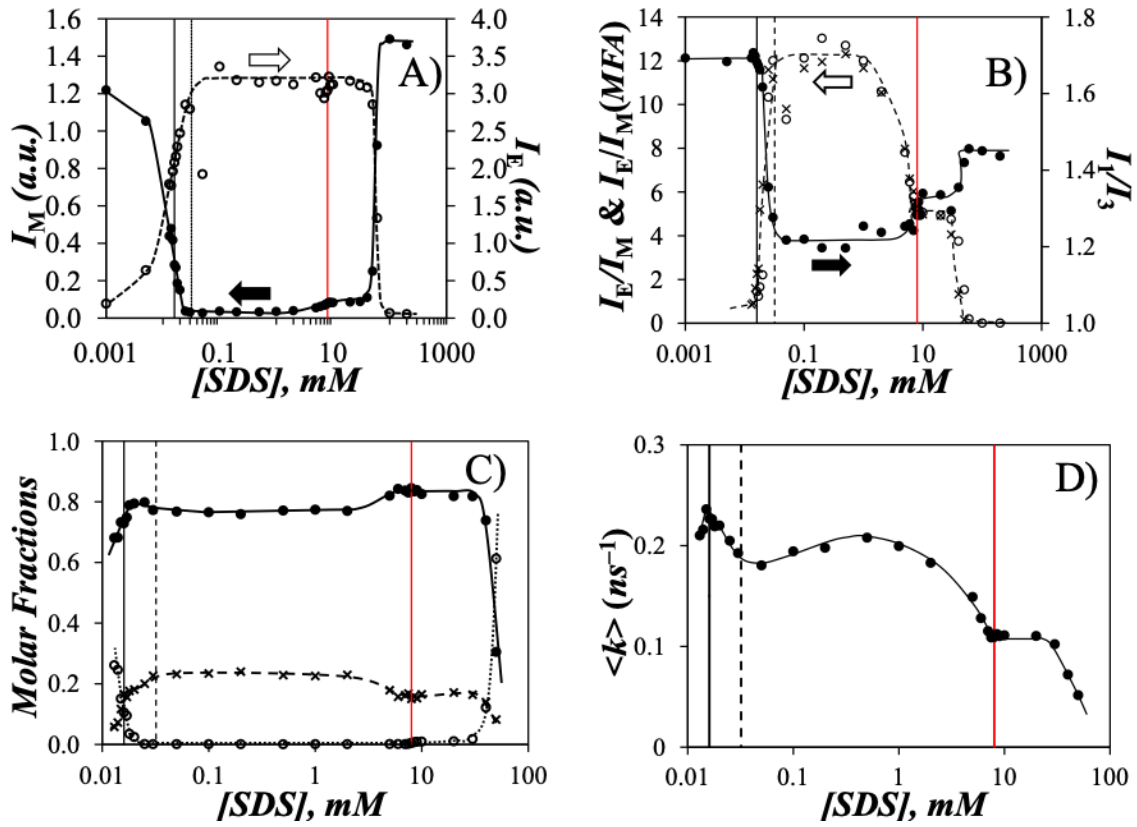

Figure 4.6 Plots of A) (●) I_M and (○) I_E, B) (×) the absolute I_E/I_M(MFA) ratio obtained from the MFA analysis of the fluorescence decays and (○) the normalized I_E/I_M ratio obtained from the analysis of the fluorescence spectra and (●) the I_1/I_3 ratio, C) the molar fractions (●) f_{diff}, (×) f_{agg}, and (○) f_{free}, and D) the average rate constant (<*k*>) of PEF as a function of SDS concentration. The solid and dashed vertical black lines represent the equimolar (16 μM) and equicharge (32 μM) SDS concentration. The red vertical line represents the CMC of SDS (8 mM). [PyO-3-12] = 16 μM.

I_M and I_E took very low and very large values, respectively, that remained constant for SDS concentration between 25 μM, which is close to the equicharge point, and 2 mM. The large I_E value indicated that PyO-3-12/SDS aggregates had formed and the constancy of I_E and I_M suggested that the PyO-3-12/SDS aggregates retained the same composition for SDS concentrations between 25 μM and 2 mM. I_M increased with increasing SDS concentration between 2 and 8 mM which reflected some interactions between PyO-3-12 and SDS, while I_E

remained constant within experimental error. Past the CMC of SDS, I_M and I_E remained constant, indicating that the PyO-3-12/SDS aggregates present at the CMC of SDS retained their chemical composition as SDS micelles formed. For SDS concentrations above 40 mM, I_M increased, and I_E decreased to zero as would be expected if the PyO-3-12 surfactants would distribute themselves among SDS micelles.

The I_1/I_3 ratio equaled 1.23 (±0.03) for the PyO-3-12/SDS aggregates, which was lower than that of 1.44 (±0.02) for PyO-3-12 in SDS micelles suggesting that PyO-3-12 was shielded from water in the surfactant aggregates, as would be expected for multilamellar PyO-3-12/SDS aggregates. Yet the I_1/I_3 ratio of 1.23 (±0.03) obtained for the PyO-3-12/SDS complexes prepared from the 16 μM PyO-3-12 solution was larger than the I_1/I_3 ratio of 1.15 (±0.03) obtained for the PyO-3-12/SDS aggregates prepared from the 4 μM PyO-3-12 solution. Since a lower I_1/I_3 ratio should reflect a stronger shielding of PyO-3-12 from water, it would suggest that PyO-3-12 in the PyO-3-12/SDS aggregates obtained with 16 μM PyO-3-12 was more exposed to water compared to PyO-3-12 in the surfactant aggregates prepared with 4 μM PyO-3-12. The TEM images obtained for a 25 μM PyO-3-12 concentration showed that the surfactant aggregates formed stacked lamellae (see red arrows in Figure 4.4B) that curled up into half vesicles (see blue arrow in Figure 4.4A). PyO-3-12 in a multilamellar aggregate would be more exposed to water at the interface between water and the top and bottom lamellae of a stack of lamellae compared to PyO-3-12 in a multilamellar vesicle, which could solely interact with water in the single outer lamella of the vesicle. The edges of the flat multilamellar aggregates for the 25 μM PyO-3-12 solutions showed the striations expected from stacked lamellae (see red arrows in Figure 4.4B). Five lamellae could be identified within the 20 nm spacing between the two red arrows, suggesting 4 nm thick lamellae. Considering that 3 dodecyl chains coexist with one 1-pyrenylmethyl hexyl ether in the PyO-3-12/SDS aggregates at the equicharge point, with the pyrenyl-label tail having a similar stretch as a dodecyl chain,

the 4 nm lamellar thickness is reasonable considering that an SDS micelle is expected to have a 4 nm diameter.[32]

The molar fractions f_{diff}, f_{agg}, and f_{free} and $<k>$ were determined from the MFA of the fluorescence decays and they were plotted as a function of SDS concentration in Figures 4.6C and D, respectively. They were used to calculate the absolute I_E/I_M(MFA) ratio with Equation S4.11. The I_E/I_M(MFA) ratio agreed well with the I_E/I_M ratio obtained from the analysis of the fluorescence spectra indicating that the MFA parameters properly reflected the PEF observed with the PyO-3-12/SDS mixtures. The plots in Figures 4.6C and D reflected the six SDS concentration regimes that had been identified based on the trends obtained earlier with the I_1/I_3 and I_E/I_M ratios, the molar fractions f_{diff}, f_{agg}, and f_{free} and the average rate constant $<k>$.

Finally, one last series of SDS and PyO-3-12 mixtures was prepared with a PyO-3-12 concentration of 1.0 μM. Due to the low PyO-3-12 concentration, the steady-state fluorescence spectra were obtained, but not the fluorescence decays as their acquisition would have taken too long at this low PyO-3-12 concentration. The I_E/I_M and I_1/I_3 ratios were plotted as a function of SDS concentration in Figures 4.6A and B, respectively, for the three PyO-3-12 series. The same six SDS concentration regimes were observed for the 1.0 μM PyO-3-12 concentration. At low SDS concentrations below the equimolar point, no PEF was detected, and the I_E/I_M ratio took a value of zero. I_E/I_M increased significantly as the SDS concentration increased between the equimolar (1 μM) and equicharge (2 μM) point. The I_E/I_M ratio retained a fairly constant and large value for SDS concentrations between 2 μM and 1 mM, before decreasing for SDS concentrations between 1 and 8 mM. At 8 mM SDS, where SDS micelles formed, the I_E/I_M ratio remained constant up to an SDS concentration of 30 mM, above which the PyO-3-12 surfactants distributed themselves randomly into the SDS micelles, where they were isolated, and I_E/I_M equaled 0.

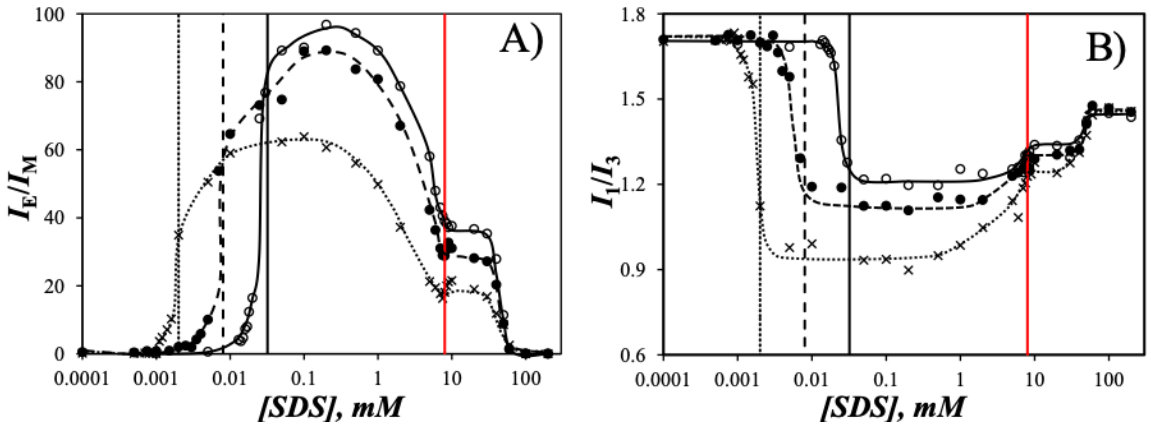

Figure 4.7 Plots of A) I_E/I_M and B) I_1/I_3 as a function of SDS concentration. (●) [PyO-3-12] = 4.0 μM, (O) [PyO-3-12] = 16 μM, and (×) [PyO-3-12] = 1.0 μM. The red vertical line represents the CMC of SDS (8 mM). The dotted, dashed, and solid black lines indicate the equicharge SDS concentration for the solutions containing 1, 4, and 16 μM PyO-3-12, respectively.

The changes in I_E/I_M were accompanied by the same changes in the I_1/I_3 ratio, that were observed for the two other PyO-3-12 concentrations and which reflected changes in the polarity of the environment experienced by the pyrenyl group as the associations of PyO-3-12 and SDS proceeded through the six different SDS concentration regimes. For SDS concentrations between 2 μM and 0.5 mM corresponding to the PyO-3-12/SDS aggregates, I_1/I_3 equaled 0.95 (±0.03) for aggregates formed from the 1 μM PyO-3-12 solution, significantly lower than the I_1/I_3 ratios of 1.15 (±0.03) and 1.23 (±0.03) obtained for the 4 and 16 μM PyO-3-12 solutions, respectively. This trend indicates that increasing the PyO-3-12 concentration used to prepare PyO-3-12/SDS aggregates reduces shielding from water. The TEM images shown in Figure 4.4 provide a rational for this observation. Lower PyO-3-12 concentrations favor the formation of vesicles that must be multilamellar considering the propensity of PyO-3-12 and SDS to form multilamellar aggregates at higher concentrations (see Figures 4.4A and B). Vesicles offer a single interface with water through the outer bilayer while multilamellar aggregates present

two interfaces with water, which result in higher exposure of PyO-3-12 to water and a larger I_1/I_3 ratio. Since more vesicles form at lower PyO-3-12 concentration, the I_1/I_3 ratio decreases with decreasing PyO-3-12 concentration as shown in Figure 4.7B for SDS concentrations between the equicharge point and 2 mM.

Addition of SDS to the multilamellar vesicles formed near the equicharge point as shown in Figure 4.8A for a solution with 1 μM PyO-3-12 and 2 μM SDS leads to their disintegration as shown in Figure 4.8B with 8 mM SDS. Objects of different sizes and shapes are observed, with many assemblies being much smaller than the vesicles in Figure 4.8A. The disintegration of the vesicles into smaller objects would be entropically favored and would result in the pyrenyl labels of PyO-3-12 being closer to water resulting in a higher I_1/I_3 ratio, as observed experimentally in Figure 4.7B.

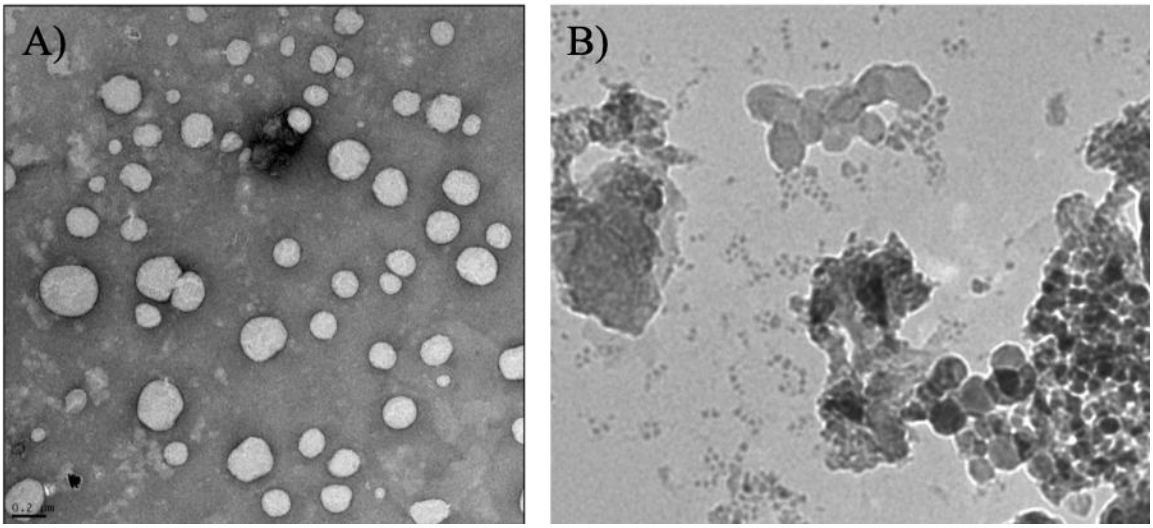

Figure 4.8 Comparison of solutions with 1 mM PyO-3-12 and A) 2 μM SDS and B) 8 mM SDS.

Since electrostatic interactions contributed to the formation of the PyO-3-12/SDS aggregates, the effect of ionic strength on aggregate formation was investigated in Supporting Information. Similar regimes based on SDS concentration were observed in Figure S4.4 for the interactions between PyO-3-12 and SDS at NaCl concentrations of 32 μM and 50 mM. The

main difference between the trends obtained with 50 mM and without NaCl was that instead of retaining their composition at SDS concentrations above the 8 mM CMC of SDS in pure water, the PyO-3-12/SDS aggregates disintegrated at the CMC of SDS of 2.6 mM with 50 mM NaCl,[24] suggesting that the electrostatic interactions, that held PyO-3-12 and SDS together inside the surfactant aggregates, were effectively screened with 50 mM NaCl for SDS concentrations approaching the CMC.

4.5. **Discussion**

The interactions between PyO-3-12 and SDS were characterized for surfactant solutions, that were extremely dilute compared to most other studies conducted with mixtures of oppositely charged surfactants.[3-19] These conditions ensured that PyO-3-12/SDS aggregates were formed between unassociated surfactants. One of the unexpected benefits of this methodology was that CSM could be studied at the equicharge point, conditions that are typically inaccessible with the higher surfactant concentrations reported in the literature to prepare CSM, since surfactant mixtures at the equicharge point are insoluble in water and precipitate out.[3-19] It seems that this complication was avoided by using the low PyO-3-12 concentrations of 1, 4, and 16 μM to prepare the PyO-3-12/SDS aggregates.

Another advantage of dealing with a pyrene-labeled surfactant was that the MFA also yields the I_E/I_M(MFA) ratio, that would be obtained in the absence of unassociated PyO-3-12, by setting f_{free} equal to 0 in Equation S4.11. The I_E/I_M(MFA) ratio obtained with and without f_{free} was plotted as a function of SDS concentration in Figure 4.9 for the 4 and 16 μM PyO-3-12 solutions. The largest discrepancy between the I_E/I_M(MFA) ratios obtained with and without f_{free} was observed at SDS concentrations below the equicharge point. This discrepancy is due to the presence of unassociated PyO-3-12 at these low SDS concentrations, where they emit strongly as monomer, which reduces the I_E/I_M(MFA) ratio when f_{free} is included. Setting f_{free} to 0 raises the I_E/I_M(MFA) ratio obtained at SDS concentrations below the equicharge point to a

value similar to that obtained for SDS concentrations above the equicharge point. Since the I_E/I_M(MFA) with f_{free} set to 0 reflects $[Py]_{loc}$ in PyO-3-12/SDS aggregates, the fact that the I_E/I_M(MFA) is more or less the same at SDS concentrations below and above the equicharge point indicates that the chemical composition of the PyO-3-12/SDS aggregates does not change with the molar ratio of PyO-3-12-to-SDS, when these aggregates are prepared from oppositely charged surfactants, that are present as unimers. This statement leads to the conclusion that the PyO-3-12/SDS aggregates must retain a same 1:2 PyO-3-12:SDS composition over a wide range of SDS concentrations that are lower and higher than the equicharge point. Under these conditions, unassociated PyO-3-12 or SDS molecules would be present in solution depending on whether the SDS concentration was lower or higher than the equicharge point, respectively, but the PyO-3-12/SDS aggregates would retain a 1:2 molar composition. The PyO-3-12/SDS aggregates would retain their composition until an SDS concentration of 2 mM, above which interactions between SDS and the PyO-3-12/SDS aggregates result in the dilution of the PyO-3-12 molecules in the aggregates and a drop in the I_E/I_M(MFA) ratio.

Consequently, the study of mixtures of PyO-3-12 and SDS led to the identification of six SDS concentration regimes, where the interactions between PyO-3-12 and SDS take place in different forms. These six regimes are depicted in Figure 4.10 for aqueous solutions of 1 μM PyO-3-12 without NaCl. Regime 0 corresponds to SDS concentrations much lower than the equicharge point, where SDS and PyO-3-12 molecules do not interact extensively. Stronger interactions between the two surfactants occur at SDS concentrations that are one-to-two orders of magnitude lower than the equicharge point and result in the progressive formation of PyO-3-12/SDS aggregates. This onset of interactions between PyO-3-12 and SDS marks the beginning of Regime I. This SDS concentration range is associated with the appearance of strong PEF with a large increase in I_E and a large decrease in the I_1/I_3 ratio indicating that PyO-3-12 molecules are in close contact and experience a hydrophobic environment, respectively,

as would be expected in PyO-3-12/SDS aggregates. These aggregates are multilamellar vesicles shown in Figures 4.4E and F, where PyO-3-12 is shielded from water.

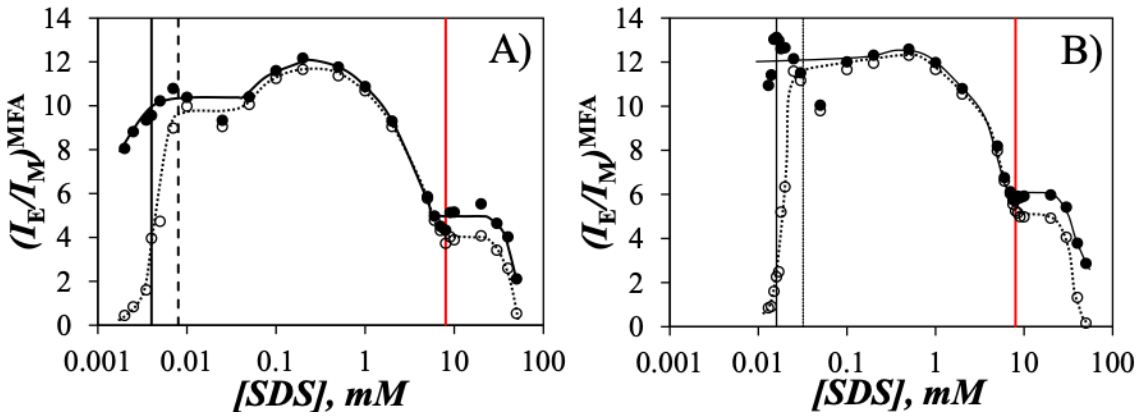

Figure 4.9 Comparison of the I_E/I_M(MFA) ratios calculated (○) with and (●) without f_{free} for solutions prepared with a PyO-3-12 concentration equal to A) 4 μM and B) 16 μM.

Regime II covers the range of SDS concentrations between the equicharge point and 2 mM. Since the formation of PyO-3-12/SDS multilamellar vesicles appears to stop at SDS concentrations above the equicharge point, the vesicles are believed to be composed of 2 meq of SDS and 1 meq of PyO-3-12 and their composition is not expected to change as the SDS concentration is increased past the equicharge point. In these 1:2 PyO-3-12:SDS aggregates, PEF occurs mainly through diffusive encounters between the pyrenyl moieties, although some residual pyrene aggregation was detected. The I_1/I_3 ratio takes a constant and small value equal to 0.97 (±0.07), 1.15 (±0.03), and 1.23 (±0.03) for the solutions prepared with 1, 4, and 16 μM PyO-3-12 indicating a hydrophobic environment. The different I_1/I_3 ratios obtained for the three different PyO-3-12 concentrations suggest that the pyrenyl labels in the PyO-3-12/SDS aggregates experience an environment, that becomes more hydrophobic with decreasing PyO-3-12 concentration. The explanation for this effect is the progressive formation of multilamellar vesicles with decreasing PyO-3-12 concentration as illustrated in Figure 4.4. PyO-3-12 molecules located in the inner leaflets of multilamellar vesicles generated with a low PyO-3-12 concentration would be better shielded from water than the PyO-3-12 molecules in the

multilamellar aggregates created at higher PyO-3-12 concentrations. The multilamellar vesicles appear to create a more rigid environment hindering PEF and resulting in the decrease in I_E/I_M observed in Figure 4.7A with the PyO-3-12 concentration decreasing from 16 to 4 and then 1 μM as more vesicles are generated.

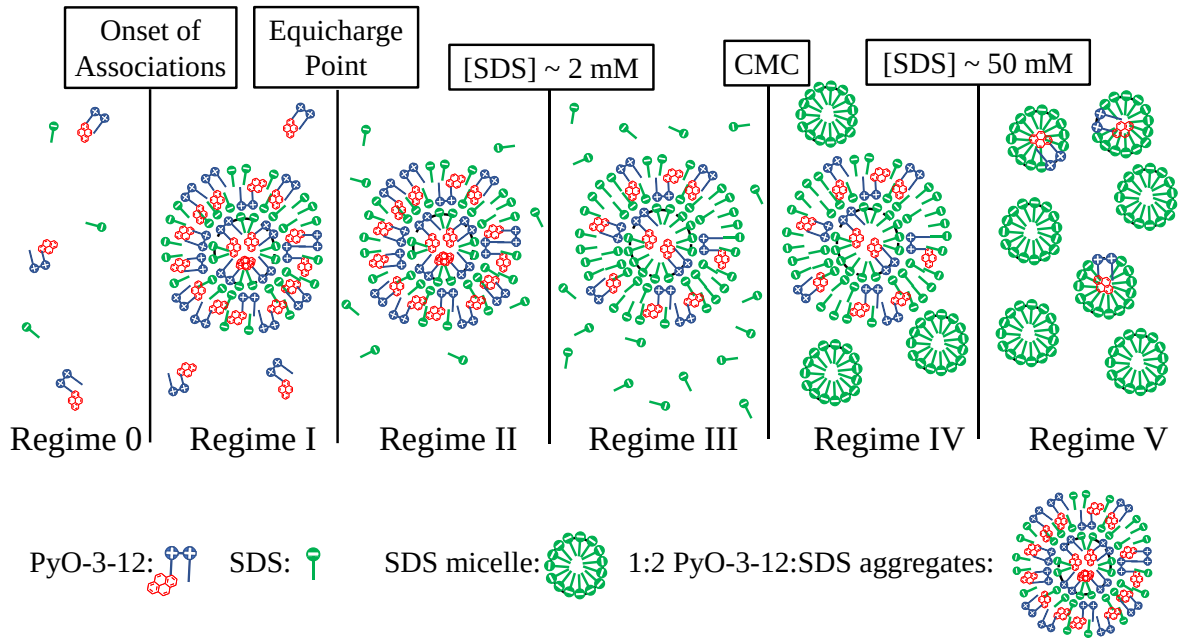

Figure 4.10 Depiction of the six SDS concentration regimes uncovered during the study of the PyO-3-12/SDS interactions in aqueous solutions without NaCl.

The onset of Regime III happens at an SDS concentration around 1 – 2 mM in Figures 4.7A and B and it marks the incorporation of more SDS molecules into the PyO-3-12/SDS aggregates. This effect is probably the result of the stronger drive by the SDS molecules present at a larger concentration to interact with the PyO-3-12/SDS aggregates as well as the entropically driven breakup of the large 1:2 PyO-3-12:SDS aggregates into smaller aggregates being richer in SDS as illustrated in Figure 4.8. The accretion of SDS molecules to the PyO-3-12/SDS aggregates continues until the SDS concentration reaches 8 mM, the CMC of SDS, which marks the boundary between Regime III and Regime IV in Figure 4.10. The incorporation of additional SDS molecules to the PyO-3-12/SDS aggregates in Regime III is marked by a decrease in I_E/I_M in Figure 4.7A, $\langle k \rangle$ in Figures 4.5C and 4.6C, and f_{agg} in Figures

4.5B and 4.6B, all parameters, which reflect a decrease in $[Py]_{loc}$ as a response to a lower PyO-3-12:SDS molar ratio in the aggregates.

Regime IV corresponds to the formation of SDS micelles independently of the existence of the PyO-3-12/SDS aggregates. I_E/I_M in Figure 4.7A, I_1/I_3 in Figure 4.7B, the molar fractions in Figures 4.5B and 4.6C, and $<k>$ in Figures 4.5C and 4.6D remain constant, indicating that the PyO-3-12/SDS aggregates retain their chemical composition. The end of Regime IV corresponds to an SDS concentration in the 30 – 40 mM range, which marks the beginning of Regime V in Figure 4.10. At this point, the large number of SDS micelles leads to the disintegration of the PyO-3-12/SDS aggregates, whereby the few PyO-3-12 molecules distribute themselves among the many SDS micelles, where they become isolated. The I_E/I_M ratio reaches 0 for SDS concentrations of 100 mM or larger as shown in Figure 4.7A.

At first glance, the results obtained in this report are intriguing. In particular, the trends shown in Figure 4.7 suggest the existence of aggregates for a CSM with a total surfactant concentration as low as 3 μM at the equicharge point corresponding to 1 μM of PyO-3-12 and 2 μM of SDS. Such a CSM concentration is much lower than the CAC values reported for mixtures of other cationic gemini surfactants (CGSs) and SDS.[16,17] For instance, Aghdastinat et al. report a CAC of 69 μM for CSMs containing 10 mol% SDS and 90 mol% of an esterquat CGS with a chemical structure similar to that of PyO-3-12.[16] However, the trends shown in Figure 4.7 indicate that a CSM containing 1 μM PyO-3-12 and 0.1 mM SDS, corresponding to 90 mol% PyO-3-12 and 10 mol% SDS, would result in the formation of hardly any PyO-3-12/SDS aggregates, as would be expected from the Aghdastinat study. In fact, the PyO-3-12 study and that of other CGS differs mainly from the representation of the data. In the fluorescence study of PyO-3-12, PyO-3-12 kept at a constant concentration was titrated with an increasing concentration of SDS and the fluorescence response of the CSMs was monitored resulting in the trends summarized in Figure 4.7. In the Aghdastinat study,[16] a solution with a

constant composition of esterquat CGS and SDS was diluted and its surface tension was monitored as a function of the total surfactant concentration to determine the CAC for that specific CSM composition. These differences in data representation reflect mainly the different goals of the two studies, which were to showcase the sensitivity of fluorescence in the PyO-3-12 study while the Aghdastinat study aimed at determining the CAC of the CSMs.[16]

4.6. **Conclusion**

The fluorescence experiments conducted with PyO-3-12 provided information about the composition of PyO-3-12/SDS aggregates formed at total surfactant concentrations as low as 2 – 32 μM, corresponding to weight fractions of 0.0001 – 0.0017 wt%. These total surfactant concentrations are 2-to-3 orders of magnitude lower than the range of concentrations typically used for structural characterization of colloids by traditional scattering (DLS, SAXS, SANS …) techniques. Yet, information about the composition of the PyO-3-12/SDS aggregates was retrieved by combining the results obtained from the I_E/I_M ratio and $<k>$ to probe $[Py]_{loc}$ and the dynamics of the surfactant tails, the molar fractions f_{diff}, f_{agg}, and f_{free} to assess the state of the PyO-3-12 surfactants, and the I_1/I_3 ratio to describe the polarity of the environment probed by the pyrenyl groups. The information garnered by all these parameters combined with the TEM images shown in Figures 4.4 and 4.8 led to the model presented in Figure 4.10, that identified six regimes describing the interactions between PyO-3-12 and SDS in pure water. These six regimes were easily identified due to the marked changes in the fluorescence properties experienced by the pyrenyl moiety of PyO-3-12, which were readily detected from the fluorescence measurements conducted on the solutions of PyO-3-12 and SDS mixtures. Another important aspect of this investigation was the extreme sensitivity of fluorescence, which enabled the study of the behavior of PyO-3-12, at concentrations of 1, 4, and 16 μM, as it interacted with SDS. Since some experiments were conducted at surfactant concentrations that were 2 to 3 orders of magnitude below their CMC, these conditions ensured that the

interactions between surfactants leading to the formation of aggregates took place between unassociated PyO-3-12 and SDS molecules. In turn, knowledge of the initial state of the surfactants simplified the interpretation of the experimental trends. These new types of experiments performed with pyrene-labeled surfactants are expected to nicely complement studies currently carried out at much higher surfactant concentrations.

Chapter 5 Characterization of the Interactions between Two Cationic Pyrene-Labeled Gemini Surfactants and DNA

5.1. **Abstract**

This study describes the interactions between calf thymus DNA (CT-DNA) and two cationic gemini surfactants referred to as Py-3-12 and PyO-3-12, which were prepared with two dimethyl ammonium bromide head groups linked with a propyl spacer, with one ammonium bearing a dodecyl tail and the other bearing either a 1-pyrenylhexyl or a 1-pyrenemethoxyhexyl group, respectively. The fluorescence of the pyrene-labeled gemini surfactants (PyLGS) was monitored through the analysis of the steady-state fluorescence spectra and time-resolved fluorescence decays. These experiments probed the state of the pyrenyl labels, indicating whether the PyLGS were free in solution or complexed with CT-DNA or another amphiphilic molecule, namely sodium dodecyl sulfate (SDS), the local pyrene concentration ($[Py]_{loc}$) inside the complexes generated with the PyLGS, and the polarity of the local environment probed by an excited pyrene. These analyses led to the conclusion that all PyLGS were bound to CT-DNA at a (-/+) ratio equal to unity, where the (-/+) ratio equals the ratio [CT-DNA]/[PyLGS] with [CT-DNA] expressed in DNA base pairs. The hydrophobic microdomains generated through the binding of the PyLGS to CT-DNA were found to retain a similar PyLGS content for (-/+) ratios between 0.2 and 11.5 for Py-3-12 and between 0.6 and 5 for PyO-3-12. The narrower range of (-/+) ratios found for PyO-3-12 suggested that it did not interact as strongly with CT-DNA as Py-3-12 did. Consequently, the release of CT-DNA from PyO-3-12/CT-DNA complexes prepared with 16 mM PyO-3-12 and a (-/+) ratio of 1.5 was monitored as SDS was added to the solution. Analysis of the fluorescence data led to the conclusion that SDS interacted with the PyO-3-12/CT-DNA complexes by isolating individual CT-DNA molecules through the formation of ternary complexes, where CT-DNA was coated by a layer of PyO-3-12, which was itself covered by a sheath of SDS molecules. The ternary complexes remained stable up to an [SDS] of 0.5 mM, above which they decomposed leading to the formation of PyO-3-12/SDS complexes and the release of CT-DNA.

5.2. **Introduction**

The delivery of therapeutic genes to the suitable cell for gene expression is a significant challenge in gene therapy.[1,2] Three main criteria must be considered when selecting a delivery vehicle for gene delivery. First, it must protect the genetic cargo from degradation, second, it should not cause any immunogenic reactions, and finally, it should be able to translocate its cargo across the membrane of its target cell.[3] Delivery vectors, that satisfy these criteria, can be divided into two main categories depending on whether they are viral and nonviral vectors.[4,5] Viral vectors are typically viruses, whose purpose is to deliver genetic material. Unfortunately, they usually trigger immunogenic reactions and their cargo size is minimal, making the use of these viral vectors undesirable.[4-6] Nonviral vehicles, on the other hand, overcome all the concerns associated with viral vectors. They transport their cargo with low toxicity, induce no immunogenic response, and there is no limit on their cargo size.[7,8] Lipids and liposomes,[9-11] cationic gemini surfactants,[12-15] and dendrimers[16,17] are examples of nonviral gene delivery vectors, that have been used over the years.

In the case of gemini surfactants, those forming higher ordered structures such as cubes and inverted hexagons were found to be more efficient at translocating membranes than those forming simpler structures like lamellae. The higher ordered structures have proven to result in better interaction with endosomal membranes,[3,18,19] although lower ordered structures showed higher stability than higher ordered structures, when interacting with model membranes.[9,10,20] Gemini surfactants can be an ideal vehicle for gene transfection because they can be fine-tuned to strike a balance between these high and low ordered structures to enhance the efficiency of gene transfection. They can be modified by altering either the length of the hydrophobic tails, the type and size of the head groups, and the type and length of the spacer.[21-24] Complexes prepared with gemini surfactants and DNA have been studied using different fluorescence techniques. However, most of these studies have been carried out with non-

covalently bonded fluorophores, that probe these complexes through physical interactions.[15,25-28]

In contrast to these earlier studies, the pyrene-labeled gemini surfactants (PyLGS) Py-3-12 and PyO-3-12, whose chemical structure is shown in Figure 5.1, were designed to have the pyrene dye covalently attached to one of their two alkyl tails. Consequently, their fluorescence signal reports directly on the state of these PyLGS, contrary to most other fluorescence experiments, where molecular pyrene is used to probe surfactant aggregates through physical interactions. Such experiments are always opened to interpretation as to whether pyrene is actually bound to a given surfactant aggregate, since pyrene can partition between the aqueous phase and the hydrophobic environment generated by the surfactants. Furthermore, Py-3-12 and PyO-3-12 take advantage of all the common fluorescent features of pyrene.[29-31] For instance, pyrene reports on the state of the PyLGS, whether they are aggregated or unassociated depending on whether they do or do not form an excimer, respectively, upon encounter between an excited and a ground-state pyrene. The magnitude of the fluorescence intensity ratio I_E/I_M of the excimer over the monomer reflects the degree of association experienced by the PyLGS. Pyrene also reports on the polarity of the environment probed by the excited pyrene of PyO-3-12 through the fluorescence intensity ratio I_1/I_3 of the first over the third band in the pyrene monomer fluorescence spectrum with I_1/I_3 for PyO-3-12 in organic solvents, taking values between 1.27 in dioxane ($\varepsilon = 2.2$) and 2.14 in DMSO ($\varepsilon = 47.2$).[30,32,33] Finally, model free analysis (MFA)[34-36] of the fluorescence decays of the pyrene monomer and excimer acquired with these PyLGS yields the average rate constant $\langle k \rangle$ of pyrene excimer formation (PEF) for aggregated surfactants, a direct measure of the internal dynamics and local pyrene concentration ($[Py]_{loc}$) experienced by these PyLGS inside a micelle or a surfactant aggregate. The combination of these unique features makes Py-3-12 and PyO-3-12 a

formidable pair of fluorescent probes to study their interactions with other negatively charged macromolecules such as DNA or RNA.

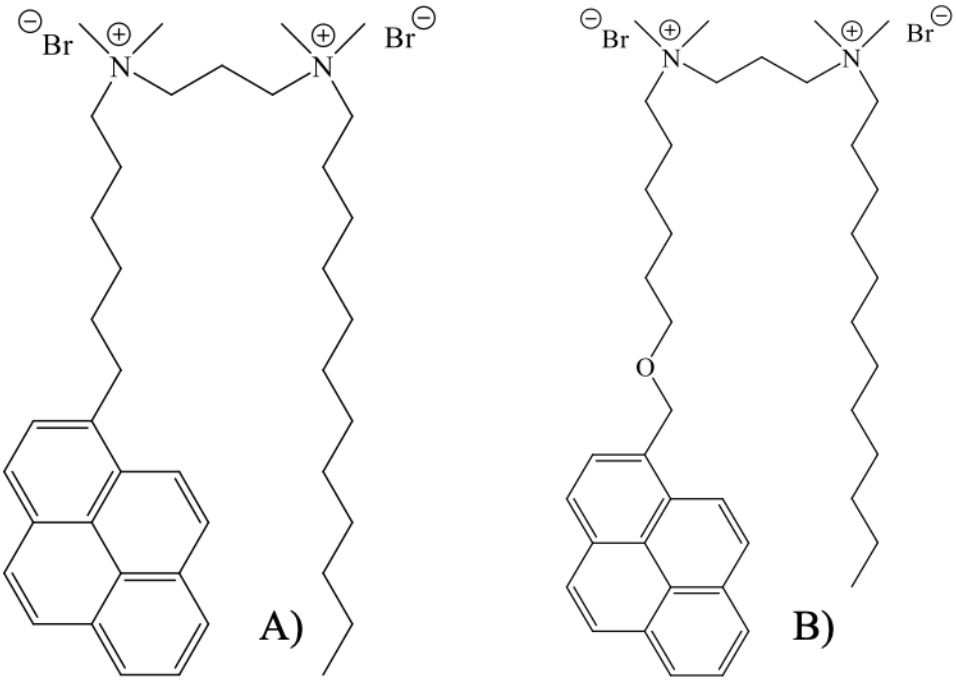

Figure 5.1 Chemical structure of the gemini surfactants A) Py-3-12 and B) PyO-3-12.

Chapter 5 describes how the fluorescence features of the PyLGS were harnessed to probe how calf thymus DNA (CT-DNA) interacts with Py-3-12 and PyO-3-12. In these experiments, the fluorescence signal of the PyLGS was monitored as a function of the CT-DNA concentration to probe the complexation of the PyLGS with CT-DNA, and the dissociation of the PyLGS/CT-DNA complexes was followed as sodium dodecyl sulfate (SDS) was added to the complex solution. To simplify the interpretation of the fluorescence data, the PyLGS concentration was kept at 10 and 16 μM for Py-3-12 and PyO-3-12, PyLGS concentrations, that were 15 and 24 times lower than their CMC of 0.15 and 0.38 mM, respectively. These conditions ensured that PEF could only arise from the formation of PyLGS/CT-DNA complexes, since the PyLGS were unable to micellize on their own at PyLGS concentrations below their respective CMC. Since the PyLGS concentrations of 10 and 16 mM corresponded to 0.0006 and 0.0012 wt%, scattering (DLS, SLS, SAXS, SANS, …) and

microscopy (cryo-TEM, AFM) techniques, typically used to obtain structural information about colloids,[37-45] were not sensitive enough. Instead, different fluorescence experiments were conducted with the PyLGS to gain some insights about the structure and chemical composition of the PyLGS/CT-DNA complexes.[29,30] The I_E/I_M ratio and $<k>$ were used to monitor the degree of association between CT-DNA and the PyLGS with and without SDS, while the I_1/I_3 ratio was employed to assess the polarity of the direct local environment of the PyLGS. The results of this study suggest that the hydrophobic domains generated along the CT-DNA by association of the PyLGS share a similar nature at [PyLGS]:[CT-DNA] ratios that are smaller or larger than the equicharge point, corresponding to a [PyLGS]:[CT-DNA] ratio of unity. In this study, [CT-DNA] is expressed in terms of DNA base pairs. Considering that the PEF measurements reflect the local pyrene concentration $[Py]_{loc}$ of the aggregated PyLGS in the complexes along CT-DNA, these results implied that the PyLGS complexed with CT-DNA generate a similar spatial arrangement regardless of the [PyLGS]:[CT-DNA] ratio, as long as it remains between 0.6 and 5 for PyO-3-12 and 0.2 and 10 for Py-3-12. Furthermore, the addition of SDS to PyLGS/CT-DNA complexes led to the complete dissociation of the PyLGS through interactions between the PyLGS and SDS. Such a behavior implies that CT-DNA was freed from the PyLGS/CT-DNA complexes upon addition of SDS. This result supports the notion that PyLGS are good transfection agents, that can release their polynucleotide load through interactions with a negatively charged cell membrane, as has been reported earlier.[46]

5.3. **Experimental**

Chemicals: Sodium dodecyl sulfate (SDS) and deoxyribonucleic acid from calf thymus (CT-DNA) were purchased from Sigma-Aldrich. Doubly distilled deionized water from Millipore Milli-RO 10 Plus and Milli-Q UF Plus (Bedford, MA) was used to prepare all aqueous solutions.

Synthesis of Py-3-12 and PyO-3-12: The procedures have been described earlier for Py-3-12[29] and PyO-3-12.[30]

Preparation of gemini surfactants and DNA solutions: The concentrations of 10 and 16 mM used in all fluorescence experiments with Py-3-12 and PyO-3-12 were below their CMC of 0.15 mM[29] and 0.38 mM,[30] respectively. The (-/+) ratio represented the concentration ratio of DNA base pairs over PyLGS, keeping in mind that a DNA base pair and a PyLGS have two negative and two positive charges, respectively. The (-/+) ratio was used to express the relative concentration of DNA with respect to the PyLGS concentration. To prepare a solution of the desired (-/+) ratio, two solutions were prepared, one with double the desired concentration of CT-DNA and the other with double the desired concentration of PyLGS. Mixing 2 mL of each solution produced a mixture of CT-DNA and PyLGS of the desired (-/+) ratio. The solutions were left for at least one hour to reach equilibrium before being analyzed by steady-state and time-resolved fluorescence.

Steady-state fluorescence (SSF): SSF spectra were acquired with a Photon Technology International (PTI) spectrofluorometer equipped with an Ushio UXL-75Xe Xenon lamp and a PTI 814 photomultiplier detection system. The low PyLGS concentrations used in these experiments enabled the acquisition of the fluorescence spectra of all the solutions with the right-angle geometry.[47] The samples were excited at 344 nm and their fluorescence intensity was scanned from 350 to 600 nm. The ratio I_E/I_M of the fluorescence intensity of the pyrene excimer (I_E) over that of the pyrene monomer (I_M) was used to quantify the efficiency of pyrene excimer formation (PEF). Integrating the fluorescence spectrum from 374 to 380 nm and from 500 to 530 nm yielded I_M and I_E, respectively. The I_1/I_3 ratio was calculated from the ratio of the fluorescence intensity of the first (I_1) and third (I_3) peaks taken at about 377 and 388 nm, respectively. The I_1/I_3 ratio reflects the polarity of the local environment probed by pyrene.[30,32,33]

Time-resolved fluorescence (TRF): The fluorescence decays of the PyLGS were acquired with a HORIBA FluoroHub equipped with a DeltaDiode laser with a wavelength of 336 nm. A 370 and 470 nm cutoff filters were placed in front of the emission monochromator during the acquisition of the monomer and excimer fluorescence decays, respectively, to minimize scattering from the solutions. A time-per-channel of 0.199 ns/ch was employed in all decay acquisitions to zoom in on the fast decay component representing PEF. All monomer and excimer fluorescence decays had 20,000 counts at their maximum. The instrument response function (IRF) was obtained by collecting the emission reflected off an aluminum monolith placed in the sample holder and acquiring a decay with 20,000 counts at the decay maximum with the emission monochromator set at the same wavelength as the 336 nm excitation wavelength. The fluorescence decays were fitted globally according to the model free analysis (MFA).[34-36] Optimization of the parameters employed in the different functions used to fit the fluorescence decays was carried out with the Marquardt-Levenberg algorithm[48] by comparing the experimental decays with the convolution products of these functions with the IRF.

Sum of exponential analysis: Sums of *n* exponentials were used to fit the fluorescence decays of the pyrene monomer ($X = M$) and excimer ($X = E$) individually according to Equation 5.1.

$$[X^*]_{(t)} = [X^*]_{(t=0)} \sum_{i=1}^{n} a_{Xi} \times \exp(-t / \tau_{Xi}) \tag{5.1}$$

The a_{Xi} coefficients in Equation 1 are the pre-exponential factors corresponding to the exponential decay time τ_{Xi}.

Global model free analysis (MFA) of the fluorescence decays: Within the framework of the MFA,[33-35] the pyrene monomer and excimer fluorescence decays are fitted globally by linking the pre-exponential factors and decay times during the analysis with the programs sumeg34bg or sumegs33bg depending on whether 3 or 4 exponentials were required to fit the monomer decays, respectively. The parameters retrieved from the MFA of the decays yield the average

rate constant <k> for PEF and the molar fractions f_{diff}, f_{free}, and f_{agg} of the pyrene species in solution, that form excimer by diffusive encounters, cannot form excimer and emit with the natural lifetime (τ_M) of pyrene, and are aggregated and form excimer instantaneously, respectively. These parameters have been listed in Tables S5.1-5.9 as Supporting Information (SI).

Transmission Electron Microscopy: Samples were adhered to Formvar coated copper grids and allowed to dry for 2 minutes. Excess liquid was blotted away before being stained with 1% (w/v) uranyl acetate. Grids were then observed using an FEI Tecnai G2 F20 transmission electron microscope operated at 200 kV and equipped with a bottom mount Gatan 4k CCD camera under standard operating conditions.

5.4. **Results and Discussion**

The interactions between Py-3-12 and CT-DNA were probed first. The SSF spectra of the 10 μM Py-3-12 solutions, with a concentration well below the 0.15 mM CMC of the surfactant, were acquired with different concentrations of CT-DNA ranging from 0.001 to 0.115 mM. Keeping the concentration of Py-3-12 constant and below its CMC ensured that any PEF could only be the result of interactions between Py-3-12 and CT-DNA. The parameters retrieved from the analysis of the SSF spectra are discussed in terms of the (-/+) ratio, which represents the ratio [CT-DNA]:[PyLGS] of the concentration of CT-DNA base pairs over the concentration of PyLGS. Figure 5.2A shows the SSF spectra for (-/+) ratios between 0.2 and 1.0, while Figure 5.2B shows the SSF spectra for (-/+) ratios ranging from 1.0 to 11.5. The SSF spectrum for a (-/+) ratio of 0.2 shows hardly any excimer, indicating that the Py-3-12 surfactants are unassociated at low CT-DNA concentration. This is expected since the Py-3-12 concentration of 10 μM is one order of magnitude lower than its CMC of 0.15 mM. As the concentration of CT-DNA increases and approaches the equicharge point ((-/+) = 1.0), a substantial increase in the excimer fluorescence can be seen in Figure 5.2A with respect to the

monomer fluorescence. This behavior indicates that as the (-/+) ratio is increased from 0.2 to 1.0, the state of the Py-3-12 surfactants changes from unassociated to aggregated. Since Py-3-12 cannot micellize below its CMC, this behavior implies that electrostatic interactions between CT-DNA and Py-3-12 must promote the formation of Py-3-12/CT-DNA complexes. The steep increase in excimer fluorescence intensity at the equicharge point was followed by a more gradual decrease in Figure 5.2B for (-/+) ratios ranging between 1.0 and 11.5. To better quantify the amount of excimer formed, Figure 5.2C shows a plot of the I_E/I_M ratio as a function of the (-/+) ratio. The I_E/I_M-*vs*-(-/+) profile shown in Figure 5.2C confirms that the formation of Py-3-12/CT-DNA complexes occurs over a narrow range of (-/+) ratios, and seems to be complete at the equicharge point since the I_M/I_M ratio reaches a maximum at a (-/+) = 1.0, followed by a small gradual decrease with increasing (-/+) ratio. While the I_1/I_3 ratio is typically taken as a measure of the polarity of the local environment probed by an excited pyrenyl label, the SSF spectra of Py-3-12 showed very little resolution between the two main fluorescence peaks to determine the location of the third peak. Consequently, the I_1/I_3 ratio was not calculated for Py-3-12, as it is well-established that its sensitivity to the polarity of its local environment is much more reduced than for PyO-3-12.[30,49] Nevertheless and regardless of this complication, the trends shown in Figure 5.2 establish that complexation between Py-3-12 and CT-DNA occurs around the equicharge point due to electrostatic interactions between the two oppositely charged molecules.

The change in the state of the Py-3-12 surfactant from unassociated to aggregated on CT-DNA, that had been identified in Figure 5.2 from the analysis of the SSF spectra, could be quantified by applying the MFA to the TRF decays acquired with the 10 μM Py-3-12 solutions prepared with different CT-DNA concentrations. he MFA yielded the molar fractions f_{free}, f_{diff}, and f_{agg} of the pyrene species in solution, where f_{free} represents the unassociated pyrenes, that emit as if they were free in solution with the pyrene monomer lifetime τ_M, f_{diff} describes the

pyrenes that form excimer via diffusive encounters, and f_{agg} accounts for the pre-aggregated pyrenes, that form excimer instantaneously upon direct excitation.[34-36] The other useful parameter retrieved from the MFA of the TRF decays is <*k*>, which is the average rate constant for PEF. Finally, the MFA also yields the lifetimes τ_{E0} and τ_D for two excimers formed between two well and two poorly stacked pyrenyl labels, respectively.[34-36]

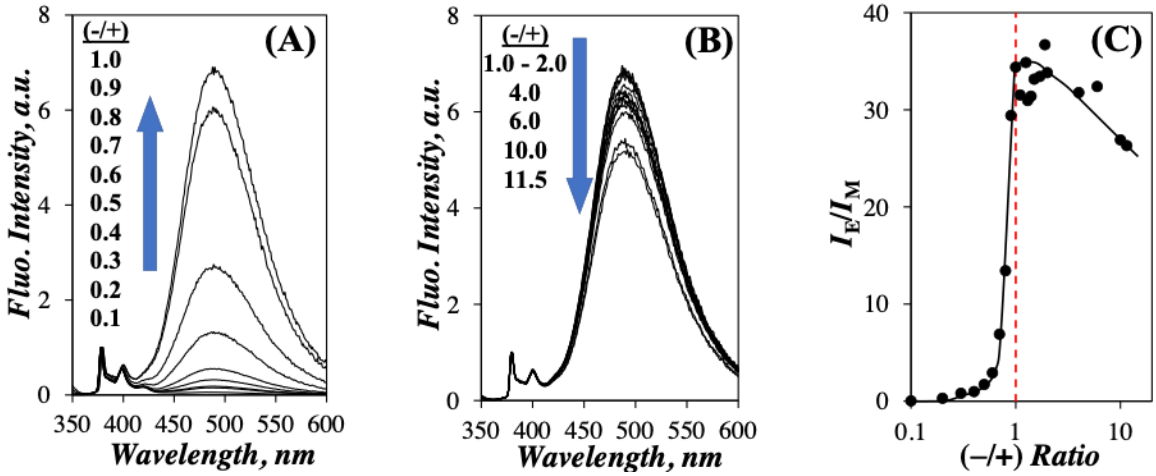

Figure 5.2 Normalized SSF spectra for (-/+) ratios ranging from A) 0.2 to 1.0 and B) 1.0 to 11.5. C) Plot of the I_E/I_M ratio as a function of the (-/+) ratio for Py-3-12 and CT-DNA. [Py-3-12] = 10 μM, λ_{ex} = 344 nm, red vertical dashed line in Figure 5.2C marks the equicharge point.

The different pyrene molar fractions were plotted as a function of the (-/+) ratio in Figure 5.3A. At a low (-/+) ratio of 0.1, where [Py-3-12] is 10 times higher than [CT-DNA], f_{free} equals 0.70 indicating that Py-3-12 is mostly unassociated. Upon increasing [CT-DNA], f_{free} decreases continuously to a value of zero at the equicharge point, where all Py-3-12 is now bound to CT-DNA, and f_{free} remains equal to zero as [CT-DNA] is increased past the equicharge point. The decrease in f_{free} observed in Figure 5.3A with increasing (-/+) ratio is accompanied by an increase in f_{diff} until it reached a maximum value of 0.8 at the equicharge point, and remained equal to 0.80 (±0.04) for (-/+) ratios ranging from 1 to 2 before decreasing slightly at higher (-/+) ratios. The molar fraction representing the aggregated pyrenes, f_{agg}, remains low and equal to 0.06 (±0.05) for (-/+) ratios below 0.6 before increasing to 0.24

(±0.03) for (-/+) ratios greater than 1.3. The simultaneous decrease in f_{free} and increase in f_{diff} observed in Figure 5.3A with increasing (-/+) ratio confirm the binding of Py-3-12 to CT-DNA, where the high local pyrene concentration $[Py]_{loc}$ results in effective PEF that occurs mostly by diffusive encounters (large f_{diff}) and partly through direct excitation of pyrene aggregates (low f_{agg}). Increasing the (-/+) ratio past the equicharge point must spread the Py-3-12 domains along CT-DNA but does not seem to affect the composition of these domains based on the fairly constant f_{diff} and f_{agg} values obtained for (-/+) ratios between 1 and 11.5.

Further information about the composition of the Py-3-12 aggregates generated around CT-DNA can be inferred from the behavior of $<k>$, which was plotted as a function of the (-/+) ratio in Figure 5.3B. One most remarkable aspect of the $<k>$-*vs*-(-/+) plot in Figure 5.3B is that $<k>$ remained more or less constant and equal to 0.25 (±0.03) ns^{-1} for (-/+) ratios between 0.2 and 11.5. As shown in Equation 5.2, $<k>$ is equal to the product $k_{diff}\times[Py]_{loc}$, where k_{diff} is the bimolecular rate constant for PEF by diffusive encounters. The constancy of $<k>$ indicates that $[Py]_{loc}$ remains constant for (-/+) ratios below and above the equicharge point suggesting that the Py-3-12/CT-DNA complexes retain a same local composition, even as increasing (-/+) ratios lead to the spreading of the Py-3-12 aggregates along CT-DNA. Yet, these separate Py-3-12 aggregates generated through complexation with CT-DNA appear to retain the same composition as the Py-3-12 aggregates generated at low (-/+) ratios, where a large excess of Py-3-12 is present compared to CT-DNA. This conclusion is supported by the constancy of the I_E/I_M ratio in Figure 5.2C, the molar fractions f_{free}, f_{diff}, f_{agg} in Figure 5.3A, and the rate constant $<k>$ in Figure 3B for (-/+) ratios larger than unity.

$$<k> = k_{diff}\times[Py]_{loc} \qquad (5.2)$$

Another interesting observation is the difference between the gradual changes observed with the molar fractions in Figure 5.3A compared to the drastic transition observed with the I_E/I_M ratio in Figure 5.2C. To assess whether the parameters retrieved form the MFA of the Py-

3-12 TRF decays properly described the photophysical phenomena taking place during PEF, these parameters were combined into Equation 5.3 to calculate $(I_E/I_M)^{MFA}$, which is the absolute I_E/I_M ratio for the Py-3-12 solutions.[50,51] In Equation 5.3, the molar fractions f_{diffE0} and f_{E0} represent those pyrenyl labels that form the well-stacked excimer *E*0* by diffusion and direct excitation of a pyrene aggregate, while the molar fractions f_{diffD} and f_D represent those pyrenyl labels that form the poorly stacked excimer *D** by diffusion and direct excitation of a pyrene aggregate, respectively. The sums $f_{diffE0} + f_{diffD}$ and $f_{E0} + f_D$ equal f_{diff} and f_{agg}, respectively, which were represented in Figure 5.3A as a function of the (-/+) ratio. $(I_E/I_M)^{MFA}$ was then compared in Figure 5.3C to the relative I_E/I_M ratio shown in Figure 5.2C, which had been determined from the analysis of the SSF spectra. The absolute $(I_E/I_M)^{MFA}$ ratio was found to match the relative I_E/I_M ratio well when plotted as a function of the (-/+) ratio, thus confirming the validity of the parameters retrieved from the MFA of the TRF decays. The main reason for the apparent difference in behavior between the gradual change in the molar fractions in Figure 5.3A and the significant change in I_E/I_M in Figures 5.2C and 5.3C around the equicharge point can be traced back to the significant difference in the 3.8 (±0.3) ns average lifetime $<\tau>$ of the pyrenyl labels forming excimer by diffusion in a Py-3-12/CT-DNA complex and the τ_M value of 100 ns for unassociated Py-3-12 surfactants in the denominator of Equation 5.3. The decrease in f_{free} from 0.7 to zero and the increase in f_{diff} from 0.29 to 0.88 in Figure 5.3A leads to a 20-fold decrease in the denominator of Equation 5.3, from 71 to 3.3 ns, resulting in the massive increase in I_E/I_M around the equicharge point in Figure 5.2C. Above the equicharge point, f_{diff} and f_{agg} remain constant within experimental error and equal to 0.75 (±0.03) and 0.24 (±0.03), respectively, indicating that PEF proceeds mainly through diffusive encounters between pyrenyl labels inside a Py-3-12/CT-DNA complex.

$$\left(I_E/I_M\right)^{MFA}=\frac{\left(f_{diffE0}\tau_{E0}+f_{diffD}\tau_D\right)<\tau><k>+f_{E0}\tau_{E0}+f_D\tau_D}{f_{diff}<\tau>+f_{free}\tau_M} \tag{5.3}$$

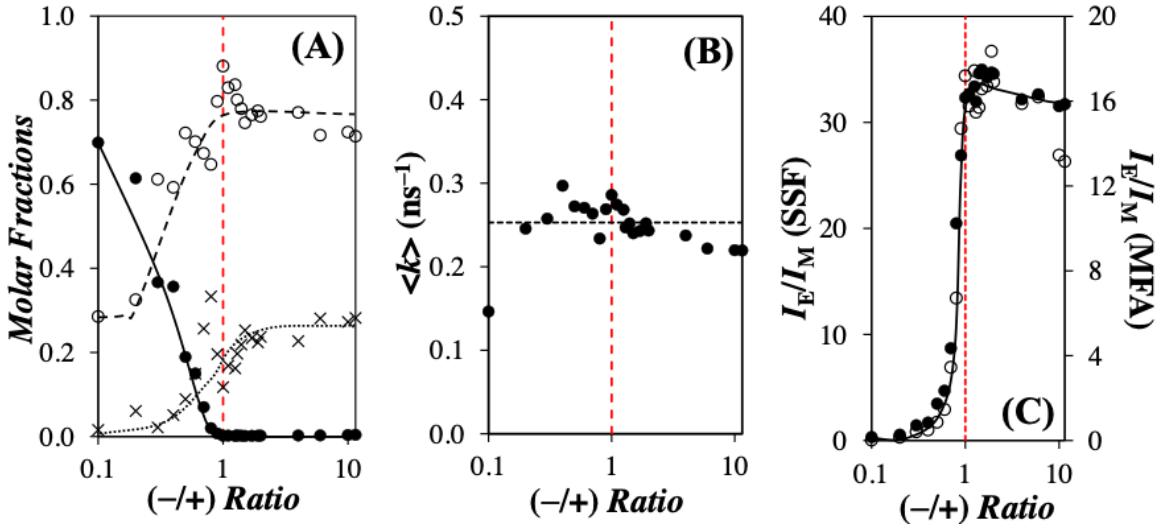

Figure 5.3 Plots of A) Py-3-12 molar fractions (●) f_{free}, (×) f_{agg}, and (○) f_{diff}, B) the average rate constant (<*k*>) for PEF, and C) the I_E/I_M ratio obtained from (●) the MFA analysis of the TRF decays and (○) the analysis of the SSF spectra as a function of the (-/+) ratio.

One aspect missing in the detailed study conducted up to this point on the interactions between Py-3-12 and CT-DNA was the characterization of the polarity of the interior of the Py-3-12/CT-DNA complexes. The lack of sensitivity of Py-3-12 to the polarity of its environment is well-established and is due to the hexyl linker connecting pyrene to the ammonium head group.[30,49] Such alkyl substituents are known to strongly attenuate the sensitivity of the resulting pyrene derivative to the polarity of its environment. Fortunately, this problem can be circumvented by introducing a heteroatom such as an oxygen in the position beta to pyrene as was done with the surfactant PyO-3-12, whose structure is shown in Figure 5.1B.[30,49] Consequently, the same fluorescence experiments conducted with Py-3-12 were repeated with PyO-3-12, starting with the SSF spectra, which are shown in Figures 5.4A and B. The SSF spectra were acquired with a constant PyO-3-12 concentration equal to 16 mM, 24-fold lower than its CMC equal to 0.38 mM. The fluorescence spectra of PyO-3-12 show the

same behavior as those of Py-3-12, with little excimer being formed at low (-/+) ratios, but showing a rapid increase in PEF as the (-/+) ratio approaches unity. Past the equicharge point, the excimer signal remained high indicating strong PEF, although a small decrease was observed for increasing (-/+) ratios. These trends were summarized in Figure 5.4C, where the I_E/I_M ratio was plotted as a function of the (-/+) ratio. The significant increase in I_E/I_M observed at the equicharge point confirms the binding of PyO-3-12 to CT-DNA, since PyO-3-12 at a concentration of 16 μM could not micellize in solution. The similarity between the plots shown in Figure 5.2 and in Figure 5.4 indicates that, despite the intrinsic differences between the CMC of Py-3-12 and PyO-3-12, their binding to CT-DNA occurs in a similar manner, suggesting that their complexation with CT-DNA is controlled exclusively through electrostatic interactions. The advantage of using PyO-3-12 over Py-3-12 is that the former PyLGS is sensitive to the polarity of its local environment through the I_1/I_3 ratio.[30] I_1/I_3 was plotted in Figure 5.4C as a function of the (-/+) ratio. For (-/+) ratios lower than the equicharge point, I_1/I_3 remained constant and equal to 1.70 (±0.01), close to the I_1/I_3 ratio reported to equal 1.73 for PyO-3-12 in water.[30] However, the I_1/I_3 ratio showed a significant and sudden drop at the equicharge point, above which it equaled 1.34 (±0.03) for (-/+) ratios larger than 1.3. An I_1/I_3 ratio of 1.34 is similar to that of PyO-3-12 in 2-propanol and 1-hexanol,[30] but is larger than the I_1/I_3 ratio of 1.23 (±0.03)[52] for PyO-3-12/SDS complexes and smaller than the I_1/I_3 ratio of 1.44 (±0.02) for PyO-3-12 in SDS micelles.[30,53] The I_1/I_3 ratio found for the PyO-3-12/CT-DNA complexes suggests that PyO-3-12 experiences a more and less polar environment than that experienced within the PyO-3-12/SDS complexes and inside the SDS micelles, respectively.

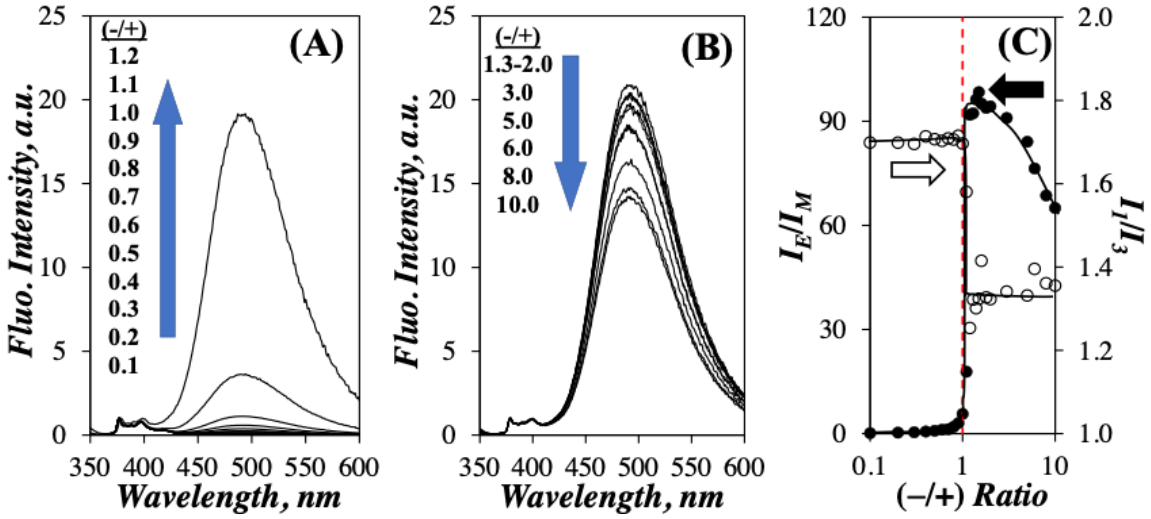

Figure 5.4 Normalized SSF spectra for (-/+) ratios ranging from A) 0 to 1.2 and B) 1.3 to 10, and C) plot of I_E/I_M and I_1/I_3 as a function of the (-/+) ratio. [PyO-3-12] = 16 μM, λ_{ex} = 344 nm.

As for Py-3-12, a more comprehensive understanding of the PyO-3-12/CT-DNA complexes was obtained through the MFA of the monomer and excimer TRF decays to yield the molar fractions f_{free}, f_{diff}, and f_{agg} and $\langle k \rangle$ shown in Figures 5.5A and B, respectively. As for Py-3-12, the molar fraction of the unassociated pyrenes, f_{free}, decreased continuously with increasing [CT-DNA] in Figure 5.5A from 0.75 at a (-/+) ratio of 0.1, indicating that PyO-3-12 is mostly unassociated at low CT-DNA concentration, to 0 at a (-/+) ratio of 1.1 slightly above the equicharge point. From this point on, all PyO-3-12 surfactants were complexed with CT-DNA and f_{free} remained equal to 0 for any (-/+) ratio greater than 1.1. Above the equicharge point, f_{diff} and f_{agg} remained constant and equal to 0.39 (±0.01) and 0.60 (±0.01), respectively. This represents a marked difference between the complexes generated with Py-3-12 and PyO-3-12, where PEF occurred mainly through diffusive encounters between pyrenyl labels and direct excitation of pyrene aggregates, respectively. As we had observed earlier for the PyO-3-12 micelles,[30] the oxygen atom in the linker connecting pyrene to the ammonium of PyO-3-12 appears to promote pyrene aggregation in the PyO-3-12/CT-DNA complexes.

<*k*> was also calculated for PyO-3-12 and plotted as a function of the (-/+) ratio in Figure 5.5B. <*k*> reached a constant value of 0.23 (±0.01) ns^{-1} for (-/+) ratios between 0.6 and 5. <*k*> obtained for the PyO-3-12/CT-DNA complexes was similar to the <*k*> value of 0.25 (±0.03) ns^{-1} found for the Py-3-12/CT-DNA complexes for (-/+) ratios between 0.2 and 11.5. The similarity of the <*k*> values obtained for both PyLGS suggests that PEF occurs in a similar manner inside a PyLGS/CT-DNA complex. The narrower range of (-/+) ratios over which <*k*> remains constant for PyO-3-12 in Figure 5.5B is most likely due to the oxygen atom in the linker connecting pyrene to the ammonium ion, which has been shown to weaken the hydrophobicity of PyO-3-12 compared to Py-3-12, resulting in an increase in the CMC from 0.15 mM for Py-3-12[29] to 0.38 mM for PyO-3-12.[30] As for the PyO-3-12 micelles, the larger f_{agg} found for the PyO-3-12/CT-DNA complexes indicates an increased aggregation of the pyrenyl labels due to their crowding at the periphery of the hydrophobic interior induced by the oxygen atom in the linker, which wants to interact with the more polar interface. On the one hand, the increased pyrene aggregation might yield more cohesive PyO-3-12/CT-DNA complexes, but on the other hand, this spatial arrangement results in heterogeneous PyO-3-12 aggregates, with a soft interior made of dodecyl chains and a hard shell made of aggregated pyrenyl labels. This heterogeneity might explain the decrease in <*k*> at (-/+) ratios greater than 6 for the PyO-3-12/CT-DNA complexes, as it indicates a less stable PyO-3-12 aggregate more prone to breakage upon increasing the CT-DNA concentration above the equicharge point. The more cohesive Py-3-12/CT-DNA complexes appear to remain stable even at a (-/+) ratio of 11.5 in Figure 5.4B, since <*k*> retains a same value at this high (-/+) ratio. Nevertheless and regardless of the different stability of the PyLGS:CT-DNA complexes, both PyLGS showed a range of (-/+) ratios centered around the equicharge point for which the chemical composition of the complexes remained constant.

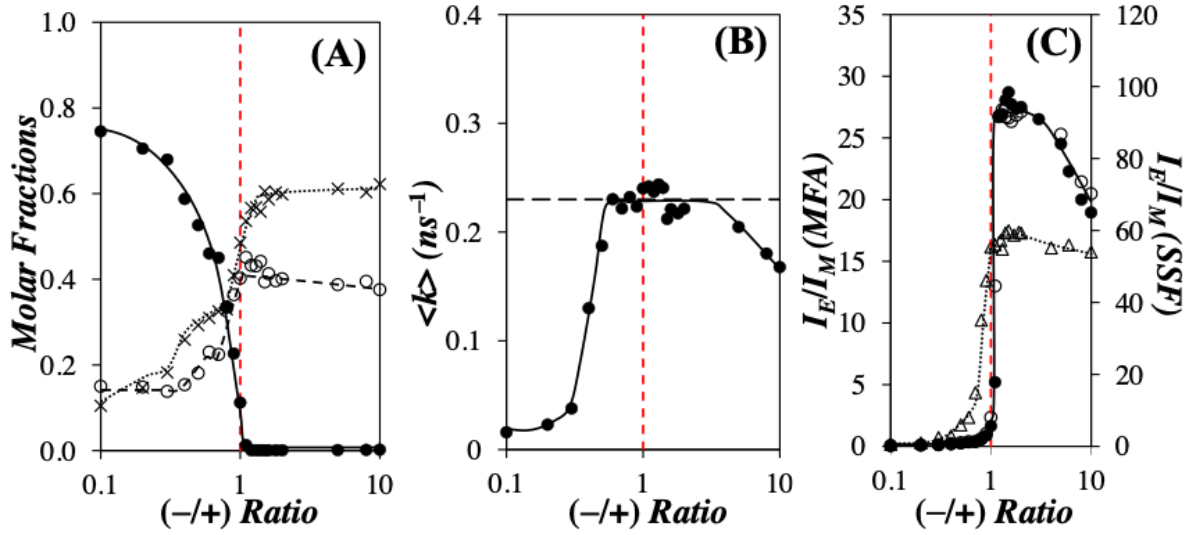

Figure 5.5 Plots of A) the PyO-3-12 molar fractions (●) f_{free}, (×) f_{agg}, and (○) f_{diff}, B) the average rate constant (<*k*>) for PEF, and C) the I_E/I_M ratio obtained from the MFA analysis of the TRF decays for (○) PyO-3-12 and (△) Py-3-12 and (●) the analysis of the SSF spectra as a function of (-/+) ratio. [PyO-3-12] = 16 μM.

The validity of the parameters retrieved through the MFA of the TRF decays of PyO-3-12 was assessed by applying Equation 3 to calculate $(I_E/I_M)^{MFA}$ for PyO-3-12 and comparing it in Figure 5.5C to the I_E/I_M ratio retrieved from the analysis of the SSF spectra of the PyO-3-12 solutions. The trends obtained with the TRF decays and SSF spectra showed a nice agreement, thus confirming the validity of the MFA. Since $(I_E/I_M)^{MFA}$ represents the absolute I_E/I_M ratio, which is not affected by changes in lamp intensity, spectral features between a 1-pyrenehexyl or 1-pyrenemethoxy derivative, or slit width that plague any quantitative comparison of I_E/I_M ratios obtained from SSF spectra,[51,52] the $(I_E/I_M)^{MFA}$ ratio could be compared for Py-3-12 and PyO-3-12 in Figure 5.5C as a function of the (-/+) ratio. Although both $(I_E/I_M)^{MFA}$-*vs*-(-/+) ratio profiles showed similar features, with a marked increase at the equicharge point for both Py-3-12 and PyO-3-12, $(I_E/I_M)^{MFA}$ for (-/+) ratios greater than unity was significantly larger for PyO-3-12 than for Py-3-12. This result is a consequence of the strong pyrene aggregation found for the PyO-3-12/CT-DNA complexes, which results in

enhanced PEF through direct excitation of pyrene aggregates, which is a more efficient process for PEF than via diffusive encounters between pyrenyl moieties.

The decreased stability of the PyO-3-12/CT-DNA complexes discussed earlier could prove to be an important feature for gene delivery, as it might allow an easier release of its polynucleotide cargo from the complex upon interaction with a cell membrane. To assess the stability of the PyO-3-12/CT-DNA complexes in the presence of other amphiphilic molecules, a complex was prepared with 16 μM of PyO-3-12 and a 1.5:1.0 (-/+) ratio. These conditions ensured that all the PyO-3-12 surfactants would be bound to CT-DNA. Furthermore, the ability of PyO-3-12 to respond to the polarity of its local environment was expected to help the characterization of the interactions expected to occur between the PyO-3-12/CT-DNA complexes and SDS. The stability of the complexes was determined by monitoring their fluorescence response as a function of the concentration of SDS, a negatively charged surfactant, which was added to the solution. To this end, the SSF spectra and TRF decays were acquired and their analysis yielded the fluorescence intensity ratios I_E/I_M, $(I_E/I_M)^{MFA}$, and I_1/I_3, the molar fractions f_{free}, f_{diff}, and f_{agg}, and the average rate constant $<k>$ for PEF, which were plotted as a function of [SDS] in Figures 5.6A – D for the PyO-3-12 solutions with and without CT-DNA for comparison purposes.

The I_E/I_M ratios obtained from the analysis of the SSF spectra and MFA of the TRF decays were plotted in Figure 5.6A as a function of [SDS]. At low [SDS], the I_E/I_M ratio equals zero for PyO-3-12 without CT-DNA, since PyO-3-12 is unassociated and cannot form excimer but takes a non-zero value for PyO-3-12 complexed with CT-DNA, since the high $[Py]_{loc}$ in the PyO-3-12/CT-DNA complexes allows PEF. For [SDS] larger than 0.5 mM, the I_E/I_M and $(I_E/I_M)^{MFA}$ ratios obtained for PyO-3-12 with CT-DNA match those obtained for PyO-3-12 without CT-DNA, indicating that in this [SDS] range, PyO-3-12 is no longer bound to CT-DNA and is now complexed with SDS. The perfect match observed between $(I_E/I_M)^{MFA}$ and

I_E/I_M for PyO-3-12 with DNA for [SDS] larger than 0.5 mM highlights the significant difference between the two ratios at low [SDS]. This difference is attributed to the large level of pyrene aggregation found with the PyO-3-12/CT-DNA complexes (see Figure 5.6B at low [SDS]). Equation 5.3 used to calculate $(I_E/I_M)^{MFA}$, assumes that excimers formed through diffusive encounters and direct excitation of a pyrene aggregate emit with the same efficiency. Departure from this ideal behavior as shown in Figure 5.6A for $(I_E/I_M)^{MFA}$ and I_E/I_M at low [SDS] indicates the presence of non-emissive pyrene aggregates, whose existence has been well-documented.[54-57] Increasing [SDS] leads to a decrease in $(I_E/I_M)^{MFA}$ as f_{agg} decreases in Figure 5.6B. These changes reflect interactions between SDS and the PyO-3-12/CT-DNA complexes, which continue up to the equicharge point, when [SDS] equals 32 mM.

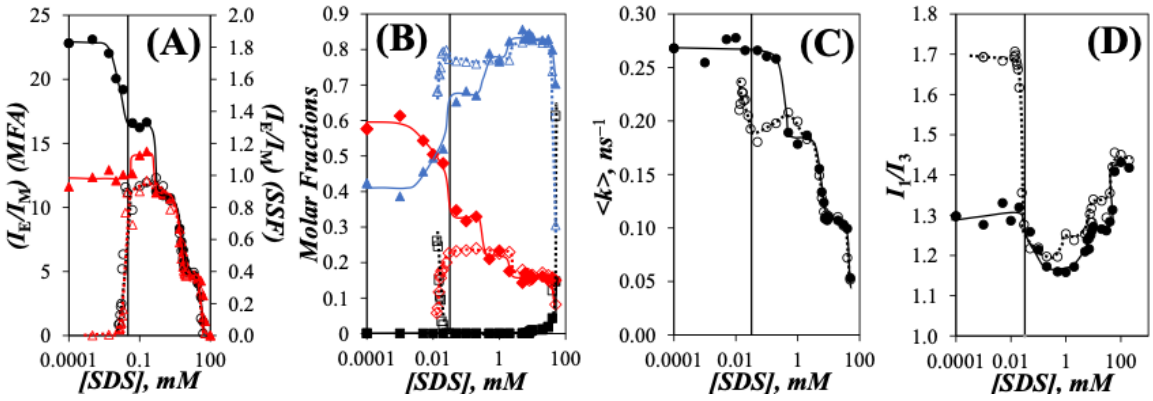

Figure 5.6 Plots of A) the ratios (red triangle) I_E/I_M and (black circle) $(I_E/I_M)^{MFA}$, B) the molar fractions (black square) f_{free}, (blue triangle) f_{diff}, and (red diamond) f_{agg}, C) the average rate constant <*k*>, and D) the I_1/I_3 ratio. (filled) PyO-3-12 with DNA and SDS and (empty) PyO-3-12 with SDS. [PyO-3-12] = 16 μM, [PyO-3-12]:[CT-DNA] = 1.5. The vertical line shows the equicharge point where [PyO-3-12]:[SDS] equals unity.

The changes in the molar fractions f_{diff} and f_{free} observed in Figure 5.6B for [SDS] between 0.1 and 32 μM can have two origins. The addition of SDS to the PyO-3-12/CT-DNA complexes could lead to either the formation of PyO-3-12/SDS complexes as was discussed in Chapter 4, or the association of SDS with the PyO-3-12/CT-DNA complexes. If the release of

PyO-3-12 from the PyO-3-12/CT-DNA complexes to form PyO-3-12/SDS complexes were complete at an [SDS] of 32 mM as indicated in Figure 5.6A-D for the PyO-3-12 solutions without CT-DNA, as was discussed in Chapter 4, all the parameters such as the I_E/I_M, $(I_E/I_M)^{MFA}$, and I_1/I_3 ratios, f_{free}, f_{diff}, and f_{agg}, and $<k>$ for the PyO-3-12 solutions with CT-DNA should approach the values obtained for the PyO-3-12 solutions without CT-DNA. Instead, the I_E/I_M and $(I_E/I_M)^{MFA}$ ratios, f_{free}, f_{diff}, and f_{agg}, and $<k>$ for the solutions with and without DNA remained different between the equicharge point and 0.5 mM in Figures 5.6A – D, suggesting that the SDS molecules associate with the PyO-3-12/CT-DNA complexes for [SDS] between 0.1 and 32 μM, and generate a PyO-3-12/CT-DNA/SDS *ter*-complex that remains stable at [SDS] between 32 μM and 0.5 mM. The association of SDS molecules with PyO-3-12/CT-DNA complexes must replace some contact points between the PyO-3-12 surfactants and the CT-DNA phosphates, resulting in looser complexes. In fact, the association of 32 mM SDS with the PyO-3-12/CT-DNA complexes prepared with 16 μM PyO-3-12 suggests that each negatively charged CT-DNA molecule might be coated with a layer of positively charged PyO-3-12 being itself coated by an additional layer of negatively charged SDS. Further addition of SDS for [SDS] between 32 μM and 0.5 mM appears to not change the composition of the PyO-3-12/CT-DNA/SDS complexes. Since the PyO-3-12/CT-DNA/SDS complexes would be negatively charged at an [SDS] equal to 32 μM, they would repel additional SDS molecules, which would explain why their composition remains unchanged for [SDS] between 32 μM and 0.5 mM based on the constant I_E/I_M ratios in Figure 5.6A, constant $<k>$ values in Figure 5.6C, and constant molar fractions in Figure 5.6B.

For [SDS] greater than 0.5 mM, all the parameters obtained for PyO-3-12 with CT-DNA behaved in the same manner as for PyO-3-12 without CT-DNA. This result strongly suggests that for [SDS] larger than 0.5 mM, PyO-3-12 no longer interacts with CT-DNA and forms complexes solely with SDS. In other words, CT-DNA has been released from the PyO-

3-12/CT-DNA complexes. The interactions between PyO-3-12 and SDS over the entire [SDS] range were described in detail in Chapter 4.

TEM imaging was conducted to confirm the nature of the conformational changes inferred from the fluorescence measurements, which occurred due to the addition of SDS to the PyO-3-12/CT-DNA aggregates. Figure 5.7 shows three different TEM micrographs for a (–/+) ratio of 1.5 with and without SDS added to the aggregates. Figure 5.7A shows that without SDS added to the PyO-3-12/CT-DNA aggregates, lamellar structures formed between PyO-3-12 and CT-DNA. The lamellar arrangement of the CT-DNA and the PyO-3-12 surfactants rationalized why the I_1/I_3 ratio of 1.34 (±0.03) for the PyO-3-12/CT-DNA aggregates was lower than that of 1.47 (±0.01) for PyO-3-12 in SDS micelles, since a lamellar arrangement minimizes exposure of pyrenyl tail of PyO-3-12 to water. The lamellae appear homogeneous suggesting that the CT-DNA molecules were oriented parallel to each other and within less than 2 nm, the resolution of the TEM instrument. This would suggest that the CT-DNA molecules might have been bridged by the two ammonium head groups of PyO-3-12 surfactants, that would hold the CT-DNA molecules within less than 2 nm.

Addition of 32 μM SDS to the PyO-3-12/CT-DNA aggregates led to a conformational change of the complexes in Figure 5.7B, whereby individual CT-DNA strands could be observed inside the PyO-3-12/CT-DNA aggregates. The dark lines representing the CT-DNA molecules stained with uranyl acetate were separated by 5-6 nm thick layers. This spacing, slightly larger than the 4.0 nm diameter of an SDS micelles, would suggest that a column of SDS might have inserted itself between two CT-DNA molecules coated with a layer of PyO-3-12 surfactants resulting in CT-DNA molecules and SDS columns being stabilized by the head groups of PyO-3-12.

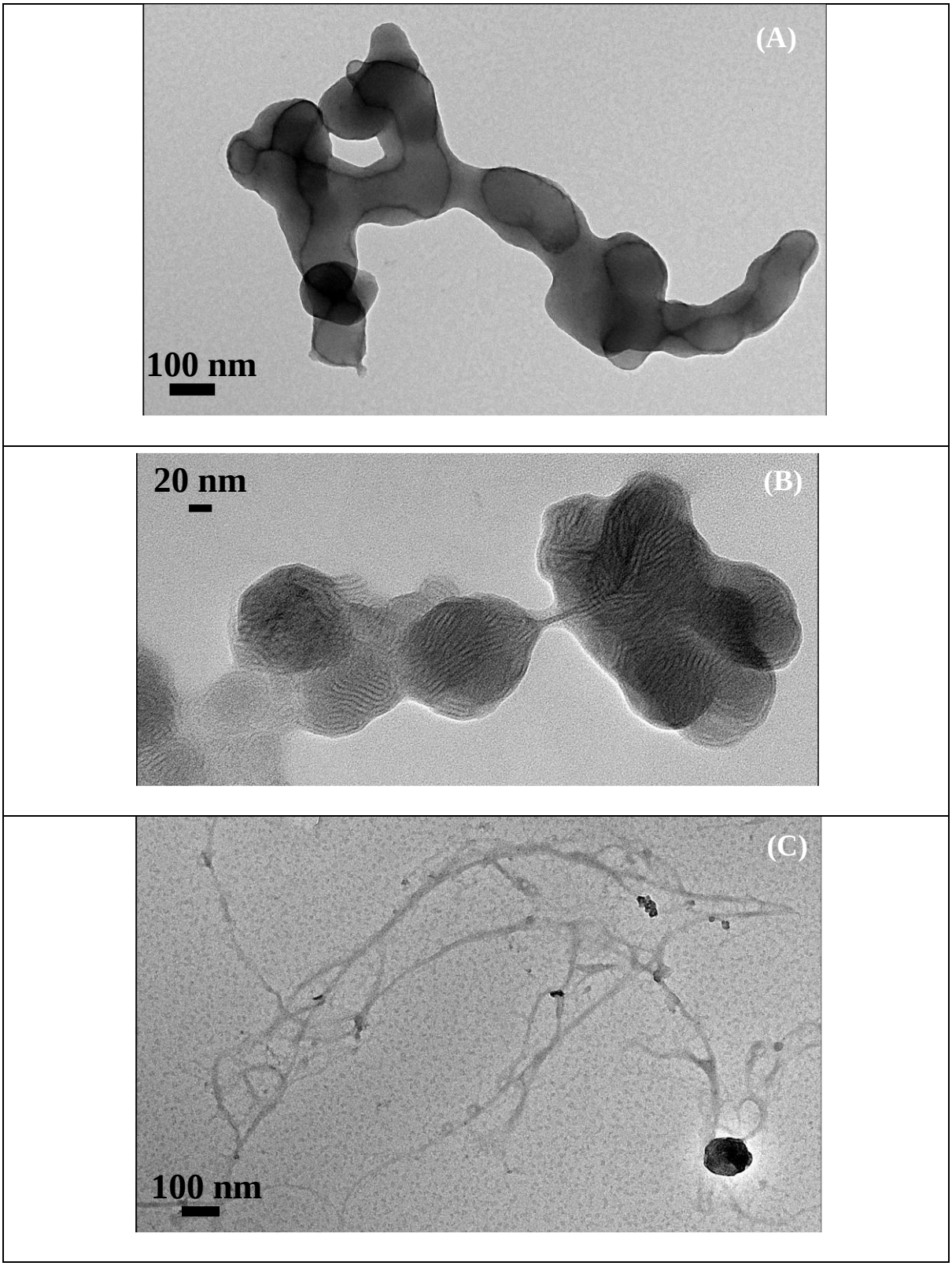

Figure 5.7 TEM micrographs for PyO-3-12/CT-DNA complexes at a (–/+) ratio of 1.5 taken (A) without SDS, (B) [SDS] = 32 μM, and (C) 100 μM. [PyO-3-12] = 16 μM, [CT-DNA] = 24 μM.

The introduction of an SDS column between the CT-DNA molecules would provide the flexibility required to generate the sacks of compacted CT-DNA observed in Figure 5.7B. The looser arrangement of the CT-DNA molecules observed in Figure 5.7B might be the result of their transition from a lamellar conformation in Figure 5.7A into a hexagonal conformation in Figure 5.7B. Further addition of SDS results in the release of some CT-DNA in Figure 5.7C, where the SDS concentration equals 100 μM. Some PyO-3-12/CT-DNA aggregates could still be observed at that SDS concentration, which was lower than 0.5 mM, where complete release of the CT-DNA cargo had been identified by the fluorescence experiments.

The observations made regarding the PyO-3-12:CT-DNA complexes and their associations with SDS are summarized in Figure 5.8. At [SDS] lower than 1 μM, the SDS molecules do not appear to interact with the PyO-3-12/CT-DNA aggregates and all the parameters in Figure 5.6 are constant. Since individual CT-DNA molecules are not observed in the lamellar PyO-3-12/CT-DNA aggregates shown in Figure 5.7A, it suggests that the CT-DNA molecules are held within less than 2 nm apart. This could be achieved if the propyl spacer of PyO-3-12 would bridge two CT-DNA molecules via the two ammonium headgroups. Such an arrangement would hold the CT-DNA molecules within less than 2 nm resulting in rigid lamellae, that would appear homogeneous in the TEM images. For [SDS] between 1 and 32 μM, changes in the molar fractions f_{free} and f_{diff} in Figure 5.6B led to the conclusions that SDS molecules would associate with the PyO-3-12/CT-DNA aggregates. This association stopped at an [SDS] of 32 μM, suggesting that each PyO-3-12 molecules in a PyO-3-12/CT-DNA aggregate was paired with two SDS molecules. This striking feature led to the conclusion that each negatively charged CT-DNA molecule must have been coated by a layer of positively charged PyO-3-12, where one ammonium cation would be paired with a CT-DNA phosphate and the other ammonium cation being associated with a negatively charged sulfate headgroup of an SDS molecule. The SDS column would have a diameter of 4 nm, equivalent to the

diameter of an SDS micelle, and would interact with a sheath of PyO-3-12 surfactants wrapping the CT-DNA molecules. The layers separating the Ct-DNA molecules would thus be constituted of the SDS column 4 nm in diameter flanked by the spacers of two PyO-3-12 surfactants amounting to a 5-6 nm thickness. These SDS columns would

This spatial arrangement of the surfactants around CT-DNA would ensure that the positively charged ammonium cations of PyO-3-12 would interact with the negatively charged phosphates of CT-DNA, while their hydrophobic tails would be surrounded by the dodecyl groups of the SDS molecules. The entire assembly would expose the SDS sulfates to the aqueous phase, preventing further interactions with SDS molecules. Further addition of SDS would increase the ionic strength of the solution, which would weaken the electrostatic interactions of the PyO-3-12/CT-DNA/SDS assemblies to the point where the formation of PyO-3-12/SDS complexes would be favored. This seemed to occur for an [SDS] of 0.5 mM, above which all PyO-3-12 molecules were associated into PyO-3-12/SDS complexes in a process that released CT-DNA from the PyO-3-12/CT-DNA/SDS assemblies.

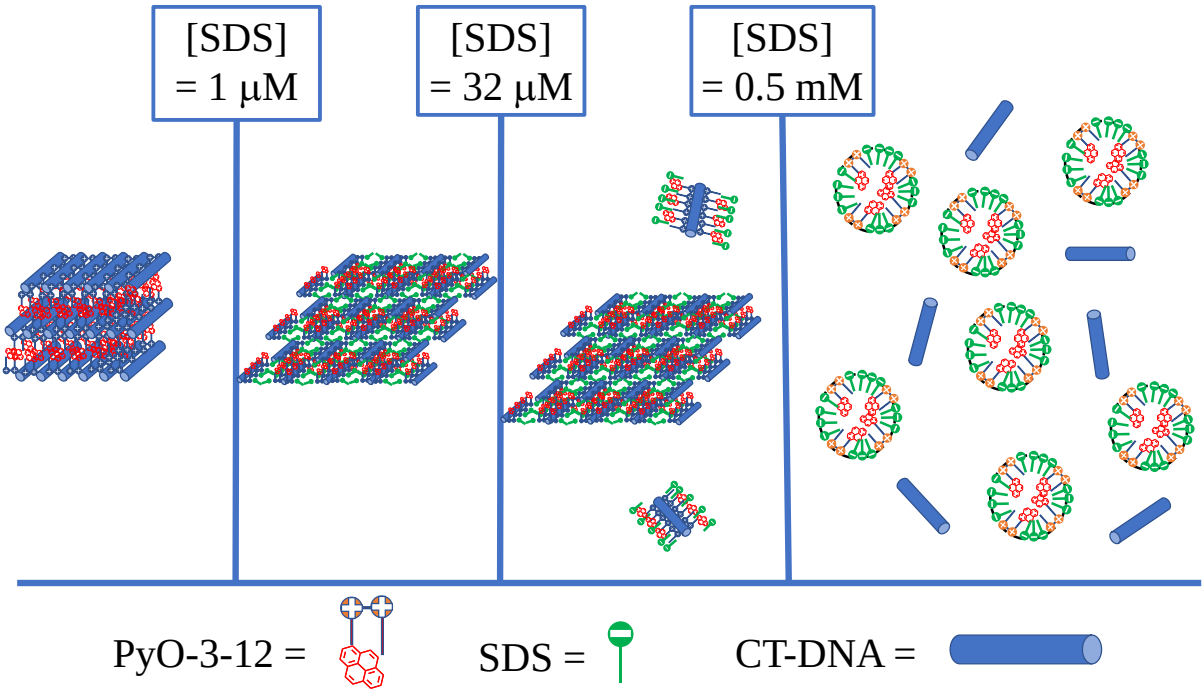

Figure 5.8 Schematic representation of the different states of the PyO-3-12:CT-DNA complexes being fully aggregated for [SDS] < 1 μM, associating with SDS for 1 μM < [SDS] < 32 μM, forming complexes of individual CT-DNA coated with one layer of PyO-3-12 and another surrounding layer of SDS for 32 μM < [SDS] < 0.5 mM, and being fully dissociated for [SDS] > 0.5 mM with released CT-DNA and PyO-3-12:SDS complexes.

5.5. **Conclusion**

The interactions between CT-DNA and two PyLGS, namely Py-3-12 and PyO-3-12, were characterized by SSF and TRF. The MFA of the TRF decays yielded the molar fractions f_{free}, f_{diff}, and f_{agg} representing the different pyrene species in solution, which provided information about the states of the different pyrenyl labels and the average rate constant $\langle k \rangle$ for PEF, which reflected $[Py]_{loc}$ inside the PyLGS/CT-DNA complexes, and the $(I_E/I_M)^{MFA}$ ratio, which represents an absolute measure of the I_E/I_M ratio determined by SSF. Analysis of the SSF spectra yielded the I_E/I_M ratio, which reflected the PEF efficiency in the PyLGS/CT-DNA complexes and the I_1/I_3 ratio for PyO-3-12, which offered an insight into the polarity of the local environment probed by an excited pyrenyl label. With all these spectroscopic tools in

hand, the association between the PyLGS and CT-DNA was investigated by taking advantage of the pyrenyl fluorescence to probe these interactions at the molecular level.

The interactions between the PyLGS and CT-DNA were investigated first. The fluorescence data indicated that all PyLGS were bound to CT-DNA at the equicharge point, since f_{free} was nil for (-/+) ratios equal to and larger than unity. Interestingly, the hydrophobic domains generated through the association of the PyLGS with CT-DNA had a similar chemical composition at (-/+) ratios lower and higher than unity, between 0.2 and 11.5 for Py-3-12 and between 0.6 and 5 for PyO-3-12. This conclusion was reached by examining the constancy of $<k>$ over this range of (-/+) ratios since $<k>$ responds to $[Py]_{loc}$ and a constant $<k>$ implied that the domains generated through the complexation of the PyLGS and CT-DNA had a similar [PyLGS]. The narrower range of constant $<k>$ values found for PyO-3-12 suggested that the PyO-3-12/CT-DNA complexes might not be as stable as the Py-3-12/CT-DNA complexes. This meant that the PyO-3-12/CT-DNA complexes might be more easily disrupted in the presence of an amphiphilic molecule like SDS, which would result in the release of their polynucleotide cargo. These considerations led to the study of the interactions of the PyO-3-12/CT-DNA complexes prepared with 16 μM of PyO-3-12 and a (-/+) ratio equal to 1.5 as SDS was added to the solution. Monitoring the parameters obtained through the analysis of the SSF spectra and TRF decays as a function of [SDS] led to the identification of four [SDS] regimes, which were described in Figure 5.8. No interactions took place between SDS and the PyO-3-12/CT-DNA complexes at [SDS] lower than 1 μM. Associations between SDS and PyO-3-12/CT-DNA complexes took place for [SDS] between 1 and 32 μM, the latter concentration marking a [SDS]/[PyO-3-12] ratio of 2. The 32 μM [SDS] denoted the point where all CT-DNA molecules were double-coated by a first layer of PyO-3-12 stabilized by a second layer of SDS. These PyO-3-12/CT-DNA/SDS assemblies were negatively charged and remained stable for [SDS] between 32 μM and 0.5 mM. For [SDS] greater than 0.5 mM, all PyO-3-12

associated with SDS molecules to form PyO-3-12/SDS complexes in a manner that released CT-DNA from the PyO-3-12/CT-DNA/SDS complexes. TEM micrographs in Figure 5.7 corroborate these findings. Consequently, this study has illustrated how PyLGS can be employed to probe the interactions between gemini surfactants and polynucleotides, and how the SSF spectra, TRF decays of PyLGS solutions, and TEM can be interpreted to better understand the complex interactions taking place between polynucleotides and positively and negatively charged surfactants.

Chapter 6 Conclusions & Future Work

6.1. **Conclusions**

The end goal of this thesis was to characterize the interactions of two pyrene-labeled gemini surfactants (PyLGS) with calf thymus (CT-DNA) using various fluorescence techniques based principally on the formation of an excimer between an excited and a ground-state pyrene and different parameters retrieved from the analysis of the steady-state fluorescence (SSF) spectra and the model free analysis (MFA) of the time-resolved fluorescence (TRF) decays. The two pyrene-labeled gemini surfactants (PyLGS) used in this thesis were referred to as Py-3-12 and PyO-3-12 and were constituted of two dimethylammonium cations linked by a propyl spacer with one ammonium bearing a dodecyl chain and the other either a 1-pyrenehexyl group or a 1-pyrenemethoxyhexyl group, respectively. The synthesis of Py-3-12 followed a modified version of the procedure described by Wang et al,[1] whereas PyO-3-12 was a novel gemini surfactant, which required that further changes be made to the protocol developed by Wang et al.[1] The interactions of these two PyLGS with oppositely charged molecules, namely sodium dodecyl sulfate (SDS) and CT-DNA, were studied.

The study of the interactions between the PyLGS and SDS or CT-DNA took full advantage of the unique spectral properties of the pyrenyl dyes. Analysis of the fluorescence data through SSF and TRF provided a comprehensive molecular level description of how the PyLGS self-assembled into micelles or formed complexes with oppositely charged molecules in solution. Analysis of the SSF spectra yielded the ratio I_E/I_M of the fluorescence intensity of the excimer over that of the monomer, which reflected the efficiency of pyrene excimer formation (PEF), and the ratio I_1/I_3 of the first to the third fluorescence peak in the fluorescence spectrum of the pyrene monomer, which provided a measure of the polarity of the local environment surrounding the pyrenyl label. The MFA of the TRF decays yielded the molar fractions f_{diff}, f_{free}, and f_{agg} of the pyrenyl labels that formed excimer through diffusive encounter between an excited and a ground-state pyrene, were isolated and could not form an excimer, or

formed excimer through direct excitation of a pyrene aggregate, respectively. In turn, these molar fractions reflected the state of the PyLGS in solution, whether they were aggregated in a micelle or a complex or unassociated. Finally, the average rate constant <*k*> for PEF provided a measure of the internal dynamics experienced by the pyrenyl label as well as a measure of the local pyrene concentration ($[Py]_{loc}$) inside a PyLGS micelle or complex. These parameters provided a battery of observables, that together depicted an accurate representation of the associations undergone by the PyLGS under a variety of conditions.

The synthesis and characterization of Py-3-12 was described in Chapter 2. First, the CMC of Py-3-12 was determined by surface tension measurements and through the MFA of the TRF decays acquired with Py-3-12 solutions, as was first described by Keyes-Baig et al.[2] The concentration of free pyrene, that does not form excimer during its lifetime and reflects the concentration of unassociated Py-3-12 ($[\text{Py-3-12}]_{free}$), was determined through the MFA of the fluorescence decays as a function of [Py-3-12]. Since $[\text{Py-3-12}]_{free}$ must plateau above the micelle critical concentration (CMC) to a value equal to the CMC, the plateau value of the $[\text{Py-3-12}]_{free}$-*vs*-[Py-3-12] plot was taken as the CMC and found to equal 0.15 (±0.01) mM, in agreement with the CMC of 0.15 (±0.02) mM determined from the surface tension. The excellent agreement between the two methods confirmed the value of the MFA to determine the CMC of pyrene-labeled surfactants.

The other parameter that needed to be determined was the aggregation number (N_{agg}) of the Py-3-12 micelles, because it defines the size of the micelles. The determination of N_{agg} for surfactants is typically achieved by introducing hydrophobic fluorophore and quencher molecules to a solution of the surfactant above its CMC, to induce the binding of the probes to the surfactant micelles. Then, analysis of the fluorescence data reporting on the inhibition of the fluorophore by the quencher yields the average number <*n*> of quencher molecules per micelle. N_{agg} can then be determined from a plot representing <*n*> as a function of quencher

concentration. However, since the pyrenyl fluorophore was covalently bound to the surfactant, pyrene could not be used as a molecular probe physically bound to the PyLGS micelles as done with the traditional procedure applied to determine N_{agg}, since the pyrenyl labels of the PyLGS in the micelles would drown the signal from pyrene used as a fluorescent probe. A modification to the well-established methodology described in the literature[3-5] was needed to determine N_{agg} for Py-3-12 and PyO-3-12 in Chapters 2 and 3, respectively. Taking advantage of the rapid pyrene excimer formation (PEF) occurring inside the Py-3-12 micelles, the fluorescence of the pyrene excimer, instead of that of the pyrene monomer, was quenched with dinitrotoluene. N_{agg} for the Py-3-12 micelles was found to equal 14.0 (±0.2). The analytical tools, that were described in Chapter 2 to determine the CMC and N_{agg} for Py-3-12, could be easily applied to study other PyLGS such as PyO-3-12 as was described in Chapter 3.

PyO-3-12 was introduced in Chapter 3 to address the problem that the hexamethylene linker used to connect pyrene to the dimethyl ammonium cation of Py-3-12 led to a significant decrease in the sensitivity of the pyrenyl label to the polarity of its local environment. Fortunately, this issue could be circumvented by introducing an oxygen atom in the linker at the β-position to pyrene. Preparation of PyO-3-12, where pyrene was connected to the dimethyl ammonium cation via a methoxyhexyl linker, restored the ability of the pyrene label to probe the polarity of its local environment, in agreement with an earlier report.[6] The improved sensitivity of PyO-3-12 to the polarity of its local environment was demonstrated from the much broader range of I_1/I_3 ratios, that were obtained for PyO-3-12 in different solvents, compared to the much narrower range of I_1/I_3 ratios found for Py-3-12. This additional feature made PyO-3-12 a better probe to study the interactions between PyLGS and oppositely charged molecules. However, the different chemical structure of PyO-3-12 compared to Py-3-12 meant that its CMC and N_{agg} values needed to be determined. The CMC was found to equal 0.33 (±0.02) mM and 0.43 (±0.04) mM by fluorescence and surface tension measurements,

respectively, taking an average value of 0.38 (±0.05) mM. The CMC values 0.15 (±0.02) and 0.38 (±0.05) mM for Py-3-12 and PyO-3-12 were reasonable. The larger CMC determined for PyO-3-12 was attributed to the oxygen atom that made the surfactant more water-soluble compared to Py-3-12, which had a lower CMC. N_{agg} for PyO-3-12 was found to equal 23 (±2). The increase in N_{agg} from 14 for Py-3-12 to 23 for PyO-3-12 was also attributed to the presence of the oxygen atom in the linker connecting pyrene to the dimethyl ammonium of PyO-3-12. By positioning itself at the micellar interface between the hydrophobic core and water, the oxygen atom induced a wider spread between the tail bearing the pyrenyl label, which located itself at the micelle interface, and the dodecyl chain, which resided in the micellar interior. This spread between the two hydrophobic tails resulted in an increase in the packing parameter of PyO-3-12 compared to that of Py-3-12, which was associated with an increase in the micellar size and N_{agg}. The full characterization of the properties of both PyLGS opened the study of their association with negatively charged SDS and CT-DNA.

The study of the interactions between PyO-3-12 and SDS was described in Chapter 4. Mixtures of oppositely charged surfactants such as PyO-3-12 and SDS have found many practical applications[7-10] and the study of their properties with fluorescence techniques, which were developed in Chapters 2 and 3, has the potential to uncover novel physical phenomena that would help improve their properties. In the experiments described in Chapter 4, the concentration of PyO-3-12 was kept equal to either 1, 4, or 16 μM, which was below its CMC of 0.38 mM to ensure that it could not micellize, while the concentration of SDS was varied from 0 to 200 mM. The PyO-3-12 and SDS mixtures were studied using both SSF and TRF. The SSF results showed that the formation of PyO-3-12/SDS complexes began below and stopped at the equicharge point, above which the complexes stayed stable up to an [SDS] of 1 – 2 mM, at which point more SDS molecules associated with the PyO-3-12/SDS complexes. The PyO-3-12/SDS complexes swelled until the CMC of 8 mM for SDS was reached. Further

addition of SDS led to its micellization and the composition of the PyO-3-12/SDS complexes remained unchanged for [SDS] between 8 and 30 mM, above which the complexes disintegrated, giving way to the formation of SDS micelles hosting a single PyO-3-12 molecule at [SDS] greater than 50 mM. The findings made about the associations between PyO-3-12 and SDS based on the analysis of the SSF spectra were supported by the parameters retrieved from the MFA of the TRF decays acquired with mixtures of PyO-3-12 and SDS. The conclusions reached about these interactions were summarized in Figure 4.8, which describes the different [SDS] regimes, controlling the association of PyO-3-12 and SDS. The three series of experiments conducted with [PyO-3-12] equal to 1, 4, and 16 μM showed similar profiles with the main difference between all three series being the [SDS] at the equicharge point, which marked the completion of the formation of the PyO-3-12/SDS complexes. The series with 1 μM PyO-3-12 was also found to have lower I_E/I_M and I_1/I_3 ratios between the equicharge point and the CMC of SDS compared to the more concentrated PyO-3-12 solutions. This difference was attributed to the size of the PyO-3-12/SDS complexes, which decreased with decreasing [PyO-3-12], larger complexes shielding the pyrenyl labels from exposure from water and resulting in lower I_1/I_3 ratios, while leading to a more rigid interior that decreased pyrene-pyrene encounters and led to lower I_E/I_M ratios. The large transitions observed by fluorescence at the equicharge point indicated that PyO-3-12 showed a high sensitivity toward the concentration of oppositely charged amphiphilic molecules, suggesting that these pyrene-labeled gemini surfactants could be applied for the detection of oppositely charged molecules and macromolecules, such as proteins, polyanions, and DNA. This observation led to the study of the interactions between the PyLGS and CT-DNA described in Chapter 5.

The use of SSF and TRF to characterize the interactions between the PyLGS and CT-DNA, and the stability of the PyO-3-12/CT-DNA complexes in the presence of SDS was illustrated in Chapter 5. The study of the associations between the three different components,

namely PyLGS, CT-DNA, and SDS, took full advantage of the pyrenyl label of the PyLGS to apply PEF for the characterization of their behavior as the three components interacted with each other. The experiments were performed at a constant concentration of 10 and 16 μM for Py-3-12 and PyO-3-12, respectively. These concentrations were below their respective CMC, thus ensuring that any excimer formed would be due to their complexation with DNA or SDS molecules, which were added to the PyLGS solutions. The results were discussed by plotting the different parameters retrieved from the analysis of the SSF spectra and TRF decays as a function of the (-/+) ratio, equal to the CT-DNA concentration expressed in base pairs divided by the Py-3-12 concentration. The parameters obtained by fluorescence led to the conclusion that the addition of CT-DNA led to the complexation of Py-3-12, whereby all the Py-3-12 surfactants were bound to CT-DNA past the equicharge point corresponding to a (–/+) ratio of 1. Since $<k>$ reported on $[Py]_{loc}$, the constancy of $<k>$ for (–/+) ratios between 0.2 and 11.5 indicated that the chemical composition of the PyO-3-12/CT-DNA complexes remained the same over this [CT-DNA] range. To assess the robustness of these conclusions, the experiments were repeated with PyO-3-12. The results were essentially the same, showing complexation of PyO-3-12 with CT-DNA around the equicharge point, with all the PyO-3-12 surfactants being bound to CT-DNA for (–/+) ratios greater than 1. The oxygen atom in the linker connecting the pyrenyl label to the ammonium cation of PyO-3-12 was found to reduce the stability of the PyO-3-12/CT-DNA complexes over a narrower range of (–/+) ratios between 0.6 and 5 compared to what had been found for Py-3-12. The lower stability of the PyO-3-12/CT-DNA complexes combined with the ability of PyO-3-12 to sense the polarity of its local environment led to the selection of these complexes for an additional study aiming to assess their stability in the presence of another amphiphilic molecule, namely SDS. PyO-3-12/CT-DNA complexes were prepared with 16 μM PyO-3-12 and a (–/+) ratio equal to 1.5 with the excess CT-DNA ensuring that all the PyO-3-12 surfactants were bound to CT-DNA.

A decrease in f_{agg} and an increase in f_{diff} observed upon addition of SDS to the PyO-3-12/CT-DNA solution led to the conclusion that the association of SDS with the complexes was taking place for [SDS] between 1 and 32 μM, with the upper [SDS] marking the point where [SDS] equals 2×[PyO-3-12]. Since further SDS addition did not change the composition of the ternary PyO-3-12/CT-DNA/SDS complexes that were generated, it suggested that the addition of SDS had led to the dissociation of the CT-DNA molecules. At this point, the dissociated CT-DNA molecules were coated with a surfactant double layer with the ammonium cations of PyO-3-12 being in direct contact with the CT-DNA phosphates and the dodecyl tails of SDS stabilizing the assembly by interacting with the hydrophobic chains of PyO-3-12 in a manner that presented the sulfate groups to the aqueous phase. Dissociation of the PyO-3-12/CT-DNA/SDS complexes occurred at [SDS] greater than 0.5 mM. At this point, the CT-DNA molecules were released and PyO-3-12 formed complexes with SDS.

6.2. **Future Work**

The procedures described in Chapters 2 and 3 to find the CMC and the aggregation number of pyrene-labeled gemini surfactants can be applied to the study and characterization of more PyLGS. These new PyLGS could have different tail lengths, spacers, and headgroups. Studying the effect that changing different parameters in these surfactants might have on CMC and N_{agg} will provide insight into the effect that the chemical composition of these PyLGS has on their properties. The synthesis and characterization of these new PyLGS should be accompanied by transfection studies to assess their ability to deliver a polynucleotide cargo to cells. The development of these different PyLGS would help the selection of the best molecular features that would favor transfection and other practical applications for gemini surfactants.

The experiments conducted in Chapters 4 and 5 highlighted the sensitivity of the I_E/I_M ratio to the complexation of PyLGS with negatively charged molecules such as SDS and CT-DNA. Considering that the interactions between SDS and the PyLGS were observed for PyLGS

concentration as low as 1 μM, these experiments suggested that PyLGS could be used for detection purposes, where the concentration of an analyte of interest in aqueous solution could be detected by monitoring the I_E/I_M ratio as a function of PyLGS concentration. In this context, it would be worthwhile to optimize the chemical composition of the PyLGS. For instance, the introduction of an oxygen atom in the linker of PyO-3-12 led to a three-fold increase in its I_E/I_M ratio compared to that of Py-3-12 for the study in Chapter 5, describing the binding of PyLGS to CT-DNA for (–/+) ratios larger than unity. Further adjustments of the molecular parameters controlling the chemical structure of the PyLGS could enhance their detection limit toward analytes of interest such as proteins, polyanions, and polypeptides. Standard proteins like bovine serum albumin BSA could be used to assess the value of this application.

The results obtained in Chapter 5 illustrated a methodology that can be employed to characterize the interactions between DNA and different PyLGS in the presence of other amphiphilic molecules. This methodology could be applied to probe how changing different molecular parameters in the PyLGS structure, such as the tail length, spacer lengths, and the nature of the headgroups, would affect the strength of these interactions. While CT-DNA is an interesting polynucleotide to study, it would be worth investigating the interactions of PyLGS with other polynucleotides such as different mRNA samples, which have become of great scientific interest during the COVID pandemic. Another aspect that could be further explored would be the addition of the helper lipid 1,2-dioleoyl-sn-glycero-3-phosphoethanolamine (DOPE), which is often used in transfection applications. Finally, the high sensitivity of fluorescence allows one to probe the interactions of PyLGS with other molecules at infinitely low concentrations, requiring minimal amounts of valuable materials. It would be worthwhile to confirm the conclusions reached about the morphologies of the PyLGS complexes formed with SDS or CT-DNA through the PEF-based methodology developed in this thesis with other techniques like cryo-TEM and small angle X-ray scattering (SAXS).

6.3. **Summary**

It was demonstrated in this thesis how a combination of SSF and TRF can be applied to provide quantitative and insightful details about the interactions between polynucleotides and oppositely charged PyLGS in solution. These studies took advantage of the recently introduced MFA of TRF decays acquired with PyLGS solutions to yield information about the state, either complexed or unassociated, of the PyLGS in aqueous solution. In turn, this information could be applied to draw conclusions about the morphology expected for different complexes involving the PyLGS. The concepts introduced in this thesis should be relevant to the study of the interactions between any cationic PyLGS and anionic molecules, a most intriguing field of research.

References

Chapter 1

1. Menger, F. M.; Littau, C. A. Gemini Surfactants: A New Class of Self-Assembling Molecules. *J. Am. Chem. Soc*. **1993**, *115*, 10083–10090.
2. De, S.; Aswal, V. K.; Goyal, P. S.; Bhattacharya, S. Characterization of New Gemini Surfactant Micelles with Phosphate Headgroups by SANS and Fluorescence Spectroscopy. *Chem. Phys. Lett.* **1999**, *303*, 295–303.
3. Zana, R.; Lévy, H.; Kwetkat, K. Mixed Micellization of Dimeric (Gemini) Surfactants and Conventional Surfactants. I. Mixtures of an Anionic Dimeric Surfactant and of the Nonionic Surfactants. *J. Colloid Interface Sci.* **1998**, *197*, 370–376.
4. Rehman, J.; Sowah-Kuma, D.; Stevens, A. L.; Bu, W.; Paige, M. F. Mixing Behavior in Binary Anionic Gemini Surfactant-Perfluorinated Fatty Acid Langmuir Monolayer. *Langmuir* **2017**, *33*, 10205–10215.
5. Wang, K.; Dou, H.-X.; Wang, M.-M.; Xing, S.-Y.; Wang, X.-Y. Synthesis of Two Anionic Gemini Surfactants and Their Self-Assembly Induced by the Complexation of Calixpyridinium. *Langmuir* **2018**, 34, 8052–8057.
6. Devínsky, F.; Lacko, I.; Imam, T. Relationship between Structure and Solubilization Properties of Some Bisquaternary Ammonium Amphiphiles. *J. Colloid Interface Sci.* **1991**, *143*, 336–342.
7. Alami, E.; Levy, H.; Zana, R.; Skoulios, A. Alkanediyl-.α.,.ω.-bis(dimethylalkyl ammonium bromide) Surfactants. 2. Structure of the Lyotropic Mesophases in the Presence of Water. *Langmuir* **1993**, 9, 940–944.
8. Zana, R.; Levy, H.; Papoutsi, D.; Beinert, G. Micellization of Two Triquaternary Ammonium Surfactants in Aqueous Solution. *Langmuir* **1995**, 11, 3694–3698.

9. Rosenzweig, H. S.; Rakhmanova, V. A.; MacDonald, R. C. Diquarternary Ammonium Compounds as Transfection Agents. *Bioconjug. Chem.* **2001**, *12*, 258-263.
10. Wang, C.; Wettig, S. D.; Foldvari, M.; Verrall, R. E. Synthesis, Characterization, and Use of Asymmetric Pyrenyl-Gemini Surfactants as Emissive Components in DNA-Lipoplex Systems. *Langmuir* **2007**, *23*, 8995–9001.
11. Zhao, W.; Song, K.; Chen, Y.; Wang, H.; Liu, Z.; Shi, Q.; Huang, J.; Wang, Y. Aggregation of a Cationic Gemini Surfactant with a Chelating Molecule and Effects from Calcium Ions. *Langmuir* **2017**, *33*, 12719–12728.
12. Pisárčik, M.; Polakovičová, M.; Markuliak, M.; Lukáč, M.; Devínsky, F. Self-Assembly Properties of Cationic Gemini Surfactants with Biodegradable Groups in the Spacer. *Molecules* **2019**, *24*, 1481.
13. Zana, R.; Benrraou, M.; Rueff, R. Alkanediyl-α,ω-bis(dimethylalkylammonium bromide) Surfactants. 1. Effect of the Spacer Chain Length on the Critical Micelle Concentration and Micelle Ionization Degree. *Langmuir* **1991**, 7, 1072–1075.
14. Zana, R.; Talmon, Y. Dependence of Aggregate Morphology on Structure of Dimeric Surfactants. *Nature* **1993**, *362*, 228–230.
15. Karaborni, S.; Esselink, K.; Hilbers, P. A.; Smit, B.; Karthauser, J.; van Os, N. M.; Zana, R. Simulating the Self-Assembly of Gemini (Dimeric) Surfactants. *Science* **1994**, *266*, 254–256.
16. Sidenko, Z. S.; Limanov, V. E.; Skvortsova, E. K.; Dziomko, V. M. Synthesis and Antibacterial Activity of some Bisammonium Compounds. *Khimiko-Farmatsevticheskii Zhurnal* **1968**, *2*, 15-18.
17. Menger, F. M.; Littau, C. A. Gemini Surfactants: Synthesis and Properties. *J. Am. Chem. Soc.* **1991**, *113*, 1451-1452.

18. Menger, F. M.; Keiper, J. S. Gemini Surfactants. *Angew. Chem. Int. Ed.* **2000**, *39*, 1906-1920.
19. Zana, R.; Xia, J. *Gemini Surfactants: Synthesis, Interfacial and Solution-Phase Behavior, and Applications*, Marcel Dekker, Inc., New York, 2004.
20. Han, Y.; Wang, Y. Aggregation Behavior of Gemini Surfactants and their Interactions with Macromolecules in Aqueous Solution. *Phys. Chem. Chem. Phys.* **2011**, *13*, 1939-1956.
21. Kirby, A. J.; Camilleri, P.; Engberts, J. B. F. N.; Feiters, M. C.; Nolte, R. J. M.; Söderman, O.; Bergsma, M.; Bell, P. C.; Fielden, M. L.; Garcia Rodriguez, C. L.; Guédat, P.; Kermer, A.; McGregor, C.; Perrin, C.; Ronsin, G.; van Eijk, M. C. P. Gemini Surfactants: New Synthetic Vectors for Gene Transfection. *Angew. Chem. Int. Ed.* **2003**, *42*, 1448-1457.
22. Cardoso, A. M. S.; Silva, S. G.; do Vale, M. L.; Marques, E. F.; Pedroso de Lima, M. C.; Jurado, A. S. Gene Delivery Mediated by Gemini Surfactants: Structure – Activity Relationships in Engineering of Nanobiomaterials – Applications of Nanobiomaterials. Ed. Grumezescu, A. M., Elsevier, 2016, pp 227 – 256.
23. Ahmed, T.; Kamel, A. O.; Wettig, S. D. Interactions Between DNA and Gemini Surfactants: Impact on Gene Therapy: Part I. *Nanomedicine* **2016**, *11*, 289-306.
24. Sharma, V. D.; Ilies, M. A. Heterocyclic Cationic Gemini Surfactants: A Comparative Overview of Their Synthesis, Self-Assembling, Physicochemical, and Biological Properties. *Med. Res. Rev.* **2012**, *34*, 1–44.
25. Kamal, M. S. A Review of Gemini Surfactants: Potential Application in Enhanced Oil Recovery. *J. Surfact. Deterg.* **2016**, *19*, 223-236.
26. Dong, Z.; Zheng, Y.; Zhao, J. Synthesis, Physico-Chemical Properties and Enhanced Oil Recovery Flooding Evaluation of Novel Zwitterionic Gemini Surfactants. *J. Surfactant Deterg.* **2014**, *17*, 1213–1222.

27. Xu, D.-Q.; Pan, Z.-W. Phase-Transfer Catalysis of a New Cationic Gemini Surfactant with Ester Groups for Nucleophilic Substitution Reaction. *Chin. Chem. Lett.* **2014**, *25*, 1169–1173.
28. Kumar, N.; Tyagi, R. Industrial Applications of Dimeric Surfactants: A Review. *J. Disper. Sci. Technol.* **2014**, *35*, 205-214.
29. Rosen, M. J.; Tracy, D. J. Gemini Surfactants. *J. Surfactants Deterg.* **1998**, *1*, 547– 554.
30. Bombelli, C.; Giansanti, L.; Luciani, P.; Mancini, G. Gemini Surfactant Based Carriers in Gene and Drug Delivery. *Curr. Med. Chem.* **2009**, *16*, 171–183.
31. Oblak, E.; Piecuch, A.; Rewak-Soroczynska, J.; Paluch, E. Activity of Gemini Quaternary Ammonium Salts against Microorganisms. *Appl. Microbiol. Biotechnol.* **2019**, *103*, 625-632.
32. Wu, Z-Y.; Fang, Z.; Qiu, L-G.; Wu, Y.; Li, Z-Q.; Xu, T.; Wang, W.; Jiang, X. Synergistic Inhibition Between the Gemini Surfactant and Bromide Ion for Steel Corrosion in Sulphuric Acid. *J. Appl. Electrochem.* **2009**, *39*, 779–784.
33. Labena, A.; Hegazy, M. A.; Horn, H.; Müller, E. Cationic Gemini Surfactant as a Corrosion Inhibitor and a Biocide for High Salinity Sulfidogenic Bacteria Originating from an Oil-field Water Tank. *J. Surfactant Deterg.* **2014**, *17*, 419–431.
34. Datir, K.; Shinde, H.; Pratap, A. P. Preparation of a Gemini Surfactant from Mixed Fatty Acid and its Use in Cosmetics. *Tenside Surfact. Det.* **2021**, *58*, 67–73.
35. Danino, D., Talmon, Y., Zana, R. Alkanediyl-.α.,.ω.-bis(dimethylalkylammonium bromide) Surfactants (Dimeric Surfactants). 5. Aggregation and Microstructure in Aqueous Solutions. *Langmuir* **1995,** *11*, 1448-1456.
36. Israelachvili, J. N. *Intermolecular and Surface Forces*; 3rd ed.; Academic Press, Elsevier: Amsterdam, 2012.

37. Alami, E.; Beinert, G.; Marie, P.; Zana, R. Alkanediyl-.α.,.ω.-bis(dimethyl alkylammonium bromide) Surfactants. 3. Behavior at the Air-Water Interface. *Langmuir* **1993,** *9*, 1465-1467.
38. Zana, R. Dimeric (Gemini) Surfactants: Effect of the Spacer Group on the Association Behavior in Aqueous Solution. *J. Colloid Interface Sci.* **2002,** *248*, 203-220.
39. Israelachvili, J. N.; Mitchell, D. J.; Ninham, B. W. Theory of Self-Assembly of Hydrocarbon Amphiphiles into Micelles and Bilayers. *J. Chem. Soc. Faraday Trans* **1976**, *72*, 1525-1568.
40. Karlsson, L.; van Eijk, M. C. P.; Söderman, O. Compaction of DNA by Gemini Surfactants: Effects of Surfactant Architecture. *J. Colloid Interface Sci.* **2002,** *252*, 290-296.
41. Myers, D. *Surfactant Science and Technology*; 3rd Ed.; John Wiley & Sons, Inc., 2006.
42. Fisicaro, E.; Compari, C.; Bacciottini, F.; Contardi, L.; Barbero, N.; Viscardi, G.; Quagliotto, P.; Donofrio, G.; Różycka-Roszak, B.; Misiak, P.; Woźniak, E.; Sansone, F. Nonviral Gene Delivery: Gemini Bispyridinium Surfactant-Based DNA Nanoparticles. *J. Phys. Chem. B* **2014**, *118*, 13183-13191.
43. Foldvari, M.; Wettig, S.; Badea, I.; Verrall, R.; Bagonluri, M. Dicationic Gemini Surfactant Gene Delivery Complexes Contain Cubic-Lamellar Mixed Polymorphic Phase. *NSTI Nanotech* **2006**. Vol. 2; Boston, MA; 400–403.
44. Foldvari, M.; Badea, I.; Wettig, S.; Verrall, R.; Bagonluri, M. Structural Characterization of Novel Gemini Non-Viral DNA Delivery Systems for Cutaneous Gene Therapy. *J. Exp. Nano Sci.* **2006,** *1*, 165-176.
45. Wang, H.; Wettig, S. D. Synthesis and Aggregation Properties of Dissymmetric Phytanyl-Gemini Surfactants for Use as Improved DNA Transfection Vectors. *Phys. Chem. Chem. Phys.* **2011,** *13*, 637-642.

46. Rädler, J. O.; Koltover, I.; Salditt, T.; Safinyia, C. R. Structure of DNA-Cationic Liposome Complexes: DNA Intercalation in Multilamellar Membranes in Distinct Interhelical Packing Regime. *Science* **1997**, *275*, 810-814.

47. Koltover, I.; Salditt, T.; Rädler, J. O.; Safinya, C. R. An Inverted Hexagonal Phase of Cationic Liposome-DNA Complexes Related to DNA Release and Delivery. *Science* **1998**, *281*, 78- 81.

48. Li, X.; Wettig, S. D.; Wang, C.; Foldvari, M.; Verrall, R. E. Synthesis and Solution Properties of Gemini Surfactants Containing Oleyl Chains. *Phys. Chem. Chem. Phys.* **2005**, *7*, 3172- 3178.

49. Fisicaro, E.; Compari, C.; Bacciottini, F.; Contardi, L.; Pongiluppi, E.; Barbero, N.; Viscardi, G.; Quagliotto, P.; Donofrio, G.; Krafft, M. P. Nonviral Gene-Delivery by Highly Fluorinated Gemini Bispyridinium Surfactant-Based DNA Nanoparticles. *J. Colloid Interface Sci.* **2017**, *487*, 182–191.

50. Quagliotto, P.; Barolo, C.; Barbero, N.; Barni, E.; Compari, C.; Fisicaro, E.; Viscardi, G. Synthesis and Characterization of Highly Fluorinated Gemini Pyridinium Surfactants. *Eur. J. Org. Chem.* **2009**, *19*, 3167–3177.

51. Mintzer, M. A.; Simanek, E. E. Nonviral Vectors for Gene Delivery. *Chem. Rev.* **2008**, *109*, 259-302.

52. Johnsson, M.; Engberts, J. B. Novel Sugar-Based Gemini Surfactants: Aggregation Properties in Aqueous Solution. *J. Phys. Org. Chem.* **2004**, *17*, 934-944.

53. Wasungu, L.; Scarzello, M.; van Dam, G.; Molema, G.; Wagenaar, A.; Engberts, J. B.; Hoekstra, D. Transfection Mediated by pH-Sensitive Sugar-Based Gemini Surfactants; Potential for in Vivo Gene Therapy Applications. *J. Mol. Med.* **2006**, *84*, 774-784.

54. Johnsson, M.; Wagenaar, A.; Stuart, M. C.; Engberts, J. B. Sugar-based Gemini Surfactants with pH-dependent Aggregation Behavior: Vesicle-to-Micelle Transition, Critical Micelle Concentration, and Vesicle Surface Charge Reversal. *Langmuir* **2003**, *19*, 4609-4618.
55. Cardoso, A. M.; Morais, C. M.; Cruz, A. R.; Silva, S. G.; do Vale, M. L.; Marques, E. F.; De Lima, M. C. P.; Jurado, A. S. New Serine-derived Gemini Surfactants as Gene Delivery Systems. *Eur. J. Pharm. Biopharm.* **2015**, *89*, 347-356.
56. Cardoso, A. M.; Morais, C. M.; Silva, S. G.; Marques, E. F.; De Lima, M. C. P.; Jurado, M. A. S. Bis-quaternary Gemini Surfactants as Components of Nonviral Gene Delivery Systems: A Comprehensive Study from Physicochemical Properties to Membrane Interactions. *Int. J. Pharm.* **2014**, *474*, 57-69.
57. Faneca, H.; Simões, S.; Pedroso de Lima, M. C. Evaluation of Lipid-based Reagents to Mediate Intracellular Gene Delivery. *Biochim Biophys Acta* **2002**, *1567*, 23-33.
58. Rosen, M. J. *Surfactants and Interfacial Phenomena*. 3rd Ed. Wiley, New York, 2004.
59. Ogino, K.; Abe, M. *Mixed Surfactant Systems*. Dekker, New York, NY, 1993.
60. Sugihara, G.; Nagadome, S.; Oh, S.-W.; Ko, J.-S. A Review of Recent Studies on Aqueous Binary Mixed Surfactant Systems. *J. Oleo Sci.* **2008**, *57*, 61–92.
61. Peyre, V. Determination of Activities of Mixed Micelles Involving Neutral Surfactants, *Langmuir* **2002**, *18*, 1014–1023.
62. Saha, D.; Ray, D.; Kumar, S.; Kohlbrecher, J.; Aswal, V. K. Interaction of a Bovine Serum Albumin (BSA) Protein with Mixed Anionic–Cationic Surfactants and the Resultant Structure. *Soft Matter* **2021**, *17*, 6972–6984.
63. Biswas, S. C.; Chattoraj, D. K. Polysaccharide–Surfactant Interaction. 1. Adsorption of Cationic Surfactants at the Cellulose–Water Interface. *Langmuir* **1997**, *13*, 4505– 4511.
64. Bao, H.; Li, N.; Gan, L. H.; Zhang, H. Interactions between Ionic Surfactants and Polysaccharides in Aqueous Solutions. *Macromolecules* **2008**, *41*, 9406– 9412.

65. Deep, S.; Ahluwalia, J. C. Interaction of Bovine Serum Albumin with Anionic Surfactants. *Phys. Chem. Chem. Phys.* **2001**, *3*, 4583–4591.
66. Brinatti, C.; Huang, J.; Berry, R. M.; Tam, K. C.; Loh, W. Structural and Energetic Studies on the Interaction of Cationic Surfactants and Cellulose Nanocrystals. *Langmuir* **2016**, *32*, 689– 698.
67. Nishikawa, K.; Yekta, A.; Pham, H. H.; Winnik, M. A.; Sau, A. C. Fluorescence Studies of Hydrophobically Modified Hydroxyethylcellulose (HMHEC) and Pyrene-Labeled HMHEC. *Langmuir* **1998**, *14*, 7119– 7129.
68. Chari, K.; Seo, Y.-S.; Satija, S. Competitive Adsorption at the Air−Water Interface from a Self-Assembling Polymer-Surfactant Mixture. *J. Phys. Chem. B* **2004**, *108*, 11442–11446.
69. Shrivastava, S.; Dey, J. Interaction of Anionic Surfactant with Polymeric Nanoparticles of Similar Charge. *J. Colloid Interface Sci.* **2010**, *350*, 220–228.
70. Kuttich, B.; Grefe, A.-K.; Stühn, B. Changes in the Bending Modulus of AOT Based Microemulsions Induced by the Incorporation of Polymers in the Water Core. *Soft Matter* **2016**, *12*, 6400–6411.
71. Bhardwaj, P.; Kamil, M.; Panda, M. Surfactant-Polymer Interaction: Effect of Hydroxypropylmethyl Cellulose on the Surface and Solution Properties of Gemini Surfactants. *Colloid Polym. Sci.* **2018**, *296*, 1879–1889.
72. Di Gregorio, M. C.; Pavel, N. V.; Miragaya, J.; Jover, A.; Meijide, F.; Tato, J. V.; Tellini, V. H. S.; Galantini, L. Catanionic Gels Based on Cholic Acid Derivatives. *Langmuir* **2013**, *29*, 12342-12351.
73. Vashishat, R.; Chabba, S.; Mahajan, R. K. Effect of Surfactant Head Group on Micellization and Morphological Transitions in Drug-Surfactant Catanionic Mixture: A Multi-Technique Approach. *Colloids Surf. A: Physicochem. Eng. Asp.* **2016**, *498*, 206-217.

74. Lioi, S. B.; Wang, X.; Islam, M. R.; Danoff, E. J.; English, D. S. Catanionic Surfactant Vesicles for Electrostatic Molecular Sequestration and Separation. *Phys. Chem. Chem. Phys.* **2009**, *11*, 9315-9325.

75. Somasundaran, P.; Fu, E.; Xu, Q. Coadsorption of Anionic and Nonionic Surfactant Mixtures at the Alumina-Water Interface. *Langmuir* **1992**, *8*, 1065–1069.

76. Huang, L.; Somasundaran, P. Changes in Micelle Compositions and Monomer Concentrations in Mixed Surfactant Solutions. *Langmuir* **1996**, *12*, 5790–5795.

77. Kwak, J. C. T. *Polymer-Surfactant Systems, Surfactant Science Series*, Marcel Dekker, New York, 1998, vol. 77.

78. Goddard, E. D. *Interactions of Surfactants with Polymers and Proteins*; CRC Press, 2018.

79. Cabane, B.; Duplessix, R. Decoration of Semidilute Polymer Solutions with Surfactant Micelles. *J. Phys.* **1987**, *48*, 651-662.

80. Dai, S.; Tam, K. C. Isothermal Titration Calorimetry Studies of Binding Interactions between Polyethylene Glycol and Ionic Surfactants. *J. Phys. Chem. B* **2001**, *105*, 10759–10763.

81. Wang, G.; Olofsson, G. Ethyl Hydroxyethyl Cellulose and Ionic Surfactants in Dilute Solution. Calorimetric and Viscosity Study of the Interaction with Sodium Dodecyl Sulfate and Some Cationic Surfactants. *J. Phys. Chem.* **1995**, *99*, 5588–5596.

82. Ghoreishi, S. M.; Fox, G. A.; Bloor, D. M.; Holzwarth, J. F.; Wyn-Jones, E. EMF and Microcalorimetry Studies Associated with the Binding of the Cationic Surfactants to Neutral Polymers. *Langmuir* **1999**, *15*, 5474–5479.

83. Hansson, P.; Lindman, B. Surfactant-Polymer Interactions. *Curr. Opin. Colloid Interface Sci.* **1996**, *1*, 604–613.

84. Nagarajan, R. Thermodynamics of Surfactant-Polymer Interactions in Dilute Aqueous Solutions. *Chem. Phys. Lett.* **1980**, *76*, 282–286.

85. Gilányi, T. Small Systems Thermodynamics of Polymer−Surfactant Complex Formation. *J. Phys. Chem. B* **1999**, *103*, 2085–2090.

86. Garret-Flaudy, F.; Freitag, R. Unusual Thermoprecipitation Behavior of Poly(N,N-Diethylacrylamide) from Aqueous Solution in the Presence of Anionic Surfactants. *Langmuir* **2001**, *17*, 4711–4716.

87. Ahn, S.; Ahn, S. W.; Song, S.-C. Thermosensitive Amphiphilic Polyphosphazenes and their Interaction with Ionic Surfactants. *Colloids Surf. A: Physicochem. Eng. Asp.* **2008**, *330*, 184–192.

88. Mondal, S.; Ray, D.; Das, B. Thermodynamics of Aggregation of Imidazolium-Based Surface Active Ionic Liquids in Aqueous Poly(Ethylene Oxide) Media. *J. Chem. Thermodyn.* **2018**, *116*, 61–66.

89. Nagarajan, R. Thermodynamics of Nonionic Polymer—Micelle Association. *Colloids Surf.* **1985**, *13*, 1–17.

90. Ruckenstein, E.; Huber, G.; Hoffmann, H. Surfactant aggregation in the presence of polymers. *Langmuir* **1987**, 3, 382– 387.

91. Druetta, P.; Picchioni, F. Surfactant–Polymer Flooding: Influence of the Injection Scheme. *Energy Fuels* **2018**, *32*, 12231–12246.

92. Heskins, M.; Guillet, J. E. Solution Properties of Poly(*N*-isopropylacrylamide) *J. Macromol. Sci.: A Chem.* **1968**, *2*, 1441-1455.

93. Kujawa, P.; Raju, B. B.; Winnik, F. M. Interactions in Water of Alkyl and Perfluoroalkyl Surfactants with Fluorocarbon- and Hydrocarbon-Modified Poly(n-Isopropylacrylamides). *Langmuir* **2005**, *21*, 10046–10053.

94. Jijo, V. J.; Sharma, K. P.; Mathew, R.; Kamble, S.; Rajamohanan, P. R.; Ajithkumar, T. G.; Badiger, M. V.; Kumaraswamy, G. Volume Transition of PNIPAM in a Nonionic Surfactant Hexagonal Mesophase. *Macromolecules* **2010**, *43*, 4782–4790.

95. Chen, J.; Gong, X.; Yang, H.; Yao, Y.; Xu, M.; Chen, Q.; Cheng, R. NMR Study on the Effects of Sodium N-Dodecyl Sulfate on the Coil-to-Globule Transition of Poly(n-Isopropylacrylamide) in Aqueous Solutions. *Macromolecules* **2011**, *44*, 6227–6231.
96. Loh, W.; Teixeira, L. A.; Lee, L.-T. Isothermal Calorimetric Investigation of the Interaction of Poly(n-Isopropylacrylamide) and Ionic Surfactants. *J. Phys. Chem. B* **2004**, *108*, 3196–3201.
97. Chee, C. K.; Rimmer, S.; Soutar, I.; Swanson, L. Time-Resolved Fluorescence Anisotropy Studies of the Interaction of *N*-Isopropyl Acrylamide Based Polymers with Sodium Dodecyl Sulphate. *Soft Matter* **2011**, *7*, 4705–4714.
98. Walter, R.; Rička, J.; Quellet, C.; Nyffenegger, R.; Binkert, T. Coil−Globule Transition of Poly(n-Isopropylacrylamide): A Study of Polymer−Surfactant Association. *Macromolecules* **1996**, *29*, 4019–4028.
99. Lee, H. J.; McAuley, A.; Schilke, K. F.; McGuire, J. Molecular Origins of Surfactant-Mediated Stabilization of Protein Drugs. *Adv. Drug Deliv. Rev.* **2011**, *63*, 1160–1171.
100. Otzen, D. Protein–Surfactant Interactions: A Tale of Many States. *Biochim. Biophys. Acta (BBA) - Proteins Proteom.* **2011**, *1814*, 562–591.
101. Malik, N. A. Surfactant–Amino Acid and Surfactant–Surfactant Interactions in Aqueous Medium: A Review. *Appl. Biochem. Biotechnol.* **2015**, *176*, 2077–2106.
102. Tucker, I. M.; Petkov, J. T.; Penfold, J.; Thomas, R. K.; Li, P.; Cox, A. R.; Hedges, N.; Webster, J. R. Spontaneous Surface Self-Assembly in Protein–Surfactant Mixtures: Interactions between Hydrophobin and Ethoxylated Polysorbate Surfactants. *J. Phys. Chem. B* **2014**, *118*, 4867–4875.
103. Castelli, F.; Sarpietro, M. G.; Micieli, D.; Ottimo, S.; Pitarresi, G.; Tripodo, G.; Carlisi, B.; Giammona, G. Differential Scanning Calorimetry Study on Drug Release from an Inulin-

Based Hydrogel and its Interaction with a Biomembrane Model: pH and Loading Effect. *Eur. J. Pharm. Sci.* **2008**, *35*, 76–85.

104. Afinjuomo, F.; Fouladian, P.; Parikh, A.; Barclay, T. G.; Song, Y.; Garg, S. Preparation and Characterization of Oxidized Inulin Hydrogel for Controlled Drug Delivery. *Pharmaceutics* **2019**, *11*, 356-377.

105. Dubey, P.; Kumar, S.; Ravindranathan, S.; Vasudevan, S.; Aswal, V. K.; Rajamohanan, P. R.; Nisal, A.; Prabhune, A. pH Dependent Sophorolipid Assemblies and their Influence on Gelation of Silk Fibroin Protein. *Mater. Chem. Phys.* **2018**, *203*, 9–16.

106. Ohadi, M.; Shahravan, A.; Dehghan, N.; Eslaminejad, T.; Banat, I. M.; Dehghannoudeh, G. Potential Use of Microbial Surfactant in Microemulsion Drug Delivery System: A Systematic Review. *Drug Des. Dev. Ther.* **2020**, *14*, 541–550.

107. Mackie, A.; Wilde, P. The Role of Interactions in Defining the Structure of Mixed Protein–Surfactant Interfaces. *Adv. Colloid Interface Sci.* **2005**, *117*, 3–13.

108. Mehan, S.; Aswal, V. K.; Kohlbrecher, J. Tuning of Protein-Surfactant Interaction to Modify the Resultant Structure. *Phys. Rev. E* **2015**, *92*, 032713.

109. Miller, R.; Leser, M. E.; Michel, M.; Fainerman, V. B. Surface Dilational Rheology of Mixed β-Lactoglobulin/Surfactant Layers at the Air/Water Interface. *J. Phys. Chem. B* **2005**, *109*, 13327–13331.

110. Taheri-Kafrani, A.; Bordbar, A.-K.; Mousavi, S. H.-A.; Haertlé, T. B-Lactoglobulin Structure and Retinol Binding Changes in Presence of Anionic and Neutral Detergents. *J. Agric. Food Chem.* **2008**, *56*, 7528–7534.

111. Li, Y.; Sato, T. Complexation of a Globular Protein, β-Lactoglobulin, with an Anionic Surfactant in Aqueous Solution. *Langmuir* **2017**, *33*, 5491–5498.

112. Fan, L.; Xie, P.; Wang, Y.; Huang, Z.; Zhou, J. Biosurfactant–Protein Interaction: Influences of Mannosylerythritol Lipids-A on β-Glucosidase. *J. Agric. Food Chem.* **2017**, *66*, 238–246.

113. Seidel, Z. P.; Lee, C. T. Enhanced Activity of the Cellulase Enzyme β-Glucosidase upon Addition of an Azobenzene-Based Surfactant. *ACS Sustain. Chem. Eng.* **2020**, *8*, 1751–1761.

114. Tanford, C.; Nozaki, Y.; Reynolds, J. A.; Makino, S. Molecular Characterization of Proteins in Detergent Solutions. *Biochemistry* **1974**, *13*, 2369–2376.

115. Fish, W. W.; Reynolds, J. A.; Tanford, C. Gel Chromatography of Proteins in Denaturing Solvents. *J. Biol. Chem.* **1970**, *245*, 5166–5168.

116. Reynolds, A.; Tanford C. The Gross Conformation of Protein–Sodium Dodecyl Sulfate Complexes, *J. Biol. Chem.* **1970**, *245*, 5161–5165.

117. Tanford, C. *The Hydrophobic Effect: Formation of Micelles and Biological Membranes*; Krieger: Malabar, FL, 1991.

118. Magdassi, S. *Surface Activity of Proteins: Chemical and Physicochemical Modifications*; M. Dekker: New York, 1996.

119. Ghosh, S.; Banerjee, A. A Multitechnique Approach in Protein/Surfactant Interaction Study: Physicochemical Aspects of Sodium Dodecyl Sulfate in the Presence of Trypsin in Aqueous Medium. *Biomacromolecules* **2001**, *3*, 9–16.

120. Tanner, R. E.; Herpigny, B.; Chen, S. H.; Rha, C. K. Conformational Change of Protein Sodium Dodecylsulfate Complexes in Solution: A Study of Dynamic Light Scattering. *J. Chem. Phys.* **1982**, *76*, 3866–3872.

121. Oakes, J. Protein–Surfactant Interactions. Nuclear Magnetic Resonance and Binding Isotherm Studies of Interactions between Bovine Serum Albumin and Sodium Dodecyl Sulphate. *J. Chem. Soc. Faraday Trans.* **1974**, *70*, 2200.

122. Turro, N. J.; Lei, X.-G.; Ananthapadmanabhan, K. P.; Aronson, M. Spectroscopic Probe Analysis of Protein-Surfactant Interactions: The BSA/SDS System. *Langmuir* **1995**, *11*, 2525–2533.

123. Shirahama, K.; Tsujii, K.; Takagi, T. Free-Boundary Electrophoresis of Sodium Dodecyl Sulfate-Protein Polypeptide Complexes with Special Reference to SDS-Polyacrylamide Gel Electrophoresis. *J. Biochem.* **1974**, *75*, 309–319.

124. Ibel, K.; May, R. P.; Sandberg, M.; Mascher, E.; Greijer, E.; Lundahl, P. Structure of Dodecyl Sulfate—Protein Complexes at Subsaturating Concentrations of Free Detergent. *Biophys. Chem.* **1994**, *53*, 77–83.

125. Ibel, K.; May, R. P.; Kirschner, K.; Szadkowski, H.; Mascher, E.; Lundahl, P. Protein-Decorated Micelle Structure of Sodium-Dodecyl-Sulfate-Protein Complexes as Determined by Neutron Scattering. *Eur. J. Biochem.* **1990**, *190*, 311–318.

126. Guo, X. H.; Zhao, N. M.; Chen, S. H.; Teixeira, J. Small-Angle Neutron Scattering Study of the Structure of Protein / Detergent Complexes. *Biopolymers* **1990**, *29*, 335–346.

127. Santos, S. F.; Zanette, D.; Fischer, H.; Itri, R. A Systematic Study of Bovine Serum Albumin (BSA) and Sodium Dodecyl Sulfate (SDS) Interactions by Surface Tension and Small Angle X-Ray Scattering. *J. Colloid Interface Sci.* **2003**, *262*, 400–408.

128. Westerhuis, W. H. J.; Sturgis, J. N.; Niederman, R. A. Reevaluation of the Electrophoretic Migration Behavior of Soluble Globular Proteins in the Native and Detergent-Denatured States in Polyacrylamide Gels. *Anal. Biochem.* **2000**, *284*, 143–152.

129. Chakraborty, T.; Chakraborty, I.; Ghosh, S. Sodium Carboxymethylcellulose−CTAB Interaction: A Detailed Thermodynamic Study of Polymer−Surfactant Interaction with Opposite Charges. *Langmuir* **2006**, *22*, 9905–9913.

130. Thongngam, M.; McClements, D. J. Characterization of Interactions between Chitosan and an Anionic Surfactant. *J. Agric. Food Chem.* **2004**, *52*, 987–991.

131. Merta, J.; Stenius, P. Interactions between Cationic Starch and Anionic Surfactants. *Colloid Polym. Sci.* **1995**, *273*, 974–983.

132. Zhang, Q.; Kim, D.; Li, L.; Patel, S.; Duhamel, J. Surfactant-Structure Dependent Interactions with Modified Starch Nanoparticles Probed by Fluorescence Spectroscopy. *Langmuir* **2019**, *35*, 3432-3444.

133. Wang, C.; Tam, K. C. New Insights on the Interaction Mechanism within Oppositely Charged Polymer/Surfactant Systems. *Langmuir* **2002**, *18*, 6484–6490.

134. Trabelsi, S.; Raspaud, E.; Langevin, D. Aggregate Formation in Aqueous Solutions of Carboxymethylcellulose and Cationic Surfactants. *Langmuir* **2007**, *23*, 10053–10062.

135. Trabelsi, S.; Albouy, P.-A.; Impéror-Clerc, M.; Guillot, S.; Langevin, D. X-Ray Diffraction Study of the Structure of Carboxymethylcellulose–Cationic Surfactant Complexes. *ChemPhysChem* **2007**, *8*, 2379–2385.

136. Mata, J.; Patel, J.; Jain, N.; Ghosh, G.; Bahadur, P. Interaction of Cationic Surfactants with Carboxymethylcellulose in Aqueous Media. *J. Colloid Interface Sci.* **2006**, *297*, 797–804.

137. Naves, A. F.; Petri, D. F. S. The Effect of Molecular Weight and Degree of Substitution on the Interactions between Carboxymethyl Cellulose and Cetyltrimethylammonium Bromide. *Colloids Surf. A: Physicochem. Eng. Asp.* **2005**, *254*, 207–214.

138. Wang, X.; Li, Y.; Li, J.; Wang, J.; Wang, Y.; Guo, Z.; Yan, H. Salt Effect on the Complex Formation between Polyelectrolyte and Oppositely Charged Surfactant in Aqueous Solution. *J. Phys. Chem. B* **2005**, *109*, 10807–10812.

139. Thongngam, M.; McClements, D. J. Influence of pH, Ionic Strength, and Temperature on Self-Association and Interactions of Sodium Dodecyl Sulfate in the Absence and Presence of Chitosan. *Langmuir* **2004**, *21*, 79–86.

140. Milinković Budinčić, J.; Petrović, L.; Đekić, L.; Aleksić, M.; Fraj, J.; Popović, S.; Bučko, S.; Katona, J.; Spasojević, L.; Škrbić, J.; Malenovi, A. Chitosan/Sodium Dodecyl Sulfate

Complexes for Microencapsulation of Vitamin E and Its Release Profile—Understanding the Effect of Anionic Surfactant. *Pharmaceuticals* **2021**, *15*, 54.

141. Kurakake, M.; Hagiwara, H.; Komaki, T. Effects of Various Surfactants on Rheological Properties of Maize Starch Granules. *Cereal Chem.* **2004**, *81*, 108–114.

142. Zhang, Q.; Kim, D.; Li, L.; Patel, S.; Duhamel, J. Surfactant Structure-Dependent Interactions with Modified Starch Nanoparticles Probed by Fluorescence Spectroscopy. *Langmuir* **2019**, *35*, 3432–3444.

143. Wang, C.; Li, X.; Li, P.; Niu, Y. Interactions between Fluorinated Cationic Guar Gum and Surfactants in the Dilute and Semi-Dilute Solutions. *Carbohydr. Polym.* **2014**, *99*, 638–645.

144. de Seixas-Junior, C. H.; de Carvalho, M. M.; Jacumazo, J.; Piazza, R. D.; Parchen, G. P.; de Freitas, R. A. Interaction of Guar Gum Galactomannans with the Anionic Surfactant Sodium Lauryl Ether Sulphate. *Int. J Biol. Macromol.* **2020**, *165*, 713–721.

145. Liu, K.; Chen, D.; Marcozzi, A.; Zheng, L.; Su, J.; Pesce, D.; Zajaczkowski, W.; Kolbe, A.; Pisula, W.; Müllen, K.; Clark, N. A. ; Herrmann A. Thermotropic Liquid Crystals from Biomacromolecules. *Proc. Natl. Acad. Sci. U.S.A.* **2014**, *111*, 18596–18600.

146. Liu, K.; Shuai, M.; Chen, D.; Tuchband, M.; Gerasimov, J. Y.; Su, J.; Liu, Q.; Zajaczkowski, W.; Pisula, W.; Müllen, K.; Clark, N. A.; Herrmann, A. Solvent-Free Liquid Crystals and Liquids from DNA. *Chem. Eur. J.* **2015**, *21*, 4898–4903.

147. Tanaka, K.; Okahata, Y. A DNA−Lipid Complex in Organic Media and Formation of an Aligned Cast Film. *J. Am. Chem. Soc.* **1996**, *118*, 10679–10683.

148. Yang, C.; Moses, D.; Heeger, A. J. Base-Pair Stacking in Oriented Films of DNA–Surfactant Complex. *Adv. Mater.* **2003**, *15*, 1364–1367.

149. Liu, K.; Zheng, L.; Ma, C.; Göstl, R.; Herrmann, A. DNA–Surfactant Complexes: Self-Assembly Properties and Applications. *Chem. Soc. Rev.* **2017**, *46*, 5147–5172.

150. Mel'nikov, S. M.; Sergeyev, V. G.; Yoshikawa, K. Transition of Double-Stranded DNA Chains between Random Coil and Compact Globule States Induced by Cooperative Binding of Cationic Surfactant. *J. Am. Chem. Soc.* **1995**, *117*, 9951–9956.

151. Delville, A.; Laszlo, P.; Schyns, R. Displacement of Sodium Ions by Surfactant Ions from DNA A ^{23}Na-NMR Investigation. *Biophys. Chem.* **1986**, *24*, 121–133.

152. Bloomfield, V. A. DNA Condensation by Multivalent Cations. *Biopolymers* **1997**, *44*, 269–282.

153. Ghirlando, R.; Wachtel, E. J.; Arad, T.; Minsky, A. DNA Packaging Induced by Micellar Aggregates: A Novel in Vitro DNA Condensation System. *Biochemistry* **1992**, *31*, 7110–7119.

154. Husale, S.; Grange, W.; Karle, M.; Bürgi, S.; Hegner, M. Interaction of Cationic Surfactants with DNA: A Single-Molecule Study. *Nucleic Acids Res.* **2008**, *36*, 1443–1449.

155. Ouyang, M.; Remy, J.-S.; Szoka, F. C. Controlled Template-Assisted Assembly of Plasmid DNA into Nanometric Particles with High DNA Concentration. *Bioconj. Chem.* **1999**, *11*, 104–112.

156. Dauty, E.; Remy, J.-S.; Blessing, T.; Behr, J.-P. Dimerizable Cationic Detergents with a Low CMC Condense Plasmid DNA into Nanometric Particles and Transfect Cells in Culture. *J. Am. Chem. Soc.* **2001**, *123*, 9227–9234.

157. Mel'nikov, S. M.; Yoshikawa, K. First-Order Phase Transition in Large Single Duplex DNA Induced by a Nonionic Surfactant. *Biochem. Biophys. Res. Comm.* **1997**, *230*, 514–517.

158. Mel'nikova, Y. S.; Lindman, B. pH-Controlled DNA Condensation in the Presence of Dodecyldimethylamine Oxide. *Langmuir* **2000**, *16*, 5871–5878.

159. Garcia, M. E. D.; Sanz-Medel, A. Dye-Surfactant Interactions: A Review. *Talanta* **1986**, *33*, 255–264.

160. Zhang, C.; Jin, S.; Li, S.; Xue, X.; Liu, J.; Huang, Y.; Jiang, Y.; Chen, W.-Q.; Zou, G.; Liang, X.-J. Imaging Intracellular Anticancer Drug Delivery by Self-Assembly Micelles with Aggregation-Induced Emission (AIE Micelles). *ACS Appl. Mater. Interfaces* **2014**, *6*, 5212–5220.

161. Pan, Y.; Ren, X.; Wang, S.; Li, X.; Luo, X.; Yin, Z. Annexin V-Conjugated Mixed Micelles as a Potential Drug Delivery System for Targeted Thrombolysis. *Biomacromolecules* **2017**, *18*, 865–876.

162. Xu, M.; Zhang, C. Y.; Wu, J.; Zhou, H.; Bai, R.; Shen, Z.; Deng, F.; Liu, Y.; Liu, J. Peg-Detachable Polymeric Micelles Self-Assembled from Amphiphilic Copolymers for Tumor-Acidity-Triggered Drug Delivery and Controlled Release. *ACS Appl. Mater. Interfaces* **2019**, *11*, 5701–5713.

163. Staples, E.; Thompson, L.; Tucker, I.; Penfold, J.; Thomas, R. K.; Lu, J. R. Surface Composition of Mixed Surfactant Monolayers at Concentrations Well in Excess of the Critical Micelle Concentration. A Neutron Scattering Study. *Langmuir* **1993**, *9*, 1651–1656.

164. Patist, A.; Bhagwat, S. S.; Penfield, K. W.; Aikens, P.; Shah, D. O. On the Measurement of Critical Micelle Concentrations of Pure and Technical-Grade Nonionic Surfactants. *J. Surfactants Deterg.* **2000**, *3*, 53–58.

165. Chiu, Y. C.; Kuo, C. Y.; Wang, C. W. Using Electrophoresis to Determine Zeta Potential of Micelles and Critical Micelle Concentration. *J. Dispers. Sci. Technol.* **2000**, *21*, 327–343.

166. Ghosh, S.; Krishnan, A.; Das, P. K.; Ramakrishnan, S. Determination of Critical Micelle Concentration by Hyper-Rayleigh Scattering. *J. Am. Chem. Soc.* **2003**, *125*, 1602–1606.

167. Pérez-Rodríguez, M.; Prieto, G.; Rega, C.; Varela, L. M.; Sarmiento, F.; Mosquera, V. A Comparative Study of the Determination of the Critical Micelle Concentration by Conductivity and Dielectric Constant Measurements. *Langmuir* **1998**, *14*, 4422–4426.

168. Rathman, J. F.; Christian, S. D. Determination of Surfactant Activities in Micellar Solutions of Dimethyldodecylamine Oxide. *Langmuir* **1990**, *6*, 391–395.

169. Tong, W.; Zheng, Q.; Shao, S.; Lei, Q.; Fang, W. Critical Micellar Concentrations of Quaternary Ammonium Surfactants with Hydroxyethyl Substituents on Headgroups Determined by Isothermal Titration Calorimetry. *J. Chem. Eng. Data* **2010**, *55*, 3766–3771.

170. Chang, C. Y.; Wang, S. J.; Liu, I. J.; Chiu, Y. C. A Simple Method for Determining the Critical Micellar Concentration of a Surfactant. *J. Chin. Chem. Soc.* **1987**, *34*, 243–246.

171. Kalyanasundaram, K.; Thomas, J. K. Environmental Effects on Vibronic Band Intensities in Pyrene Monomer Fluorescence and Their Application in Studies of Micellar Systems. *J. Am. Chem. Soc.* **1977**, *99*, 2039–2044.

172. Aguiar, J.; Carpena, P.; Molina-Bolívar J.A.; Carnero Ruiz, C. On the Determination of the Critical Micelle Concentration by the Pyrene 1:3 Ratio Method. *J. Colloid Interface Sci.* **2003**, *258*, 116–122.

173. Anand, U.; Jash, C.; Mukherjee, S. Spectroscopic Determination of Critical Micelle Concentration in Aqueous and Non-Aqueous Media Using a Non-Invasive Method. *J. Colloid Interface Sci.* **2011**, *364*, 400–406.

174. Prazeres, T. J. V.; Beija, M.; Fernandes, F. V.; Marcelino, P. G. A.; Farinha, J. P.; Martinho, J. M. G. Determination of the Critical Micelle Concentration of Surfactants and Amphiphilic Block Copolymers Using Coumarin 153. *Inorg. Chim. Acta* **2012**, *381*, 181–187.

175. Scholz, N.; Behnke, T.; Resch-Genger, U. Determination of the Critical Micelle Concentration of Neutral and Ionic Surfactants with Fluorometry, Conductometry, and Surface Tension—a Method Comparison. *J. Fluoresc.* **2018**, *28*, 465–476.

176. Chaudhuri, R.; Guharay, J.; Sengupta, P. K. Fluorescence Polarization Anisotropy as a Novel Tool for the Determination of Critical Micellar Concentrations. *J. Photochem. Photobiol. A* **1996**, *101*, 241–244.

177. Zana, R.; Weill, C. Effect of Temperature on the Aggregation Behaviour of Nonionic Surfactants in Aqueous Solutions. *J. Phys. Lett.* **1985**, *46*, 953–960.

178. Binana-Limbelé, W.; Zana, R. Effect of Temperature on the Aggregation Behavior of the Nonionic Surfactant $C_{12}E_8$ in H_2O and D_2O Solutions. *J. Colloid Interface Sci.* **1988**, *121*, 81–84.

179. Missel, P. J.; Mazer, N. A.; Carey, M. C.; Benedek, G. B. Influence of Alkali-Metal Counterion Identity on the Sphere-to-Rod Transition in Alkyl Sulfate Micelles. *J. Phys. Chem.* **1989**, *93*, 8354–8366.

180. Alargova, R.; Petkov, J.; Petsev, D.; Ivanov, I. B.; Broze, G.; Mehreteab, A. Light Scattering Study of Sodium Dodecyl Polyoxyethylene-2-Sulfonate Micelles in the Presence of Multivalent Counterions. *Langmuir* **1995**, *11*, 1530–1536.

181. Lianos, P.; Lang, J.; Strazielle, C.; Zana, R. Fluorescence Probe Study of Oil-in-Water Microemulsions. 1. Effect of Pentanol and Dodecane or Toluene on Some Properties of Sodium Dodecyl Sulfate Micelles. *J. Phys. Chem.* **1982**, *86*, 1019–1025.

182. Alargova, R. G.; Kochijashky, I. I.; Sierra, M. L.; Zana, R. Micelle Aggregation Numbers of Surfactants in Aqueous Solutions: A Comparison between the Results from Steady-State and Time-Resolved Fluorescence Quenching. *Langmuir* **1998**, *14*, 5412–5418.

183. Debye, P.; Anacker, E. W. Micelle Shape from Dissymmetry Measurements. *J. Phys. Chem.* **1951**, *55*, 644–655.

184. Turro, N. J.; Yekta, A. Luminescent Probes for Detergent Solutions. A Simple Procedure for Determination of the Mean Aggregation Number of Micelles. *J. Am. Chem. Soc.* **1978**, *100*, 5951–5952.

185. Infelta, P. P. Fluorescence Quenching in Micellar Solutions and its Application to the Determination of Aggregation Numbers. *Chem. Phys. Lett.* **1979**, *61*, 88–91.

186. Tachiya, M. Application of a Generating Function to Reaction Kinetics in Micelles. Kinetics of quenching of Luminescent Probes in Micelles. *Chem. Phys. Lett.* **1975**, *33*, 289-292.

187. Safinya, C. R.; Ewert, K. K.; Majzoub, R. N.; Leal, C. Cationic Liposome–Nucleic Acid Complexes for Gene Delivery and Gene Silencing. *New J. Chem.* **2014**, *38*, 5164–5172.

188. Spiering, V. J.; Prause, A.; Noirez, L.; Appavou, M.-S.; Gradzielski, M. Structural Characterization of Nonionic Surfactant Micelles with CO_2/Ethylene Oxide Head Groups and their Temperature Dependence. *Langmuir* **2021**, *37*, 13235–13243.

189. Mel'nikova, Y. S.; Mel'nikov, S. M.; Löfroth, J.-E. Physico-Chemical Aspects of the Interaction between DNA and Oppositely Charged Mixed Liposomes. *Biophys. Chem.* **1999**, *81*, 125–141.

190. Chen, Q.; Kang, X.; Li, R.; Du, X.; Shang, Y.; Liu, H.; Hu, Y. Structure of the Complex Monolayer of Gemini Surfactant and DNA at the Air/Water Interface. *Langmuir* **2012**, *28*, 3429–3438.

191. Grueso, E.; Kuliszewska, E.; Prado-Gotor, R.; Perez-Tejeda, P.; Roldan, E. Improving the Understanding of DNA–Propanediyl-1,3-Bis(Dodecyldimethylammonium) Dibromide Interaction Using Thermodynamic, Structural and Kinetic Approaches. *Phys. Chem. Chem. Phys.* **2013**, *15*, 20064-20074.

192. Chen, X.; Wang, J.; Shen, N.; Luo, Y.; Li, L.; Liu, M.; Thomas, R. K. Gemini Surfactant/DNA Complex Monolayers at the Air−Water Interface: Effect of Surfactant

Structure on the Assembly, Stability, and Topography of Monolayers. *Langmuir* **2002**, *18*, 6222–6228.

193. Lasic, D. D.; Strey, H.; Stuart, M. C.; Podgornik, R.; Frederik, P. M. The Structure of DNA−Liposome Complexes. *J. Am. Chem. Soc.* **1997**, *119*, 832–833.

194. Keyes, C.; Duhamel, J.; Wettig, S. Characterization of the Behavior of a Pyrene Substituted Gemini Surfactant in Water by Fluorescence. *Langmuir* **2011**, *27*, 3361–3371.

195. Chu, B. *Laser Light Scattering*; Academic Press: New York, 1991.

196. Sutherland, E.; Mercer, S. M.; Everist, M.; Leaist, D. G. Diffusion in Solutions of Micelles. What Does Dynamic Light Scattering Measure? *J. Chem. Eng. Data* **2008**, *54*, 272–278.

197. Kumar, C. S. S. R. *X-Ray and Neutron Techniques for Nanomaterials Characterization*; Springer Berlin Heidelberg: Berlin, Heidelberg, **2016**.

198. Narayanan, T.; Konovalov, O. Synchrotron Scattering Methods for Nanomaterials and Soft Matter Research. *Materials* **2020**, *13*, 752.

199. Gómez-Graña, S.; Hubert, F.; Testard, F.; Guerrero-Martínez, A.; Grillo, I.; Liz-Marzán, L. M.; Spalla, O. Surfactant (Bi)Layers on Gold Nanorods. *Langmuir* **2011**, *28*, 1453–1459.

200. Ewert, K. K.; Evans, H. M.; Zidovska, A.; Bouxsein, N. F.; Ahmad, A.; Safinya, C. R. A Columnar Phase of Dendritic Lipid−Based Cationic Liposome−DNA Complexes for Gene Delivery: Hexagonally Ordered Cylindrical Micelles Embedded in a DNA Honeycomb Lattice. *J. Am. Chem. Soc.* **2006**, *128*, 3998–4006.

201. Binnig, G.; Quate, C. F.; Gerber, Ch. Atomic Force Microscope. *Phys. Rev. Lett.* **1986**, *56*, 930-933.

202. Miyazawa, N.; Sakaue, T.; Yoshikawa, K.; Zana, R. Rings-on-a-String Chain Structure in DNA. *J. Chem. Phys.* **2005**, *122*, 044902.

203. Lakowicz, J. R. *Principles of Fluorescence Spectroscopy*; Springer: New York, 2016.

204. McNelles, S. A.; Thoma, J. L.; Adronov, A.; Duhamel, J. Quantitative Characterization of the Molecular Dimensions of Flexible Dendritic Macromolecules in Solution by Pyrene Excimer Fluorescence. *Macromolecules* **2018**, *51*, 1586–1590.

205. Dong, D. C.; Winnik, M. A. The Py Scale of Solvent Polarities. *Photochem. Photobiol.* **1982**, *35*, 17−21.

206. Farhangi, S.; Duhamel, J. A Pyrenyl Derivative with a Four Atom-Linker that Can Probe the Local Polarity of Pyrene-Labeled Macromolecules. *J. Phys. Chem. B* **2016**, *120*, 834-842.

207. Mathew, A. K.; Siu, H.; Duhamel, J. A Blob Model to Study Chain Folding by Fluorescence. *Macromolecules* **1999**, *32*, 7100–7108.

208. Duhamel, J. Internal Dynamics of Dendritic Molecules Probed by Pyrene Excimer Formation. *Polymers* **2012**, *4*, 211-239.

209. Duhamel, J. New Insights in the Study of Pyrene Excimer Fluorescence to Characterize Macromolecules and their Supramolecular Assemblies in Solution. *Langmuir* **2012**, *28*, 6527-6538.

210. Duhamel, J. Global Analysis of Fluorescence Decays to Probe the Internal Dynamics of Fluorescently Labeled Macromolecules. *Langmuir* **2014**, *30*, 2307-2324.

211. Siu, H.; Duhamel, J. Comparison of the Association Level of a Hydrophobically Modified Associative Polymer Obtained from an Analysis Based on Two Different Models. *J. Phys. Chem. B* **2005**, *109*, 1770-1780.

212. Farhangi, S.; Duhamel, J. A Pyrenyl Derivative with a Four Atom-Linker that Can Probe the Local Polarity of Pyrene-Labeled Macromolecules. *J. Phys. Chem. B* **2016**, *120*, 834-842.

213. Thoma, L. J.; McNelles, S. A.; Adronov, A.; Duhamel, J. Direct Measure of the Local Concentration of Pyrenyl Groups in Pyrene-Labeled Dendrons Derived from the Rate of Fluorescence Collisional Quenching. *Polymers* **2020**, *12*, 2919.

214. Raimbault, J.; Casier, R.; Little, H.; Duhamel, J. Hydrophobic and Elastic Forces Experienced by a Series of Pyrene End-Labeled Poly(ethylene oxide)s Interacting with Sodium Dodecyl Sulfate Micelles. *Macromolecules* **2018**, *51*, 5933-5943.

215. Siu, H.; Duhamel, J.; Sasaki, D.; Pincus, J. L. Nanodomain Formation in Lipid Membranes Probed by Time-Resolved Fluorescence. *Langmuir* **2010**, *26*, 10985-10994.

Chapter 2

1. Sidenko, Z. S.; Limanov, V. E.; Skvortsova, E. K.; Dziomko, V. M. Synthesis and Antibacterial Activity of some Bisammonium Compounds. *Khimiko-Farmatsevticheskii Zhurnal* **1968**, *2*, 15-18.
2. Menger, F. M.; Littau, C. A. Gemini Surfactants: Synthesis and Properties. *J. Am. Chem. Soc.* **1991**, *113*, 1451-1452.
3. Kirby, A. J.; Camilleri, P,; Engberts, J. B. F. N. ; Feiters, M. C. ; Nolte, R. J. M.; Söderman, O.; Bergsma, M.; Bell, P. C.; Fielden, M. L.; Garcia Rodriguez, C. L.; Guédat, P.; Kermer, A.; McGregor, C.; Perrin, C.; Ronsin, G.; van Eijk, Gemini Surfactants: New Synthetic Vectors for Gene Transfection. *Angew. Chem. Int. Ed.* **2003**, *42*, 1448-1457.
4. Cardoso, A. M. S.; Silva, S. G.; do Vale, M. L.; Marques, E. F.; Pedroso de Lima, M. C.; Jurado, A. S. Gene Delivery Mediated by Gemini Surfactants: Structure – Activity Relationships in Engineering of Nanobiomaterials – Applications of Nanobiomaterials. Ed. Grumezescu, A. M., Elsevier, **2016**, pp 227 – 256.
5. Ahmed, T.; Kamel, A. O.; Wettig, S. D. Interactions between DNA and Gemini Surfactants: Impact on Gene Therapy: Part I. *Nanomedicine* **2016**, *11*, 289-306.

6. Sharma, R.; Kamal, A.; Abdinejad, M.; Mahajan, R. K.; Kraatz, H.-B. Advances in the Synthesis, Molecular Architectures, and Potential Applications of Gemini Surfactants. *Adv. Colloid Interface Sci.* **2017**, *248*, 35-68.
7. Oblak, E.; Piecuch, A.; Rewak-Soroczynska, J.; Paluch, E. Activity of Gemini Quaternary Ammonium Salts against Microorganisms. *Appl. Microbiol. Biotechnol.* **2019**, *103*, 625-632.
8. Kamal, M. S. A Review of Gemini Surfactants: Potential Application in Enhanced Oil Recovery. *J. Surfact. Deterg.* **2016**, *19*, 223-236.
9. Menger, F. M.; Keiper, J. S. Gemini Surfactants. *Angew. Chem. Int. Ed.* **2000**, *39*, 1906-1920.
10. Zana, R.; Xia, J. In *Gemini Surfactants: Synthesis, Interfacial and Solution-Phase Behavior, and Applications*, Marcel Dekker, Inc., New York, **2004**.
11. Han, Y.; Wang, Y. Aggregation Behavior of Gemini Surfactants and their Interactions with Macromolecules in Aqueous Solution. *Phys. Chem. Chem. Phys.* **2011**, *13*, 1939-1956.
12. Kumar, N.; Tyagi, R. Industrial Applications of Dimeric Surfactants: A Review. *J. Disper. Sci. Technol.* **2014**, *35*, 205-214.
13. Rosen, M. J.; Tracy, D. J. Gemini Surfactants. *J. Surfactants Deterg.* **1998**, *1*, 547– 554.
14. Zana, R. Gemini (Dimeric) Surfactants. *Curr. Opin. Colloid Interface Sci.* **1996**, *1*, 566–571.
15. Ahmed, T.; Kamel, A. O.; Wettig, S. D. Interactions between DNA and Gemini Surfactants: Impact on Gene Therapy: Part II. *Nanomedicine* **2016**, *11*, 403-420.
16. Rädler, J. O.; Koltover, I.; Salditt, T.; Safinyia, C. R. Structure of DNA-Cationic Liposome Complexes: DNA Intercalation in Multilamellar Membranes in Distinct Interhelical Packing Regime. *Science* **1997**, *275*, 810-814.

17. Koltover, I.; Salditt, T.; Rädler, J. O.; Safinyia, C. R. An Inverted Hexagonal Phase of Cationic Liposome-DNA Complexes Related to DNA Release and Delivery. *Science* **1998**, *281*, 78-81.
18. Rosenzweig, H. S.; Rakhmanova, V. A.; MacDonald, R. C. Diquarternary Ammonium Compounds as Transfection Agents. *Bioconjug. Chem.* **2001**, *12*, 258-263.
19. Wang, C.; Wettig, S. D.; Foldvari, M.; Verrall, R. E. Synthesis, Characterization, and Use of Asymmetric Pyrenyl-Gemini Surfactants as Emissive Components in DNA-Lipoplex Systems. *Langmuir* **2007**, *23*, 8995–9001.
20. Keyes-Baig, C.; Duhamel, J.; Wettig, S. Characterization of the Behavior of a Pyrene Substituted Gemini Surfactant in Water by Fluorescence. *Langmuir*, **2011**, *27*, 7, 3361-3371.
21. Turro, N. J.; Yekta, A. Luminescent Probes for Detergent Solutions. A Simple Procedure for the Determination of the Mean Aggregation Number of Micelles. *J. Am. Chem. Soc.* **1978**, *100*, 5951-5952.
22. Infelta, P. P.; Gratzel, M.; Thomas J. K. Luminescence Decay of Hydrophobic Molecules Solubilized in Aqueous Micellar Systems. Kinetic Model. *J. Phys. Chem.* **1974**, *78*, 190-195.
23. Tachiya, M. Application of a Generating Function to Reaction Kinetics in Micelles. Kinetics of quenching of Luminescent Probes in Micelles. *Chem. Phys. Lett.* **1975**, *33*, 289-292.
24. Patel, S.; Seet, J.; Li, L.; Duhamel, J. Detection of Nitroaromatics by Pyrene-Labeled Starch Nanoparticles. *Langmuir* **2019**, *35*, 13145-13156.
25. Black, J. W.; Jennings, M. C.; Azarewicz, J.; Paniak, T. J.; Grenier, M. C.; Wuest, W. M.; Minbiole, K. P. C. TMEDA-Derived Biscationic Amphiphiles: An Economical Preparation of Potent Antibacterial Agents. *Bioorg. Med. Chem. Lett*. **2014**, *24*, 99.

26. Siu, H.; Prazeres, T. J. V.; Duhamel, J.; Olesen, K.; Shay, G. Characterization of the Aggregates Made by Short Poly(ethylene oxide) Chains Labelled at one End With the Dye Pyrene. *Macromolecules* **2005**, *38*, 2865-2875.
27. Farhangi, S.; Duhamel, J. A Pyrenyl Derivative with a Four Atom-Linker that Can Probe the Local Polarity of Pyrene-Labeled Macromolecules. *J. Phys. Chem. B* **2016**, *120*, 834-842.
28. Press, W.H.; Flanery, B.P.; Tenkolsky, S.A.; Vetterling, W.T. *Numerical Receipes in Fortran: The Art of Scientific Computing*; Cambridge University Press: New York, NY, USA, 1992; pp 523−528.
29. Siu, H.; Duhamel, J. Comparison of the Association Level of a Hydrophobically Modified Associative Polymer Obtained from an Analysis Based on Two Different Models. *J. Phys. Chem. B* **2005**, *109*, 1770-1780.
30. Duhamel, J. Internal Dynamics of Dendritic Molecules Probed by Pyrene Excimer Formation. *Polymers* **2012**, *4*, 211-239.
31. Duhamel, J. New Insights in the Study of Pyrene Excimer Fluorescence to Characterize Macromolecules and their Supramolecular Assemblies in Solution. *Langmuir* **2012**, *28*, 6527-6538.
32. Duhamel, J. Global Analysis of Fluorescence Decays to Probe the Internal Dynamics of Fluorescently Labeled Macromolecules. *Langmuir* **2014**, *30*, 2307-2324.
33. Thoma, L. J.; McNelles, S. A.; Adronov, A.; Duhamel, J. Direct Measure of the Local Concentration of Pyrenyl Groups in Pyrene-Labeled Dendrons Derived from the Rate of Fluorescence Collisional Quenching. *Polymers* **2020**, *12*, 2919.
34. Luning Prak, D. J.; O'Sullivan, D. W. Solubility of 4-Nitrotoluene, 2,6-Dinitrotoluene, 2,3-Dinitrotoluene, and 1,3,5-Trinitrobenzene in Pure Water and Seawater. *J. Chem. Eng. Data* **2007**, *52*, 2446–2450.

35. Lakowicz, J. R. Principles of Fluorescence, 3rd Ed. Springer, NY, **2006**, pp 56, 284-287.
36. Wattebled, L.; Laschewsky, A.; Moussa, A.; Habib-Jiwan, J.-L. Aggregation Numbers of Cationic Oligomeric Surfactants: A Time-Resolved Fluorescence Quenching Study. *Langmuir* **2006**, *22*, 2551-2557.
37. Tehrani-Bagha, A. R.; Kärnbratt, J.; Löfroth, J.-E.; Holmberg, K. Cationic Ester-Containing Gemini Surfactants: Determination of Aggregation Numbers by Time-Resolved Fluorescence Quenching. *J. Colloid Interface Sci.* **2012**, *376*, 126-132.
38. Feng, L.; Xie, D.; Song, B.; Zhang, J.; Pei, X.; Cui, Z. Aggregate Evolution in Aqueous Solutions of Gemini Surfactants Derived from Dehydroabietic Acid. *Soft Matter* **2018**, *14*, 1210-1218.
39. Pisárčik, M.; Polakovičova, M.; Markuliak, M.; Lukáč, M.; Devínsky, F. Self-Assembly Properties of Cationic Gemini Surfactants with Biodegradable Groups in the Spacer. *Molecules* **2019**, *24*, 1481.
40. Robertson, J. M.; White, J. G. The Crystal Structure of Pyrene. A Quantitative X-Ray Investigation. *J. Chem. Soc.* **1947**, 358-368.
41. Almgren, M.; Swarup, S. Size of Sodium Dodecyl Sulfate Micelles in the Presence of Additives. 2. Aromatic and Saturated Hydrocarbons. *J. Phys. Chem.* **1982**, *86*, 4212-4216.

Chapter 3

1. Menger, F. M.; Littau, C. A. Gemini Surfactants: Synthesis and Properties. *J. Am. Chem. Soc.* **1991**, *113*, 1451-1452.
2. Sidenko, Z. S.; Limanov, V. E.; Skvortsova, E. K.; Dziomko, V. M. Synthesis and Antibacterial Activity of some Bisammonium Compounds. *Khimiko-Farmatsevticheskii Zhurnal* **1968**, *2*, 15-18.

3. Menger, F. M.; Keiper, J. S. Gemini Surfactants. *Angew. Chem. Int. Ed.* **2000**, *39*, 1906-1920.
4. Zana, R.; Xia, J. In *Gemini Surfactants: Synthesis, Interfacial and Solution-Phase Behavior, and Applications*, Marcel Dekker, Inc., New York, **2004**.
5. Han, Y.; Wang, Y. Aggregation Behavior of Gemini Surfactants and their Interactions with Macromolecules in Aqueous Solution. *Phys. Chem. Chem. Phys.* **2011**, *13*, 1939-1956.
6. Zana, R. Dimeric (gemini) surfactants: effect of the spacer group on the association behavior in aqueous solution. *J. Colloid Interface Sci.* **2002**, *248*, 203.
7. Zana, R.; Benrraou, M.; Rueff, R. Alkanediyl-.α.,.ω.-bis(dimethylalkylammonium bromide) surfactants. 1. Effect of the spacer chain length on the critical micelle concentration and micelle ionization degree. *Langmuir* **1991**, *7*, 1072.
8. Danino, D.; Talmon, Y.; Zana, R. Alkanediyl-.α.,.ω.-Bis(Dimethylalkylammonium Bromide) Surfactants (Dimeric Surfactants). 5. Aggregation and Microstructure in Aqueous Solutions. *Langmuir* 1995, *11*, 1448.
9. Zana, R.; Talmon, Y. Dependence of aggregate morphology on structure of dimeric surfactants. *Nature* **1993**, *362*, 228.
10. Kirby, A. J.; Camilleri, P,; Engberts, J. B. F. N. ; Feiters, M. C. ; Nolte, R. J. M.; Söderman, O.; Bergsma, M.; Bell, P. C.; Fielden, M. L.; Garcia Rodriguez, C. L.; Guédat, P.; Kermer, A.; McGregor, C.; Perrin, C.; Ronsin, G.; van Eijk, Gemini Surfactants: New Synthetic Vectors for Gene Transfection. *Angew. Chem. Int. Ed.* **2003**, *42*, 1448-1457.
11. Cardoso, A. M. S.; Silva, S. G.; do Vale, M. L.; Marques, E. F.; Pedroso de Lima, M. C.; Jurado, A. S. Gene Delivery Mediated by Gemini Surfactants: Structure – Activity Relationships in Engineering of Nanobiomaterials – Applications of Nanobiomaterials. Ed. Grumezescu, A. M., Elsevier, **2016**, pp 227 – 256.

12. Ahmed, T.; Kamel, A. O.; Wettig, S. D. Interactions between DNA and Gemini Surfactants: Impact on Gene Therapy: Part I. *Nanomedicine* **2016**, *11*, 289-306.
13. Kamal, M. S. A Review of Gemini Surfactants: Potential Application in Enhanced Oil Recovery. *J. Surfact. Deterg.* **2016**, *19*, 223-236.
14. Lyu, Y. Y.; Yi, S. H.; Shon, J. K.; Chang, S.; Pu, L. S.; Lee, S. Y.; Yie, J. E.; Char, K.; Stucky, G. D.; Kim, J. M. Highly Stable Mesoporous Metal Oxides Using Nano-Propping Hybrid Gemini Surfactants *J. Am. Chem. Soc.* **2004**, *126*, 2310-2311.
15. Kumar, N.; Tyagi, R. Industrial Applications of Dimeric Surfactants: A Review. *J. Disper. Sci. Technol.* **2014**, *35*, 205-214.
16. Rosen, M. J.; Tracy, D. J. Gemini Surfactants. *J. Surfactants Deterg.* **1998**, *1*, 547– 554.
17. Zana, R. Gemini (Dimeric) Surfactants. *Curr. Opin. Colloid Interface Sci.* **1996**, *1*, 566–571.
18. Rädler, J. O.; Koltover, I.; Salditt, T.; Safinyia, C. R. Structure of DNA-Cationic Liposome Complexes: DNA Intercalation in Multilamellar Membranes in Distinct Interhelical Packing Regime. *Science* **1997**, *275*, 810-814.
19. Koltover, I.; Salditt, T.; Rädler, J. O.; Safinyia, C. R. An Inverted Hexagonal Phase of Cationic Liposome-DNA Complexes Related to DNA Release and Delivery. *Science* **1998**, *281*, 78-81.
20. Rosenzweig, H. S.; Rakhmanova, V. A.; MacDonald, R. C. Diquarternary Ammonium Compounds as Transfection Agents. *Bioconjug. Chem.* **2001**, *12*, 258-263.
21. Wang, C.; Wettig, S. D.; Foldvari, M.; Verrall, R. E. Synthesis, Characterization, and Use of Asymmetric Pyrenyl-Gemini Surfactants as Emissive Components in DNA-Lipoplex Systems. *Langmuir* **2007**, *23*, 8995–9001.

22. Keyes-Baig, C.; Duhamel, J.; Wettig, S. Characterization of the Behavior of a Pyrene Substituted Gemini Surfactant in Water by Fluorescence. *Langmuir,* **2011**, *27*, 7, 3361-3371.

23. Ba-Salem, A. O., Duhamel, J.; Determination of the Aggregation Number of Pyrene-Labeled Gemini Surfactant Micelles by Pyrene Fluorescence Quenching Measurements. *Langmuir,* **2021**, *37*, 19, 6069-6079.

24. Kalyanasundaram, K.; Thomas, J. K. Environmental Effects on Vibronic Band Intensities in Pyrene Monomer Fluorescence and their Application in Studies of Micellar Systems. *J. Am. Chem. Soc.* **1977**, *99*, 2039−2044.

25. Dong, D. C.; Winnik, M. A. The Py Scale of Solvent Polarities. *Photochem. Photobiol.* **1982**, *35*, 17−21.

26. Farhangi, S.; Duhamel, J. A Pyrenyl Derivative with a Four Atom-Linker that Can Probe the Local Polarity of Pyrene-Labeled Macromolecules. *J. Phys. Chem. B* **2016**, *120*, 834-842.

27. Dai, Q.; Liu, W. M.; Zhuang, X. Q.; Wu, J. S.; Zhang, H. Y.; Wang, P. F. *Anal. Chem.* **2011**, *83*, 6559−6564.

28. Black, J. W.; Jennings, M. C.; Azarewicz, J.; Paniak, T. J.; Grenier, M. C.; Wuest, W. M.; Minbiole, K. P. C. *Bioorg. Med. Chem. Lett.* **2014**, *24*, 99.

29. Siu, H.; Prazeres, T. J. V.; Duhamel, J.; Olesen, K.; Shay, G. Characterization of the Aggregates Made by Short Poly(ethylene oxide) Chains Labelled at one End With the Dye Pyrene. *Macromolecules* **2005**, *38*, 2865-2875.

30. Luning Prak, D. J.; O'Sullivan, D. W. Solubility of 4-Nitrotoluene, 2,6-Dinitrotoluene, 2,3-Dinitrotoluene, and 1,3,5-Trinitrobenzene in Pure Water and Seawater. *J. Chem. Eng. Data* **2007**, *52*, 2446–2450.

31. Press, W.H.; Flanery, B.P.; Tenkolsky, S.A.; Vetterling, W.T. *Numerical Receipes in Fortran: The Art of Scientific Computing*; Cambridge University Press: New York, NY, USA, 1992; pp 523−528.
32. Infelta, P. P.; Gratzel, M.; Thomas J. K. Luminescence Decay of Hydrophobic Molecules Solubilized in Aqueous Micellar Systems. Kinetic Model. *J. Phys. Chem.* **1974**, *78*, 190-195.
33. Tachiya, M. Application of a Generating Function to Reaction Kinetics in Micelles. Kinetics of quenching of Luminescent Probes in Micelles. *Chem. Phys. Lett.* **1975**, *33*, 289-292.
34. Siu, H.; Duhamel, J. Comparison of the Association Level of a Hydrophobically Modified Associative Polymer Obtained from an Analysis Based on Two Different Models. *J. Phys. Chem. B* **2005**, *109*, 1770-1780.
35. Duhamel, J. Internal Dynamics of Dendritic Molecules Probed by Pyrene Excimer Formation. *Polymers* **2012**, *4*, 211-239.
36. Duhamel, J. New Insights in the Study of Pyrene Excimer Fluorescence to Characterize Macromolecules and their Supramolecular Assemblies in Solution. *Langmuir* **2012**, *28*, 6527-6538.
37. Lakowicz, J. R. Principles of Fluorescence, 3rd Ed. Springer, NY, **2006**, pp 56, 284-287.
38. Turro, N. J.; Yekta, A. Luminescent Probes for Detergent Solutions. A Simple Procedure for the Determination of the Mean Aggregation Number of Micelles. *J. Am. Chem. Soc.* **1978**, *100*, 5951-5952.
39. Raimbault, J.; Casier, R.; Little, H.; Duhamel, J. Hydrophobic and Elastic Forces Experienced by a Series of Pyrene End-Labeled Poly(ethylene oxide)s Interacting with Sodium Dodecyl Sulfate Micelles. *Macromolecules* **2018**, *51*, 5933-5943.

40. Cao, X.; Casier, R.; Little, H.; Duhamel, J. Characterization of the Distribution of Pyrene Molecules in Confined Geometries with the Model Free Analysis and its Applications. *J. Phys. Chem. B* **2017**, *121*, 11325-11332.
41. Li, H.; Hu, D.; Liang, F.; Huang, X.; Zhu, Q. Influence Factors on the Critical Micelle Concentration Determination Using Pyrene as a Probe and a Simple Method of Preparing samples. *R. Soc. Open Sci.* **2020**, *7*, 192092.
42. Thoma, L. J.; McNelles, S. A.; Adronov, A.; Duhamel, J. Direct Measure of the Local Concentration of Pyrenyl Groups in Pyrene-Labeled Dendrons Derived from the Rate of Fluorescence Collisional Quenching. *Polymers* **2020**, *12*, 2919.
43. Patel, S.; Seet, J.; Li, L.; Duhamel, J. Detection of Nitroaromatics by Pyrene-Labeled Starch Nanoparticles. *Langmuir* **2019**, *35*, 13145-13156.
44. Wattebled, L.; Laschewsky, A.; Moussa, A.; Habib-Jiwan, J.-L. Aggregation Numbers of Cationic Oligomeric Surfactants: A Time-Resolved Fluorescence Quenching Study. *Langmuir* **2006**, *22*, 2551-2557.
45. Tehrani-Bagha, A. R.; Kärnbratt, J.; Löfroth, J.-E.; Holmberg, K. Cationic Ester-Containing Gemini Surfactants: Determination of Aggregation Numbers by Time-Resolved Fluorescence Quenching. *J. Colloid Interface Sci.* **2012**, *376*, 126-132.
46. Feng, L.; Xie, D.; Song, B.; Zhang, J.; Pei, X.; Cui, Z. Aggregate Evolution in Aqueous Solutions of Gemini Surfactants Derived from Dehydroabietic Acid. *Soft Matter* **2018**, *14*, 1210-1218.
47. Pisárčik, M.; Polakovičova, M.; Markuliak, M.; Lukáč, M.; Devínsky, F. Self-Assembly Properties of Cationic Gemini Surfactants with Biodegradable Groups in the Spacer. *Molecules* **2019**, *24*, 1481.

48. Israelachvili, J. N.; Mitchell, D. J.; Ninham, B. W. Theory of Self-Assembly of Hydrocarbon Amphiphiles into Micelles and Bilayers. *J. Chem. Soc., Faraday Trans.* **1976**, *72*, 1525-1568.

Chapter 4

1. Ba-Salem, A. O.; Duhamel, J. Synthesis and Characterization of a Pyrene-Labeled Gemini Surfactant Sensitive to the Polarity of its Environment. *Langmuir* **2021**, *37*, 13824-13837.
2. Farhangi, S.; Duhamel, J. A Pyrenyl Derivative with a Four Atom-Linker that Can Probe the Local Polarity of Pyrene-Labeled Macromolecules. *J. Phys. Chem. B* **2016**, *120*, 834-842.
3. Kaler, E. W.; Murthy, A. K.; Rodriguez, B. E.; Zasadzinski, J. A. N. Spontaneous Vesicle Formation in Aqueous Mixtures of Single-Tailed Surfactants. *Science* **1989**, *245*, 1371-1374.
4. Kaler, E. W.; Herrington, K. L.; Murthy, A. K.; Zasadzinski, J. A. N. Phase Behavior and Structures of Mixtures of Anionic and Cationic Surfactants. *J. Phys. Chem.* **1992**, *96*, 6698-6707.
5. Koehler, R. D.; Raghavan, S. R.; Kaler, E. W. Microstructure and Dynamics of Wormlike Micellar Solutions Formed by Mixing Cationic and Anionic Surfactants. *J. Phys. Chem. B* **2000**, *104*, 11035-11044.
6. Hubbard, F. P.; Abbott, N. L. A Small Angle Neutron Scattering Study of the Thicknesses of Vesicle Bilayers Formed from Mixtures of Alkyl Sulfates and Cationic Bolaform Surfactants. *Soft Matter* **2008**, *4*, 2225-2231.
7. Song, S.; Zheng, Q.; Song, A.; Hao, J. Self-Assembled Aggregates Originated from the Balance of Hydrogen-Bonding, Electrostatic, and Hydrophobic Interactions. *Langmuir* **2012**, *28*, 219-226.

8. Bhattacharjee, J.; Aswal, V. K.; Hassan, P. A.; Pamu, R.; Narayanan, J.; Bellare, Structural evolution in catanionic mixtures of cetylpyridinium chloride and sodium deoxycholate. *Soft Matter* **2012**, *8*, 10130-10140.
9. Di Gregorio, M. C.; Pavel, N. V.; Miragaya, J.; Jover, A.; Meijide, F.; Tato, J. V.; Tellini, V. H. S.; Galantini, L. Catanionic Gels Based on Cholic Acid Derivatives. *Langmuir* **2013**, *29*, 12342-12351.
10. Vashishat, R.; Chabba, S.; Mahajan, R. K. Effect of Surfactant Head Group on Micellization and Morphological Transitions in Drug-Surfactant Catanionic Mixture: A Multi-Technique Approach. *Colloids Surf. A Physicochem. Eng. Asp.* **2016**, *498*, 206-217.
11. Zhang, J.; Pi, B.; Wang, X.; Yang, Z.; Lv, Q.; Lim, M. Formation of Polyhedral Vesicle Gels from Catanionic Mixtures of Hydrogenated and Perfluorinated Surfactants: Effect of Fluoro-Carbon Alkyl Chain Length. *Soft Matter* **2018**, *14*, 8231-8238.
12. Sharma, V. K.; Mitra, S.; Mukhopadhyay, R. Dynamic Landscape in Self-Assembled Surfactant Aggregates. *Langmuir* **2019**, *35*, 14151-14172.
13. Medos, Z.; Friesen, S.; Buchner, R.; Bester-Rogac, M. Interplay between Aggregation Number, Micelle Charge, and Hydration of Catanionic Surfactants. *Phys. Chem. Chem. Phys.* **2020**, *22*, 9998-10009.
14. Lioi, S. B.; Wang, X.; Islam, M. R.; Danoff, E. J.; English, D. S. Catanionic Surfactant Vesicles for Electrostatic Molecular Sequestration and Separation. *Phys. Chem. Chem. Phys.* **2009**, *11*, 9315-9325.
15. Wang, Y.; Marques, E. Non-Ideal Behavior of Mixed Micelles of Cationic Gemini Surfactants with Varying Spacer Length and Anionic Surfactants: A Conductimetry Study. *J. Mol. Liq.* **2008**, *142*, 136-142.
16. Aghdastinat, H.; Javadian, S.; Tehrani-Gagha, A.; Gharibi, H. Spontaneous Formation of Nanocubic Particles and Spherical Vesicles in Catanionic Mixtures of Ester-Containing

Gemini Surfactants and Sodium Dodecyl Sulfate in the Presence of Electrolyte. *J. Phys. Chem. B* **2014**, *118*, 3063-3073.

17. Ruiz, A.; Pinazo, A.; Pérez, L.; Manresa, A.; Marqués, A. M. Green Catanionic Gemini Surfactants-Lychenysin Mixture: Improved Surface, Antimicrobial, and Physiological Properties. *ACS Appl. Mater. Interfaces* **2017**, *9*, 22121-22131.
18. Mondal, S.; Pan, A.; Patra, A.; Mitra, R. K.; Ghosh, S. Ionic Liquid Mediated Micelle to Vesicle Transition of a Cationic Gemini Surfactant: A Spectroscopic Investigation. *Soft Matter* **2018**, *14*, 4185-4193.
19. Pinazo, A.; Pons, R.; Marqués, A.; Farfan, M.; da Silva, A.; Perez, L. Niocompatible Catanionic Vesicles from Arginine-Based Surfactants: A New Strategy to Tune the Antibacterial Activity and Cytotoxicity of Vesicular Systems. *Pharmaceutics* **2020**, *12*, 857.
20. Fendler, J. *Membrane Mimetic Chemistry*; Wiley: New York, **1983**.
21. Ostro, M. J., Ed. *Liposomes; From Biophysics to Therapeutics*; Marcel Dekker: New York, **1987**.
22. Bhandarkar, S.; Bose, A. Synthesis of Submicrometer Crystals of Aluminum Oxide by Aqueous Intravesicular Precipitation *J. Colloid Interface Sci*. **1990**, *135*, 531-538.
23. Turro, N. J.; Yekta, A. Luminescent Probes for Detergents Solutions. A Simple Procedure for the Determination of the Mean Aggregation Number of Micelles. *J. Am. Chem. Soc.* **1978**, *100*, 5951-5952.
24. Fowler, M.; Hisko, V.; Henderson, J.; Casier, R.; Li, L.; Thoma, L. J.; Duhamel, J. DiPyMe in SDS Micelles: Artifacts and their Implications in the Interpretation of Micellar Properties. *Langmuir* **2015**, *31*, 11971-11981.

25. Press, W.H.; Flanery, B.P.; Tenkolsky, S.A.; Vetterling, W.T. *Numerical Recipes in Fortran: The Art of Scientific Computing*; Cambridge University Press: New York, NY, USA, 1992; pp 523−528.
26. Siu, H.; Duhamel, J. Comparison of the Association Level of a Hydrophobically Modified Associative Polymer Obtained from an Analysis Based on Two Different Models. *J. Phys. Chem. B* **2005**, *109*, 1770-1780.
27. Duhamel, J. Internal Dynamics of Dendritic Molecules Probed by Pyrene Excimer Formation. *Polymers* **2012**, *4*, 211-239.
28. Duhamel, J. New Insights in the Study of Pyrene Excimer Fluorescence to Characterize Macromolecules and their Supramolecular Assemblies in Solution. *Langmuir* **2012**, *28*, 6527-6538.
29. Duhamel, J. Global Analysis of Fluorescence Decays to Probe the Internal Dynamics of Fluorescently Labeled Macromolecules. *Langmuir* **2014**, *30*, 2307-2324.
30. Kalyanasundaram, K.; Thomas, J. K. Environmental Effects on Vibronic Band Intensities in Pyrene Monomer Fluorescence and their Applications in Studies of Micellar Systems. *J. Am. Chem. Soc.* **1977**, 99, 2039-2044.
31. Chippisi, L.; Yalcinkaya, H.; Gopalakrishnam, V. K.; Gradzielski, M.; Zemb, T. Catanionic Surfactant Systems – Thermodynamic and Structural Conditions Revisited. *Colloid Polym. Sci.* **2015**, *293*, 3131-3143.
32. Raimbault, J.; Casier, R.; Little, H.; Duhamel, J. Hydrophobic and Elastic Forces Experienced by a Series of Pyrene End-Labeled Poly(ethylene oxide)s Interacting with Sodium Dodecyl Sulfate Micelles. *Macromolecules* **2018**, *51*, 5933-5943.

Chapter 5

1. Li S.; Huang L., Nonviral Gene Therapy: Promises and Challenges. *Gene Ther*. **2000**, *7*, 31 – 34.
2. Wolff J. A., The 'Grand' Problem of Synthetic Delivery. *Nat. Biotechnol*. **2002**, *20*, 768 – 769.
3. Wang, H.; Kaur, T.; Tavakoli, N.; Joseph, J.; Wettig, S. Transfection and Structural Properties of Phytanyl Substituted Gemini Surfactant-Based Vectors for Gene Delivery. *Phys. Chem. Chem. Phys.* **2013**, *15* (47), 20510 - 20516.
4. Mountain A. Gene Therapy: The First Decade. *Trends Biotechnol*. **2000**, *18*, 119 – 128.
5. Graham F. L. Adenovirus Vectors for High-Efficiency Gene Transfer into Mammalian Cells. *Immunol. Today* **2000**, *21*, 426 – 428.
6. Ledford H., Death in Gene Therapy Trial Raises Questions about Private IRBs. *Nat. Biotechnol*. **2007**, *25*, 1067.
7. Lehn P.; Fabrega S.; Oudrhiri N.; Navarro J. Gene Delivery Systems: Bridging the Gap between Recombinant Viruses and Artificial Vectors. *Adv. Drug Delivery Rev*. **1998**, *30*, 5 – 11.
8. Mintzer M. A.; Simanek E. E. Nonviral Vectors for Gene Delivery. *Chem. Rev*. **2009**, *109*, 259 – 302.
9. Koltover I.; Salditt T.; Rädler J. O.; Safinya C. R. Structure of DNA-Cationic Liposome Complexes: DNA Intercalation in Multilamellar Membranes in Distinct Interhelical Packing Regimes. *Science* **1997**, *275*, 810 – 814.
10. Koltover, I.; Salditt, T.; Rädler, J. O.; Safinya, C. R. An Inverted Hexagonal Phase of Cationic Liposome-DNA Complexes Related to DNA Release and Delivery. *Science* **1998**, *281*, 78 – 81.

11. Corsi J.; Hawtin R. W.; Ces O.; Attard G. S.; Khalid S. DNA Lipoplexes: Formation of the Inverse Hexagonal Phase Observed by Coarse-Grained Molecular Dynamics Simulation. *Langmuir* **2010**, *26*, 12119-12125.
12. Bell P. C.; Bergsma M.; Dolbnya I. P.; Bras W.; Stuart M. C. A.; Rowan A. E.; Feiters M. C.; Engberts J. B. F. N. Transfection Mediated by Gemini Surfactants: Engineered Escape from the Endosomal Compartment. *J. Am. Chem. Soc*. **2003**, *125*, 1551−1558.
13. Kirby, A. J.; Camilleri, P.; Engberts, J. B. F. N.; Feiters, M. C.; Nolte, R. J. M.; Söderman, O.; Bergsma, M.; Bell, P. C.; Fielden, M. L.; Garcia Rodriguez, C. L.; Guédat, P.; Kermer, A.; McGregor, C.; Perrin, C.; Ronsin, G.; van Eijk, M. C. P. Gemini Surfactants: New Synthetic Vectors for Gene Transfection. *Angew. Chem. Int. Ed*. **2003**, *42*, 1448– 1457.
14. Ronsin, G.; Perrin, C.; Guedat, P.; Kremer, A.; Camilleri, P.; Kirby, A. Novel Spermine-Based Cationic Gemini. *J. Chem. Commun*. **2001**, 2234- 2235.
15. Wang, C.; Wettig, S. D.; Foldvari, M.; Verrall, R. E. Synthesis, Characterization, and Use of Asymmetric Pyrenyl-Gemini Surfactants as Emissive Components in DNA-Lipoplex Systems. *Langmuir* **2007**, *23*, 8995–9001.
16. Wolfert, M. A.; Dash, P. R.; Nazarova, O.; Oupicky, D.; Seymour, L. W.; Smart, S.; Strohalm, J.; Ulbrich, K. Polyelectrolyte Vectors for Gene Delivery: Influence of Cationic Polymer on Biophysical Properties of Complexes Formed with DNA *Bioconjugate Chem*. **1999**, *10*, 993 – 1004.
17. Dufès, C.; Uchegbu, I. F.; Schätzlein, A.G., Dendrimers in Gene Delivery. *Adv. Drug Deliv. Rev*. **2005**, *15*, 2177-2202.
18. Badea, I.; Wettig, S.; Verrall, R. E.; Foldvari, M. Topical Non-invasive Gene Delivery Using Gemini Nanoparticles in Interferon-gamma-deficient Mice. *Eur. J. Pharm. Biopharm.* **2007**, *65*, 414–422.

19. Wasungu, L.; Stuart, M. C.; Scarzello, M.; Engberts, J. B.; Hoekstra, D. Lipoplexes Formed from Sugar-based Gemini Surfactants Undergo a Lamellar-to-micellar Phase Transition at Acidic pH. Evidence for a Non-inverted Membrane-destabilizing Hexagonal Phase of Lipoplexes. *Biochim. Biophys. Acta Biomembr.* **2006**, *1758,* 1677–1684.
20. Hato, M.; Minamikawa, H.; Tamada, K.; Baba, T.; Tanabe, Y. Self-Assembly of Synthetic Glycolipid/Water Systems. *Adv. Colloid Interface Sci*. **1999**, *80*, 233–270.
21. Wettig, S. D.; Verrall, R. E.; Foldvari, M. Gemini Surfactants: A New Family of Building Blocks for Non-viral Gene Delivery Systems. *Curr. Gene Ther*. **2008**, *8*, 9 – 23.
22. Bombelli, C.; Giansanti, L.; Luciani, P.; Mancini, G. Gemini Surfactant based Carriers in Gene and Drug Delivery. *Curr. Med. Chem*. **2009**, *16*, 171 – 18.
23. Snyder, E. L.; Dwody, S. F. Cell Penetrating Peptides in Drug Delivery. *Pharm. Res*. **2004**, *21*, 389 – 393.
24. Oda, R.; Candau, S.; Huc, I. Gemini Surfactants, the Effect of Hydrophobic Chain Length and Dissymmetry *J. Chem. Commun*. **1997**, *21*, 2105 – 2106.
25. Jiang, N.; Wang, J.; Wang, Y.; Yan, H.; Thomas, R. K. Microcalorimetric Study on the Interaction of Dissymmetric Gemini Surfactants with DNA. *J. Colloid Interface Sci.* **2005**, *284*, 759 – 764.
26. Rosen, M. J.; Mathias, J. H.; Davenport, L. Aberrant Aggregation Behavior in Cationic Gemini Surfactants Investigated by Surface Tension, Interfacial Tension, and Fluorescence Methods. *Langmuir* **1999**, *15*, 7340 – 7346.
27. Zhao, X.; Shang, Y.; Liu, H.; Hu, Y. Complexation of DNA with Cationic Gemini Surfactant in Aqueous Solution. *J. Colloid Interface Sci*. **2007**, *314*, 478 – 483.
28. Zhao, X.; Shang, Y.; Hu, J.; Liu, H.; Hu, Y. Biophysical Characterization of Complexation of DNA Oppositely Charged Gemini Surfactant 12-3-12. *Biophys. Chem*. **2008**, *138*, 144 – 149.

29. Ba-Salem, A. O., Duhamel, J. Determination of the Aggregation Number of Pyrene-Labeled Gemini Surfactant Micelles by Pyrene Fluorescence Quenching Measurements. *Langmuir,* **2021**, *37*, 19, 6069-6079.
30. Ba-Salem, A.; Duhamel, J. Synthesis and Characterization of a Pyrene-Labeled Gemini Surfactant Sensitive to the Polarity of its Environment. *Langmuir*, **2021**, *37*, 47, 13824-13837.
31. Winnik, F. M. Photophysics of pre-Associated Pyrenes in Aqueous Polymer Solutions and in Other Organized Media. *Chem. Rev.* **1993**, *93*, 587-614.
32. Kalyanasundaram, K.; Thomas, J. K. Environmental Effects on Vibronic Band Intensities in Pyrene Monomer Fluorescence and their Application in Studies of Micellar Systems. *J. Am. Chem. Soc.* **1977**, *99*, 2039−2044.
33. Dong, D. C.; Winnik, M. A. The Py Scale of Solvent Polarities. *Photochem. Photobiol.* **1982**, *35*, 17−21.
34. Siu, H.; Duhamel, J. Comparison of the Association Level of a Hydrophobically Modified Associative Polymer Obtained from an Analysis Based on Two Different Models. *J. Phys. Chem. B* **2005**, *109*, 1770-1780.
35. Duhamel, J. New Insights in the Study of Pyrene Excimer Fluorescence to Characterize Macromolecules and their Supramolecular Assemblies in Solution. *Langmuir* **2012**, *28*, 6527-6538.
36. Duhamel, J. Internal Dynamics of Dendritic Molecules Probed by Pyrene Excimer Formation. *Polymers* **2012**, *4*, 211-239.
37. Sharma, V. K.; Mitra, S.; Mukhopadhyay, R. Dynamic Landscape in Self-Assembled Surfactant Aggregates. *Langmuir* **2019**, *35*, 14151-14172.

38. Kaler, E. W.; Murthy, A. K.; Rodriguez, B. E.; Zasadzinski, J. A. N. Spontaneous Vesicle Formation in Aqueous Mixtures of Single-Tailed Surfactants. *Science* **1989**, *245*, 1371-1374.

39. Zhang, J.; Pi, B.; Wang, X.; Yang, Z.; Lv, Q.; Lim, M. Formation of Polyhedral Vesicle Gels from Catanionic Mixtures of Hydrogenated and Perfluorinated Surfactants: Effect of Fluoro-Carbon Alkyl Chain Length. *Soft Matter* **2018**, *14*, 8231-8238.

40. Vashishat, R.; Chabba, S.; Mahajan, R. K. Effect of Surfactant Head Group on Micellization and Morphological Transitions in Drug-Surfactant Catanionic Mixture: A Multi-Technique Approach. *Colloids Surf. A Physicochem. Eng. Asp.* **2016**, *498*, 206-217.

41. Aghdastinat, H.; Javadian, S.; Tehrani-Gagha, A.; Gharibi, H. Spontaneous Formation of Nanocubic Particles and Spherical Vesicles in Catanionic Mixtures of Ester-Containing Gemini Surfactants and Sodium Dodecyl Sulfate in the Presence of Electrolyte. *J. Phys. Chem. B* **2014**, *118*, 3063-3073.

42. Di Gregorio, M. C.; Pavel, N. V.; Miragaya, J.; Jover, A.; Meijide, F.; Tato, J. V.; Tellini, V. H. S.; Galantini, L. Catanionic Gels Based on Cholic Acid Derivatives. *Langmuir* **2013**, *29*, 12342-12351.

43. Bhattacharjee, J.; Aswal, V. K.; Hassan, P. A.; Pamu, R.; Narayanan, J.; Bellare, Structural evolution in catanionic mixtures of cetylpyridinium chloride and sodium deoxycholate. *Soft Matter* **2012**, *8*, 10130-10140.

44. Song, S.; Zheng, Q.; Song, A.; Hao, J. Self-Assembled Aggregates Originated from the Balance of Hydrogen-Bonding, Electrostatic, and Hydrophobic Interactions. *Langmuir* **2012**, *28*, 219-226.

45. Hubbard, F. P.; Abbott, N. L. A Small Angle Neutron Scattering Study of the Thicknesses of Vesicle Bilayers Formed from Mixtures of Alkyl Sulfates and Cationic Bolaform Surfactants. *Soft Matter* **2008**, *4*, 2225-2231.

46. Muslim, A. A. *Synthesis and Characterization of Dissymmetric Gemini Surfactants for Gene Delivery Applications*, PhD Thesis, University of Waterloo, Canada, **2016**, pp135 – 154.

47. Lakowicz, J. R. *Principles of Fluorescence Spectroscopy*, 3rd Ed. Springer, Singapore, **2006**, p 55.

48. Press, W.H.; Flanery, B.P.; Tenkolsky, S.A.; Vetterling, W.T. *Numerical Recipes in Fortran: The Art of Scientific Computing*; Cambridge University Press: New York, NY, USA, **1992**; pp 523−528.

49. Farhangi, S.; Duhamel, J. A Pyrenyl Derivative with a Four Atom-Linker that Can Probe the Local Polarity of Pyrene-Labeled Macromolecules. *J. Phys. Chem. B* **2016**, *120*, 834-842.

50. Cabane, B.; Duplessix, R. Decoration of Semidilute Polymer Solutions with Surfactant Micelles. *J. Phys.* **1987**, *48*, 651-662.

51. Fowler, M. A.; Duhamel, J.; Bahun, G. J.; Adronov, A.; Zaragoza-Galán, G.; Rivera, E. Studying Pyrene-Labeled Macromolecules with the Model Free Analysis. *J. Phys. Chem. B* **2012**, *116*, 14689-14699.

52. Farhangi, S.; Casier, R.; Li, L.; Thoma, J.; Duhamel, J. Characterization of the Long Range Internal Dynamics of Pyrene-Labeled Macromolecules by Pyrene Excimer Fluorescence. *Macromolecules* **2016**, *49*, 9597-9604.

53. Ba-Salem, A.; Gong, R.; Duhamel, J. Characterization of the Interactions between a Cationic Pyrene-Labeled Gemini Surfactant and the Anionic Surfactant Sodium Dodecyl Sulfate. *Langmuir* Submitted.

54. Winnik, F. M.; Regismond, S. T. A.; Goddard, E. D. Interactions of an Anionic Surfactant with a Fluorescent Dye-Labeled Hydrophobically Modified Cationic Cellulose Ether. *Langmuir* **1997**, *13*, 111-114.

55. Anghel, D. F.; Toca-Herrera, J. L.; Winnik, F. M.; Rettig, W.; v. Kliting, R. Steady-State Fluorescence Investigation of Pyrene-Labeled Poly(acrylic acid)s in Aqueous Solution and in the Presence of Sodium Dodecyl Sulfate. *Langmuir* **2002**, *18*, 5600-5606.
56. Anghel, D. F.; Alderson, V.; Winnik, F. M.; Mizusaki, M.; Morishima, Y. Fluorescent Dyes as Model 'Hydrophobic Modifiers' of Polyelectrolytes: A Study of Poly(acrylic acid)s Labeled with Pyrenyl and Naphthyl Groups. *Polymer* **1998**, *39*, 3035-3044.
57. Siu, H.; Duhamel, J. The Importance of Considering Nonfluorescent Pyrene Aggregates for the Study of pyrene-Labeled Associative Thickeners by Fluorescence. *Macromolecules* **2005**, *38*, 7184-7186.

Chapter 6

1. Wang, C.; Wettig, S. D.; Foldvari, M.; Verrall, R. E. Synthesis, Characterization, and Use of Asymmetric Pyrenyl-Gemini Surfactants as Emissive Components in DNA-Lipoplex Systems. *Langmuir* **2007**, *23*, 8995–9001.
2. Keyes-Baig, C.; Duhamel, J.; Wettig, S. Characterization of the Behavior of a Pyrene Substituted Gemini Surfactant in Water by Fluorescence. *Langmuir*, **2011**, *27*, 7, 3361-3371.
3. Turro, N. J.; Yekta, A. Luminescent Probes for Detergent Solutions. A Simple Procedure for the Determination of the Mean Aggregation Number of Micelles. *J. Am. Chem. Soc.* **1978**, *100*, 5951-5952.
4. Infelta, P. P.; Gratzel, M.; Thomas J. K. Luminescence Decay of Hydrophobic Molecules Solubilized in Aqueous Micellar Systems. Kinetic Model. *J. Phys. Chem.* **1974**, *78*, 190-195.

5. Tachiya, M. Application of a Generating Function to Reaction Kinetics in Micelles. Kinetics of quenching of Luminescent Probes in Micelles. *Chem. Phys. Lett.* **1975**, *33*, 289-292.
6. Farhangi, S.; Duhamel, J. A Pyrenyl Derivative with a Four Atom-Linker that Can Probe the Local Polarity of Pyrene-Labeled Macromolecules. *J. Phys. Chem. B* **2016**, *120*, 834-842.
7. Bhattacharjee, J.; Aswal, V. K.; Hassan, P. A.; Pamu, R.; Narayanan, J.; Bellare, Structural evolution in catanionic mixtures of cetylpyridinium chloride and sodium deoxycholate. *Soft Matter* **2012**, *8*, 10130-10140.
8. Di Gregorio, M. C.; Pavel, N. V.; Miragaya, J.; Jover, A.; Meijide, F.; Tato, J. V.; Tellini, V. H. S.; Galantini, L. Catanionic Gels Based on Cholic Acid Derivatives. *Langmuir* **2013**, *29*, 12342-12351.
9. Vashishat, R.; Chabba, S.; Mahajan, R. K. Effect of Surfactant Head Group on Micellization and Morphological Transitions in Drug-Surfactant Catanionic Mixture: A Multi-Technique Approach. *Colloids Surf. A Physicochem. Eng. Asp.* **2016**, *498*, 206-217.
10. Lioi, S. B.; Wang, X.; Islam, M. R.; Danoff, E. J.; English, D. S. Catanionic Surfactant Vesicles for Electrostatic Molecular Sequestration and Separation. *Phys. Chem. Chem. Phys.* **2009**, *11*, 9315-9325.

References: Appendix Supporting Information (SI)

S3

1. Dong, D. C.; Winnik, M. A. The Py Scale of Solvent Polarities. *Photochem. Photobiol.* **1982**, *35*, 17−21.
2. Siu, H.; Duhamel, J. Molar Extinction Coefficient of Pyrene Aggregates in Water. *J. Phys. Chem. B* **2008**, *112*, 15301-15312.

3. Siu, H., Duhamel, J. Molar Absorption Coefficient of Pyrene Aggregates in Water Generated by a Poly(ethylene oxide) Capped at a Single End with Pyrene. *J. Phys. Chem. B* **2012**, *116*, 1226-1233.

S4

1. Ba-Salem, A.; Duhamel, J. Synthesis and Characterization of a Pyrene-Labeled Gemini Surfactant Sensitive to the Polarity of its Environment. *Langmuir*, **2021**, *37*, 47, 13824-13837.
2. Siu, H.; Duhamel, J. Molar Extinction Coefficient of Pyrene Aggregates in Water. *J. Phys. Chem. B* **2008**, *112*, 15301-15312.
3. Siu, H., Duhamel, J. Molar Absorption Coefficient of Pyrene Aggregates in Water Generated by a Poly(ethylene oxide) Capped at a Single End with Pyrene. *J. Phys. Chem. B* **2012**, *116*, 1226-1233.

Appendix Supporting Information (SI)

S2 - Supporting information for Chapter 2

^{1}H NMR Spectra of Chemicals Prepared in Chapter 2

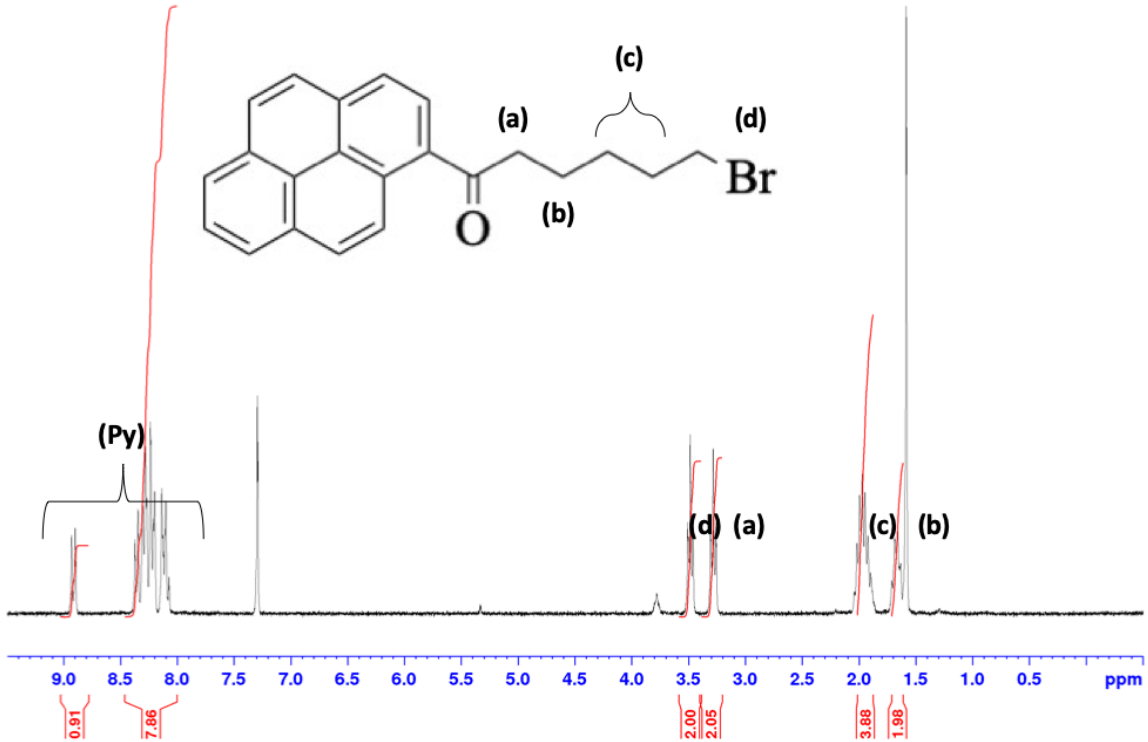

Figure S2.1: ^{1}H NMR spectrum of 5-bromohexane-1-pyrene ketone ($CDCl_3$, 300 MHz) δ (ppm): 8.91 (d, 1H, Py-H), 8.36-8.07 (m, 8H, Py-H), 3.48 (t, 2H, CH_2Br), 3.28 (t, 2H, α-CH_2), 1.97 (m, 4H, β-CH_2 and δ-CH_2), 1.66 (m, 2H, γ-CH_2).

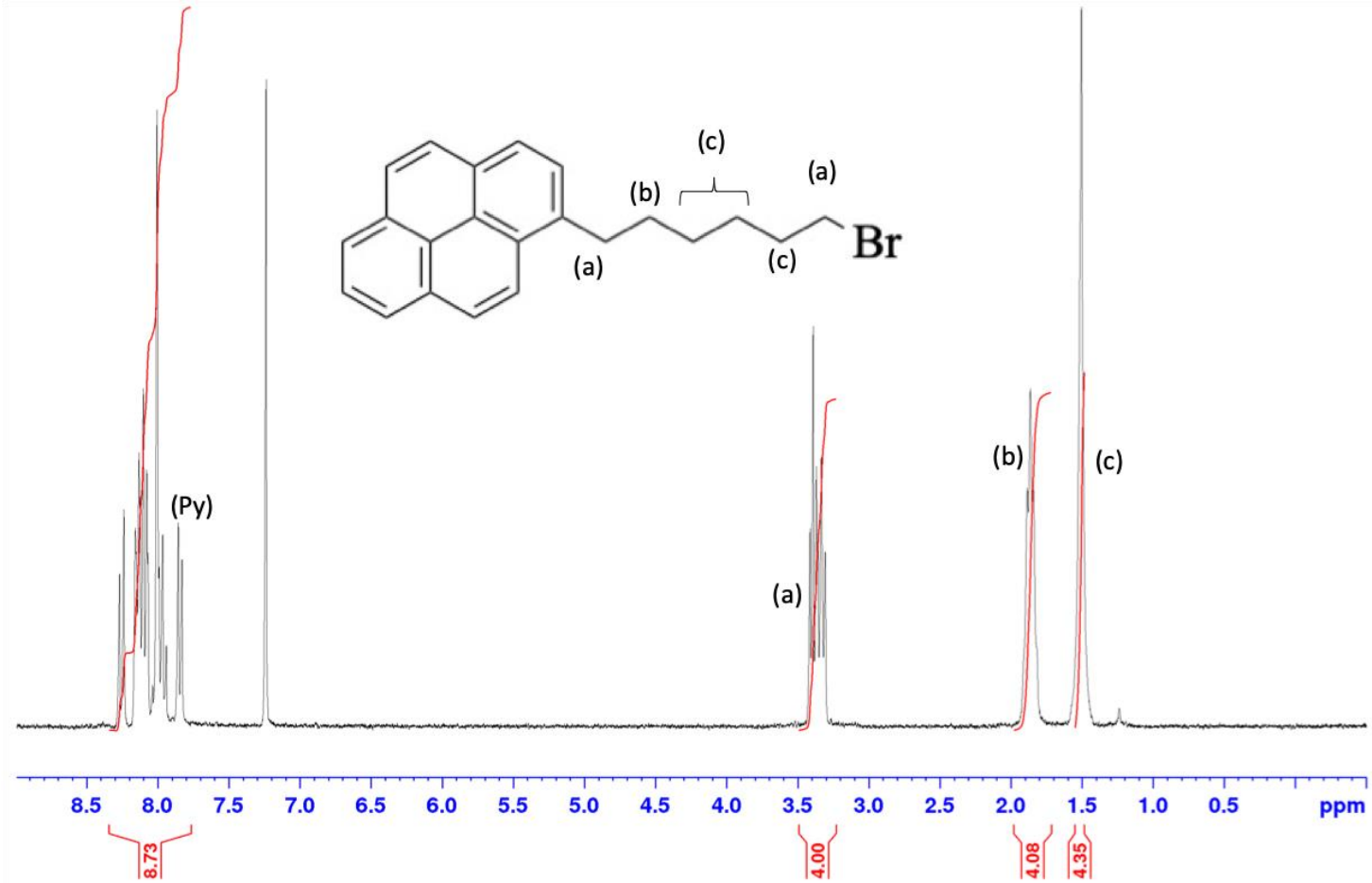

Figure S2.2: ^{1}H NMR spectrum of 6-(1-pyrenebromohexane) ($CDCl_3$, 300 MHz) δ (ppm): 8.26-7.85 (m, 9H, Py-H), 3.36 (m, 4H, CH_2Br and Py-CH_2), 1.86 (broad, 4H, β-CH_2 and ε-CH_2), 1.51 (broad, 4H, γ-CH_2 and δ-CH_2).

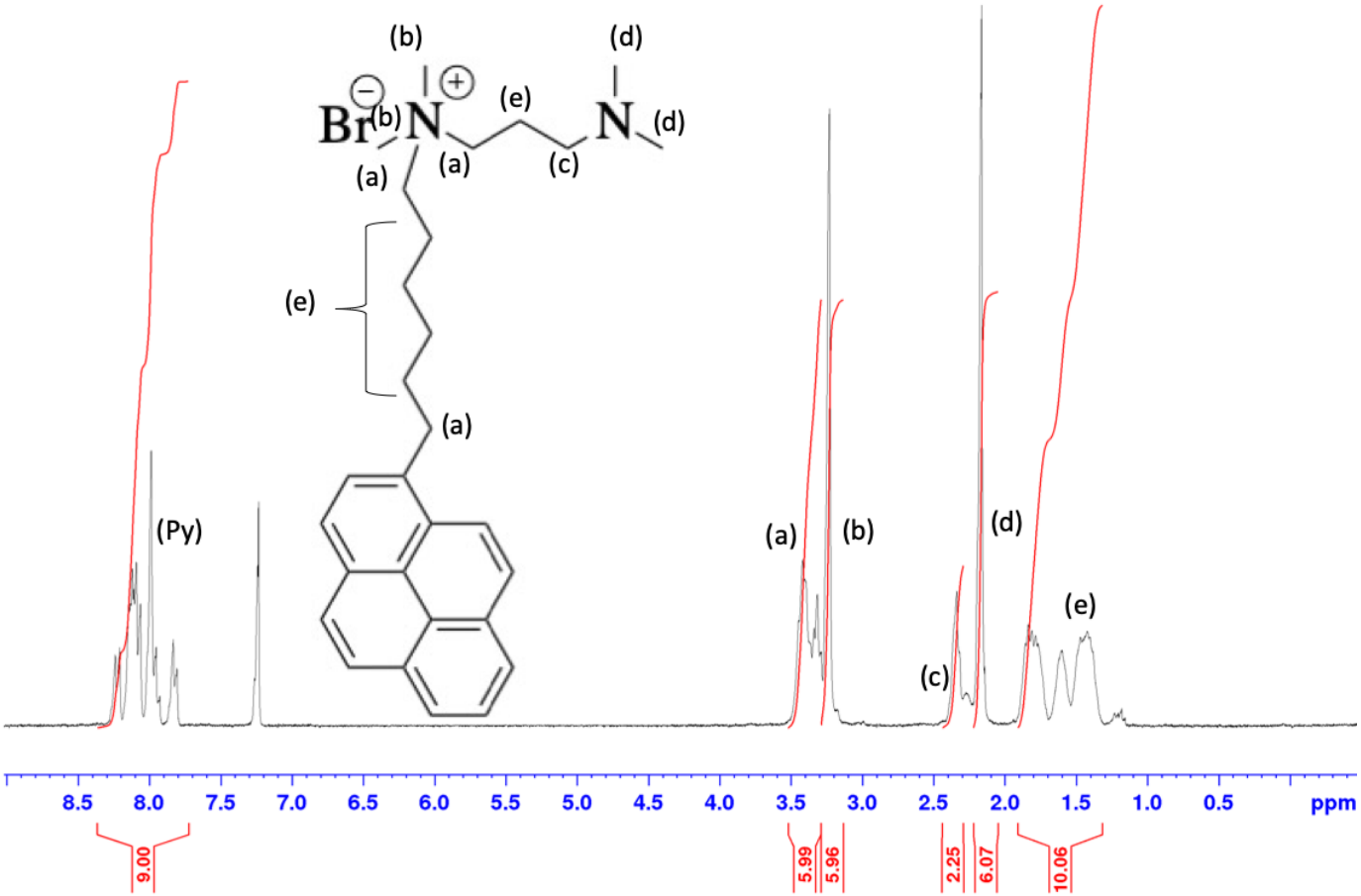

Figure S2.3: ^{1}H NMR spectrum of (N-(3-dimethylaminopropyl)-N,N-dimethyl-6-(pyren-6-yl)-hexan-1-ammonium bromide) ($CDCl_3$, 300 MHz) δ (ppm): 8.22-7.82 (m, 9H, Py-H), 3.50-3.29 (m, 6H, $^{+}N-CH_2$, Py-CH_2 and CH_2-N^{+}), 3.24 (s, 6H, $^{+}N(CH_3)_2$), 2.24 (t, 2H, CH_2-N), 2.10 (s, 6H, N-$(CH_3)_2$), 1.85-1.35 (m, 10H, $(CH_2)_5$, β-CH2 spacer).

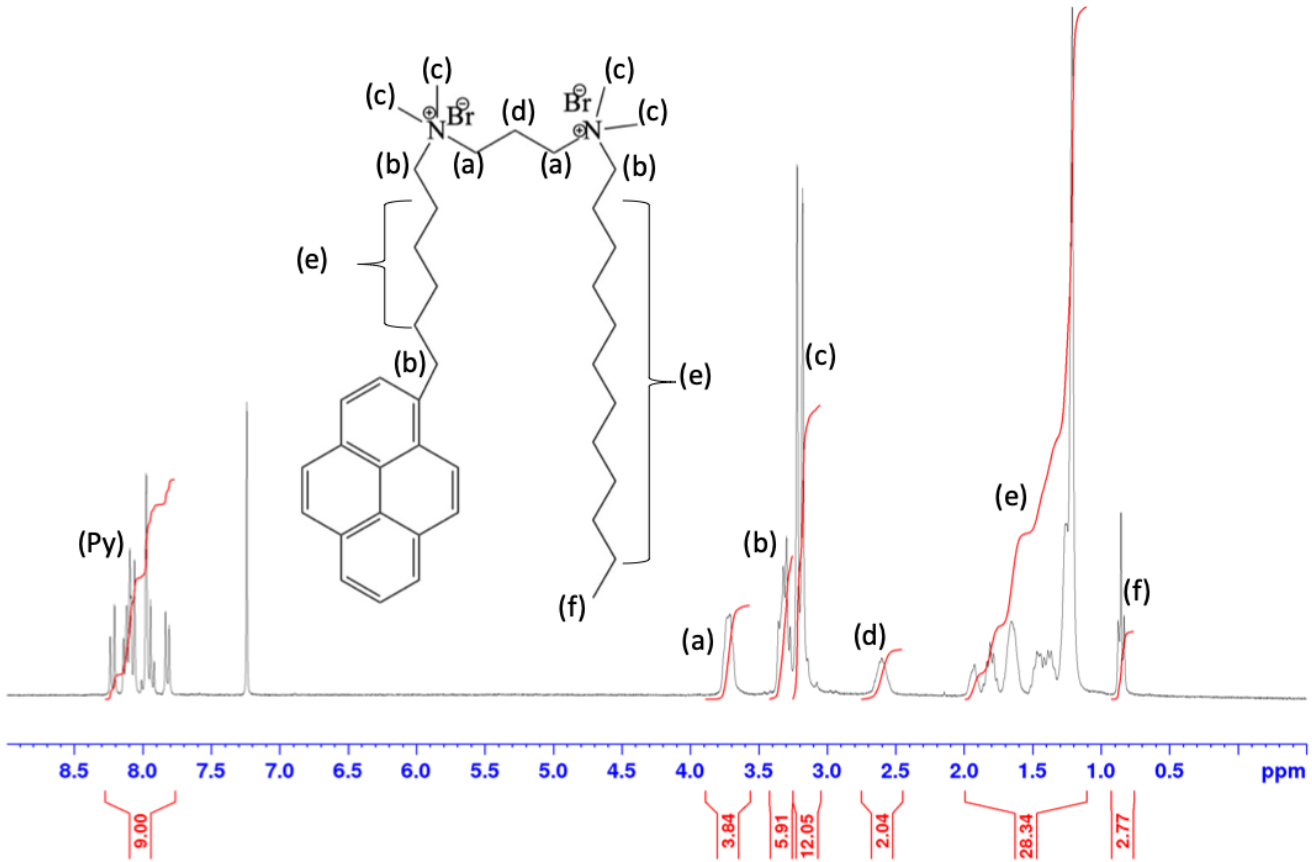

Figure S2.4: ^{1}H NMR spectrum of N^{1}-dodecyl,N^{1},N^{1},N^{3},N^{3}-tetramethyl-N^{3}-(6-(pyren-6-yl)-hexyl)propane-1,3-diammonium dibromide (Py-3-12) ($CDCl_3$, 300 MHz) δ (ppm): 8.23-7.80 (m, 9H, Py-H), 3.72 (broad, 4H, Spacer $^{+}$N-CH_2), 3.31 (m, 6H, Py-CH_2 and chain's N-CH_2), 3.21-3.18 (2 superimposed singlets, 12H, $^{+}$N-$(CH_3)_2$ on the Py side and $^{+}$N-$(CH_3)_2$ chain's side, 2.56 (broad, 2H, spacer's CH_2), 1.92-1.20 (m, 28H, -CH_2- from Py chain and C12 chain), 0.85 (t, 3H, CH_3 (C12 terminal)).

Quenching study of Py-3-12 by NaBr

The fluorescence decays of a 2.5×10^{-6} M Py-3-12 solution in water were acquired with different NaBr concentrations to generate the Stern-Volmer plot shown in Figure S5. The slope of the plot yielded the quenching rate constant of Py-3-12 by NaBr equal to 5.0 ($\pm$0.2)$\times10^{7}$ $M^{-1}\cdot s^{-1}$.

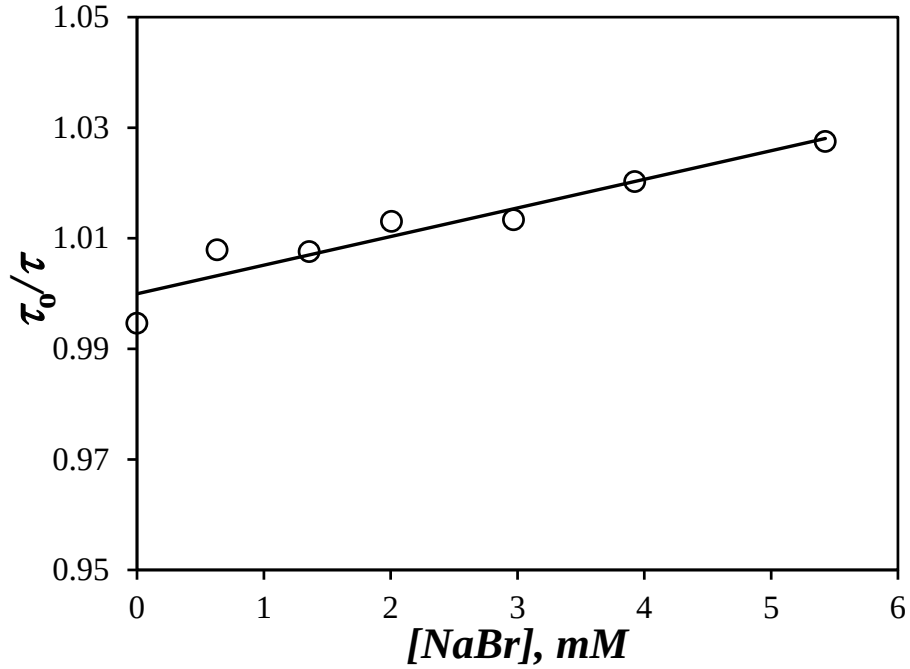

Figure S2.5. Stern-Volmer plot for the quenching of Py-3-12 by NaBr.

Model free analysis (MFA) of the pyrene monomer and excimer fluorescence decays:

The monomer and excimer fluorescence decays were fit globally according to the model free analysis (MFA) using Equations S2.1 and S2.2, respectively. The monomer decays were fit according to the sum of exponentials shown in Equation S2.1, which split into a first and second component describing the pyrenyl labels Py_{diff}*, that form excimer by diffusive encounters excimer formation (PEF), and Py_{free}*, that do not form excimer and emit with the natural lifetime (τ_M) of pyrene, respectively. The first component in Equation S2.1 handles pyrene excimer formation (PEF) with a sum of exponentials using the pre-exponential factors (a_i) and decay times (τ_i). Depending on whether a diffusive encounter between Py_{diff}* results in well

(*E*0*) or poorly (*D**) stacked excimer, Py_{diff}* is referred to as Py_{diffE0}* or Py_{diffD}*, respectively. The species *E*0* and *D**, which can be formed by diffusive encounters or direct excitation of a pyrene aggregate, emit with their lifetime τ_{E0} and τ_{EL}, respectively.

$$[Py^*]_{(t)} = ([Py^*_{diffE0}]_{(t=0)} + [Py^*_{diffD}]_{(t=0)}) \times \sum_{i=1}^{n} a_i \times \exp(-t/\tau_i) + [Py^*_{free}]_{(t=0)} \times \exp(-t/\tau_M) \quad \text{(S2.1)}$$

$$[E^*]_{(t)} = -[Py^*_{diffE0}]_{(t=0)} \times \sum_{i=1}^{n} a_i \frac{\frac{1}{\tau_i} - \frac{1}{\tau_M}}{\frac{1}{\tau_i} - \frac{1}{\tau_{E0}}} \exp(-t/\tau_i)$$

$$+ \left([E0^*]_{(t=0)} + [Py^*_{diffE0}]_{(t=0)} \times \sum_{i=1}^{n} a_i \frac{\frac{1}{\tau_i} - \frac{1}{\tau_M}}{\frac{1}{\tau_i} - \frac{1}{\tau_{E0}}} \right) \times \exp(-t/\tau_{E0})$$

$$-[Py^*_{diffD}]_{(t=0)} \times \sum_{i=1}^{n} a_i \frac{\frac{1}{\tau_i} - \frac{1}{\tau_M}}{\frac{1}{\tau_i} - \frac{1}{\tau_D}} \exp(-t/\tau_i) + \left([D^*]_{(t=0)} + [Py^*_{diffD}]_{(t=0)} \times \sum_{i=1}^{n} a_i \frac{\frac{1}{\tau_i} - \frac{1}{\tau_M}}{\frac{1}{\tau_i} - \frac{1}{\tau_D}} \right) \times \exp(-t/\tau_D)$$

(S2.2)

The MFA program retrieves parameters that yields the molar fractions f_{diffE0}, f_{diffEL}, f_{free}, f_{E0}, and f_{EL} of the species Py_{diffE0}*, Py_{diffEL}*, Py_{free}*, *E*0*, and *EL**, respectively. The state of the different pyrene molecules, that are forming by diffusive encounters, isolated, and aggregated, is then represented by the molar fractions f_{diff} (= f_{diffE0} + f_{diffEL}), f_{free}, and f_{agg} (= f_{E0} + f_{EL}), respectively. The average rate constant <*k*> of pyrene excimer formation is obtained from the a_i and τ_i parameters retrieved from the MFA of the fluorescence decays as shown in Equation S2.3.

$$< k > = \frac{\sum_{i=1}^{n} a_i}{\sum_{i=1}^{n} a_i \times \tau_i} - \frac{1}{\tau_M} \quad \text{(S2.3)}$$

Parameters retrieved from the analysis of the fluorescence decays

Table S2.1. Parameters retrieved from the MFA of the Py-3-12 monomer decays.

[Py-3-12] (mM)	τ_1 (ns)	a_1	τ_2 (ns)	a_2	τ_3 (ns)	a_3	τ_M (ns)	a_M	χ^2
2.00	1.07	0.72	2.89	0.20	1.00	0.00	92.2	0.09	1.03
1.50	0.93	0.60	2.40	0.30	1.00	0.00	91.5	0.10	1.00
1.25	1.05	0.66	2.78	0.20	1.00	0.00	91.9	0.13	1.10
1.00	1.20	0.73	3.97	0.09	1.00	0.00	92.2	0.18	1.03
0.90	1.19	0.69	3.79	0.10	1.00	0.00	94.6	0.21	1.03
0.80	1.09	0.49	2.32	0.24	1.00	0.00	94.7	0.27	1.00
0.75	1.22	0.59	2.97	0.13	1.00	0.00	96.7	0.28	1.02
0.65	1.09	0.53	2.91	0.15	1.00	0.00	97.4	0.32	1.09
0.60	1.23	0.54	3.85	0.10	1.00	0.00	98.3	0.36	0.98
0.50	1.15	0.47	2.93	0.11	1.00	0.00	97.6	0.42	1.02
0.45	1.03	0.47	2.83	0.12	1.00	0.00	97.1	0.41	1.03
0.40	0.87	0.40	2.21	0.19	1.00	0.00	97.1	0.41	1.01
0.35	0.86	0.34	2.66	0.11	1.00	0.00	96.6	0.55	1.04
0.30	0.99	0.24	3.03	0.06	1.00	0.00	95.6	0.70	1.07
0.28	0.76	0.21	2.23	0.11	1.00	0.00	95.6	0.68	0.98
0.25	0.15	0.87	0.05	2.81	1.00	0.00	95.3	0.80	1.02
0.22	0.11	0.59	0.07	1.84	1.00	0.00	91.5	0.82	1.06
0.20	0.08	0.64	0.03	2.37	1.00	0.00	94.7	0.89	1.04
0.18	0.47	0.04	1.59	0.03	17.97	0.03	97.0	0.90	1.09
0.15	0.77	0.03	3.03	0.02	18.10	0.02	97.0	0.93	1.01
0.10	1.15	0.03	5.19	0.01	20.32	0.02	97.0	0.95	1.06

Table S2.2. Parameters retrieved from the MFA of the Py-3-12 excimer decays.

[Py-3-12] (mM)	$f_{E_{diff}}^{E0}$	f_{EE0}	τ_{E0} (ns)	$f_{E_{diff}}^{D}$	f_{ED}	τ_{D} (ns)	χ^2
2.00	0.39	0.16	31.6	0.38	0.07	65.7	1.03
1.50	0.43	0.14	32.5	0.37	0.06	67.3	1.00
1.25	0.40	0.14	31.8	0.36	0.10	65.7	1.10
1.00	0.40	0.11	31.7	0.36	0.13	64.3	1.03
0.90	0.36	0.15	31.4	0.39	0.10	64.7	1.03
0.80	0.36	0.02	28.4	0.27	0.35	65.1	1.00
0.75	0.30	0.12	29.0	0.34	0.25	66.3	1.02
0.65	0.39	0.02	29.5	0.27	0.32	66.0	1.09
0.60	0.36	0.00	27.8	0.28	0.36	63.2	1.00
0.50	0.34	0.01	27.5	0.39	0.25	62.7	1.02
0.45	0.43	0.05	31.6	0.34	0.18	67.8	1.03
0.40	0.53	0.05	35.1	0.37	0.05	73.9	1.01
0.35	0.40	0.01	29.5	0.40	0.20	64.0	1.04
0.30	0.39	0.18	33.8	0.23	0.20	73.2	1.07
0.28	0.38	0.03	30.5	0.39	0.20	63.8	0.98
0.25	0.31	0.16	33.0	0.28	0.24	66.1	1.02
0.22	0.40	0.16	35.9	0.32	0.12	69.9	1.06
0.20	0.36	0.25	37.0	0.26	0.13	71.5	1.04
0.18	0.49	0.07	24.4	0.24	0.20	71.7	1.09
0.15	0.32	0.16	24.7	0.26	0.26	66.9	1.01
0.10	0.30	0.17	24.6	0.21	0.33	65.1	1.06

Table S2.3. Molar fractions of the different pyrene species and <k> values from MFA of the Py-3-12 decays.

[Py-3-12] (mM)	<k>	f_{free}	f_{diff}^{E0}	f_{diff}^{D}	f_{diff}	f_{E0}	f_{D}	f_{agg}	[Py_{free}]
2.00	0.673	0.067	0.365	0.353	0.718	0.146	0.069	0.215	0.134
1.50	0.695	0.085	0.395	0.337	0.732	0.126	0.057	0.183	0.128
1.25	0.675	0.106	0.357	0.324	0.680	0.121	0.093	0.214	0.132
1.00	0.659	0.146	0.344	0.305	0.649	0.090	0.114	0.205	0.146
0.90	0.643	0.163	0.299	0.324	0.623	0.127	0.087	0.214	0.147
0.80	0.660	0.192	0.293	0.219	0.512	0.013	0.283	0.296	0.154
0.75	0.645	0.201	0.238	0.268	0.506	0.092	0.201	0.293	0.151
0.65	0.661	0.236	0.299	0.204	0.503	0.017	0.243	0.261	0.154
0.60	0.624	0.265	0.267	0.206	0.473	0.000	0.262	0.262	0.160
0.50	0.661	0.343	0.222	0.259	0.481	0.010	0.166	0.176	0.171
0.45	0.708	0.350	0.280	0.221	0.502	0.030	0.119	0.149	0.157
0.40	0.755	0.380	0.327	0.229	0.556	0.034	0.031	0.064	0.152
0.35	0.761	0.497	0.199	0.203	0.402	0.003	0.099	0.101	0.174
0.30	0.708	0.593	0.158	0.092	0.250	0.074	0.083	0.157	0.178
0.28	0.786	0.624	0.142	0.146	0.287	0.012	0.077	0.088	0.175
0.25	0.751	0.705	0.093	0.082	0.175	0.048	0.072	0.120	0.172
0.22	0.910	0.763	0.096	0.075	0.171	0.038	0.029	0.067	0.167
0.20	0.847	0.828	0.061	0.045	0.106	0.043	0.022	0.065	0.163
0.18	0.167	0.867	0.065	0.032	0.097	0.010	0.027	0.036	0.156
0.15	0.131	0.890	0.035	0.028	0.064	0.017	0.028	0.046	0.134
0.10	0.118	0.899	0.030	0.021	0.052	0.017	0.033	0.050	0.090

Table S2.4. Parameters retrieved from the biexponential fits of the monomer decays for Py-3-12 DNT quenching experiment to find k_q (see Figure 2.6). [Py-3-12] = 7.9 μM

[DNT] (mM)	τ_1 (ns)	a_1	τ_M (ns)	a_M	χ^2
0.36	8.89	0.40	84.5	0.60	1.12
0.24	8.63	0.44	89.7	0.56	1.14
0.18	9.35	0.42	92.5	0.58	1.15
0.14	9.08	0.41	95.0	0.59	1.12
0.09	8.91	0.37	97.5	0.63	1.09
0.07	10.7	0.14	98.6	0.86	0.94
0.00	40.0	0.05	103.1	0.94	1.08

Table S2.5. Parameters retrieved from the biexponential fits of the monomer decays for Py-3-12 DNT quenching experiment to find N_{agg} (see Figure 2.7). [Py-3-12] = 2.2 M

[DNT] (mM)	τ_1 (ns)	a_1	τ_M (ns)	a_M	χ^2
1.63	6.17	0.11	58.2	0.89	1.09
1.45	18.2	0.06	60.6	0.94	0.95
1.24	28.0	0.06	64.3	0.94	1.03
1.02	26.2	0.07	68.4	0.93	1.05
0.83	14.3	0.07	72.0	0.93	1.01
0.67	17.1	0.07	75.9	0.93	1.10
0.55	20.1	0.07	79.0	0.93	1.05
0.45	7.2	0.17	81.6	0.83	1.04
0.35	28.6	0.08	99.6	0.92	1.04

Table S2.6. Parameters retrieved from the biexponential fits of the excimer decays for Py-3-12 DNT quenching experiment to find N_{agg} (see Figure 2.7). [Py-3-12] = 2.2 M.

[DNT] (mM)	τ_1 (ns)	a_1	τ_2 (ns)	a_2	χ^2
1.63	12.9	0.56	34.1	0.44	1.17
1.45	14.2	0.55	36.3	0.45	1.27
1.24	16.7	0.53	39.2	0.47	1.20
1.02	18.6	0.51	42.1	0.49	1.17
0.83	19.3	0.47	44.5	0.53	1.25
0.67	21.1	0.44	47.0	0.56	1.10
0.55	24.3	0.47	49.7	0.53	0.95
0.45	25.5	0.46	51.7	0.54	0.87
0.35	38.5	0.57	64.7	0.43	0.95

Table S2.7. Parameters retrieved from the fits of the excimer decays with the micellar model for Py-3-12 DNT quenching experiment to find N_{agg} (see Figure 2.7). [Py-3-12] = 2.2 mM.

[DNT] (mM)	f_{E0}	f_D	k_q ($\times 10^7$ s^{-1})	$\langle n \rangle_D$	χ^2	$\langle n \rangle_s$
1.63	1.00	0.00	2.1	1.22	1.14	2.11
1.45	0.99	0.01	2.3	1.02	1.15	1.90
1.24	0.96	0.04	2.2	0.83	1.01	1.70
1.02	0.94	0.06	2.7	0.58	1.12	1.48
0.83	0.91	0.09	3.3	0.42	1.16	1.22
0.67	0.88	0.12	4.1	0.30	0.95	0.96
0.55	0.84	0.16	3.6	0.23	0.93	0.84
0.45	0.80	0.20	4.1	0.18	0.97	0.66

S3 - Supporting information for Chapter 3

^{1}H NMR Spectra of chemicals prepared in Chapter 3

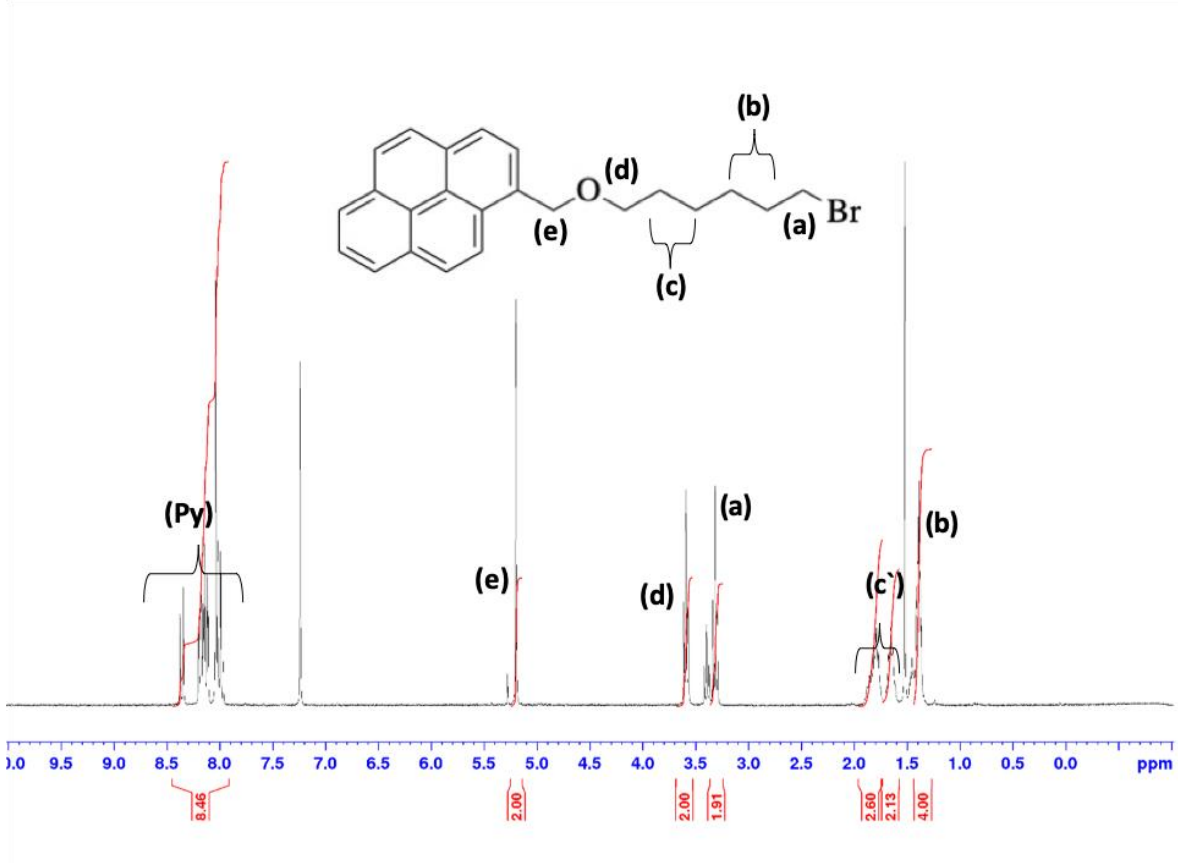

Figure S3.1. ^{1}H NMR spectrum of 1-(((6-bromohexyl)oxy)methyl)pyrene (**1**) ($CDCl_3$, 300 MHz) δ (ppm): 8.37-7.99 (m, 9H, py-H), 5.20 (s, 2H, py-CH_2-O), 3.59 (t, 2H, O-CH_2-), 3.37 (t, 2H, -CH_2-Br), 1.81-1.63 (m, 4H, $(CH_2)_2$ close to oxygen), 1.44 (m, 4H, $(CH_2)_2$ close to Br).

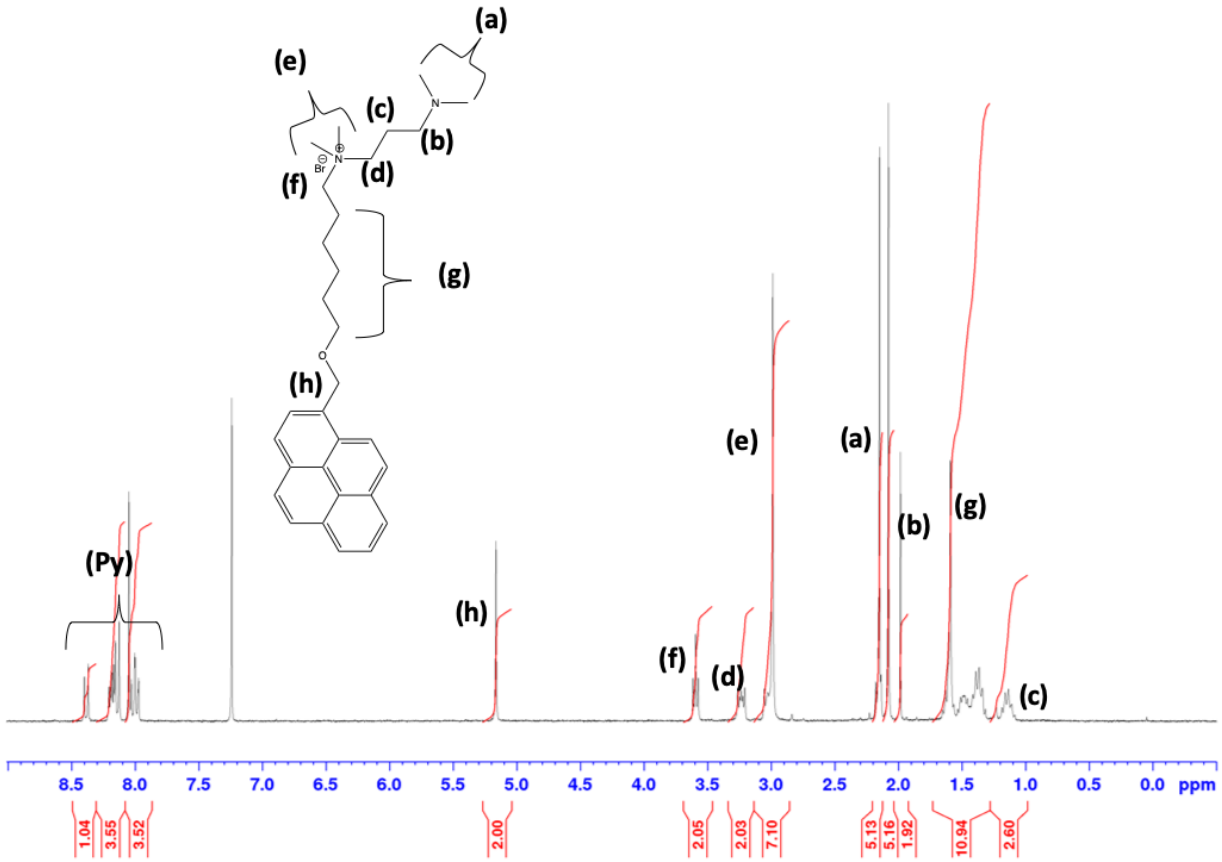

Figure S3.2. ^{1}H NMR spectrum of N-(3-(dimethylamino)propyl)-N,N-dimethyl-6-(pyren-1-ylmethoxy)hexan-1-aminium bromide (**2**). ($CDCl_3$, 300 MHz): 8.43-8.01 (m, 9H, py-H), 5.17 (s, 2H, py-CH_2-O), 3.60 (t, 2H, O-CH_2-), 3.23 (broad, 2H, $^{+}$N-CH_2), 2.99 (s, 6H, +N-$(CH_3)_2$), 2.14 (s, 6H, N-$(CH_3)_2$), 1.98 (broad, 2H, N-CH_2), 1.63-1.27 (broad m, 10H, $(CH_2)_5$).

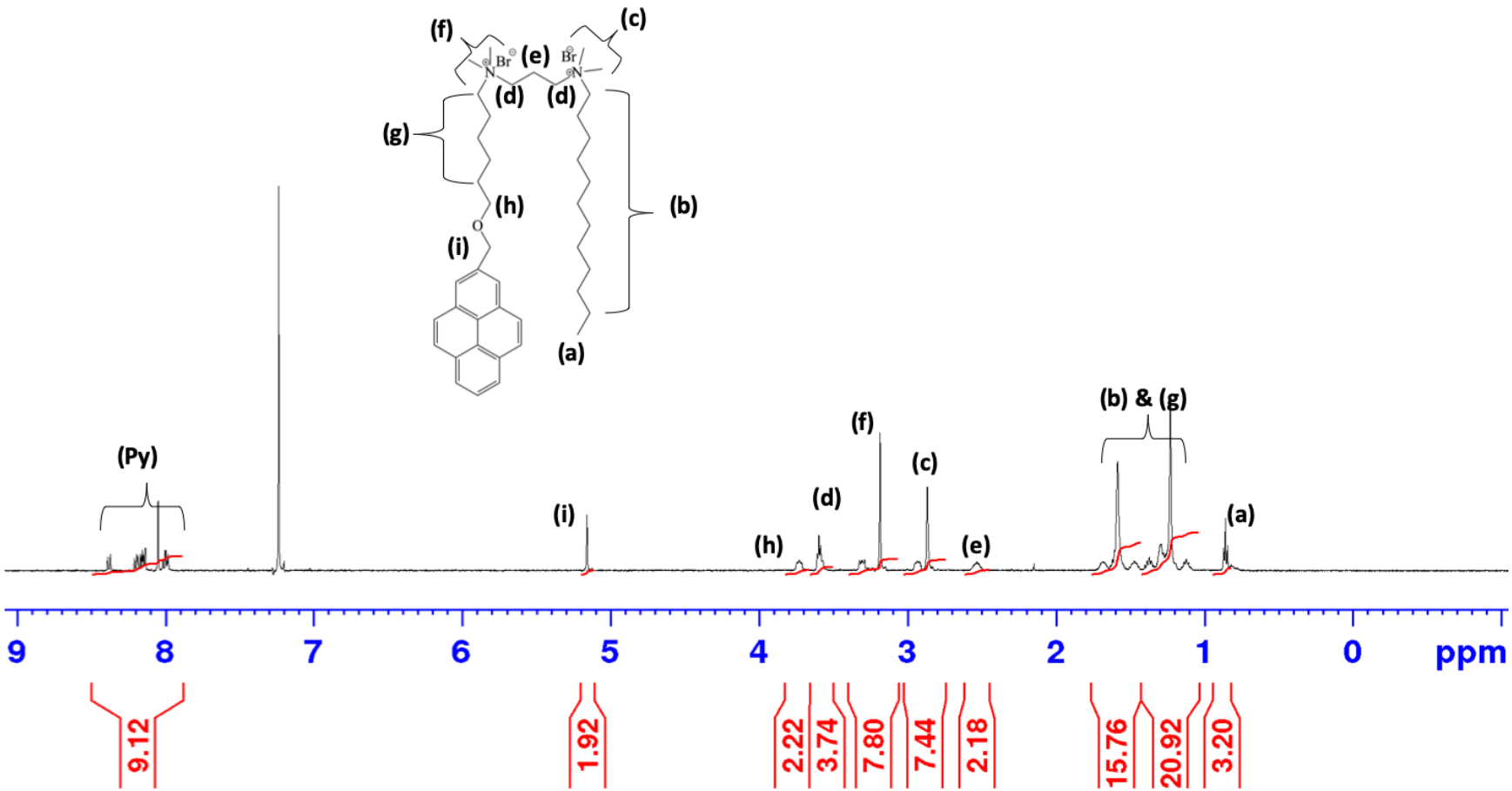

Figure S3.3. ^{1}H NMR spectrum of mono(N^1-dodecyl-N^1,N^1,N^3,N^3-tetramethyl-N^3-(6-(pyren-2-ylmethoxy)hexyl)propane-1,3-diaminium) monobromide (**3**, PyO-3-12) (CDCl3, 300 MHz): 8.38-8.01 (m, 9H py-H), 5.14 (s,2H, py-CH2-O) 3,56 (broad, 4H, (+N-CH2)2), 3.17 (s, 6H, +N-(CH3)2 py tail), 2.90 (s, 6H, +N-(CH3)2 C12 tail), 2.51 (m, 2H, CH2 spacer), 1.66-1.12 (m, 28H, -CH2-), 0.85 (t, 3H, CH3 C12 tail).

Fluorescence spectra of PyO-3-12 and Py-3-12

The complete fluorescence of PyO-3-12 and Py-3-12 acquired in different solvents are presented in Figure S3.4A and B, respectively. While pyrene excimer formation (PEF) is observed for PyO-3-12 and Py-3-12 in some solvents, the amount of excimer emission at 480 nm is very low compared to that observed in Figure 3.5A. The low excimer fluorescence observed in Figures S3.4A and B indicates that residual aggregation of PyO-3-12 and Py-3-12 occurs in some organic solvents, but that this level of aggregation is too low to affect any conclusions reached in this study of PyO-3-12 and Py-3-12 based on the analysis of their fluorescence spectra.

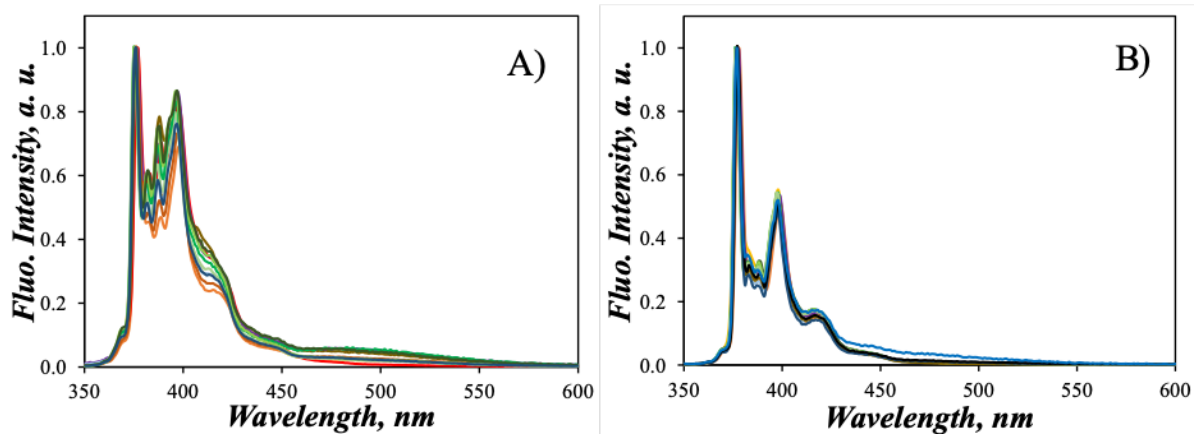

Figure S3.4. Steady-state fluorescence spectra of (A) PyO-3-12 and (B) Py-3-12 in 14 solvents: ( ) 1,4-dioxane, ( ) toluene, ( ) ethyl acetate, ( ) tetrahydrofuran, ( ) dichloromethane, ( ) 1-hexanol, ( ) 2-propanol, ( ) acetone, ( ) ethanol, ( ) methanol, ( ) acetonitrile, ( ) *N*,*N*-dimethylformamide, ( ) dimethylsulfoxide, ( ) water). [*Py*] = 2.5×10^{-6} M; spectra were normalized to 1.0 at the first peak corresponding to the 0-0 transition.

I_1/I_3 values for Py-3-12, PyO-3-12 and molecular pyrene in 14 solvents

Table S3.1. I_1/I_3 values for Py-3-12, PyO-3-12, and molecular pyrene in 14 solvents.

Solvent	Dielectric Constant	I_1/I_3 (Py-3-12)	I_1/I_3 (PyO-3-12)	I_1/I_3 (Py)[1]
Water	78.5	3.24	1.69	1.87
DMSO	47.2	3.76	2.14	1.95
DMF	38.3	3.69	1.92	1.81
Acetonitrile	36.6	3.78	1.71	1.79
Methanol	32.7	3.22	1.57	1.35
Ethanol	24.6	3.09	1.44	1.18
Acetone	19.7	3.98	N/A	1.64
2-Propanol	13.4	3.07	1.34	N/A
1-Hexanol	12.1	3.05	1.32	N/A
Dichloromethane	8.9	3.34	1.43	N/A
Tetrahydrofuran	7.5	3.50	N/A	1.35
Ethyl acetate	6.1	3.34	N/A	1.37
Toluene	2.4	N/A	1.42	1.04
1,4-Dioxane	2.2	3.65	1.27	1.5

Quenching study of PyO-3-12 by NaBr

The fluorescence decays of a 3.6×10^{-6} M PyO-3-12 solution in water were acquired with different NaBr concentrations to generate the Stern-Volmer plot shown in Figure S3.5. The slope of the plot yielded the quenching rate constant of PyO-3-12 by NaBr equal to 5.6 $(\pm0.9)\times10^{7}$ $M^{-1}\cdot s^{-1}$.

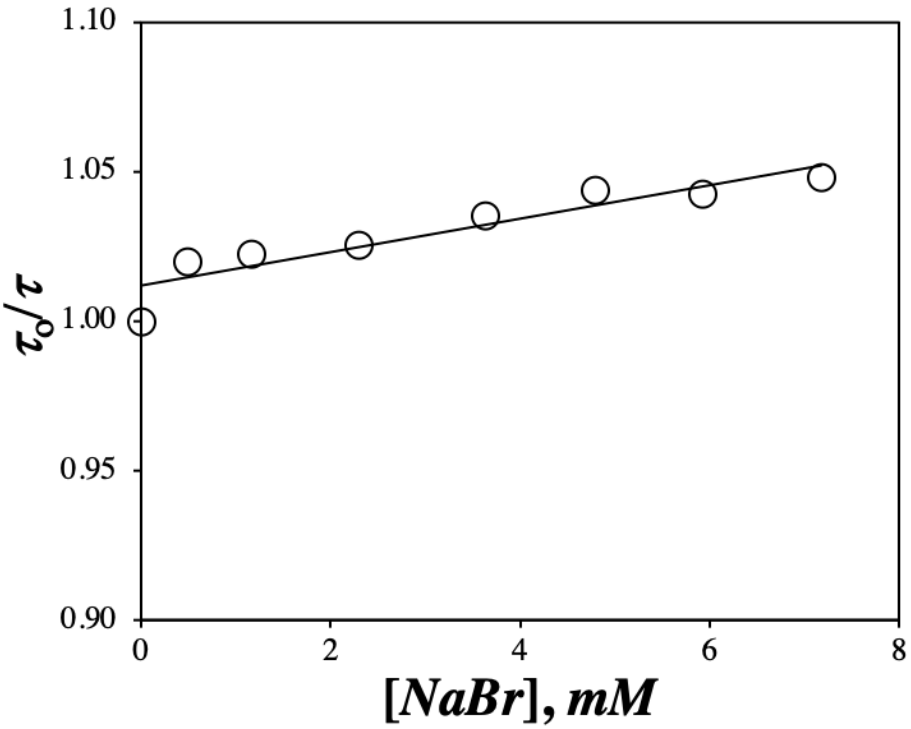

Figure S3.5. Stern-Volmer plot for the quenching of PyO-3-12 by NaBr.

Equations used for the model free analysis (MFA) of the pyrene monomer and excimer fluorescence decays and determination of the molar fractions:

The pyrene monomer and excimer fluorescence decays were fitted globally according to the model free analysis (MFA) with Equations S3.1 and S3.2, respectively. The normalized pre-exponential factors (a_i so that $\Sigma a_i = 1$) and decay times (τ_i) were optimized according to the Marquardt-Levenberg algorithm and were constrained to remain the same in both Equations S3.1 and S3.2. They were used to calculate the average rate constant ($<k>$) for pyrene excimer formation (PEF) according to Equation S3.3. Equations S3.1 and S3.2 use the radiative rate constants of the pyrene monomer in water ($k_{M,wat}^{rad}$) and in the PyO-3-12 micelles ($k_{M,mic}^{rad}$) and of the species $E0^*$ ($k_{E0,mic}^{rad}$) and D^* ($k_{D,mic}^{rad}$) in the PyO-3-12 micelles. They also use the molar absorption coefficients of the pyrene monomer in water ($\varepsilon_{M,wat}$) and in the PyO-3-12 micelles ($\varepsilon_{M,mic}$) and of the species $E0^*$ ($\varepsilon_{E0,mic}$) and D^* ($\varepsilon_{D,mic}$) in the PyO-3-12 micelles.

$$[Py^*]_{(t)} = k^{rad}_{M,mic}\varepsilon_{M,mic}[Py^*_{diff}]_{(t=0)} \times \sum_{i=1}^{n} a_i \times \exp(-t/\tau_i) + k^{rad}_{M,wat}\varepsilon_{M,wat}[Py^*_{free}]_{(t=0)} \times \exp(-t/\tau_M) \quad \text{(S3.1)}$$

$$[E^*]_{(t)} = -k^{rad}_{E0,mic}\varepsilon_{M,mic}[Py^*_{diff}]_{(t=0)} \times \sum_{i=1}^{n} a_i \frac{\frac{1}{\tau_i} - \frac{1}{\tau_M}}{\frac{1}{\tau_i} - \frac{1}{\tau_{E0}}} \exp(-t/\tau_i)$$

$$+k^{rad}_{E0,mic}\left(\varepsilon_{E0,mic}[E0^*]_{(t=0)} + \varepsilon_{M,mic}[Py^*_{diff}]_{(t=0)} \times \sum_{i=1}^{n} a_i \frac{\frac{1}{\tau_i} - \frac{1}{\tau_M}}{\frac{1}{\tau_i} - \frac{1}{\tau_{E0}}} \right) \times \exp(-t/\tau_{E0})$$

$$+k^{rad}_{D,mic}\varepsilon_{D,mic}[D^*]_{(t=0)} \times \exp(-t/\tau_D) \quad \text{(S3.2)}$$

$$< k > = \frac{\sum_{i=1}^{n} a_i}{\sum_{i=1}^{n} a_i \tau_i} - \frac{1}{\tau_M} \quad \text{(S3.3)}$$

The pre-exponential factors in the monomer and excimer fluorescence decays were employed to determine the fractions f_{Mdiff}, f_{Mfree}, f_{Ediff}, f_{EE0}, and f_{ED} whose expressions are provided in Equations S3.4 – S3.8.

$$f_{Mdiff} = \frac{[Py^*_{diff}]}{[Py^*_{diff}] + (k^{rad}_{M,wat}\varepsilon_{M,wat} / k^{rad}_{M,mic}\varepsilon_{M,mic})[Py^*_{free}]} \quad \text{(S3.4)}$$

$$f_{Mfree} = \frac{(k^{rad}_{M,wat}\varepsilon_{M,wat} / k^{rad}_{M,mic}\varepsilon_{M,mic})[Py^*_{free}]}{[Py^*_{diff}] + (k^{rad}_{M,wat}\varepsilon_{M,wat} / k^{rad}_{M,mic}\varepsilon_{M,mic})[Py^*_{free}]} \quad \text{(S3.5)}$$

$$f_{Ediff} = \frac{[Py^*_{diff}]}{[Py^*_{diff}] + (k^{rad}_{E0,mic}\varepsilon_{E0,mic} / k^{rad}_{E0,mic}\varepsilon_{M,mic})[E0^*] + (k^{rad}_{D,mic}\varepsilon_{D,mic} / k^{rad}_{E0,mic}\varepsilon_{M,mic})[D^*]} \quad \text{(S3.6)}$$

$$f_{EE0} = \frac{(k^{rad}_{E0,mic}\varepsilon_{E0,mic} / k^{rad}_{E0,mic}\varepsilon_{M,mic})[E0^*]}{[Py^*_{diff}] + (k^{rad}_{E0,mic}\varepsilon_{E0,mic} / k^{rad}_{E0,mic}\varepsilon_{M,mic})[E0^*] + (k^{rad}_{D,mic}\varepsilon_{D,mic} / k^{rad}_{E0,mic}\varepsilon_{M,mic})[D^*]} \quad \text{(S3.7)}$$

$$f_{ED} = \frac{(k^{rad}_{D,mic}\varepsilon_{D,mic} / k^{rad}_{E0,mic}\varepsilon_{M,mic})[D^*]}{[Py^*_{diff}] + (k^{rad}_{E0,mic}\varepsilon_{E0,mic} / k^{rad}_{E0,mic}\varepsilon_{M,mic})[E0^*] + (k^{rad}_{D,mic}\varepsilon_{D,mic} / k^{rad}_{E0,mic}\varepsilon_{M,mic})[D^*]} \quad \text{(S3.8)}$$

In order to determine the molar fractions f_{diff}, f_{free}, f_{E0}, and f_{D} given in Equations S3.9 – S3.12 of the species Py_{diff}*, Py_{free}*, $E0$*, and D*, respectively, the parameters $k^{rad}_{M,wat}$, $k^{rad}_{M,mic}$, $k^{rad}_{E0,mic}$,

$k_{D,mic}^{rad}$, $\varepsilon_{M,wat}$, $\varepsilon_{M,mic}$, $\varepsilon_{E0,mic}$, and $\varepsilon_{D,mic}$ needed to be determined. Unfortunately, this task is complicated, particularly for the pyrene monomer in PyO-3-12 micelles, where it forms excimer preventing its study as an isolated pyrene monomer species. To circumvent this issue, PyO-3-12 was studied in an aqueous solution of 200 mM SDS. The large SDS concentration ensured the formation of numerous SDS micelles among which the PyO-3-12 molecules present at a concentration of 1.8×10^{-6} M would distribute themselves randomly, thus preventing the formation of excimer. The environment provided by the SDS micelles was expected to mimic that experienced in a PyO-3-12 micelle with the advantage of allowing the study of an isolated PyO-3-12 monomer in an SDS micelle. The molar absorbance coefficient of PyO-3-12 in water ($\varepsilon_{M,wat}$) and SDS micelles ($\varepsilon_{M,mic}$) was found to equal 30,800 and 33,500 $M^{-1}\cdot cm^{-1}$, respectively. The ratio $k_{M,wat}^{rad}/k_{M,mic}^{rad}$ is equal to $\phi_{M,wat}\times\tau_{M,mic}/\phi_{M,mic}\times\tau_{M,wat}$ (= 1.07), where $\phi_{M,wat}$ and $\phi_{M,mic}$ are the quantum yield the PyO-3-12 monomer in water and the SDS micelles and the ratio $\phi_{M,wat}/\phi_{M,mic}$ equals 1.00 as determined from integration of the fluorescence spectra acquired with two solutions of PyO-3-12 in water and in 200 mM SDS with an absorbance of 0.05 (see Figure 3.4A in Chapter 3), and $\tau_{M,wat}$ (=149 ns) and $\tau_{M,mic}$ (=160 ns) are the lifetime of the PyO-3-12 monomer in water and SDS micelles, respectively. In turn, the ratio $k_{M,wat}^{rad}\varepsilon_{M,wat}/k_{M,mic}^{rad}\varepsilon_{M,mic}$ was found to equal 0.99. These results suggested that f_{Mdiff} and f_{Mfree} could be approximated by the expressions given in Equations S3.13 and S3.14, respectively.

$$f_{diff}=\frac{[Py_{diff}^{*}]_o}{[Py_{diff}^{*}]_o+[Py_{free}^{*}]_o+[E0^{*}]_o+[D^{*}]_o} \quad \text{(S3.9)}$$

$$f_{free}=\frac{[Py_{free}^{*}]_o}{[Py_{diff}^{*}]_o+[Py_{free}^{*}]_o+[E0^{*}]_o+[D^{*}]_o} \quad \text{(S3.10)}$$

$$f_{E0}=\frac{[E0^{*}]_o}{[Py_{diff}^{*}]_o+[Py_{free}^{*}]_o+[E0^{*}]_o+[D^{*}]_o} \quad \text{(S3.11)}$$

$$f_D = \frac{[D^*]_o}{[Py^*_{diff}]_o + [Py^*_{free}]_o + [E0^*]_o + [D^*]_o} \quad \text{(S3.12)}$$

The species *E*0* and *D** being indistinguishable in the fluorescence experiments beside their different lifetimes, the assumption $e_{E0,mic} \sim e_{D,mic}$ was made in Equations S3.6 and S3.7. The molar absorption coefficient of pyrene aggregates at 346 nm was taken to equal 22,300 $M^{-1} \cdot cm^{-1}$ based on earlier studies.[2,3] Consequently, the ratios $(k^{rad}_{E0,mic} e_{E0,mic} / k^{rad}_{E0,mic} e_{M,mic})$ and $(k^{rad}_{D,mic} e_{D,mic} / k^{rad}_{D,mic} e_{M,mic})$ took a value of 0.67. These simplifications were implemented in Equations S3.13 – S3.17.

$$f_{Mdiff} = \frac{[Py^*_{diff}]}{[Py^*_{diff}] + 0.99 \times [Py^*_{free}]} \quad \text{(S3.13)}$$

$$f_{Mfree} = \frac{0.99 \times [Py^*_{free}]}{[Py^*_{diff}] + 0.99 \times [Py^*_{free}]} \quad \text{(S3.14)}$$

$$f_{Ediff} = \frac{[Py^*_{diff}]}{[Py^*_{diff}] + 0.67 \times ([E0^*] + [D^*])} \quad \text{(S3.15)}$$

$$f_{EE0} = \frac{0.67 \times [E0^*]}{[Py^*_{diff}] + 0.67 \times ([E0^*] + [D^*])} \quad \text{(S3.16)}$$

$$f_{ED} = \frac{0.67 \times [D^*]}{[Py^*_{diff}] + 0.67 \times ([E0^*] + [D^*])} \quad \text{(S3.17)}$$

The molar fractions f_{diff}, f_{free}, and f_{agg} (= f_{E0} + f_D) were obtained by using Equations S3.13 – S3.17 and applying Equations S3.18 – S3.20. The molar fractions were plotted as a function of PyO-3-12 concentration in Figure 3.7A in Chapter 3.

$$f_{diff} = \frac{1}{1 + (f_{Mfree} / f_{Mdiff}) / 0.99 + [(f_{EE0} + f_{ED}) / f_{Ediff}] / 0.67} \quad \text{(S3.18)}$$

$$f_{free} = f_{diff} \times \frac{f_{Mfree}}{0.99 \times f_{Mdiff}} \quad \text{(S3.19)}$$

$$f_{agg} = f_{diff} \times \frac{(f_{EE0} + f_{ED})}{0.67 \times f_{Ediff}} \quad \text{(S3.20)}$$

Parameters retrieved from the analysis of the fluorescence decays

Table S3.2. Parameters retrieved from the MFA of the PyO-3-12 monomer decays.

[PyO-3-12] (mM)	τ_1 (ns)	a_1	τ_2 (ns)	a_2	τ_M (ns)	a_2	χ^2
2.50	0.91	0.53	14.93	0.23	118.00	0.23	1.04
2.25	0.88	0.53	15.80	0.22	120.00	0.25	1.08
2.05	0.89	0.50	14.89	0.22	123.00	0.29	1.06
1.95	0.79	0.48	15.76	0.21	124.00	0.31	1.13
1.75	0.81	0.45	14.94	0.21	126.00	0.34	1.07
1.50	0.77	0.39	15.70	0.22	129.00	0.39	1.09
1.25	0.75	0.38	15.75	0.19	131.00	0.42	1.10
1.00	1.95	0.21	12.62	0.25	135.00	0.54	0.99
0.75	0.97	0.20	18.36	0.20	136.00	0.60	1.05
0.65	0.97	0.19	17.37	0.20	138.00	0.61	1.08
0.55	0.91	0.15	18.18	0.19	139.00	0.66	1.09
0.50	0.98	0.12	17.10	0.19	139.00	0.69	1.10
0.45	1.06	0.10	19.23	0.17	140.00	0.73	1.04
0.40	1.46	0.07	17.53	0.21	140.00	0.72	1.09
0.35	1.65	0.06	16.02	0.19	141.00	0.75	1.09
0.30	1.63	0.06	18.33	0.14	141.00	0.80	1.02
0.25	2.27	0.06	22.74	0.13	142.00	0.81	1.08
0.20	2.01	0.07	24.10	0.13	142.00	0.80	1.13
0.15	2.05	0.07	27.14	0.11	143.00	0.82	1.05
0.10	1.94	0.08	74.82	0.09	144.00	0.83	1.15
0.05	1.87	0.09	87.27	0.10	144.00	0.81	1.08

Table S3.3. Parameters retrieved from the MFA of the PyO-3-12 excimer decays.

[PyO-3-12] (mM)	$f_{E_{diff}}^{E0}$	f_{EE0}	τ_{E0} **(*ns*)**	f_D	τ_D **(*ns*)**	χ^2
2.50	0.23	0.21	38.54	0.56	10.29	1.04
2.25	0.20	0.26	37.56	0.54	10.19	1.08
2.05	0.21	0.26	37.08	0.53	9.13	1.06
1.95	0.24	0.20	37.29	0.57	10.88	1.13
1.75	0.24	0.20	36.50	0.56	9.74	1.07
1.50	0.26	0.19	35.81	0.56	10.17	1.09
1.25	0.29	0.13	38.34	0.59	11.67	1.10
1.00	0.43	0.00	45.24	0.56	13.70	0.99
0.75	0.22	0.29	33.87	0.49	9.04	1.05
0.65	0.23	0.25	33.46	0.52	8.69	1.08
0.55	0.23	0.28	33.40	0.49	8.74	1.09
0.50	0.28	0.20	34.71	0.52	9.96	1.10
0.45	0.24	0.25	32.82	0.52	9.22	1.04
0.40	0.36	0.12	35.25	0.52	11.02	1.09
0.35	0.35	0.16	38.35	0.49	10.53	1.09
0.30	0.34	0.19	41.43	0.47	13.63	1.02
0.25	0.19	0.30	31.63	0.51	7.64	1.08
0.20	0.14	0.38	34.37	0.47	10.11	1.13
0.15	0.11	0.43	34.22	0.46	8.94	1.05
0.10	0.04	0.59	39.68	0.37	10.00	1.15
0.05	0.03	0.56	40.59	0.41	10.00	1.08

Table S3.4. Molar fractions of the different pyrene species and <k> values from MFA of the PyO-3-12 decays.

[PyO-3-12] (mM)	**<*k*>**	f_{free}	f_{diff}	f_{E0}	f_{D}	f_{agg}	**[Py$_{free}$]**
2.50	0.19	0.14	0.48	0.18	0.20	0.38	0.36
2.25	0.18	0.15	0.46	0.22	0.17	0.39	0.34
2.05	0.19	0.18	0.44	0.21	0.17	0.38	0.36
1.95	0.18	0.20	0.45	0.16	0.19	0.35	0.39
1.75	0.18	0.22	0.44	0.16	0.18	0.34	0.39
1.50	0.16	0.26	0.41	0.14	0.19	0.33	0.39
1.25	0.17	0.30	0.41	0.09	0.20	0.29	0.38
1.00	0.12	0.40	0.34	0.00	0.26	0.26	0.40
0.75	0.10	0.43	0.28	0.16	0.13	0.29	0.32
0.65	0.10	0.45	0.29	0.14	0.13	0.27	0.29
0.55	0.09	0.49	0.25	0.14	0.12	0.26	0.27
0.50	0.08	0.54	0.24	0.09	0.13	0.22	0.27
0.45	0.07	0.59	0.21	0.10	0.10	0.20	0.26
0.40	0.07	0.57	0.22	0.05	0.15	0.21	0.23
0.35	0.07	0.59	0.20	0.06	0.14	0.21	0.21
0.30	0.07	0.65	0.16	0.07	0.12	0.19	0.19
0.25	0.05	0.69	0.16	0.09	0.06	0.15	0.17
0.20	0.05	0.66	0.16	0.13	0.05	0.18	0.13
0.15	0.05	0.67	0.15	0.14	0.03	0.18	0.10
0.10	0.02	0.64	0.13	0.21	0.01	0.23	0.06
0.05	0.01	0.63	0.15	0.21	0.01	0.21	0.03

Table S3.5. Parameters retrieved from the biexponential fits of the monomer decays for PyO-3-12 DNT quenching experiment to find k_q (see Figure 3.8). [PyO-3-12] = 9.5 μM

[DNT] (mM)	τ_1 (ns)	a_1	τ_M (ns)	a_M	χ^2
0.52	18.33	0.07	106.15	0.93	0.92
0.44	14.06	0.10	106.79	0.90	1.10
0.35	18.83	0.07	112.60	0.93	1.07
0.28	18.77	0.07	119.48	0.93	0.99
0.21	29.32	0.06	124.88	0.94	0.91
0.15	24.65	0.06	130.23	0.94	0.97
0.10	26.02	0.05	134.31	0.95	1.08
0.07	28.65	0.06	139.57	0.94	1.05
0.00	30.76	0.05	147.06	0.95	0.93

Table S3.6. Parameters retrieved from the biexponential fits of the monomer decays for PyO-3-12 DNT quenching experiment to find N_{agg} (see Figure 3.9). [PyO-3-12] = 2.3 M

[DNT] (mM)	τ_1 (ns)	a_1	τ_M (ns)	a_M	χ^2
1.88	16.02	0.07	66.61	0.93	0.95
1.58	19.83	0.08	71.47	0.92	1.05
1.29	14.92	0.09	77.66	0.91	0.95
1.07	22.15	0.07	83.62	0.93	0.96
0.87	22.02	0.07	89.84	0.93	1.03
0.70	21.88	0.09	95.89	0.91	0.97
0.55	26.63	0.07	102.60	0.93	0.91
0.41	36.93	0.08	110.12	0.92	1.20
0.18	47.71	0.07	124.04	0.93	0.98
0.00	52.89	0.08	140.28	0.92	1.06

Table S3.7. Parameters retrieved from the triexponential fits of the excimer decays for PyO-3-12 DNT quenching experiment to find N_{agg} (see Figure 3.9). [PyO-3-12] = 2.3 M.

[DNT] (mM)	τ_1 (ns)	a_1	τ_2 (ns)	a_2	τ_3 (ns)	a_3	χ^2
1.88	4.04	0.46	16.03	0.44	40.51	0.10	1.09
1.58	4.51	0.40	17.04	0.48	40.52	0.12	1.23
1.29	5.96	0.37	20.27	0.52	44.63	0.11	1.10
1.07	6.39	0.34	21.75	0.53	44.76	0.13	1.06
0.87	6.28	0.26	22.22	0.58	45.26	0.17	1.09
0.70	8.12	0.27	26.54	0.61	52.66	0.11	1.06
0.55	9.29	0.25	29.60	0.65	57.38	0.10	1.01
0.41	11.79	0.25	33.94	0.69	66.02	0.06	1.00
0.18	21.31	0.29	41.21	0.69	90.36	0.02	1.04
0.00	18.53	0.15	44.37	0.83	123.65	0.02	1.12

Table S3.8. Parameters retrieved from the fits of the excimer decays with the micellar model for PyO-3-12 DNT quenching experiment to find N_{agg} (see Figure 3.9). The lifetime τ_{E0} and τ_D were fixed to equal 18.5 and 44.4 ns in the analysis. [PyO-3-12] = 2.3 mM.

[DNT] (mM)	f_{E0}	f_D	k_q ($\times 10^7$ s^{-1})	$\langle n \rangle_D$	$\langle n \rangle_s$	χ^2
1.88	0.88	0.12	2.04	2.12	1.83	1.04
1.58	0.82	0.18	1.79	2.04	1.61	1.19
1.29	0.85	0.15	1.63	1.94	1.33	1.19
1.07	0.86	0.14	1.44	1.76	1.12	1.23
0.87	0.88	0.12	1.49	1.53	0.97	1.09
0.70	0.87	0.13	1.49	1.26	0.80	1.17
0.55	0.98	0.02	1.62	1.10	0.63	1.15
0.41	0.88	0.12	1.44	0.77	0.51	1.18

S4 - Supporting information for Chapter 4

Equations used for the model free analysis (MFA) of the pyrene monomer and excimer fluorescence decays and determination of the molar fractions

The model free analysis (MFA) of the pyrene monomer and excimer fluorescence decays was accomplished with Equations S1 and S2, respectively. The normalized pre-exponential factors (a_i so that $\Sigma a_i = 1$) and decay times (τ_i) were optimized according to the Marquardt-Levenberg algorithm and were constrained to remain the same in both Equations S1 and S2. Their values were input into Equations S3 and S4 to calculate the average monomer lifetime ($<\tau>$) and the rate constant ($<k>$) for pyrene excimer formation (PEF), respectively. Equations S1 and S2 account for the ability of the different pyrene species present in solution to absorb and emit photons through the radiative rate constants of the pyrene monomer in water ($k^{rad}_{M,wat}$) and in the PyO-3-12 micelles ($k^{rad}_{M,mic}$) and of the species $E0^*$ ($k^{rad}_{E0,mic}$) and D^* ($k^{rad}_{D,mic}$) in the PyO-3-12 micelles and the molar absorption coefficients of the pyrene monomer in water ($\varepsilon_{M,wat}$) and in the PyO-3-12 micelles ($\varepsilon_{M,mic}$) and of the species $E0^*$ ($\varepsilon_{E0,mic}$) and D^* ($\varepsilon_{D,mic}$) in the PyO-3-12 micelles. The MFA also needs to distinguish between those pyrenyl labels $Py_{diff \rightarrow E0}^*$ and $Py_{diff \rightarrow D}^*$, that form the well ($E0^*$) and poorly ($D^*$) stacked excimer.

$$[Py^*]_{(t)} = k^{rad}_{M,mic}\varepsilon_{M,mic}[Py^*_{diff}]_{(t=0)} \times \sum_{i=1}^{n} a_i \times \exp(-t/\tau_i) + k^{rad}_{M,wat}\varepsilon_{M,wat}[Py^*_{free}]_{(t=0)} \times \exp(-t/\tau_M) \quad \text{(S1)}$$

$$+k^{rad}_{E0,mic}\left(\varepsilon_{E0,mic}[E0^*]_{(t=0)} + \varepsilon_{M,mic}[Py^*_{diff \rightarrow E0}]_{(t=0)} \times \sum_{i=1}^{n} a_i \frac{\frac{1}{\tau_i} - \frac{1}{\tau_M}}{\frac{1}{\tau_i} - \frac{1}{\tau_{E0}}}\right) \times \exp(-t/\tau_{E0})$$

$$-k^{rad}_{D,mic}\varepsilon_{M,mic}[Py^*_{diff \rightarrow D}]_{(t=0)} \times \sum_{i=1}^{n} a_i \frac{\frac{1}{\tau_i} - \frac{1}{\tau_M}}{\frac{1}{\tau_i} - \frac{1}{\tau_D}} \exp(-t/\tau_i)$$

$$+k_{D,mic}^{rad}\left(\varepsilon_{D,mic}[D^*]_{(t=0)}+\varepsilon_{M,mic}[Py^*_{diff\rightarrow D}]_{(t=0)}\times\sum_{i=1}^{n}a_i\frac{\frac{1}{\tau_i}-\frac{1}{\tau_M}}{\frac{1}{\tau_i}-\frac{1}{\tau_D}}\right)\times\exp(-t/\tau_D) \quad \text{(S2)}$$

$$<\tau>=\frac{\sum_{i=1}^{n}a_i\tau_i}{\sum_{i=1}^{n}a_i} \quad \text{(S3)}$$

$$<k>=\frac{\sum_{i=1}^{n}a_i}{\sum_{i=1}^{n}a_i\tau_i}-\frac{1}{\tau_M}=\frac{1}{<\tau>}-\frac{1}{\tau_M} \quad \text{(S4)}$$

The fractions f_{Mdiff}, f_{Mfree}, f_{EdiffE0}, f_{EdiffD}, f_{EE0}, and f_{ED}, whose expressions are provided in Equations S5 – S10, were derived from the pre-exponential factors used in Equations S1 and S2 for the monomer and excimer fluorescence decays after assuming that $k_{E0,mic}^{rad}$ and $k_{D,mic}^{rad}$ on the one hand and $\varepsilon_{\text{E0,mic}}$ and $\varepsilon_{\text{D,mic}}$ are equal and using the fact that $k_{M,wat}^{rad}\varepsilon_{M,wat}/k_{M,mic}^{rad}\varepsilon_{M,mic}$ and $\varepsilon_{\text{E0,mic}}/\varepsilon_{\text{M,mic}}$ equal 0.99 and 0.67, respectively, as was done in earlier publications.[1-3]

$$f_{Mdiff}=\frac{[Py^*_{diff}]}{[Py^*_{diff}]+0.99\times[Py^*_{free}]} \quad \text{(S5)}$$

$$f_{Mfree}=\frac{0.99\times[Py^*_{free}]}{[Py^*_{diff}]+0.99\times[Py^*_{free}]} \quad \text{(S6)}$$

$$f_{EdiffE0}=\frac{[Py^*_{diff\rightarrow E0}]}{[Py^*_{diff\rightarrow E0}]+[Py^*_{diff\rightarrow D}]+0.67\times([E0^*]+[D^*])} \quad \text{(S7)}$$

$$f_{EdiffD}=\frac{[Py^*_{diff\rightarrow D}]}{[Py^*_{diff\rightarrow E0}]+[Py^*_{diff\rightarrow D}]+0.67\times([E0^*]+[D^*])} \quad \text{(S8)}$$

$$f_{EE0}=\frac{0.67\times[E0^*]}{[Py^*_{diff\rightarrow E0}]+[Py^*_{diff\rightarrow D}]+0.67\times([E0^*]+[D^*])} \quad \text{(S9)}$$

$$f_{ED} = \frac{0.67 \times [D^*]}{[Py^*_{diff \rightarrow E0}] + [Py^*_{diff \rightarrow D}] + 0.67 \times ([E0^*] + [D^*])} \quad \text{(S10)}$$

The absolute I_E/I_M(MFA) ratio could be determined by using the various parameters determined through the MFA and introducing them into Equation S11.

$$(I_E / I_M)^{SPC} = \frac{f_{Mdiff}}{(f_{EdiffE0} + f_{EdiffD})} \frac{< k > \times < \tau > \times (f_{EdiffE0}\tau_{E0} + f_{EdiffD}\tau_D) + f_{EE0}\tau_{E0} + f_{ED}\tau_D}{f_{Mdiff} < \tau > + f_{Mfree}\tau_M} \quad \text{(S11)}$$

The molar fractions f_{diff}, f_{free}, f_{E0}, and f_D given in Equations S9 – S12 of the species Py_{diff}*, Py_{free}*, $E0$*, and D*, respectively, can be extracted from the fractions f_{Mdiff}, f_{Mfree}, $f_{EdiffE0}$, f_{EdiffD}, f_{EE0}, and f_{ED} as shown in Equations S12 – S14, where f_{agg} was taken to equal the sum $f_{E0} + f_D$. The molar fractions were plotted as a function of PyO-3-12 concentration in Figure 7A in the main text.

$$f_{diff} = \frac{1}{1 + (f_{Mfree} / f_{Mdiff}) / 0.99 + [(f_{EE0} + f_{ED}) / (f_{EdiffE0} + f_{EdiffD})] / 0.67} \quad \text{(S12)}$$

$$f_{free} = f_{diff} \times \frac{f_{Mfree}}{0.99 \times f_{Mdiff}} \quad \text{(S13)}$$

$$f_{agg} = f_{diff} \times \frac{(f_{EE0} + f_{ED})}{0.67 \times (f_{EdiffE0} + f_{EdiffD})} \quad \text{(S14)}$$

Associations between pyrene and SDS probed by fluorescence

The interactions between SDS and a neutral molecule, namely molecular pyrene, were characterized in Figure S1 to illustrate the major differences in behavior between PyO-3-12 and molecular pyrene. Figure S1A shows the fluorescence spectra normalized at 378 nm, corresponding to the 0-0 transition of pyrene, for a 0.6 μM pyrene concentration in an SDS aqueous solution below the 0.7 μM solubility limit of pyrene in water,[4,5] where the SDS concentration was increased from 0 to 8 mM, which is the CMC of SDS in water.[6,7] The fluorescence intensity of the third peak (I_3) around 385 nm increased with increasing SDS

concentration relative to the fluorescence intensity of the first peak around 378 nm (I_1). The increase in I_3 relative to I_1 is a clear indication, that pyrene experiences a more hydrophobic environment, as would be expected if pyrene interacts with the hydrophobic tail of SDS molecules. The fluorescence intensity of the excimer shown in the inset also increased with increasing SDS concentration, reflecting an increase in the concentration of the pyrene molecules in the hydrophobic domains generated by pre-micellar aggregates. The fluorescence spectra normalized at the first peak of pyrene obtained at SDS concentrations of 8 mM and higher are shown in Figure S1B. I_3 remains relatively constant relative to I_1, indicating that the polarity of the environment experienced by pyrene does not change above an SDS concentration of 8 mM. As SDS micelles are present above 8 mM SDS, the hydrophobic interior of the SDS micelles host the pyrene molecules, which experience a same environment and the I_1/I_3 ratio remains constant. Upon increasing the SDS concentration, the excimer fluorescence intensity decreases with respect to that of the monomer, as pyrene molecules distribute themselves among different SDS micelles, where they are isolated and can no longer form excimer.

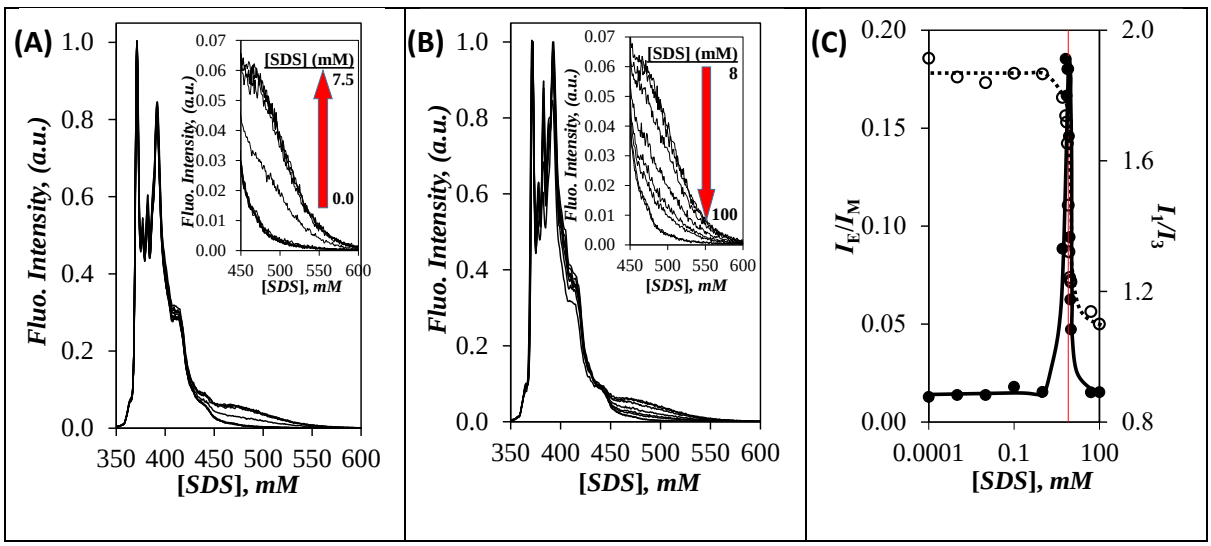

Figure S1. Fluorescence spectra of molecular pyrene in SDS aqueous solutions for A) 0 < [SDS] ≤ 7.5 mM and B) 8 mM ≤ [SDS] ≤ 100 mM. The inset shows a zoomed in view of the

excimer region of the spectra. C) Plot of I_E/I_M and I_1/I_3 as a function of SDS concentration in water. The red vertical line indicates the 8 mM CMC of SDS in water.[6,7] [Pyrene] = 0.6 μM; λ_{ex} = 338 nm.

These features are summarized in Figure S1C, where I_1/I_3 and I_E/I_M are plotted as a function of SDS concentration. Since the pyrene concentration used in these experiments equals 0.6 μM, below the saturation concentration of pyrene in water equal to 0.7 μM,[4,5] the chance for an excited pyrene molecule of meeting a ground-state pyrene molecule in water are nil, no excimer is formed, and the I_E/I_M ratio is vanishingly small at low SDS concentration. Thus, any excimer formation is due to the interactions between pyrene and SDS molecules. Before the CMC, the I_1/I_3 values take an average value of 1.87 (± 0.03), indicating that the pyrene molecules reside in an aqueous environment.[8,9] A drop in the I_1/I_3 ratio is observed as the SDS concentration approaches the CMC. This drop in I_1/I_3 is attributed to pyrene molecules being in the more hydrophobic microenvironment generated by the interior of the SDS micelles. Above the CMC, I_1/I_3 remains constant and equal to 1.17 (± 0.06) indicating that pyrene resides in the less polar environment generated by the interior of SDS micelles.[7,10] As the SDS concentration passes through the CMC and SDS micelles are formed, the pyrene molecules are concentrated inside a few SDS micelles resulting in PEF and I_E/I_M passes through a maximum. Further increase in SDS concentration generated more SDS micelles and induced the separation of the pyrene molecules among different micelles, thus reducing PEF and resulting in a decrease in I_E/I_M approaching 0 in Figure S1C. The I_1/I_3 and I_E/I_M profiles described in Figure S1C represent the typical behavior of pyrene in micellar solution of SDS.[7,11]

Fluorescence spectra for the 16 and 1 μM PyO-3-12 series

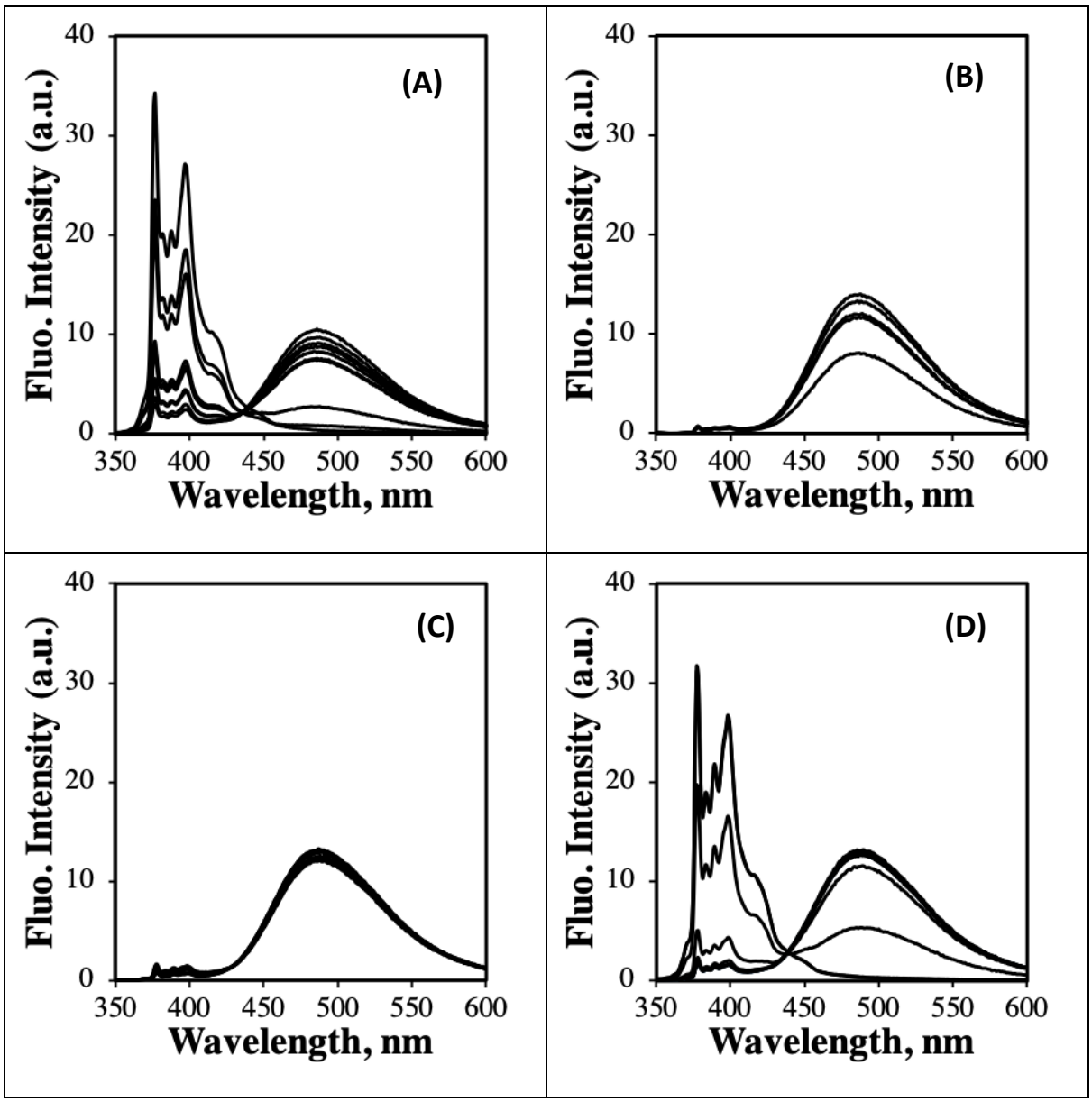

Figure S2. Fluorescence spectra for 16 μM PyO-3-12 with SDS concentrations ranges (A) 0 to 0.02 mM, (B) 0.025 to 0.2 mM, (C) 0.5 to 8 mM, and (D) 8.5 to 200 mM.

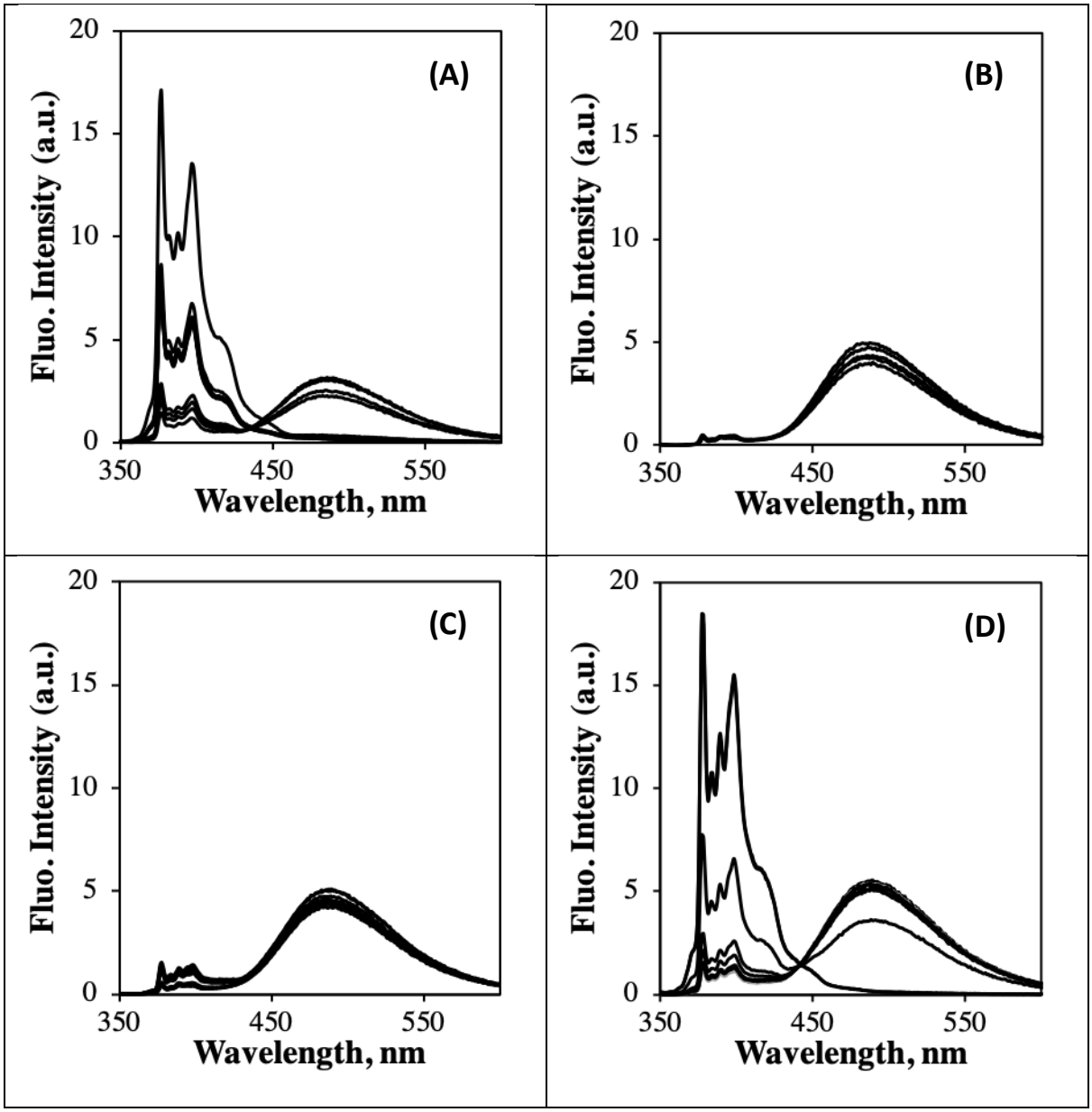

Figure S3. Fluorescence spectra for 1 μM PyO-3-12 with SDS concentrations ranging from (A) 0 to 0.0016 mM, (B) 0.002 to 0.1 mM, (C) 0.2 to 8 mM, and (D) 8.5 to 200 mM.

Effect of ionic strength on the fluorescence results

As the experimental results have indicated that electrostatic forces strongly influence the associations between PyO-3-12 and SDS, the effect of ionic strength on the formation and stability of the PyO-3-12/SDS aggregates was investigated. To this end, experiments were conducted with aqueous solutions of PyO-3-12 and SDS prepared with a final 1 μM PyO-3-12 concentration and SDS concentration ranging from 0.1 μM to 200 mM in the presence of 32 μM and 50 mM NaCl. The I_E/I_M and I_1/I_3 ratios obtained for the 32 μM and 50 mM NaCl solutions were plotted in Figure S4 as a function of SDS concentration and compared to the trends obtained for 1 μM PyO-3-12 without NaCl in Figure 7. The solutions containing 1 μM PyO-3-12 and 32 μM NaCl were expected to generate an ionic strength similar to that of the 16 μM PyO-3-12 solution, whose I_E/I_M and I_1/I_3 profiles had shown significant differences compared to those obtained with the 1 μM PyO-3-12 solution in Figure 7. The aqueous solutions with 50 mM NaCl were expected to result in a more substantial change in ionic strength. The I_E/I_M profiles presented in Figure S4A showed some noticeable differences for SDS concentrations between the equicharge point and the CMC. However, this range of SDS concentration also corresponds to the weakest fluorescence intensity of the pyrene monomer (see Figures 3, S1, and S2). Under these conditions, small errors in I_M can have a major effect on the I_E/I_M ratio. As a result, the variations in I_E/I_M observed between the equicharge point and the CMC in Figure S4A were attributed to small fluctuations in the I_M values. Similarly, the ~ 5% variation observed for the I_1/I_3 ratio obtained at SDS concentrations between the equicharge point and the CMC were also attributed to experimental error. Consequently, the discussion of the data presented in Figure S4 focuses instead on the SDS concentrations marking the boundaries between the regimes, where large changes in I_E/I_M and I_1/I_3 ratios were observed.

Within this context, the addition of 32 μM NaCl was found to have little effect on the transitions observed with the I_E/I_M and I_1/I_3 ratios when compared to the trends obtained without NaCl. This was probably because a 32 μM NaCl concentration was simply too low to affect the ionic strength of the solution, even though it had the same ionic strength as that of the 16 μM PyO-3-12 solution. Since the 1 μM PyO-3-12 solution without or with 32 μM NaCl behaved similarly, the six SDS concentration regimes were unaffected, with the formation of the PyO-3-12/SDS aggregate being terminated at the equicharge point, accretion of SDS molecules onto PyO-3-12/SDS aggregates starting at 2 mM and stopping at the 8 mM CMC of SDS, where SDS micelles started to form, before complete dissociation of the PyO-3-12/SDS aggregates took place at SDS concentrations greater than 30 mM.

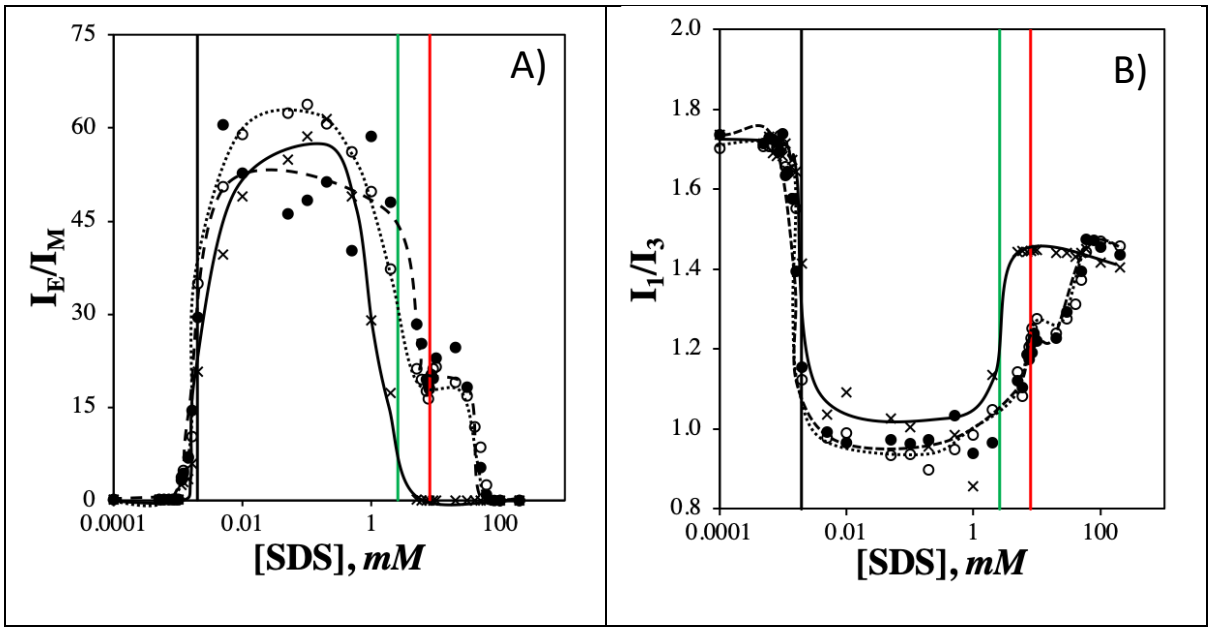

Figure S4. Plots of the A) I_E/I_M and B) I_1/I_3 ratios as a function of SDS concentration with [PyO-3-12] = 1 μM. (O) [NaCl] = 0 mM, (●) [NaCl] = 32 μM, and (×) [NaCl] = 50 mM. The black vertical line represents the equicharge concentration (2 μM). The green vertical line represents the 2.6 mM CMC of SDS in 50 mM SDS.[Error! Bookmark not defined.] The red vertical line represents the 8 mM CMC of SDS in water.

These experiments were repeated with a 50 mM NaCl concentration. As for the experiments conducted with 0 and 32 μM NaCl, the PyO-3-12/SDS aggregates formed at the equicharge point as indicated by the significant increase and decrease in the I_E/I_M and I_1/I_3 ratios, respectively. The main difference was observed at higher SDS concentrations where I_E/I_M and I_1/I_3 showed a large decrease and increase, respectively, at an SDS concentration, which was not equal to 8 mM as had been observed for the solutions without and with 32 μM NaCl, but rather at 2.6 mM corresponding to the CMC of SDS with 50 mM NaCl.**Error! Bookmark not defined.** With 50 mM NaCl, the PyO-3-12/SDS aggregates were found to dissociate completely at the CMC contrary to what had been observed for the solutions without NaCl (see Figure 7A), where the formation of SDS micelles occurred independently of the presence of the PyO-3-12/SDS aggregates, resulting in a non-zero I_E/I_M ratio above the 8 mM CMC. In contrast, the I_E/I_M ratio was found to equal zero for SDS concentrations above the 2.6 mM CMC of SDS with 50 mM NaCl.**Error! Bookmark not defined.** The I_1/I_3 ratio took an average value of 1.44 (±0.01) for SDS concentrations between 5 and 200 mM indicating that the PyO-3-12 molecules had been incorporated inside SDS micelles just after the CMC of SDS. The decomposition of the PyO-3-12/SDS aggregates at the CMC was attributed to the weaker electrostatic interactions between the positive ammoniums of PyO-3-12 and negative sulfates of SDS resulting from the higher ionic strength of the solution with 50 mM NaCl.

Consequently, the trends shown in Figure S4 demonstrate that an increase in the solution ionic strength does not seem to affect the formation of the PyO-3-12/SDS aggregates, which appears to be finalized at the equicharge point. However, an increase in ionic strength affects the stability of the PyO-3-12/SDS micelles at the CMC of SDS, where weaker electrostatic interactions between the oppositely charged surfactant head groups leads to the dissociation of the PyO-3-12/SDS aggregates as soon as SDS micelles form.

Parameters retrieved from the analysis of the fluorescence decays

Table S1. Parameters retrieved from the MFA of pyrene monomer for 4 μM PyO-3-12 with SDS concentration ranging from 0.002 to 50 mM.

[PyO-3-12] (mM)	τ_1 (ns)	a_1	τ_2 (ns)	a_2	τ_3 (ns)	a_3	τ_M (ns)	a_M	χ^2
50	2.61	0.11	11.5	0.40	41.93	0.21	144	0.28	1.00
40	2.43	0.18	10.0	0.66	31.23	0.12	144	0.04	1.08
30	2.32	0.19	9.56	0.69	27.79	0.09	144	0.02	1.11
20	1.96	0.19	8.66	0.70	18.90	0.09	144	0.02	1.11
10	1.52	0.21	8.94	0.70	25.44	0.07	144	0.02	1.12
9	1.80	0.19	9.05	0.73	26.01	0.07	144	0.02	1.09
8	3.18	0.20	10.8	0.73	29.21	0.06	144	0.01	0.99
7	3.61	0.23	11.0	0.74	38.22	0.03	144	0.00	1.03
6	3.41	0.22	10.2	0.74	34.01	0.03	144	0.00	1.04
5	3.31	0.29	9.44	0.69	42.66	0.02	144	0.00	1.09
2	2.40	0.33	6.75	0.65	30.62	0.01	144	0.00	1.00
1	2.43	0.39	6.23	0.60	35.69	0.01	144	0.00	1.15
0.5	1.89	0.36	5.65	0.63	29.23	0.01	144	0.00	1.11
0.2	2.07	0.39	5.74	0.59	25.37	0.01	144	0.00	1.04
0.1	2.23	0.42	6.19	0.57	27.61	0.01	144	0.00	1.06
0.05	2.10	0.37	6.41	0.59	20.11	0.03	144	0.00	1.07
0.025	2.16	0.40	6.85	0.57	21.89	0.03	144	0.00	1.13
0.01	2.25	0.43	6.78	0.54	25.85	0.02	144	0.00	1.06
0.007	2.02	0.43	6.49	0.54	25.83	0.02	144	0.01	1.06
0.005	1.42	0.36	5.64	0.56	22.46	0.04	144	0.04	1.11
0.004	1.60	0.39	6.10	0.52	21.93	0.05	144	0.05	1.14
0.0035	1.39	0.35	5.73	0.46	27.53	0.04	144	0.15	1.07
0.0025	1.26	0.31	5.61	0.38	30.31	0.05	144	0.26	1.04
0.002	1.29	0.26	5.56	0.29	33.62	0.04	144	0.41	1.02

Table S2. Parameters retrieved from the MFA of pyrene excimer for 4 μM PyO-3-12 with SDS concentration ranging from 0.002 to 50 mM.

[PyO-3-12] (mM)	$f_{E_{diff}}^{E0}$	f_{EE0}	τ_{E0} (*ns*)	$f_{E_{diff}}^{D}$	f_{ED}	τ_D (*ns*)	χ^2
50	0.97	0.03	45.1	_	_	_	1.00
40	0.96	0.04	46.3	_	_	_	1.08
30	0.96	0.04	46.8	_	_	_	1.11
20	0.96	0.04	47.0	_	_	_	1.11
10	0.97	0.03	46.0	_	_	_	1.12
9	0.96	0.04	46.3	_	_	_	1.09
8	0.93	0.07	45.1	_	_	_	0.99
7	0.92	0.08	45.2	_	_	_	1.03
6	0.91	0.09	45.5	_	_	_	1.04
5	0.91	0.09	46.1	_	_	_	1.09
2	0.27	0.00	39.6	0.62	0.12	50.8	1.00
1	0.29	0.00	40.8	0.58	0.13	52.3	1.15
0.5	0.55	0.11	45.1	0.34	0.00	56.7	1.11
0.2	0.35	0.00	41.7	0.53	0.12	55.0	1.04
0.1	0.36	0.00	41.1	0.52	0.13	55.6	1.06
0.05	0.34	0.00	38.8	0.53	0.13	54.7	1.07
0.025	0.37	0.04	38.1	0.51	0.08	52.2	1.13
0.01	0.35	0.00	37.5	0.53	0.12	55.3	1.06
0.007	0.38	0.00	38.1	0.50	0.12	55.7	1.06
0.005	0.50	0.00	37.9	0.44	0.06	57.9	1.11
0.004	0.47	0.00	35.5	0.44	0.09	55.1	1.14
0.0035	0.54	0.00	37.5	0.42	0.04	59.0	1.07
0.0025	0.56	0.00	36.9	0.40	0.04	59.8	1.04
0.002	0.58	0.00	37.6	0.41	0.01	61.7	1.02

Table S3. Molar fractions of the different pyrene species and <k> values from MFA of 4 μM PyO-3-12 with SDS concentration ranging from 0.002 to 50 mM.

[Py-3-12] (mM)	<*k*>	f_{free}	f_{diff}^{E0}	f_{diff}^{D}	f_{diff}	f_{E0}	f_{D}	f_{agg}	I_E/I_M
50	0.04	0.28	0.70	0.00	0.70	0.03	0.00	0.03	0.54
40	0.08	0.04	0.92	0.00	0.92	0.04	0.00	0.04	2.59
30	0.09	0.02	0.94	0.00	0.94	0.04	0.00	0.04	3.42
20	0.11	0.02	0.94	0.00	0.94	0.04	0.00	0.04	4.08
10	0.11	0.02	0.95	0.00	0.95	0.03	0.00	0.03	3.89
9	0.11	0.02	0.94	0.00	0.94	0.04	0.00	0.04	4.02
8	0.09	0.01	0.92	0.00	0.92	0.07	0.00	0.07	3.73
7	0.09	0.00	0.91	0.00	0.91	0.08	0.00	0.08	4.32
6	0.10	0.00	0.91	0.00	0.91	0.09	0.00	0.09	4.78
5	0.11	0.00	0.90	0.00	0.90	0.09	0.00	0.09	5.78
2	0.17	0.00	0.27	0.62	0.88	0.00	0.12	0.12	9.05
1	0.19	0.00	0.29	0.58	0.87	0.00	0.13	0.13	10.68
0.5	0.21	0.00	0.55	0.34	0.89	0.11	0.00	0.11	11.37
0.2	0.21	0.00	0.35	0.53	0.88	0.00	0.12	0.12	11.66
0.1	0.20	0.00	0.36	0.52	0.87	0.00	0.12	0.12	11.25
0.05	0.18	0.00	0.34	0.53	0.87	0.00	0.13	0.13	10.06
0.025	0.18	0.00	0.37	0.51	0.88	0.04	0.08	0.12	9.06
0.01	0.18	0.00	0.35	0.53	0.87	0.00	0.12	0.12	9.98
0.007	0.19	0.01	0.38	0.50	0.87	0.00	0.12	0.12	8.98
0.005	0.20	0.04	0.48	0.42	0.91	0.00	0.06	0.06	4.73
0.004	0.19	0.04	0.45	0.42	0.87	0.00	0.09	0.09	3.96
0.0035	0.19	0.14	0.47	0.36	0.83	0.00	0.03	0.03	1.60
0.0025	0.18	0.25	0.42	0.30	0.72	0.00	0.03	0.03	0.84
0.002	0.17	0.40	0.34	0.25	0.59	0.00	0.01	0.01	0.44

Table S4. Parameters retrieved from the MFA of pyrene monomer for 16 μM PyO-3-12 with SDS concentration ranging from 0.013 to 50 mM.

[PyO-3-12] (mM)	τ_1 (ns)	a_1	τ_2 (ns)	a_2	τ_3 (ns)	a_3	τ_M (ns)	a_M	χ^2
50	1.00	0.00	8.27	0.24	38.53	0.10	144	0.67	1.17
40	4.65	0.31	12.2	0.47	46.51	0.08	144	0.14	1.09
30	3.16	0.24	9.73	0.69	30.23	0.05	144	0.02	1.09
20	3.45	0.27	9.71	0.69	30.46	0.03	144	0.01	1.04
10	2.95	0.24	9.40	0.71	24.83	0.04	144	0.01	1.06
9	2.70	0.19	9.07	0.75	23.48	0.05	144	0.01	1.02
8.5	2.74	0.21	9.15	0.74	24.88	0.04	144	0.01	1.05
8	2.86	0.21	9.45	0.76	30.57	0.03	144	0.01	1.1
7.5	3.26	0.24	9.59	0.74	32.47	0.02	144	0.00	1.04
7	3.06	0.24	9.22	0.73	31.46	0.02	144	0.00	1.03
6	2.15	0.20	7.96	0.74	19.37	0.05	144	0.00	1.07
5	2.33	0.24	7.20	0.73	20.57	0.03	144	0.00	1.07
2	2.27	0.32	6.28	0.67	30.44	0.01	144	0.00	1.05
1	1.95	0.31	5.73	0.68	28.61	0.01	144	0.00	1.06
0.5	1.90	0.34	5.70	0.65	32.53	0.01	144	0.00	1.12
0.2	2.90	0.35	5.56	0.64	27.62	0.01	144	0.00	1.07
0.1	2.12	0.37	6.23	0.61	28.38	0.01	144	0.00	1.07
0.05	2.22	0.38	6.75	0.61	30.69	0.01	144	0.00	1.07
0.03	2.03	0.38	6.35	0.61	33.88	0.01	144	0.00	1.12
0.025	1.92	0.38	5.94	0.60	33.31	0.01	144	0.00	1.14
0.02	1.51	0.35	5.44	0.60	28.22	0.02	144	0.03	0.94
0.018	1.59	0.37	5.35	0.57	39.39	0.01	144	0.04	1.1
0.017	1.45	0.35	4.93	0.53	43.04	0.02	144	0.11	1.04
0.016	1.49	0.35	4.84	0.51	44.12	0.02	144	0.12	1.07
0.015	1.10	0.29	4.26	0.52	43.01	0.02	144	0.17	1.06
0.014	0.95	0.26	3.96	0.45	45.05	0.03	144	0.26	1.07
0.013	0.84	0.23	3.72	0.47	45.21	0.03	144	0.28	1.03

Table S5. Parameters retrieved from the MFA of pyrene excimer for 16 μM PyO-3-12 with SDS concentration ranging from 0.013 to 50 mM.

[PyO-3-12] (mM)	$f_{E_{diff}}^{E0}$	f_{EE0}	τ_{E0} (*ns*)	$f_{E_{diff}}^{D}$	f_{ED}	τ_D (*ns*)	χ^2
50	0.85	0.15	46.2	_	_	_	1.17
40	0.89	0.11	46.2	_	_	_	1.09
30	0.88	0.12	46.4	_	_	_	1.09
20	0.88	0.12	47.2	_	_	_	1.04
10	0.88	0.12	46.7	_	_	_	1.06
9	0.89	0.11	47.0	_	_	_	1.02
8.5	0.89	0.11	46.4	_	_	_	1.05
8	0.89	0.11	46.6	_	_	_	1.1
7.5	0.88	0.12	46.3	_	_	_	1.04
7	0.89	0.11	46.8	_	_	_	1.03
6	0.13	0.02	35.9	0.76	0.09	48.6	1.07
5	0.17	0.05	38.9	0.70	0.08	50.2	1.07
2	0.31	0.00	39.6	0.53	0.17	52.5	1.05
1	0.36	0.00	42.2	0.48	0.16	54.3	1.06
0.5	0.32	0.00	40.6	0.52	0.17	54.7	1.12
0.2	0.35	0.00	42.3	0.48	0.17	55.7	1.07
0.1	0.29	0.00	39.2	0.54	0.17	55.8	1.07
0.05	0.26	0.00	35.2	0.58	0.17	49.7	1.07
0.03	0.34	0.00	38.7	0.50	0.16	55.3	1.12
0.025	0.38	0.00	40.8	0.48	0.14	56.5	1.14
0.02	0.39	0.00	40.1	0.47	0.13	55.9	0.94
0.018	0.41	0.00	40.8	0.46	0.13	56.1	1.1
0.017	0.41	0.00	41.3	0.46	0.12	56.2	1.04
0.016	0.42	0.02	41.9	0.45	0.11	56.3	1.07
0.015	0.44	0.00	41.9	0.46	0.10	55.8	1.06
0.014	0.51	0.00	42.4	0.43	0.07	56.3	1.07
0.013	0.52	0.00	42.6	0.43	0.05	56.3	1.03

Table S6. Molar fractions of the different pyrene species and <k> values from MFA of 16 μM PyO-3-12 with SDS concentration ranging from 0.013 to 50 mM.

[Py-3-12] (mM)	<*k*>	f_{free}	f_{diff}^{E0}	f_{diff}^{D}	f_{diff}	f_{E0}	f_{D}	f_{agg}	I_E/I_M
50	0.05	0.63	0.32	0.00	0.32	0.06	0.00	0.06	0.16
40	0.07	0.13	0.78	0.00	0.78	0.10	0.00	0.10	1.33
30	0.10	0.02	0.87	0.00	0.87	0.12	0.00	0.12	4.06
20	0.11	0.01	0.87	0.00	0.87	0.12	0.00	0.12	4.92
10	0.11	0.01	0.87	0.00	0.87	0.12	0.00	0.12	4.98
9	0.11	0.01	0.88	0.00	0.88	0.11	0.00	0.11	4.99
8.5	0.11	0.01	0.88	0.00	0.88	0.11	0.00	0.11	5.16
8	0.11	0.00	0.89	0.00	0.89	0.11	0.00	0.11	5.25
7.5	0.11	0.00	0.88	0.00	0.88	0.12	0.00	0.12	5.55
7	0.12	0.00	0.88	0.00	0.88	0.11	0.00	0.11	6.03
6	0.13	0.00	0.13	0.76	0.89	0.02	0.09	0.11	6.61
5	0.15	0.00	0.17	0.70	0.87	0.05	0.08	0.13	7.98
2	0.18	0.00	0.31	0.53	0.83	0.00	0.17	0.17	10.55
1	0.20	0.00	0.36	0.48	0.84	0.00	0.16	0.16	11.66
0.5	0.21	0.00	0.32	0.52	0.83	0.00	0.17	0.17	12.31
0.2	0.20	0.00	0.35	0.48	0.82	0.00	0.17	0.17	11.95
0.1	0.19	0.00	0.29	0.54	0.83	0.00	0.17	0.17	11.66
0.05	0.18	0.00	0.26	0.58	0.83	0.00	0.17	0.17	9.80
0.03	0.19	0.00	0.34	0.50	0.84	0.00	0.16	0.16	11.16
0.025	0.20	0.00	0.38	0.48	0.86	0.00	0.14	0.14	11.59
0.02	0.22	0.03	0.38	0.46	0.85	0.00	0.13	0.13	6.34
0.018	0.22	0.04	0.39	0.44	0.84	0.00	0.13	0.13	5.20
0.017	0.23	0.10	0.37	0.42	0.79	0.00	0.11	0.11	2.49
0.016	0.23	0.11	0.37	0.40	0.77	0.02	0.10	0.12	2.26
0.015	0.24	0.16	0.37	0.39	0.76	0.00	0.08	0.08	1.60
0.014	0.22	0.25	0.38	0.32	0.70	0.00	0.05	0.05	0.92
0.013	0.21	0.26	0.38	0.31	0.70	0.00	0.04	0.04	0.85

S5 - Supporting information for Chapter 5

Parameters retrieved from the analysis of the fluorescence decays of Py-3-12 and CT-DNA complexes

Table S5.1. Parameters retrieved from the MFA of pyrene monomer for [Py-3-12] = 10 μM with CT-DNA concentration ranging from 0.001 to 0.115 mM and both concentrations expressed by the (-/+) ratio.

(-/+) ratio	τ_1 (ns)	a_1	τ_2 (ns)	a_2	τ_3 (ns)	a_3	τ_M (ns)	a_M	χ^2
11.50	1.64	0.61	6.68	0.34	22.22	0.05	100.00	0.01	1.17
10.00	1.59	0.60	6.56	0.35	21.95	0.05	100.00	0.00	1.16
6.00	1.71	0.61	6.63	0.34	19.60	0.05	100.00	0.00	1.09
4.00	1.39	0.56	5.63	0.37	17.02	0.07	100.00	0.00	1.09
2.00	1.44	0.57	5.48	0.35	15.68	0.08	100.00	0.00	1.04
1.90	1.27	0.56	5.26	0.37	15.59	0.08	100.00	0.00	1.08
1.70	1.44	0.59	5.97	0.36	18.11	0.05	100.00	0.00	1.24
1.50	1.49	0.60	6.11	0.35	18.00	0.06	100.00	0.00	1.04
1.40	1.34	0.57	5.35	0.35	15.72	0.07	100.00	0.00	1.09
1.30	1.21	0.53	5.13	0.38	15.51	0.08	100.00	0.00	1.07
1.25	1.52	0.64	5.64	0.30	15.56	0.06	100.00	0.00	1.00
1.10	1.36	0.60	5.06	0.32	14.09	0.08	100.00	0.00	1.09
1.00	1.35	0.62	4.95	0.30	13.61	0.08	100.00	0.00	1.10
0.90	1.54	0.62	5.68	0.33	20.16	0.04	100.00	0.01	1.05
0.80	1.61	0.58	6.21	0.35	22.74	0.04	100.00	0.03	1.15
0.70	1.26	0.50	4.79	0.36	23.04	0.04	100.00	0.09	1.05
0.60	1.00	0.00	2.20	0.66	9.07	0.16	99.65	0.18	1.17
0.50	1.00	0.00	2.55	0.69	9.95	0.11	99.57	0.21	1.28
0.40	1.00	0.00	2.11	0.55	11.52	0.08	101.02	0.38	1.08
0.30	1.00	0.00	2.64	0.59	23.20	0.03	100.58	0.37	1.16
0.20	1.00	0.00	1.77	0.31	24.05	0.03	102.14	0.65	1.04
0.10	1.00	0.00	2.22	0.26	40.26	0.03	101.12	0.71	1.09

Table S5.2. Parameters retrieved from the MFA of pyrene excimer for [Py-3-12] = 10 μM with CT-DNA concentration ranging from 0.001 to 0.115 mM and both concentrations expressed by the (-/+) ratio.

(-/+) ratio	$f_{E_{diff}}^{E0}$	f_{EE0}	τ_{E0} (*ns*)	$f_{E_{diff}}^{D}$	f_{ED}	τ_{D} (*ns*)	χ^2
11.50	0.27	0.13	39.16	0.45	0.15	70.06	1.17
10.00	0.27	0.13	38.63	0.46	0.14	69.60	1.16
6.00	0.20	0.08	32.72	0.52	0.20	66.10	1.09
4.00	0.09	0.21	32.55	0.68	0.02	66.38	1.09
2.00	0.23	0.03	31.77	0.53	0.21	66.19	1.04
1.90	0.22	0.07	32.62	0.56	0.15	66.02	1.08
1.70	0.05	0.23	31.76	0.71	0.01	65.90	1.24
1.50	0.05	0.25	33.95	0.69	0.00	66.11	1.04
1.40	0.30	0.00	33.35	0.48	0.22	66.39	1.09
1.30	0.17	0.10	30.84	0.63	0.10	65.28	1.07
1.25	0.45	0.00	36.97	0.39	0.16	68.33	1.00
1.10	0.43	0.00	34.29	0.40	0.17	66.33	1.09
1.00	0.38	0.00	32.99	0.51	0.12	64.69	1.10
0.90	0.31	0.11	31.59	0.50	0.08	63.18	1.05
0.80	0.38	0.24	38.75	0.28	0.10	68.14	1.15
0.70	0.25	0.21	29.90	0.47	0.06	58.96	1.05
0.60	0.38	0.18	35.18	0.44	0.00	67.72	1.17
0.50	0.47	0.11	33.69	0.42	0.00	65.73	1.28
0.40	0.49	0.08	36.82	0.43	0.00	70.32	1.08
0.30	0.59	0.00	32.52	0.38	0.03	64.90	1.16
0.20	0.44	0.15	32.30	0.40	0.01	67.54	1.04
0.10	0.70	0.00	30.18	0.25	0.05	65.50	1.09

Table S5.3. Molar fractions of the different pyrene species and <k> values from MFA of [Py-3-12] = 10 μM with CT-DNA concentration ranging from 0.001 to 0.115 mM and both concentrations expressed by the (-/+) ratio.

(-/+) ratio	<k>	f_{free}	f_{diff}^{E0}	f_{diff}^{D}	f_{diff}	f_{E0}	f_{D}	f_{agg}	I_E/I_M
11.50	0.22	0.00	0.27	0.45	0.71	0.13	0.15	0.28	15.85
10.00	0.22	0.00	0.27	0.46	0.72	0.13	0.14	0.27	15.76
6.00	0.22	0.00	0.20	0.52	0.72	0.08	0.20	0.28	16.32
4.00	0.24	0.00	0.09	0.68	0.77	0.21	0.02	0.23	16.08
2.00	0.24	0.00	0.23	0.53	0.76	0.03	0.21	0.24	17.29
1.90	0.25	0.00	0.22	0.55	0.77	0.07	0.15	0.22	17.35
1.70	0.24	0.00	0.05	0.71	0.76	0.23	0.01	0.23	17.12
1.50	0.24	0.00	0.05	0.69	0.75	0.25	0.00	0.25	17.48
1.40	0.25	0.00	0.30	0.48	0.78	0.00	0.22	0.22	17.31
1.30	0.25	0.00	0.17	0.63	0.80	0.10	0.10	0.20	15.98
1.25	0.27	0.00	0.45	0.38	0.84	0.00	0.16	0.16	16.69
1.10	0.27	0.00	0.43	0.40	0.83	0.00	0.17	0.17	16.34
1.00	0.29	0.00	0.38	0.50	0.88	0.00	0.12	0.12	16.16
0.90	0.27	0.01	0.30	0.49	0.80	0.11	0.08	0.20	13.44
0.80	0.23	0.02	0.37	0.27	0.65	0.23	0.10	0.33	10.23
0.70	0.26	0.07	0.23	0.44	0.67	0.20	0.06	0.26	4.35
0.60	0.27	0.15	0.32	0.38	0.70	0.15	0.00	0.15	2.34
0.50	0.27	0.19	0.38	0.34	0.72	0.09	0.00	0.09	1.73
0.40	0.30	0.36	0.32	0.28	0.59	0.05	0.00	0.05	0.84
0.30	0.26	0.37	0.37	0.24	0.61	0.00	0.02	0.02	0.71
0.20	0.25	0.61	0.17	0.15	0.33	0.06	0.00	0.06	0.27
0.10	0.15	0.70	0.21	0.07	0.29	0.00	0.02	0.02	0.16

Parameters retrieved from the analysis of the fluorescence decays of PyO-3-12 and CT-DNA complexes

Table S5.4. Parameters retrieved from the MFA of pyrene monomer for [PyO-3-12] = 16 μM with CT-DNA concentration ranging from 0.001 to 0.100 mM and both concentrations expressed by the (-/+) ratio.

(-/+) ratio	τ_1 (ns)	a_1	τ_2 (ns)	a_2	τ_3 (ns)	a_3	τ_M (ns)	a_M	χ^2
10.00	2.26	0.66	8.00	0.28	33.87	0.06	144.00	0.01	1.08
8.00	2.22	0.68	8.13	0.27	34.62	0.05	144.00	0.00	1.01
5.00	2.07	0.67	7.20	0.29	29.79	0.04	144.00	0.00	1.06
2.00	1.98	0.67	7.03	0.29	28.27	0.04	144.00	0.00	1.06
1.80	2.00	0.67	7.08	0.28	27.12	0.04	144.00	0.00	1.07
1.60	1.99	0.67	6.98	0.29	26.98	0.04	144.00	0.00	1.12
1.50	2.17	0.68	7.27	0.28	27.55	0.04	144.00	0.00	1.18
1.40	1.77	0.67	6.62	0.29	26.23	0.03	144.00	0.00	1.10
1.30	1.77	0.68	6.58	0.29	25.66	0.04	144.00	0.00	1.11
1.20	1.82	0.67	6.73	0.29	25.83	0.04	144.00	0.00	1.11
1.10	1.60	0.61	5.94	0.31	20.85	0.05	144.00	0.03	1.06
1.00	1.45	0.46	5.32	0.28	22.47	0.05	144.00	0.22	0.99
0.90	1.43	0.37	5.42	0.20	25.88	0.04	144.00	0.38	1.06
0.80	1.16	0.28	4.36	0.18	23.67	0.04	144.00	0.50	1.08
0.70	1.00	0.00	2.09	0.26	12.75	0.07	141.90	0.67	0.99
0.60	1.00	0.00	2.06	0.26	11.74	0.07	141.76	0.67	1.00
0.50	1.00	0.00	2.38	0.21	16.54	0.05	142.52	0.74	0.96
0.40	1.00	0.00	2.76	0.17	25.35	0.04	143.75	0.79	1.06
0.30	1.00	0.00	2.68	0.10	53.91	0.07	147.46	0.83	1.09
0.20	1.00	0.00	2.70	0.09	65.61	0.09	149.06	0.83	1.05
0.10	1.00	0.00	2.47	0.07	71.37	0.10	151.61	0.83	1.14

Table S5.5. Parameters retrieved from the MFA of pyrene excimer for [PyO-3-12] = 16 μM with CT-DNA concentration ranging from 0.001 to 0.100 mM and both concentrations expressed by the (-/+) ratio.

(-/+) ratio	$f_{E_{diff}}^{E0}$	f_{EE0}	τ_{E0} (ns)	$f_{E_{diff}}^{D}$	f_{ED}	τ_{D} (ns)	χ^2
10.00	0.00	0.31	31.53	0.38	0.32	60.33	1.08
8.00	0.00	0.31	32.23	0.40	0.29	60.27	1.01
5.00	0.00	0.28	30.45	0.39	0.33	59.45	1.06
2.00	0.00	0.27	30.38	0.40	0.33	59.28	1.06
1.80	0.00	0.28	30.53	0.40	0.32	59.87	1.07
1.60	0.00	0.26	29.54	0.41	0.32	59.23	1.12
1.50	0.00	0.28	30.22	0.39	0.33	59.44	1.18
1.40	0.00	0.30	31.48	0.44	0.26	59.81	1.10
1.30	0.00	0.32	30.79	0.43	0.25	59.83	1.11
1.20	0.00	0.34	33.10	0.43	0.23	60.89	1.11
1.10	0.00	0.32	30.62	0.46	0.22	57.95	1.06
1.00	0.09	0.24	30.21	0.36	0.31	56.40	0.99
0.90	0.00	0.38	31.67	0.47	0.15	56.81	1.06
0.80	0.20	0.21	31.84	0.30	0.29	57.83	1.08
0.70	0.17	0.15	25.79	0.24	0.44	56.01	0.99
0.60	0.18	0.10	25.37	0.25	0.47	56.43	1.00
0.50	0.15	0.25	30.96	0.23	0.37	60.02	0.96
0.40	0.18	0.32	33.72	0.20	0.31	62.82	1.06
0.30	0.28	0.39	37.14	0.15	0.17	62.61	1.09
0.20	0.32	0.31	37.62	0.18	0.19	54.16	1.05
0.10	0.25	0.28	39.20	0.34	0.13	42.02	1.14

Table S5.6. Molar fractions of the different pyrene species and <k> values from MFA of [PyO-3-12] = 16 μM with CT-DNA concentration ranging from 0.001 to 0.100 mM and both concentrations expressed by the (-/+) ratio.

(-/+) ratio	<k>	f_{free}	f_{diff}^{E0}	f_{diff}^{D}	f_{diff}	f_{E0}	f_{D}	f_{agg}	I_E/I_M
10.00	0.17	0.00	0.00	0.38	0.38	0.31	0.32	0.62	20.47
8.00	0.18	0.00	0.00	0.40	0.40	0.31	0.29	0.60	21.45
5.00	0.20	0.00	0.00	0.39	0.39	0.28	0.33	0.61	25.29
2.00	0.22	0.00	0.00	0.40	0.40	0.27	0.33	0.60	27.12
1.80	0.22	0.00	0.00	0.40	0.40	0.28	0.32	0.60	26.82
1.60	0.22	0.00	0.00	0.41	0.41	0.26	0.32	0.59	26.32
1.50	0.21	0.00	0.00	0.39	0.39	0.28	0.33	0.61	26.62
1.40	0.24	0.00	0.00	0.44	0.44	0.30	0.26	0.56	26.69
1.30	0.24	0.00	0.00	0.43	0.43	0.32	0.25	0.57	27.29
1.20	0.24	0.00	0.00	0.43	0.43	0.34	0.23	0.57	26.72
1.10	0.24	0.01	0.00	0.45	0.45	0.32	0.22	0.54	13.00
1.00	0.24	0.11	0.08	0.32	0.40	0.21	0.27	0.49	2.35
0.90	0.22	0.23	0.00	0.36	0.36	0.29	0.11	0.41	1.05
0.80	0.23	0.34	0.13	0.20	0.33	0.14	0.19	0.33	0.62
0.70	0.22	0.45	0.09	0.13	0.22	0.08	0.24	0.33	0.39
0.60	0.23	0.46	0.10	0.13	0.23	0.06	0.25	0.31	0.38
0.50	0.19	0.53	0.07	0.11	0.18	0.12	0.18	0.29	0.30
0.40	0.13	0.59	0.07	0.08	0.15	0.13	0.13	0.26	0.23
0.30	0.04	0.68	0.09	0.05	0.14	0.13	0.06	0.18	0.13
0.20	0.02	0.71	0.09	0.05	0.15	0.09	0.06	0.15	0.10
0.10	0.02	0.75	0.06	0.09	0.15	0.07	0.03	0.10	0.07

Parameters retrieved from the analysis of the fluorescence decays of PyO-3-12, CT-DNA, and SDS complexes

Table S5.7. Parameters retrieved from the MFA of pyrene monomer for [PyO-3-12] = 16 μM, [PyO-3-12]:[CT-DNA] = 1.5 and SDS concentration ranging from 0.0001 to 50 mM.

(-/+) ratio	τ_1 (ns)	a_1	τ_2 (ns)	a_2	τ_3 (ns)	a_3	τ_M (ns)	a_M	χ^2
50.00	3.22	0.13	10.70	0.39	43.87	0.12	144.00	0.35	1.06
40.00	3.18	0.20	9.64	0.68	34.29	0.06	144.00	0.05	1.06
30.00	3.00	0.23	9.64	0.72	33.99	0.04	144.00	0.02	1.05
20.00	2.54	0.19	8.91	0.75	27.25	0.05	144.00	0.02	1.03
10.00	2.81	0.22	9.24	0.73	28.48	0.04	144.00	0.01	1.08
9.00	2.48	0.18	9.18	0.77	28.01	0.04	144.00	0.01	1.03
8.00	2.73	0.20	10.20	0.76	33.14	0.03	144.00	0.01	1.01
7.00	2.81	0.19	9.74	0.78	32.86	0.03	144.00	0.00	1.01
6.00	2.99	0.24	9.23	0.74	34.29	0.02	144.00	0.00	1.08
5.00	2.42	0.22	8.48	0.76	31.07	0.02	144.00	0.00	1.07
2.00	2.27	0.31	6.79	0.68	40.34	0.01	144.00	0.00	1.01
1.00	2.09	0.32	6.23	0.67	35.84	0.01	144.00	0.00	1.00
0.50	1.95	0.34	6.22	0.65	40.16	0.01	144.00	0.00	1.07
0.30	1.94	0.34	5.91	0.64	39.52	0.01	144.00	0.00	1.05
0.10	2.02	0.52	5.02	0.47	42.17	0.01	144.00	0.00	1.09
0.05	2.03	0.54	4.75	0.44	38.30	0.01	144.00	0.00	1.11
0.02	1.93	0.59	4.64	0.39	34.88	0.01	144.00	0.00	1.18
0.01	1.60	0.64	4.86	0.34	29.44	0.02	144.00	0.00	1.16
0.005	1.35	0.66	4.85	0.31	24.23	0.03	144.00	0.00	1.07
0.001	1.33	0.67	5.21	0.29	22.20	0.04	144.00	0.00	1.16
0.0001	1.35	0.70	5.76	0.27	24.21	0.04	144.00	0.00	1.05

Table S5.8. Parameters retrieved from the MFA of pyrene excimer for [PyO-3-12] = 16 μM, [PyO-3-12]:[CT-DNA] = 1.5 and SDS concentration ranging from 0.0001 to 50 mM.

(-/+) ratio	$f_{E_{diff}}^{E0}$	f_{EE0}	τ_{E0} (ns)	$f_{E_{diff}}^{D}$	f_{ED}	τ_{D} (ns)	χ^2
50.00	0.91	0.09	46.61	0.00	0.00	1.00	1.06
40.00	0.89	0.11	47.58	0.00	0.00	1.00	1.06
30.00	0.89	0.11	47.43	0.00	0.00	1.00	1.05
20.00	0.90	0.10	47.86	0.00	0.00	1.00	1.03
10.00	0.90	0.10	47.44	0.00	0.00	1.00	1.08
9.00	0.90	0.10	47.79	0.00	0.00	1.00	1.03
8.00	0.91	0.09	46.63	0.00	0.00	1.00	1.01
7.00	0.91	0.09	47.14	0.00	0.00	1.00	1.01
6.00	0.79	0.10	48.63	0.11	0.00	31.63	1.08
5.00	0.60	0.10	40.41	0.30	0.00	50.82	1.07
2.00	0.35	0.00	40.28	0.51	0.14	54.28	1.01
1.00	0.38	0.00	42.16	0.48	0.14	55.49	1.00
0.50	0.36	0.00	41.06	0.50	0.14	55.83	1.07
0.30	0.39	0.01	42.21	0.47	0.13	56.75	1.05
0.10	0.49	0.00	41.13	0.26	0.24	59.45	1.09
0.05	0.48	0.00	42.15	0.27	0.24	61.09	1.11
0.02	0.45	0.00	40.24	0.25	0.30	60.92	1.18
0.01	0.43	0.00	37.03	0.26	0.31	60.97	1.16
0.005	0.41	0.00	35.87	0.23	0.36	61.29	1.07
0.001	0.26	0.00	30.20	0.33	0.40	59.60	1.16
0.0001	0.11	0.20	33.22	0.49	0.20	60.93	1.05

Table S5.9. Molar fractions of the different pyrene species and <k> values from MFA of [PyO-3-12] = 16 μM, [PyO-3-12]:[CT-DNA] = 1.5 and SDS concentration ranging from 0.0001 to 50 mM.

(-/+) ratio	<k>	f_{free}	f_{diff}^{E0}	f_{diff}^{D}	f_{diff}	f_{E0}	f_{D}	f_{agg}	I_E/I_M
50.00	0.06	0.33	0.61	0.00	0.61	0.06	0.00	0.06	0.49
40.00	0.09	0.05	0.85	0.00	0.85	0.10	0.00	0.10	2.76
30.00	0.10	0.02	0.87	0.00	0.87	0.11	0.00	0.11	4.12
20.00	0.11	0.02	0.89	0.00	0.89	0.10	0.00	0.10	4.47
10.00	0.11	0.01	0.89	0.00	0.89	0.10	0.00	0.10	4.80
9.00	0.11	0.01	0.89	0.00	0.89	0.09	0.00	0.09	4.70
8.00	0.10	0.01	0.91	0.00	0.91	0.09	0.00	0.09	4.65
7.00	0.10	0.00	0.91	0.00	0.91	0.09	0.00	0.09	5.20
6.00	0.11	0.00	0.79	0.11	0.90	0.10	0.00	0.10	5.80
5.00	0.12	0.00	0.60	0.30	0.90	0.10	0.00	0.10	5.80
2.00	0.17	0.00	0.35	0.51	0.86	0.00	0.14	0.14	9.44
1.00	0.18	0.00	0.38	0.48	0.86	0.00	0.14	0.14	10.49
0.50	0.19	0.00	0.36	0.50	0.86	0.00	0.14	0.14	10.90
0.30	0.20	0.00	0.39	0.47	0.86	0.01	0.13	0.14	11.52
0.10	0.25	0.00	0.49	0.26	0.76	0.00	0.24	0.24	16.68
0.05	0.27	0.00	0.48	0.27	0.76	0.00	0.24	0.24	17.94
0.02	0.28	0.00	0.45	0.25	0.70	0.00	0.30	0.30	20.31
0.01	0.30	0.00	0.43	0.26	0.69	0.00	0.31	0.31	20.84
0.005	0.31	0.00	0.41	0.23	0.64	0.00	0.36	0.36	23.54
0.001	0.30	0.00	0.26	0.33	0.60	0.00	0.40	0.40	24.16
0.0001	0.29	0.00	0.11	0.49	0.60	0.20	0.20	0.40	23.47